

https://dspace.org/

Fast oxide ion conductors for solid oxide fuel cells: average and local structure – property correlations in solid solutions of bi2o3

Masina,Sikhumbuzo Mfanawemphi

2023
University of the Witwatersrand, Johannesburg
https://hdl.handle.net/10539/42076
Masina,Sikhumbuzo Mfanawemphi. (2023). Fast oxide ion conductors for solid oxide fuel cells: average and local structure – property correlations in solid solutions of bi2o3 [PhD thesis, University of the Witwatersrand, Johannesburg]. WireDSpace.

Downloaded from a DSpace repository. https://dspace.org/

FAST OXIDE ION CONDUCTORS FOR SOLID OXIDE FUEL CELLS: AVERAGE AND LOCAL STRUCTURE – PROPERTY CORRELATIONS IN SOLID SOLUTIONS OF Bi_2O_3

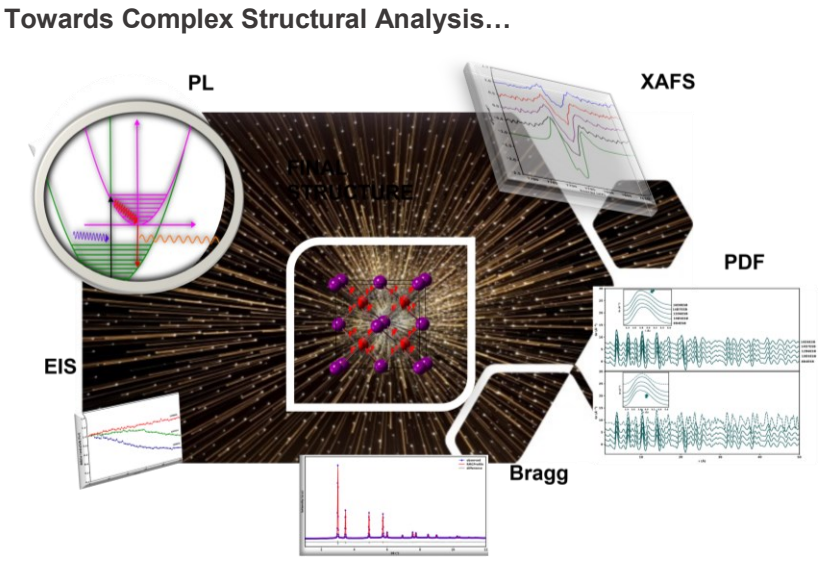

Sikhumbuzo Mfanawemphi Masina

Principal supervisor: Prof. David Gordon Billing

Co-supervisor: Prof. Caren Billing

A thesis submitted to the Faculty of Science, University of the Witwatersrand, Johannesburg, in fulfilment of the requirements for the degree of Doctor of Philosophy.

Signed on 12/04/2023.

DECLARATION

I declare that this thesis is my own, unaided work. It is being submitted for the Degree of Doctor of Philosophy at the University of the Witwatersrand, Johannesburg. It has not been submitted before for any degree or examination at any other University.

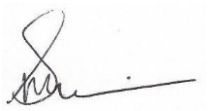

_____

(Signature of candidate)

12th day of April 2023 at Wits University, Johannesburg, South Africa

ABSTRACT

In this thesis, substituted Bi_2O_3 systems were fabricated and characterized. W, Dy, Er and Nb were used as substituents in a goal to stabilise the highly conductive δ-Bi_2O_3 like phases (hence forth referred to as the δ-phases) to ambient temperatures. Changes in both the average and local structures of the substituted Bi_2O_3 systems were correlated with the physical property conductivity. In the first part of the thesis, powder X-ray diffraction and Raman spectroscopy were used to show that WO_3 on its own did not stabilise the δ-phase at ambient temperatures. The true equilibrium phase in the Bi_2O_3-WO_3 system was a mixture of two tetragonal phases $7Bi_2O_3 \cdot 2WO_3$ and $7Bi_2O_3 \cdot WO_3$. The co-doping strategy was used to fabricate the Bi_2O_3-Dy_2O_3-WO_3 system (DWSB, where D =Dy, SB = stabilised Bi_2O_3). The δ-phase was stabilised with a minimum of 15 mol% total substituent concentration. Powder X-ray diffraction indicated that the δ-phases obtained in this system were metastable and degraded after isothermal annealing at ~ 500 °C for 100 hours. Addition of Er to the DWSB system to create the novel system Bi_2O_3-Dy_2O_3-Er_2O_3-WO_3 (DEWSB, where E=Er) was found to significantly improve the stability of the δ-phase when annealed at virtually identical conditions as DWSB.

The rest of the thesis is focused on the effect of each substituent cation on phase stability, local structure and the ageing phenomenon–the decrease in ionic conductivity upon isothermal annealing without any observable changes in average structure under powder X-ray diffraction. X-ray pair distribution function, X-ray absorption spectroscopy and photoluminescence were used to probe the local structure around the host Bi cations and some of the substituent cations (Dy, Er, W). The results indicated that some of the Bi cations are displaced away from the 4*a* site of the defect fluorite structure (*Fm*-3*m*) and that at the local level, the Bi cations assume an arrangement similar to that found in the monoclinic α-Bi_2O_3 phase. Dy and Er were also found to prefer local environments similar to those in their parent oxides. The resemblance increased as the material aged and might explain why the conductivity decreases upon ageing.

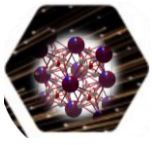

STRUCTURE AND OUTPUTS OF THE THESIS

The thesis is divided into 8 chapters:

(a) Chapter 1: Introduction

(b) Chapter 2: Experimental Methods

(c) Chapters 3-7: Results and Discussion

(d) Chapter 8: General Conclusions and Recommendations

Research outputs comprises one published manuscript, one submitted manuscript, oral and poster presentations in local and international conferences.

Publications:

1. **Masina, S.M.**, Billing, C., Erasmus, R.M. and Billing, D.G., 2021. Insights on the phase transitions, stability and conductivity in the Bi_2O_3-WO_3 system. *Journal of Electroceramics*, *46*(2), pp.47-56.

   Masina S.M. (Conducted the research and wrote the manuscript).

   Billing, C. (Supervised the research and reviewed the manuscript).

   Erasmus, R.M. (Assisted with Raman Spectroscopy data analysis and reviewed the manuscript).

   Billing, D.G. (Supervised the research and reviewed the manuscript).

2. **Masina, S.M.**, Billing, C., Erasmus, R.M. and Billing, D.G. A Temperature Dependent Phase Evolution Study of a Quaternary Bi_2O_3 Solid Electrolyte (submitted to Solid State Sciences).

   Masina S.M. (Conducted the research and wrote the manuscript).

   Billing, C. (Supervised the research and reviewed the manuscript).

   Erasmus, R.M. (Assisted with Raman Spectroscopy data analysis and reviewed the manuscript).

   Billing, D.G. (Supervised the research and reviewed the manuscript).

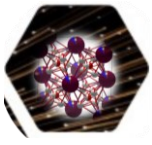

Conferences:

1. Bi^{3+}, Er^{3+}, Nb^{5+} and W^{6+}: "The Fantastic Four" in "Solid Solutions" of Bi_2O_3 (Poster)

   S. M. Masina, G. C. Nkala, D. Olds, Y. Zhang, R.M. Erasmus, C. Billing, D. G. Billing, 17th European Powder Diffraction Conference, 31 May-3 June 2022

2. The Neglected Cation Sublattice in Solid Solutions of Bismuth Oxide: "There is More to it than Meets the Eye" (Poster)

   S. M. Masina, G. C. Nkala, K. H. Stone, C. Billing, D. G. Billing, 4th US School on Total Scattering Analysis, Virtual, 20 October to 12 November 2021

3. Probing the Local Structure of Bi_2O_3 Chemical Derivatives: The Tale of the Neglected Cation Sublattice (oral)

   S. M. Masina, G. C. Nkala, K. H. Stone, Y. Zhang, C. Billing, D. G. Billing, ASNAEM-2021 Workshop, African Synchrotron Network for Advanced Energy Materials, Virtual, 6 October 2021

4. Symmetry Mode: Fitting Subtle Peak Splitting in the Bi_2O_3-Dy_2O_3-Er_2O_3 System (Oral)

   S.M. Masina, C. Billing, D.G. Billing, 70th Annual Denver X-ray Conference, Virtual, 2-6 August 2021

5. Superionic conductors for solid oxide fuel cells: structure-bulk property relationships in Bi_2O_3 based solid solutions (Oral)
   S.M. Masina, C. Billing, D.G. Billing, 5th International Symposium on Electrochemistry (Oral)–August 2019
6. Fast oxide ion conductors: structure-property correlations in Bi_2O_3 solid solutions (Poster)
   S.M. Masina, C. Billing, D.G. Billing, The 43rd SACI Conference-Chemistry for a sustainable African Economy–December 2018

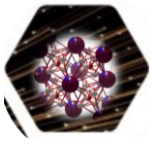

To my family:

I will forever be indebted to you.

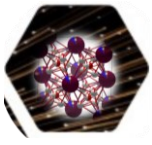

ACKNOWLEDGEMENTS

With great indebtedness and sincere gratitude, I would like to thank my supervisors Prof. Dave Billing and Prof. Caren Billing for their keen insights, unwavering support and wonderful memories shared through the years spent on this work. I grew both intellectually and as a person under their tutelage. Their guidance was phenomenal. I would also like to thank Prof. Rudolph Erasmus of the School of Physics, University of the Witwatersrand who was instrumental in making sure we have quality Raman spectroscopy and photoluminescence data. His deep knowledge was a treasure trove.

Gratitude goes also to the University of the Witwatersrand, School of Chemistry, Global Challenge Research Funds-Synchrotron Techniques for African Research and Technology (GCRF-START) and the International Centre for Diffraction Data for financial support.

The support and insights provided by Dr Daniel Olds at NSLS II, Brookhaven National Laboratory was highly appreciated. His deep knowledge of total scattering was vital in ensuring we got quality data. I would like to thank Dr Milinda Abeykoon and Dr Eric Dooryhee for making sure that we had all the needed equipment and support in their beamline 28-ID-1 at NSLS II.

Dr Kevin Stone from Stanford Synchrotron Radiation lightsource was instrumental in us getting our first X-ray absorption spectroscopy (XAS) data. His contribution to the success of this work is highly appreciated. I would also like to thank Dr Bruce Ravel from 6-BM, at NSLS II, Brookhaven National Laboratory for enabling us to collect high quality XAS data. His expertise was incredible. Dr Yuanpeng Zhang from Oak Ridge National Laboratory selflessly shared his program Topas4RMC and provided incredible support on setting up RMCProfile for big-box modelling. His time and contribution are well appreciated.

Without the support from my family and friends it would be nearly impossible for me to start and finish this work. Their support was unwavering through tough times, but most importantly shared the joyful moments with me.

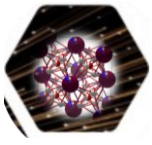

Finally, I would like to express my profound gratitude to my colleague, collaborator, and biggest cheerleader, Ms. Gugulethu Nkala. Her support and love were rock solid throughout the duration of this work. Her intelligence and advice played a significant role in making sure that I finish this work. Thank you very much.

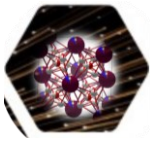

Contents

FAST OXIDE ION CONDUCTORS FOR SOLID OXIDE FUEL CELLS: AVERAGE AND LOCAL STRUCTURE – PROPERTY CORRELATIONS IN SOLID SOLUTIONS OF Bi_2O_3 ..... **i**

DECLARATION ii

ABSTRACT iii

STRUCTURE AND OUTPUTS OF THE THESIS iv

ACKNOWLEDGEMENTS vii

LIST OF FIGURES xiv

LIST OF TABLES xxvi

LIST OF ABBREVIATIONS xxvii

COMPOSITION CONVERSION TABLE xxix

Chapter 1 ..... **1**

1.1 Introduction 1

1.1.1 Solid Oxide Fuel Cells 1

1.1.2 Structure of a SOFC 2

1.1.3 Operation of a SOFC 2

1.2 Pure Bismuth Oxide 6

1.3 The Bi_2O_3-WO_3 system 12

1.4 The Bi_2O_3-Dy_2O_3 system 14

1.5 The Bi_2O_3-Er_2O_3 system 15

1.6 The Bi_2O_3-Dy_2O_3-WO_3 system 16

1.7 Aims and Objectives of the Project 16

1.8 References 17

Chapter 2: Experimental Techniques **24**

2.1 Synthetic Methods 24

2.1.1 Solid-state Reactions 24

2.1.2 Citrate-gel Method 26

2.2 Diffraction 27

2.2.1 Bragg's Law 27

2.2.2 Crystal Systems and the Crystallographic Lattices 29

2.2.3 Symmetry Relationships Between Space Groups 33

2.2.4 Powder X-ray Diffraction 35

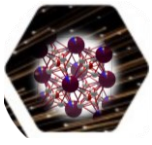

2.2.5 The Rietveld Method 37
2.2.6 Total Scattering and the PDF Method 40
2.3 X-ray Absorption Spectroscopy (XAS) 44
2.3.1 Absorption 44
2.3.2 X-ray Absorption Fine Structure 46
2.3.3 The XANES region 47
2.3.4 The EXAFS region 48
2.4 Raman and Photoluminescence spectroscopy 50
2.4.1 Raman spectroscopy 50
2.4.2 Photoluminescence 52
2.5 Electrochemical Impedance Spectroscopy (EIS) 54
2.6 References 58
2.7 Bibliography 63
Chapter 3: Insights on the phase transitions, stability and conductivity in the Bi_2O_3-WO_3 system **66**
3.1 Introduction 67
3.2 Experimental 69
3.2.1 Synthetic procedures and materials 69
3.2.2 Characterization techniques 70
3.3 Results and discussion 72
3.3.1 Ambient temperature phase studies 72
3.3.2 Variable temperature phase studies 77
3.3.3 Conductivity studies 78
3.4 Conclusion 82
3.5 Acknowledgements 82
3.6 References 83
3.7 Supporting Information 86
Chapter 4: A Temperature Dependent Phase Evolution Study of a Quaternary Bi_2O_3 Solid Electrolyte **100**
4.1 Introduction 101
4.2 Experimental 102
4.2.1 Synthetic procedures 102
4.2.2 Characterization techniques 103
4.3 Results and discussion 105

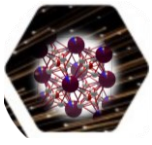

4.3.1 Initial phase assessment 105
4.3.2 Conductivity measurements 108
4.3.3 Variable temperature-PXRD and Rietveld studies 109
4.3.4 Raman spectroscopy 114
4.4 Conclusion 117
4.5 Acknowledgements 118
4.6 References 118
4.7 Supporting Information 123
Chapter 5: Symmetry Mode Analysis: Uncovering the Ambiguities and Complexities Between Related Phases in the Bi_2O_3-Dy_2O_3-Er_2O_3 System **134**
5.1 Introduction 135
5.2 Experimental methods 137
5.2.1 Synthetic method 137
5.2.2 Data collection and analysis 137
5.1 Results and Discussion 139
5.1.1 Preliminary Phase Analysis and Conductivity Measurements 139
5.1.2 The Local Structure from X-ray Total Scattering 144
5.1.3 Symmetry Mode Based Parametric Rietveld Refinement 148
5.2 Conclusion 153
5.3 Acknowledgements 154
5.4 References 154
5.5 Supporting Information 160
Chapter 6: Probing the Local Structure of Bi_2O_3 Chemical Derivatives: The Neglected Cation Sublattice **179**
6.1 Introduction 180
6.2 Experimental Methods 181
6.2.1 Synthetic methods 181
6.2.2 Bragg data 182
6.2.3 Total scattering and the PDF technique 182
6.2.4 X-ray Absorption Spectroscopy 183
6.3 Results and Discussion 184
6.3.1 Average Structure Analysis 184
6.3.2 Total scattering and the PDF Technique 186
6.3.3 The L_3-edge XANES analyses of Dy, Er and W dopants 191

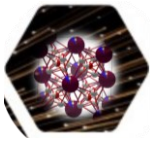

6.4 Conclusions 196
6.5 Acknowledgements 196
6.6 References 197
6.7 Supporting Information 203
Chapter 7: Application of "Pseudo-Complex" Structural Analysis Methods to Unravel the Complexities of the Ageing Process in Bi_2O_3 "Solid Solutions" **214**
7.1 Introduction 215
Experimental Methods 217
7.1.1 Synthetic method 217
7.1.2 Powder X-ray diffraction 217
7.1.3 Differential thermal analysis 218
7.1.4 Electrochemical Impedance Spectroscopy (EIS) 219
7.1.5 Photoluminescence Spectroscopy (PL) 219
7.1.6 X-ray Absorption Fine Structure (XAFS) 219
7.2 Results and Discussion 220
7.2.1 Phase Stability and Ageing in the DEWSB System 220
7.2.2 Phase Stability in the DWSB System–A Comparison with the DEWSB System 222
7.2.4 Phase stability in the DESB System−A Comparison with the DEWSB System 226
7.2.5 The DENSB System−the Role of Nb^{5+} in the Order–Disorder Transition 226
7.2.6 Electrochemical Impedance Spectroscopy 228
7.2.7 Photoluminescence Spectroscopy 229
7.2.8 X-ray Absorption Fine Structure 230
7.2.9 Total scattering Analysis 236
7.3 Conclusions 239
7.4 Acknowledgements 239
7.5 References 240
7.1 Supporting Information 247
Chapter 8: General Conclusions and Recommendations **260**
8.1 The effects of W, Dy and/or Er on phase stability 260
8.2 The Bi_2O_3-Dy_2O_3-Er_2O_3 (DESB) system compared to DWSB and DEWSB ...262
8.3 The Effects of the Dy and Nb Cations on Phase Stability and the Ageing Phenomenon 263

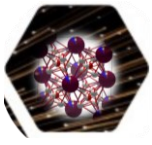

8.4 The Effects of the Substituents on the Metal Sublattice in the δ-phase.....264
8.5 References 266

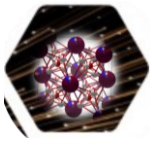

LIST OF FIGURES

Figure: 1.1. Structure of a solid oxide fuel cell showing the cathode, anode, and electrolyte……..2

Figure 1.2. Structure of a SOFC showing the redox reactions on the electrodes and the flow of oxide ions through the electrolyte. YSZ-Ni is a composite of yttria stabilized zirconia and metallic nickel……3

Figure 1.3. Three possible vacancy migration pathways in the fluorite structure. Purple spheres represent cations, red ones represent oxide ions and the square represents a vacant site. The inset shows the bottle neck in one of the migration paths……..4

Figure 1.4. One of the quadrants of a fluorite unit cell showing how the oxygens are distributed around the cation in a different representation of the fluorite structure. Purple and red spheres are Bi^{3+} and $O^{2-,}$ respectively……..5

Figure 1.5. A unit cell representation of the monoclinic α–Bi_2O_3 phase showing how the layers of the Bi^{3+}cations sandwich the O^{2-} anions. Purple and red spheres are Bi^{3+} and O^{2-}, respectively……...7

Figure 1.6. A unit cell representation of the Sillen model showing how the O^{2-} vacancies are ordered along the <111> direction. Purple and red spheres are Bi^{3+} and $O^{2-,}$ respectively……...8

Figure 1.7. The Gattow and Schroder model showing how the O^{2-} vacancies are statistically distributed in the regular 8*c* sites. Only 75% of the 8 available oxygen sites are statistically occupied as indicated by the fraction in each O atom…….....9

Figure 1.8. The Battle **(a)** and Hull **(b)** models showing the are distribution of oxide ions in the 8*c* and 32f sites. Purple and red spheres are Bi^{3+} and O^{2-}, respectively. Grey spheres represent vacancies……..10

Figure 1.9. Unit cell of the γ–Bi_2O_3 phase showing the vacancies on some of the O^{2-} and Bi^{3+} sites. Grey spheres represent vacancies……..11

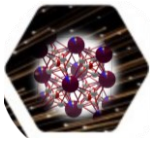

Figure 1.10. A unit cell representation of the tetragonal phase with space group $I4_1$ showing the mixed-metal sites, different polyhedral (octahedra and tetrahedra) and the oxide ion vacancies (white fractions in otherwise red spheres) ……13

Figure 2.1. Reaction mechanism of the solid-state reaction at the interfaces of MgO and Al_2O_3……24

Figure 2.2. Structure of a citric acid molecule and the fully ionized citrate ion…..…..26

Figure 2.3. Illustration of Bragg's law. The layers of atoms reflect the incident beam. When two layers are parallel and separated by a distance d, the incident ray reflected at the layer a distance d from the first layer will have travelled a distance 2dsinθ by the time they reach an observation point provided they are approximated to be parallel at that point……..28

Figure 2.4. A single crystal diffraction pattern. The red, green and white spots are reflections from planes that constitute atoms of different types and/or positions in the crystal……...29

Figure 2.5. A partial subgroup tree showing the relationship between the aristotype ($Fm\bar{3}m$) and its isotropy subgroups ($P\bar{4}2_1m$ and $P\bar{1}$)……....34

Figure 2.6. The Debye-Scherrer nested cones in 3D **(a)** are shown to transform into nested circles in 2D **(b)**. After integration of the intensity of each circle or part thereof, the 1D intensity is obtained **(c)**. Structure determination methods are employed to obtain a structure from the data **(d)**……...36

Figure 2.7. A fragment of a diffraction pattern showing the digitized intensity values as a function of 2θ. The open circles represent y_{calc} values and the closed circles represent y_{obs} values…….37

Figure 2.8. The difference profile plot showing the progress and merit of a Rietveld refinement. (a) illustrates how a mismatch in lattice parameter appears in the difference profile plot, and (b) illustrates an apparent good profile fit, yet the corresponding

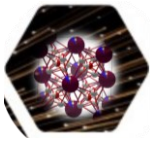

structure in (c) shows atoms are outside the unit cell in positions forbidden by symmetry and have wrong occupancies (more than 1)……..…..40

Figure 2.9. Illustration of the PDF as the measure of the probability of finding an atom centre in a given thin spherical shell of volume $dV = 4\pi r^2 dr$ within a radius r from a reference atom……..41

Figure 2.10. Crystal structure of Ni viewed along the a_1 axis **(a)** and its reduced total PDF **(b)** The arrows show the peak positions representing the first and second nearest neighbours' distances……...43

Figure 2.11. The absorption coefficient as a function of energy measured across the Bi L_3-edge in monoclinic Bi_2O_3. ……..44

Figure 2.12. The fall in intensity of an X-ray transmitted through a material follows an exponential decay function inside the material of thickness t…….45

Figure 2.13. A schematic showing a simplified version of the setup in a typical XAS beamline at a third-generation synchrotron. Both transmission and fluorescence detection modes are shown……...46

Figure: 2.14. A normalized XAFS spectrum of Dy_2O_3 measured in transmission mode and across the Dy L_3-edge showing some of the regions found in an XAFS spectrum……...47

Figure 2.15. A Schematic showing the origin of EXAFS. An electron is ejected from the absorber by a photon. The outgoing electron spherical wave spreads out and scatters from an absorber. The back-scattered electron wave interferes with the outgoing wave either destructively or constructively and modulates the absorption coefficient function……....49

Figure: 2.16. An illustration of the Rayleigh and Raman scattering events…….51

Figure: 2.17. Raman spectrum of 28.5DSB at ambient temperature showing the broad T_{2g} and external modes. This spectrum is typical for most δ-Bi_2O_3 like phases……52

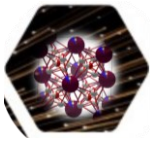

Figure: 2.18. Configuration-coordinate diagram illustrating the PL process……...53

Figure: 2.19. Excitation spectrum (solid line) and emission spectrum (dashed line) of 20ESB……..53

Figure 2.20. A Flow diagram showing the process involved in EIS. This involves the perturbation of an electrochemical system at equilibrium and measuring its response. Data analysis is usually done by using equivalent circuits and mechanistic insights are correlated with structural changes……54

Figure 2.21. An impedance plane plot showing the parameters normally used as initial starting values in data fitting. R_s represents the uncompensated resistance of the setup of the system, R_b is the bulk resistance of the material being probed……57

Figure 2.22. An equivalent circuit used in data fitting. Q represent a constant phase element; R is the resistance and W is the Warburg diffusion……57

Figure 3.1. XRD patterns showing the effect of annealing temperature (from 500-650°C) for samples with (a) 22% and (b) 25% WO_3……73

Figure 3.2. XRD patterns for samples with 22% and 25% WO_3 annealed at 800°C for 24 hours and slow cooled back to room temperature. The 25% sample was also annealed for a further 72 hours. The insets show more pronounced peak splitting due to improved crystallinity of the $7Bi_2O_3{\cdot}2WO_3$ phase upon further annealing……...74

Figure 3.3. XRD patterns showing the influence of concentration on phase composition for samples fabricated using **(a)** the citrate-gel method and **(b)** solid-state reactions, all annealed at 800°C. The * represents the resynthesised samples……..75

Figure 3.4. Raman spectra of the 22% WO_3 composition synthesised using the citrate-gel method and solid-state reactions where both samples were annealed at 800°C…...77

Figure 3.5. VT-Raman spectra from 200 cm^{-1} of the 27% WO_3 sample (fabricated via the citrate-gel method) showing phase stability up to 850°C. Intensities at 680°C were

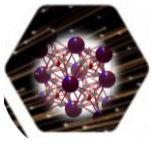

doubled and at 850°C were multiplied by a factor of twelve to enhance features……78

Figure 3.6. Arrhenius plots showing the temperature dependant bulk conductivities (in units of S cm^{-1}) for **(a)** 23%-26% WO_3 content samples for the heating cycle and **(b)** the 26% WO_3 content sample for both the heating and cooling cycles……...80

Figure 3.7. A DTA thermograms for the 23% WO_3 content sample (mass = 18.478 mg) showing only a slight endothermic displacement between 550-650 °C in the heating cycle. No baseline subtraction was done……..81

Figure 4.1. Diffraction patterns (λ = 1.7903 Å) showing results when optimising the total metal oxide dopant concentration. **(a)** The doubly substituted DWSB system employing a 2:1 ratio of Dy_2O_3:WO_3 showed the dominant δ-phase only for the 15 mol% total dopant concentration. The 6D6WSB with a 1:1 ratio clearly showed mixed phases. **(b)** The triply substituted DEWSB system needed 12 mol% total metal oxide dopant concentration for 8:3:1 Dy_2O_3:Er_2O_3:WO_3 for the δ-phase to appear dominant……105

Figure 4.2. Diffraction patterns (λ = 1.7903 Å) of the pellets sintered for a total time of 70 h or 24 h for (a) 8D3E1WSB and (b) 8D4WSB. Unmarked peaks indicate unknown phases.……106

Figure 4.3. Diffraction patterns (λ = 1.7903 Å) reflecting the phase behaviour of the two systems after annealing at 500°C for 50 hours and 100 hours. **(a)** 8D3E1WSB exhibited minor peak broadening while **(b)** 8D4WSB showed anisotropic peak broadening and peak splitting characteristic of phase separation……108

Figure 4.4. The Arrhenius plots of total conductivity of **(a)** 8D3E1WSB and **(b)** 8D4WSB showing both the heating and cooling cycles. Both systems show hysteresis on the onset of the phase transition evident from the step change at around 500-600°C as highlighted……109

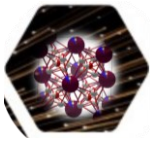

Figure 4.5. Stacked diffraction patterns (λ = 1.5419 Å) for VT-PXRD measurements of **(a)** 8D3E1WSB and **(b)** 8D4WSB showing phase changes during the heating cycle……...110

Figure 4.6. Rietveld refinements of the diffraction patterns (λ = 1.5419 Å) for 8D4WSB where the dots represent observed data, the red line shows the fit and grey line is the difference curve. This was done by incorporating **(a)** the δ-phase at 30°C, **(b)** the δ-phase and the $Bi_{14}W_2O_{27}$ phase at 30°C, **(c)** the δ-, $Bi_{14}WO_{24}$ and $Bi_{14}W_2O_{27}$ phases at 30°C and **(d)** only the δ-phase at 750°C. The red arrows show how the $Bi_{14}WO_{24}$ phase improves the fit on the peak at 31.8° 2θ……111

Figure 4.7. Rietveld refinements of the diffraction patterns (λ = 1.5419 Å) for 8D3E1WSB where the dots represent observed data, the red line shows the fit and grey line is the difference curve. This was done by including **(a)** the δ-phase only at 30°C, **(b)** the mixture of δ- and β-phases at 30°C and **(c)** the single δ-phase at 810°C. **(d)** An enlarged view depicting how the shoulders transform to become the main peaks…112

Figure 4.8. Comparison of diffraction patterns (λ = 1.7903 Å) for the tetragonal β-phase obtained from the 8D3E1WSB sample calcined at 500°C and then after further annealing at 750°C a mixture of the β and δ phases results. ICSD 189995 and 189996 are the collection codes of the β- and δ-phases from the Inorganic Crystal structure Database (ICSD)……113

Figure 4.9. Stacked diffraction patterns (λ = 1.5419 Å) for VT-PXRD measurements of 8D3E1WSB showing anisotropic peak broadening from 510°C during the cooling cycle. All peaks exhibited broadening except those with Miller indices (111) and (222). Green colour indicates onset of anisotropic peak broadening. Indexing only applies to the pure δ-phase above 510°C……...114

Figure 4.10. Raman spectra of **(a)** 8D3E1WSB at 170°C and **(b)** 8D4WSB and 22WSB at 22°C. Intensities from 22WSB were doubled to enhance features……115

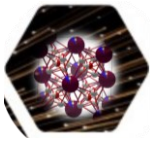

Figure 4.11. VT-Raman spectra of **(a)** 8D3E1WSB and **(b)** 8D4WSB. Intensities above 170°C were increased by a factor of five to enhance features in both system...116

Figure 5.1. (a) Plot of the lattice constant *a* as a function of total substituent concentration showing how the DESB system closely obeyed Vegard's law. Error bars were included and are smaller than symbols used (b) Diffractograms of the DESB system; the 10D5ESB and 12D6ESB compositions had the highest impurity phases (inset)…….139

Figure 5.1. The Arrhenius plot of 8D4ESB shows a discontinuity indicative of a phase change during the heating cycle, which is absent in the Arrhenius plot of 20ESB measured under similar conditions. ……...141

Figure 5.2. (a) Raman spectra of 8D4ESB and commercial pure β-Bi_2O_3 at ambient temperature showing that the peak at 304 cm^{-1} for 8D4ESB could be from the β-Bi_2O_3 phase. This is compared to **(b)** the Raman spectra of 20ESB for the pure δ-phase…..142

Figure 5.4. (a) Shows a plot of the fit obtained from a Rietveld refinement of the experimental Bragg data of 8D4ESB measured at room temperature presented as a square root of the intensity to accentuate the low intensity peaks from the calculated plot (as highlighted in the inset). **(b)** Shows a plot of the calculated Bragg data (red) from a weighted sum of the β- (20%) and δ- (80%) phases…….143

Figure 5.5. (a) The total PDFs of pure β-Bi_2O_3- and the δ-phase show a close relationship in the local structure of these two phases. It is also illustrated how the simulated total PDF of the β*-phase resembles that of 8D4ESB. **(b)** The Bragg data of the pure β-Bi_2O_3- and the δ-phases are totally distinguishable, yet the Bragg data of the β*- and δ-phases, as well as 8D4ESB, are all virtually the same……145

Figure 5.6. (a) Illustrates a model unit cell of the structure of the δ-phase adapted from that of Hull *et. al* [19], **(b)** shows a model unit cell of the structure of the β^*-phase obtained by exploiting the group-subgroup relationship between the δ- and β^*-phases, and **(c)** is a model unit cell of the structure for the β-phase adapted from that reported by Blower and Greaves [41]……...146

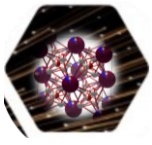

Figure 5.7. Total PDFs of all the compositions explored illustrating how an increase in total substituent concentration results in a better stabilisation of the δ-phase…….147

Figure 5.8. VT-PDF of 8D4ESB showing changes in the medium-range structure as a function of temperature. Green total PDFs highlight a section where the phase changes are essentially complete at higher temperatures. The rectangle and the red arrows at 9.59 and 12.34 Å highlight the features from the β*-phase and illustrate how these evolve with changes in temperature.……..148

Figure 5.9. (a) VT-SXRD Bragg data showing a phase transition and subtle anisotropic peak broadening, as highlighted for certain peaks **(b-d)**. Extraction of information from these Bragg data required a joint parametric and symmetry mode Rietveld refinement using both the β*- and δ-phases……...149

Figure 5.10. A calculated diffraction pattern of the β*-phase showing how the GM3+ strain mode leads to anisotropic peak broadening during a phase transition. Red rectangles highlight peaks with prominent peak broadening……..150

Figure 5.11. A calculated diffraction pattern of the β*-phase illustrating the absence of anisotropic peak broadening when the amplitude of the GM3+ strain mode is zero and the β*-phase is essentially the δ-phases……...150

Figure 5.12. The lattice parameter a as a function of temperature of the δ-phase during the heating and cooling cycles obtained via the SMA-based parametric Rietveld refinement. The dotted straight line merely indicates deviation from linearity in the range 97–451 °C during the cooling cycle……..151

Figure 5.13. The weight fraction of the β*- and δ-phases in **(a)** shows a strong correlation with the total conductivity of the 8D4ESB composition shown in the Arrhenius plots in **(b)** during the heating and cooling cycles……..152

Figure 6.1. Bragg data showing that the average structure of the solid solutions belong to the same space group type (*Fm*-3*m*) as that of δ–Bi_2O_3. The inset shows significant

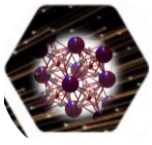

variations in the peak positions of the second peak. Diamond powder was used as an internal standard…….184

Figure 6.2. (a) Rietveld refinement fit of the 10D5ESB composition (R_{wp} =1.62). Green hkl's are for the diamond internal standard. **(b)** The correlation between the unit cell parameter a and the number of oxygens (n_O) in the 8c site per unit cell as the concentration of Er is reduced. **(c)** and **(d)** show the position of the O ions in the 48i and the 32f and 8c sites, respectively, relative to the cations. Purple spheres represent cations, red fractions represent oxide ions and white fractions represent oxide ion vacancies……185

Figure 6.3. Simulated and experimental reduced total PDFs of 25ESB and 10D5ESB, respectively……186

Figure 6.4. Small-box modelling of the reduced total PDF data of 10D5ESB. The inset and arrows highlight the misfit and asymmetry on the second peak dominated by the shortest M–M distances……..187

Figure 6.5. Reduced experimental total PDFs of the four specified systems as well as that simulated for 25ESB are shown. Evolution of the PDFs as a function of TSC is also shown. The insets and arrows highlight the shoulders on the second peak dominated by the shortest M–M distances……..188

Figure 6.6. Small-box modelling of the reduced total PDF data of 10D5ESB illustrating how the P-42_1c model reproduces the asymmetry on the first M–M peak……189

Figure 6.7. Simulated reduced total PDFs of the different polymorphs of Bi_2O_3…...190

Figure 6.8. Small-box modelling of the reduced total PDF data of 10D5ESB illustrating how the $P2_1/c$ model fits the data at low r……191

Figure 6.9. Normalized spectra of the Dy L_3-edge. The arrow indicates the peak characteristic of the *C-type* (*Ia*-3) structure of Dy_2O_3……192

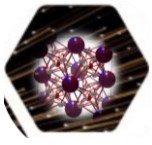

Figure 6.10. Normalized first **(a)** and second **(b)** derivative Dy L_3-edge XANES spectra of the Dy containing compositions……193

Figure 6.11. The Normalized W L_3-edge XANES spectra of WO_3, 10D3.75E1.25WSB and 10D3.75N2.5WSB……..194

Figure 6.12. Normalized first **(a)** and second **(b)** derivative W L_3-edge XANES spectra of 10D3.75E1.25WSB, 10D3.75N2.5WSB and WO_3. The arrow indicates an inflection point characteristic of 6-coordinated W^{6+} species……..195

Figure 7.1. (a) PXRD data of the pellets of the DEWSB system before and after annealing at 500 °C for 100 hrs showing phase stability. Plots are stacked for clarity. **(b)** DTA curves showing how an increase in substituent concentration reduces the endothermic displacement characteristic of the order-disorder transition. Plots are stacked for clarity. **(c)** The reduced total PDFs from powders of from ground pellets showing how the 8D3E1WSB composition exhibited very little change on the metal sublattice upon annealing……...221

Figure 7.2. PXRD data of the pellets of the DWSB system before and after annealing at 500 °C for 100 h of the pellets showing phase separation across the composition range from 12-24 mol% TSC. Plots are stacked for clarity…….222

Figure 7.3. (a) PXRD data of the pellets of the ENWSB system before and after annealing at 500 °C for 100 showing phase stability across the composition range explored. **(b)** DTA curves showing how the 12E4.75N2.25WSB exhibit an endothermic displacement characteristic of the order-disorder transition yet the 16E6N4WSB does not. Plots are stacked for clarity……...224

Figure 7.4. (a) PXRD data of the pellets of the DNWSB system before and after annealing at 500 °C for 100 h showing phase separation across the composition range explored. Plots are stacked for clarity. **(b)** DTA curves showing how the 12D4.75N2.25WSB exhibit an endothermic displacement characteristic of the order-disorder transition yet the 16N6N4WSB does not. No extra displacements were

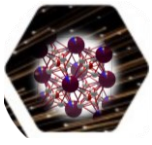

observed despite a mixture of phases forming upon annealing. Plots are stacked for clarity…….225

Figure 7.5. PXRD data of the pellets of the DESB system before and after annealing at 500 °C for 100 hrs showing phase separation from the δ-phase to a rhombohedral phase across the composition range from 12-24 mol% TSC. Plots are stacked for clarity…….226

Figure 7.6. (a) PXRD data of the pellets of the DENSB system after annealing at 500 °C for 100 h showing phase stability across the composition range explored. Plots are stacked for clarity. **(b)** shows DTA curves of 18 and 24 mol% TSC compositions exhibiting the endothermic displacement characteristic of the order-disorder transition. This was absent after cycle II in the 24 mol% TSC composition indicating that the process is reversible. Plots are stacked for clarity……...227

Figure 7.7. (a) Relative conductivity and **(b)** log of the conductivity at 500 °C showing ageing for the 12E4.75N2.5WSB, and 16E6DWSB compositions and resistance to ageing for 16E6N4WSB composition for up to 100 h……228

Figure 7.8. PL spectra of **(a)** 12E4.5N3WSB, and **(b)** 16E6D2WSB measured at ambient temperature after quenching from 850 °C, and after annealing at 500 °C for 50 and 100 hours. The peak with an asterisk (*) at ~ 782 .nm represents an instrument contribution……230

Figure 7.9. (a) k^2-weighted Bi L_3-edge EXAFS spectra and **(b)** the magnitude of their Fourier transforms without phase correction before and after annealing at 500 °C for 100 hrs for the 12E4.5N3WSB, 16E6N4WSB and 16E6D2WSB compositions. Plots are stacked for clarity…….231

Figure 7.10. A fit to the magnitude of the Fourier transform and its real component of Bi L_3-edge k^2-weighted EXAFS spectra: **(a)** before and **(b)** after annealing at 500 °C for 100 hrs of the 16E6D2WSB composition. **(c)** A fit to the k^2-weighted Bi L_3-edge EXAFS spectrum (fitting range was from 3.000 to ~12.500 $Å^{-1}$). Backscattering paths

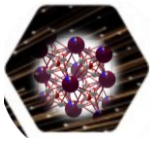

from both *Fm*-3*m and P2₁/c* models were used for the fitting. Plots are stacked for clarity…….232

Figure 7.11. The magnitude of the Fourier transforms of the k^2-weighted Er L_3-edge EXAFS data for the Er_2O_3 and 16E6D2WSB compositions. The plots are stacked for clarity…….234

Figure 7.12. Second derivative spectra of commercial Er_2O_3, as sintered and annealed **(a)** 12E4.5N3WSB **(b)** 16E6N4WSB and **(c)** 16E6D2WSB. Some plots are stacked for clarity…….235

Figure 7.13. (a) Big-box fits of the reduced total scattering function and **(b)** the differential pair correlation function of the 16E6D2WSB composition…….237

Figure 7.14. Ion-ion pair correlation functions for selected **(a)** M–M pairs and **(b)** M–O and O–O pairs of the annealed 16E6D2WSB composition…….238

Figure 7.15. Representation of the distorted 8b and 24d-like environments around Er^{3+} cations in the 16E6D2WSB compositions obtained from both EXAFS and RMC modelling. The distances between the Er^{3+} cations were obtained from RMC and comparable to those obtained by Refs. [64, 65, 74]. The small solid cubes represent oxide ion vacancies……...238

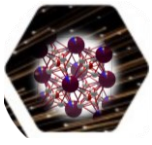

LIST OF TABLES

Table 2.1. The seven crystal systems……..30

Table 2.2. The fourteen Bravais lattices…….31

Table 2.3. Table of agreement factors of a Rietveld refinement and their meanings...39

Table 2.4. Capacitance values and the associated mechanism or regions in an electrochemical cell……..56

Table 3.1. Comparison of temperature related bulk conductivities for related materials……...81

Table 5.1. Relative weight percent of each phase in each composition as obtained from Rietveld refinement……140

Table 7.1. Summary of the fitted parameters from EXAFS for the 12E4.5N3WSB, 16E6N4WSB and 16E6D2WSB compositions at the Bi L_3-edge. N is coordination number, R is bond length, σ^2 is mean-square displacement of R. Backscattering paths from both *Fm*-3*m and* $P2_1/c$ models were used for the fitting…….233

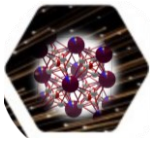

LIST OF ABBREVIATIONS

SOFCs: Solid Oxide Fuel Cells

MIECs: Mixed Ionic-Electronic Conductors

TPB: Triple-Phase Boundary

ORR: Oxygen Reduction Reaction

LSM: Strontium-doped Lanthanum Manganite

YSZ: Yttria-Stabilized Zirconia

SG: Space Group

HR-TEM: High-Resolution Transmission Electron Microscopy

OPD: Order Parameter Direction

PXRD: Powder X-ray Diffraction

PDF: Pair Distribution Function

XAS: X-ray Absorption Spectroscopy

XAFS: X-ray Absorption Fine Structure

XANES: X-ray Absorption Near Edge Structure

EXAFS: Extended X-ray Absorption Fine Structure

DFT: Density Functional Theory

RS: Raman Spectroscopy

PL: Photoluminescence

EIS: Electrochemical Impedance Spectroscopy

CNLS: Complex Non-linear Least Squares

COD: Open Database

ICSD: Inorganic Crystal Structure Database

PVA: Polyvinyl Alcohol

DTA: Differential Thermal Analysis

SMA: Symmetry Mode Analysis

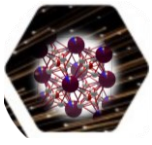

TSC: Total Substituent Concentration

RMC: Reverse Monte Carlo

NNN: Next Nearest Neighbour

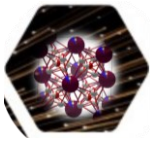

COMPOSITION CONVERSION TABLE

Composition	Equivalent composition	Equivalent composition
$Bi_2O_3 \cdot WO_3$	Bi_2WO_6	$(Bi_2O_3)_{0.5}(WO_3)_{0.5}$
$3Bi_2O_3 \cdot WO_3$	Bi_6WO_{12}	$(Bi_2O_3)_{0.75}(WO_3)_{0.25}$
$7Bi_2O_3 \cdot 2WO_3$	$Bi_{14}W_2O_{27}$	$(Bi_2O_3)_{0.778}(WO_3)_{0.222}$
$7Bi_2O_3 \cdot WO_3$	$Bi_{14}WO_{24}$	$(Bi_2O_3)_{0.875}(WO_3)_{0.125}$

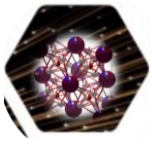

Chapter 1

1.1 Introduction

Fossil fuels continue to dominate the energy landscape. These energy sources are non-renewable and produce noxious gases such as CO_2, SO_x and NO_x that are deleterious to the environment when used in internal combustion engines. They contribute to air pollution and climate change. The internal combustion engines used to convert the chemical energy to electrical energy via heat and mechanical energies from these non-renewable energy sources are inherently inefficient and are governed by the Carnot efficiency that puts a cap on the maximum efficiency that can be achieved by such engines. The Carnot efficiency is given by $e = 1 - T_c/T_h$, where $T_h$is the temperature of the environment where input energy is drawn from (hot reservoir e.g. burning coal) and T_c is the temperature of the environment where unused output energy is discarded (cold reservoir e.g. atmosphere) such that the flow of heat is from the hot reservoir to the cold reservoir. On the other hand, population growth and industrialization need efficient and reliable supply of energy which means a continued over-reliance on the available, inefficient heavily polluting energy production systems to meet the energy demands. The use of alternative, renewable energy sources and the renaissance of solid oxide fuel cell technology promise to circumvent the problems plaguing the use of internal combustion engines and fossil fuels.

1.1.1 Solid Oxide Fuel Cells

Solid oxide fuel cells (SOFCs) are electrochemical devices that convert chemical energy directly to electrical energy by using fuels, oxidants, and redox reactions. Among the different types of fuel cells, the SOFC promises to play an important role in solving the environmental and efficiency problems plaguing non-renewable energy production systems. A SOFC has high specific energy and specific power density compared to combustion engines and other types of fuel cell technologies [1]. SOFCs operate at high temperatures, from 600 ℃ to 1000 ℃ [2]. This enables SOFCs to have high fuel flexibility due to internal steam reforming, which in turn, eliminates the need for expensive external reforming systems used in other fuel cells to produce H_2 gas from natural gas [2]. Fuels such as biogas, natural gas, CO, and hydrocarbons can be used with reduced greenhouse gas emissions compared to internal combustion engines [3]. When H_2 gas is used as fuel, the greenhouse gas emission is zero. Efficiencies can be as high as 80% if systems are operated in combined heat and power mode, where the quality by-product heat and gases are

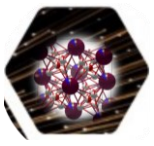

recovered and used to heat water directly in hot water systems in municipalities [4]. SOFCs are non-vibrational, noise-free and can be used as distributed power sources for residential use or stationary systems that can deliver megawatts of power [4]. This eliminates the need for long transmission lines and other expensive infrastructure for power transmission. For developing countries, this would provide access to electricity for rural places in remote locations that are not supplied by electricity at all.

1.1.2 Structure of a SOFC

A SOFC comprises three main components; a cathode (where molecular oxygen is reduced to oxide ions), a solid oxide conducting electrolyte (a dense ceramic which is gas impermeable but oxide ion conducting) and an anode where the fuel is oxidized. Fig. 1.1 illustrates a typical structure of a SOFC. The anode is usually a composite – a combination of a ceramic and a metal called a cermet. The two electrodes are mixed ionic-electronic conductors (MIECs) i.e., they conduct both ions and electrons. They are also porous, so gases can flow through them during operation.

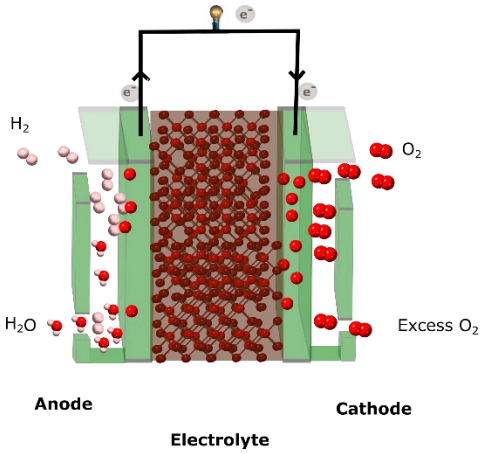

Figure 1.1. Structure of a solid oxide fuel cell showing the cathode, anode, and electrolyte.

1.1.3 Operation of a SOFC

An oxidant, normally air is fed into the cathode side. The porous cathode has a triple-phase boundary (TPB) region i.e., the interface between the cathode, electrolyte and air, where oxygen molecules are reduced to oxide ions in an oxygen reduction reaction (ORR) [5]. A MIEC such as strontium-doped lanthanum manganite (LSM) with a perovskite structure type is predominantly used as the cathode material. From the cathode, the oxide ions are conducted through the solid oxide electrolyte to the anode side where fuel is oxidized. Electrons are liberated and heat is

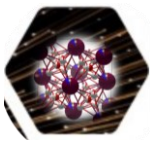

released from the exothermic reaction between the fuel and oxygen. The cathode is at a lower potential than the anode, so this potential difference will force electrons through an external circuit from the anode to the cathode and electrical energy is harnessed as illustrated in Fig. 1.2.

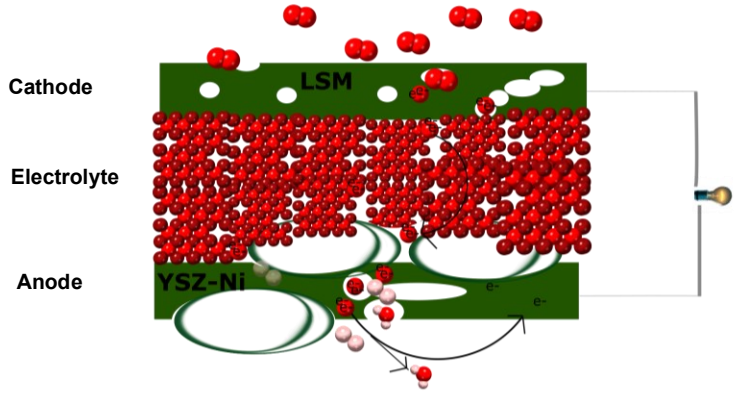

Figure 1.2. Structure of a SOFC showing the redox reactions on the electrodes and the flow of oxide ions through the electrolyte. YSZ-Ni is a composite of yttria stabilized zirconia and metallic nickel.

The heat that is released during the redox reaction keeps the temperatures high, which is essential for the internal reforming of fuel, and it also facilitates the conduction of oxide ions across the dense solid oxide electrolyte. However, these high temperatures require the use of expensive, high melting point materials for interconnects– materials that connect cells in series to form a cell stack. This drives up the capital costs of SOFCs and it is one of the principal reasons why SOFCs, despite their high efficiency and fuel flexibility, have not been extensively commercialized [6]. Chemical stability, thermal compatibility and degradation of cell components are the other issues associated with the operation of SOFCs at high temperatures. The last two decades have seen a renaissance in SOFC research [6]. The possibility of developing intermediate temperature fast oxide ion conductors that would enable the cells to operate at moderate temperatures in the range of 500 – 750 °C has revived interest in SOFCs [7, 8]. At such temperatures, failure of the cell due to thermochemical degradation and materials' thermomechanical incompatibility would be delayed significantly, hence increasing cell life. Low-cost metals can then be used for interconnects, reducing the capital cost of SOFCs.

1.2 Fast oxide ion conductors

Solid electrolytes with ionic conductivities ranging from 0.01 – 10 S cm^{-1} are called high or fast-ion conductors [9, 10]. They share similar properties: they have a large number of ions of one species being mobile and a large number of vacant sites or interstitial sites for the mobile ions to

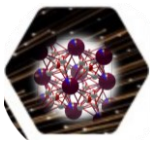

hop into. The empty (vacancies and interstitial sites) and occupied sites have similar potential energies and equivalent volume with a low activation energy barrier (certainly less than about 1 eV) for ease of diffusion of ions [9, 10]. When the mobile ion is an oxide ion, the electrolyte is called a fast oxide ion conductor. The structure of fast oxide ion conductors is usually three dimensional and is highly symmetric, for instance, the cubic defect fluorite structure is the classic structure type for these types of conductors. However, there are emerging lower symmetry fast oxide ion conductors based on $Bi_4V_2O_{11}$ [11, 12].

In the cubic defect fluorite structure, the cations form a face-centred cubic (*fcc*) framework and the tetrahedral holes between them are occupied by the anions while some are vacant. The cation framework should be highly polarizable to facilitate anion diffusion [13, 14]. For the anion to jump from one site to an adjacent vacant site, it must pass through a bottleneck created by three cations in three of the 4 intersecting faces as shown by the dotted lines in Fig. 1.3 and the inset.

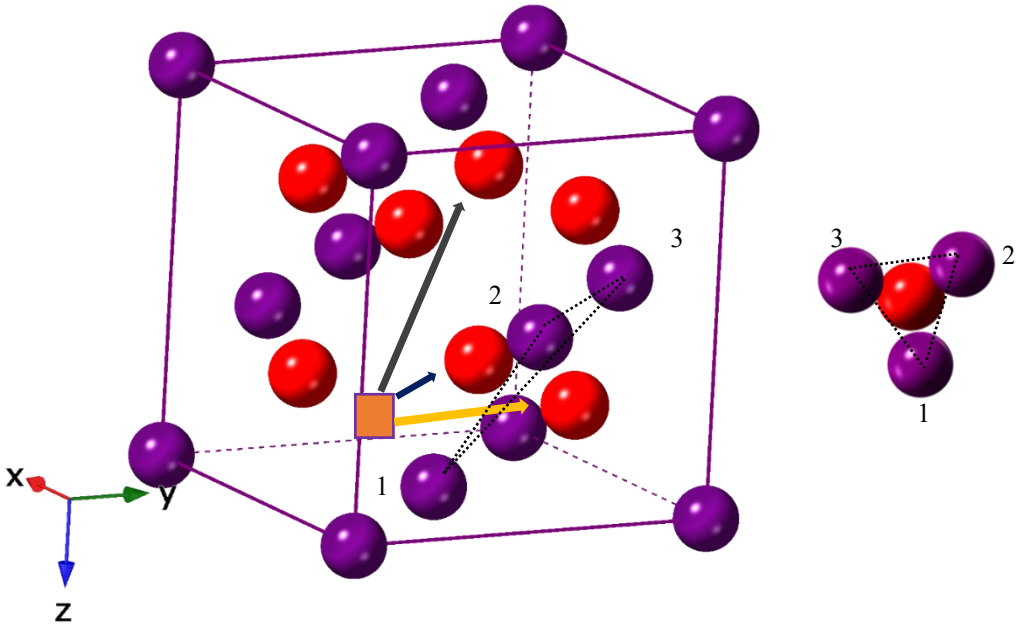

Figure 1.3. Three possible vacancy migration pathways in the fluorite structure. Purple spheres represent cations, red ones represent oxide ions and the square represents a vacant site. The inset shows the bottle neck in one of the migration paths.

The fluorite structure has five main types of unique lattice sites in the structure that can be occupied by different species viz: *4a*, *24e*, *8c*, *32f* and *48i*. These sites are called the Wyckoff positions. The *24e* and *48i* are interstitial sites. The cations usually occupy the *4a* regular lattice sites to form the

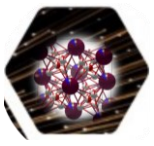

cation sublattice and can relax to the *24e*. The anions occupy the regular *8c* lattice sites between the cations to form the anion sublattice but can relax to the *32f* and *48i* sites. The fluorite structure can be represented in a different way where the anions form a simple cubic arrangement around some of the cations (Fig. 1.4). This kind of representation facilitates the understanding of the local structure of some fluorite materials.

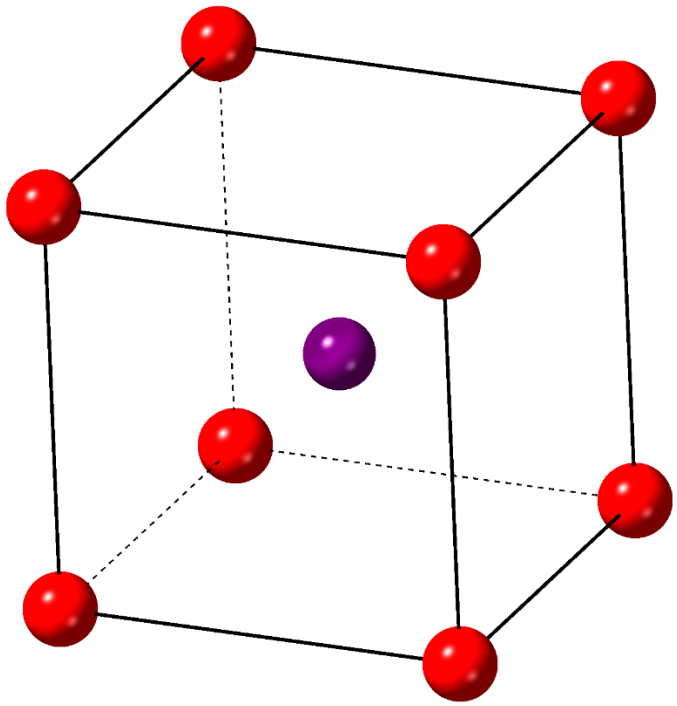

Figure 1.4. One of the quadrants of a fluorite unit cell showing how the oxygens are distributed around the cation in a different representation of the fluorite structure. Purple and red spheres are cations (e.g., Ce^{4+}) and O^{2-}, respectively.

In fast oxide ion conductors, current flow occurs through the movement of oxide ions in the crystal lattice. The ionic conductivity (σ) is strongly temperature-dependent and is given by equation (1.1):

$$\sigma = \left(\frac{A}{T}\right) e^{-E_a/k_B T} \qquad (1.1)$$

where A is the Arrhenius constant which increases with the fraction of vacant anion sites, E_a is the activation energy, T is absolute temperature and k_B is Boltzmann's constant. The atomistic understanding of the oxide ion movement through the crystal structure of fast oxide ion electrolytes is a subject of intense research [15-17].

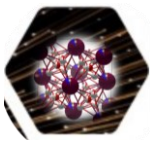

In defect fluorite structures, the widely accepted conduction model is the vacancy mechanism. The movement of oxide ions in this mechanism emanates from the hopping of thermally activated oxide ions. The ions move from one lattice site to a vacant one such that the net effect is the movement of vacancies through the crystal structure from one end to the other. This model and the A parameter in equation 1.1 suggest that to increase the conductivity, the fraction of vacant anion sites should be increased. In the cubic fluorites of ZrO_2 and CeO_2, the fraction of vacant sites is increased by partially substituting the host cations Zr^{4+} and Ce^{4+} with impurity cations of lower valency such as Ca^{2+}, Y^{3+}, Sc^{3+} and Gd^{3+} [18-20]. This leads to some of the well-known extrinsic fast oxide ion conductors such as yttria-stabilized zirconia (YSZ) and gadolinia doped ceria (GDC). However, from experimental results and theoretical calculations, it has been found that the conductivity can only be increased to a certain limit by introducing impurity cations [10]. After a certain concentration of impurity cations, well before half of the oxide ion sites become vacant, the conductivity starts to decrease. The decrease has been attributed to vacancy-impurity cation interactions and is described by Catlow [10] as the back-and-forth movement of the oxide ions around the impurity cations that do not lead to any net movement of the oxide ions. They used a model called the percolation model—which is associated with the free volume inside the crystal structure—to explain their results.

He *et al.* [21] suggested a different model for the migration of the ions in fast ionic conductors to illustrate the effect of the activation energy E_a on ionic conductivity. They used ab initio molecular dynamics calculations to show that concerted diffusion of ions leads to the decreased overall energy barrier (E_a) for the diffusing species when compared to the model where each ion diffuses independently. Keeping all other factors constant, the decrease in activation energy in equation (1.0) leads to an increase in conductivity. The challenge, therefore, is to design a solid oxide ion-conducting electrolyte that will allow oxygen-ion conduction at intermediate temperatures (500 – 750℃) to be technically useful, i.e. exhibit high ionic conduction for application in electrochemical devices. Materials with low E_a and numerous intrinsic vacant sites, such as bismuth oxide in its δ-phase (δ–Bi_2O_3), are desirable and have attracted considerable attention.

1.2 Pure Bismuth Oxide

Bismuth oxide (Bi_2O_3) and its chemical derivatives continue to dominate in the fabrication of devices of technological importance such as gas sensors, glasses for electronics and fuel cells [22-

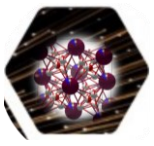

26]. This is due in part to its peculiar ability to dissolve many oxides and elements across the periodic table as reported by Valant and Suvorov [27]. Its ability to exist as different polymorphs depending on the environment also creates a variety of structures that exhibit physical properties key to technological advancements [22-26]. This has made Bi_2O_3 a target of intense research in the past century.

Among the various Bi_2O_3 polymorphs, the first four includes a monoclinic α–Bi_2O_3 phase with a space group (SG) $P2_1/c$ (b-axis as unique axis). Upon heating, the α–Bi_2O_3 phase transitions to the cubic defect fluorite δ–Bi_2O_3 phase (SG $Fm\bar{3}m$) at ~730 °C [28, 29]. On slow cooling, the δ–Bi_2O_3 phase can either transform into a tetragonal β–Bi_2O_3 phase (SG $P\bar{4}2_1c$) at ~650 °C before it reverts to the α–Bi_2O_3 phase between 550 and 500 °C [29, 30] or to the body centered cubic (*bcc*) γ–Bi_2O_3 (SG $I23$) at ~640 °C which can persist to ambient temperature if slow cooled [30].

The α–Bi_2O_3 phase is structurally related to the high-temperature δ–Bi_2O_3 phase. In an ordered defect fluorite structure the vacant sites of O^{2-} ions would order along the ½ $<111>_f$ and ½ $<110>_f$ directions (where the f subscript denotes the fluorite cell) to form the α–Bi_2O_3 phase [31]. The Bi^{3+} cations forms planes parallel to the 100 plane as Fig. 1.5 shows. These cation planes sandwich the anion planes, giving unit cell lattice parameters of a = 5.843 Å, b = 8.160 Å, c = 7.510 Å and β = 112.92° [32].

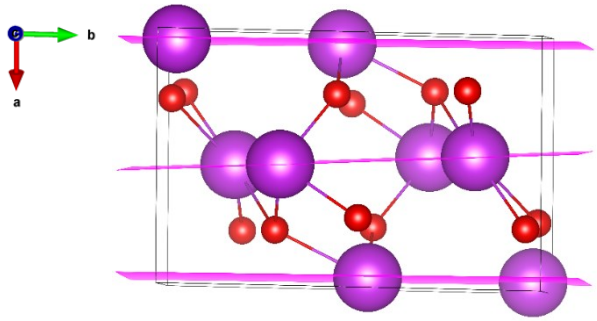

Figure 1.5. A unit cell representation of the monoclinic α–Bi_2O_3 phase showing how the layers of the Bi^{3+}cations sandwich the O^{2-} anions. Purple and red spheres are Bi^{3+} and O^{2-}, respectively.

Due to the highly ordered nature of the O^{2-} sublattice, the α–phase is a poor ionic conductor, and it exhibits some p-type conductivity in the temperature range of 650-729 °C in air [28]. Due to the estimated bandgap of 2.80 eV, it has found application in the photocatalytic degradation of organic dyes [33].

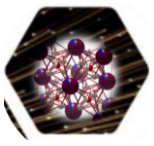

The δ–Bi_2O_3 phase has the highest ionic conductivity ever reported for a ceramic oxide ion conductor. Its conductivity at 730 °C is about 1 S cm^{-1} and is comparable to the conductivities of molten salts [28, 34]. With such high ionic conductivity, it remains the benchmark used to design, compare and optimize other solid oxide electrolytes for application in devices of technological importance such as SOFCs and oxygen sensors. However, its use in SOFCs is limited by the narrow temperature range (730 to 824 °C) at which this phase is thermodynamically stable and the reduction of $Bi^{3+}$to metallic Bi in some solid solutions of Bi_2O_3 at low oxygen partial pressures (~10^{-21} atm) in reducing environments [35].

Due to the high conductivity of the δ–Bi_2O_3 phase and its potential uses, it has attracted huge research interest. There is a consensus on the average structure of this phase being the cubic defect fluorite phase. However, its local structure has proven to be elusive. Three models as discussed in the following sections, have failed to accurately describe the oxygen sublattice and correlate it with the conductivity results reported [29]. This is ascribed to the massive disorder shown by the oxygen sublattice of this phase. When the α–Bi_2O_3 phase transitions to the δ–Bi_2O_3 phase, the currently accepted value of the heat of transformation is 29.53 kJ/mol [29]. This value is 2.7 times the heat of fusion for pure Bi_2O_3 and demonstrates the extent of the disorder in the δ–Bi_2O_3 phase.

In the cubic defect fluorite phase of Bi_2O_3, the Bi^{3+} cations have been reported to occupy the *4a* sites [36, 37]. There are more lattice sites than the O^{2-} anions in each unit cell, therefore the distribution of the oxide ions and the vacancies makes the structure solution of the δ–Bi_2O_3 phase

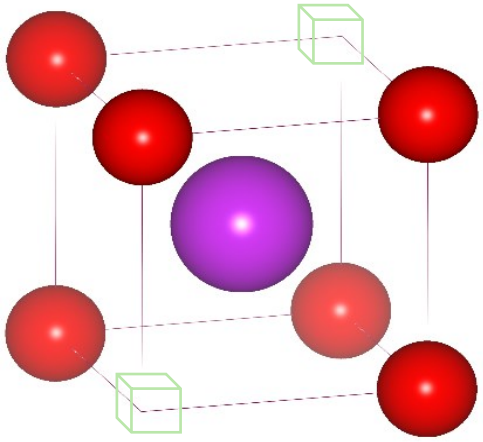

Figure 1.6. A unit cell representation of the Sillen model showing how the O^{2-} vacancies (squares with green outline) are ordered along the <111> direction. Purple and red spheres are Bi^{3+} and O^{2-}, respectively.

challenging. Sillen *et al.* [38] proposed a model and solved the structure of the δ–Bi_2O_3 phase to have the space group $Pn\bar{3}m$. In the cubic defect fluorite structure, this would mean the vacant sites of the oxide ions should order along the <111> direction (Fig. 1.6). This model was inconsistent with the high ionic conductivity exhibited by the δ–Bi_2O_3 phase, as well as with *ab initio* structure calculations done by Aidhy *et al.* [39].

Gattow and Schroder proposed the $Fm\bar{3}m$ space group for the δ–Bi_2O_3 phase with a statistical distribution of the oxide ions among the *8c* sites (Fig. 1.7) [40]. This meant a completely random distribution of the oxygen ions and that 25% of the *8c* sites were vacant. This was consistent with the high oxide ion conductivity reported for this phase, but their model could not be reconciled with the occupation of the *32f* sites observed from neutron diffraction data from Battle *et al.* [37] and Hull *et al.* [36].

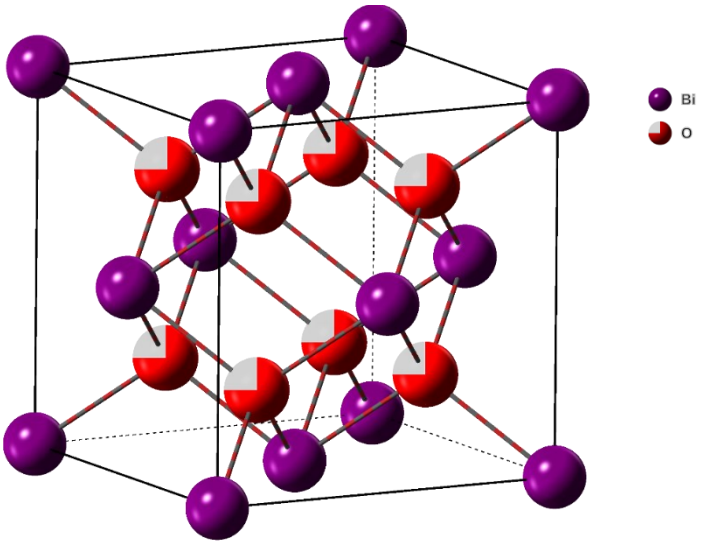

Figure 1.7. The Gattow and Schroder model showing how the O^{2-} vacancies are statistically distributed in the regular 8*c* sites. Only 75% of the 8 available oxygen sites are statistically occupied as indicated by the fraction in each O atom.

Using the Willis model [41], the structure was modelled with all the oxide ions in the 32*f* sites with an occupancy of 3/16 per site [42]. This meant a completely random oxide ion distribution and a complete positional disorder compared to the Gattow and Schroder model [40]. This model accounted for the high oxide ion conductivity observed in the δ–Bi_2O_3 phase. However, neutron data from Battle *et al.* [37] and Hull *et al.* [36] indicated that the 8c site can still be occupied. The

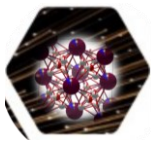

models by Battle *et al.* [37] (formulated from data measured at 750 °C) and Hull *et al.* [36] (formulated from data measured at 760 °C) are the currently accepted models. In the Battle model, about 57.3% of the oxide ions are randomly distributed among the *8c* sites with coordinates (0.25 0.25 0.25) [37]. The remaining 42.7% are statistically distributed among the *32f* sites at (0.354 0.354 0.354) with a lattice parameter *a* of 5.648 Å as illustrated by Fig. 1.8 (a). In the Hull model, about 32.3% of the oxide ions occupy the *8c* sites statistically with fractional coordinates (0.25 0.25 0.25) [36]. About 67.7% of the oxide ions occupy the *32f* sites with fractional coordinates of (0.3344 0.3344 0.3344) as shown in Fig. 1.8 (b). The lattice parameter *a* in this model is 5.6607 Å.

The difference in lattice parameter *a* between the two models might be attributed to the difference in the temperatures at which the measurements were performed. Hull *et al.* [36] attributed the discrepancy in occupancy of the two oxide ion sites in the two models to the accuracy associated with measuring to very low d-spacings in their measurements compared to those of Battle. This was reported to have the effect of reducing correlations between site occupancy and thermal vibration parameters [36]. However, this highlights the elusive nature of the local structure of the δ–Bi_2O_3 phase which warrants further probing.

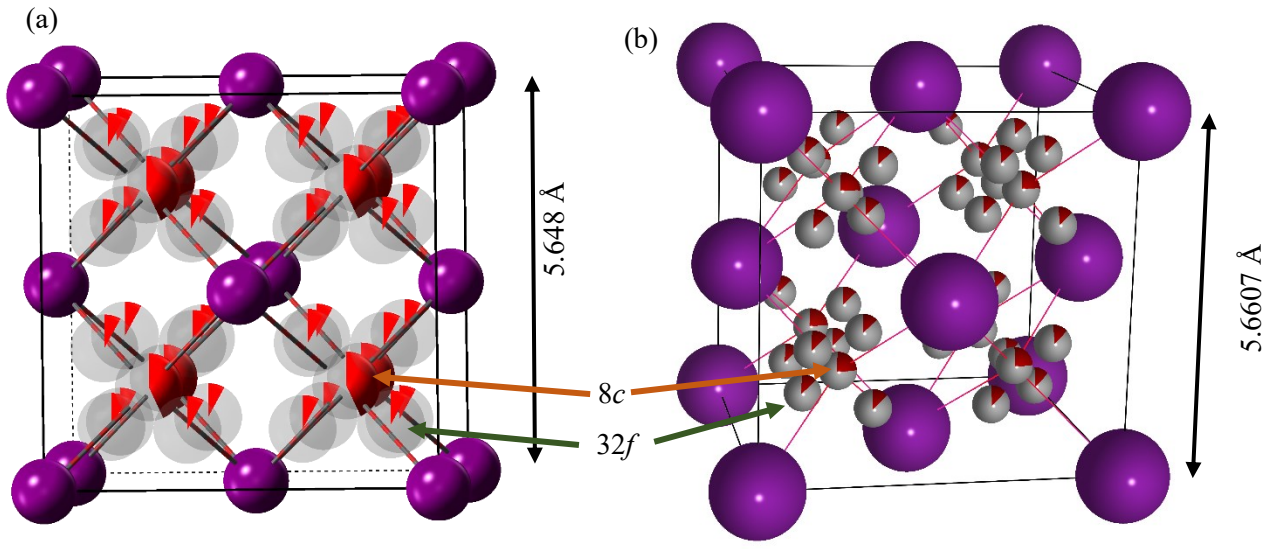

Figure 1.8. The Battle **(a)** and Hull **(b)** models showing the are distribution of oxide ions in the 8*c* and 32f sites. Purple and red spheres are Bi^{3+} and O^{2-}, respectively. Grey spheres represent vacancies.

As mentioned earlier, upon cooling, the δ–Bi_2O_3 phase can transition to one of the metastable phases, the β–Bi_2O_3 phase. This phase has a structure symmetrically related to the δ–Bi_2O_3. Harwig and Weenk [31] found that the vacancies in the O^{2-} sublattice in the defect fluorite structure order along the ½ $<100>_f$ direction to form the β–Bi_2O_3 phase. Additionally, the SG $P\bar{4}2_1c$ is an isotropy subgroup of the supergroup $Fm\bar{3}m$, i.e., the symmetry of $P\bar{4}2_1c$ can be decomposed to give the symmetry modes of the supergroup $Fm\bar{3}m$. For β–Bi_2O_3 the metal ions essentially maintain the fcc structure of the defect fluorite in this tetragonal system. The *a* lattice of this structure is 7.7439 Å and the *c* lattice parameter is 5.6287 Å at 297 K [36]. Since the O^{2-} sublattice is highly ordered, the ionic conductivity is about 2-3 orders of magnitude lower compared to the δ–Bi_2O_3 phase at corresponding temperatures [28]. Due to its metastability, the β–Bi_2O_3 phase is usually stabilized by reducing the particle size to the nanometer regime or by substituting the Bi^{3+} cation with a low total substituent concentration of supervalent cations like W^{6+} and Nb^{5+} [43]. This phase has also found an application in photocatalytic degradation of organic dyes and exhibits high performance compared to the α–Bi_2O_3 phase [33].

The δ–Bi_2O_3 phase can also transition to the γ–Bi_2O_3 as mentioned earlier. The γ–Bi_2O_3 phase is isomorphous with the system $Bi_{12}GeO_{20}$ and is also called the sillenite phase. The lattice parameter *a* of the γ–Bi_2O_3 is 10.2501 Å at room temperature [44]. The oxygen sublattice of this structure is reported to be more complex. Since the ionic conductivity of this phase is 2-3 orders of magnitude

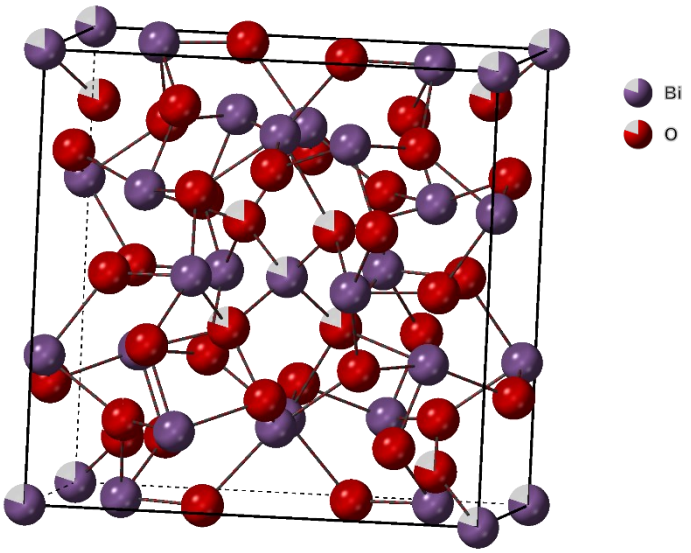

Figure 1.9. Unit cell of the γ–Bi_2O_3 phase showing the vacancies on some of the O^{2-} and Bi^{3+} sites. Grey spheres represent vacancies.

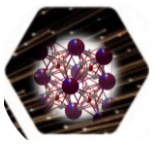

lower than that of the δ–Bi_2O_3 phase at corresponding temperatures, little research effort has been shown to its local structure compared to the δ–Bi_2O_3 phase. However, Radaev and Simonov [44] solved the structure of the γ–Bi_2O_3 phase by using neutron diffraction data. They indicated that about 4% of the O^{2-} ion sites are vacant and about 1.5% of the Bi^{3+}sites are vacant as shown in Fig. 1.9.

To stabilize the δ–Bi_2O_3 like phases henceforth referred to as δ–phases to ambient temperatures, isovalent and aliovalent cations have been used to substitute for the Bi^{3+} in numerous studies. Sammes *et al.* [29] and Azad *et al.* [45] provided good reviews on the impurity cations that stabilize the δ–phase to ambient temperatures to offer a plethora of different systems. In this work, the aim is to establish phase stability and to explore structure-property correlations in those systems that show the highest ionic conductivity for any of the solid solutions of Bi_2O_3.

1.3 The Bi_2O_3-WO_3 system

Among the transition elements, W offers solid solutions of Bi_2O_3 with relatively high ionic conductivities at intermediate temperature ranges. Takahashi and Iwahara [46] reported conductivities of 0.01 and 0.062 S cm^{-1} at 500 and 700 °C, respectively, for the $(Bi_2O_3)_{0.78}(WO_3)_{0.22}$ composition. The conductivities are almost an order of magnitude higher compared to YSZ (which is the state-of-the-art electrolyte for SOFCs) at corresponding temperatures [46]. The Bi_2O_3-WO_3 system was reported to exhibit ionic conductivity even at low oxygen partial pressures of about 10^{-15} atm [46]. Most solid solutions of Bi_2O_3 show mixed conductivities at such low oxygen partial pressures [45].

Earlier studies in the 70s and early 80s determined the structure of the solid solutions of the compound $3Bi_2O_3 \cdot WO_3$ in the range 20 – 28 mol% to have the defect fluorite δ–phase at ambient temperatures [46-48]. However, later studies indicated that the structure of the solid solutions of this compound is tetragonal (SG $I4_1$) which is closely related to the structure of the δ–phase [49-51]. Therefore, the authors might have erroneously identified the tetragonal phase as the defect fluorite δ–phase. Watanabe *et al.* [52] established the relationships between the lattice parameters a_t and c_t of the tetragonal unit cell to the a_c parameter of the δ–phase as: $a_t \approx \sqrt{5}\, a_c$, and $c_t \approx 2a_c$

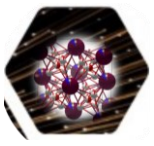

(where the subscripts t and c denote tetragonal and cubic, respectively). The transformation matrix equation between the unit cells is given by:

$$(a \quad b \quad c)_c \begin{pmatrix} 2 & -1 & 0 \\ 1 & 2 & 0 \\ 0 & 0 & 2 \end{pmatrix} = (a \quad b \quad c)_t \qquad (1.2)$$

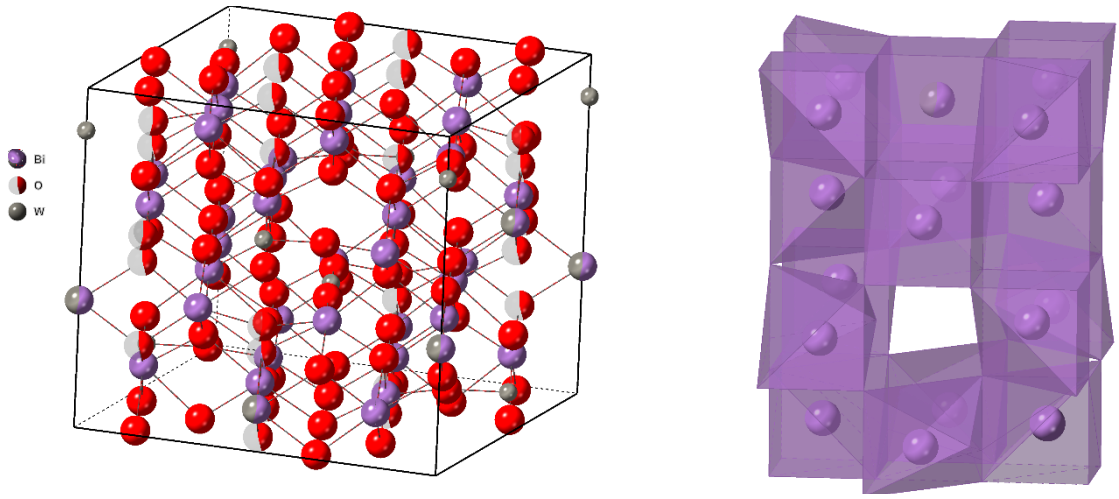

Figure 1.10. A unit cell representation of the tetragonal phase with space group $I4_1$ showing the mixed-metal sites, different polyhedral (octahedra and tetrahedra) and the oxide ion vacancies (white fractions in otherwise red spheres).

The tetragonal phase is a superstructure of the δ–phase (Fig. 1.10). This, however, implies an ordered structure and conflicts with the high conductivity measurements exhibited by the solid solutions of $3Bi_2O_3{\cdot}WO_3$. Watanabe and Ono ascribed the high conductivities of the tetragonal phase to a mixed-metal site *8b* in the $I4_1$ space group and vacant oxygen sites [50]. Since Bi^{3+} and W^{6+} share this site and the coordination and polyhedra formed around the two metal centres are different (due to different coordination numbers around W^{6+} and Bi^{3+}), disorder is introduced in the O^{2-} sublattice. They attribute the high conductivity to the presence of vacancies and disorder.

The Bi rich materials of the Bi_2O_3-WO_3 system exhibit a range of other phases that are interrelated. The $7Bi_2O_3{\cdot}WO_3$ has a tetragonal phase (SG *I*4*a*) with a relatively low conductivity because it does not exhibit the mixed metal effect (i.e., high ionic conductivity due to different coordination numbers around different types of cations occupying the same crystallographic site) [50]. Watanabe and Ono reported that the true equilibrium phases of the Bi_2O_3-WO_3 system below 670 °C are a mixture of the two tetragonal phases/structures $7Bi_2O_3{\cdot}2WO_3$ ($I4_1$) and $7Bi_2O_3{\cdot}WO_3$ (*I*4*a*) [50]. Another phase, the $Bi_2O_3{\cdot}WO_3$ phase in the Bi_2O_3-WO_3 system is of the orthorhombic crystal

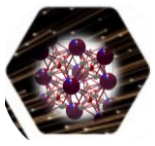

system with space group $Pca2_1$ and is observed from ambient temperature to 850 °C for the pure phase [50]. It has the lowest ionic conductivity among the three phases [50]. In this work, the phase evolution as a function of annealing temperature, composition, and synthetic methods of the Bi_2O_3-WO_3 system was explored (Chapter 3). The conductivities of the resultant phases were determined and correlated with the phase compositions.

1.4 The Bi_2O_3-Dy_2O_3 system

Verkerk and Burggraaf studied the Bi_2O_3-Dy_2O_3 system comprehensively [53]. They reported that the addition of Dy_2O_3 with total substituent concentration in the range 28.5 – 50 mol% stabilizes the δ–phase to ambient temperatures. However, below this range, there is a mixture of the δ–, rhombohedral, and β–phases at low temperatures [53]. In the total substituent concentration range 28.5 – 40 mol%, the solid solutions were reported to be ionic conductors with an oxygen transference number close to unity [53].

The composition $(Bi_2O_3)_{0.715}(Dy_2O_3)_{0.285}$ (written as 28.5DSB) was reported to have the highest ionic conductivity among the compositions with a monophasic δ–phase [53]. This was the lowest total substituent concentration that gave a monophasic δ–phase and the highest ionic conductivity. This is a common feature of most solid oxide electrolytes; the lowest total substituent concentration that stabilizes the most conductive phase tends to give the highest conductivity. The conductivity of 28.5DSB was reported to be 0.007 and 0.144 S cm^{-1} at 500 and 700 °C, respectively [53]. At 700 °C, the conductivity of 28.5 DSB is more than an order of magnitude higher than that reported for YSZ (0.01 S cm^{-1}) [1].

Apart from the high solubility of Dy^{3+} in Bi_2O_3, the Bi_2O_3-Dy_2O_3 system was found to have the highest time constant for the onset of the ageing phenomenon among the rare earth substituted Bi_2O_3 systems (Bi_2O_3-RE_2O_3) explored by Ref. [54]. The ageing phenomenon is the significant decline in ionic conductivity for some of the solid solutions of Bi_2O_3 upon prolonged isothermal annealing at temperatures between 500 and 600 °C. The decline is observed without any observable change in the average structure of the material by XRD. The causes of ageing are not well understood. Fung *et al.* [55] suggested that the ageing is caused by the ordering of the cation sublattice in the space group $Fm\bar{3}m$. However, several studies have reported a correlation between the ordering of the O^{2-} sublattice and the decline in conductivity [54, 56-59]. Presumably due to

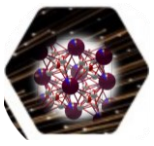

the small structure factor of O^{2-} compared to that of Bi^{3+}, the superlattice reflections from the superstructure that results from an ordered phase are hard to observe by XRD. The ageing phenomenon will be explored further in Chapter 7.

High-resolution transmission electron microscopy (HR-TEM) and neutron diffraction studies have been done to try and elucidate the structural changes that take place upon ageing. Jiang *et al.* [60] and Wachsman *et al.* [54] concluded that the ageing phenomenon is significantly due to the ordering of the O^{2-} sublattice. They provided models that explained the presence of the superlattice reflections in HR-TEM images. The increased resistance to ageing shown by solid solutions of the Bi_2O_3-Dy_2O_3 system, the high solubility of Dy_2O_3 in Bi_2O_3 and the relatively high ionic conductivity exhibited by this system makes it a good candidate for designing solid solutions of Bi_2O_3 with both high conductivity and improved resistance to ageing.

1.5 The Bi_2O_3-Er_2O_3 system

The $(Bi_2O_3)_{0.80}(Er_2O_3)_{0.20}$ composition (written as 20ESB) has the highest oxide ionic conductivity for any of the reported singly substituted solid solutions of Bi_2O_3 that have a monophasic δ–phase at ambient temperature [61]. Er_2O_3 has a high solubility in Bi_2O_3. The δ–phase is reported to be stabilized to low temperatures in solid solutions with a total Er_2O_3 concentration in the range 17.5 – 45.5 mol% [61]. Below and above this range, the Bi_2O_3-Er_2O_3 systems exhibit polyphasic mixtures [60]. It was reported that due to the ionic radius of Er^{3+}, Er_2O_3 provides the optimum total substituent concentration needed to stabilize the δ–phase and give solid solutions with higher conductivity among the Bi_2O_3-RE_2O_3 systems where RE represent the rare earths [62].

Despite its high ionic conductivity, 20ESB is reported to exhibit the ageing phenomenon when annealed at 500 °C for over 100 h [60, 63-64]. It has a smaller time constant compared to the Bi_2O_3-Dy_2O_3 system for the ageing process [54]. This is because Er was found to be less polarizable compared to Dy [54]. To inhibit the ageing effect, 1 mol% Hf was added into the $(Bi_2O_3)_{0.80}(Er_2O_3)_{0.20}$ composition to create a doubly substituted system [65]. This Bi_2O_3-Er_2O_3-HfO_2 ternary system exhibited improved stability and the original conductivity of the 20ESB composition was not affected [65].

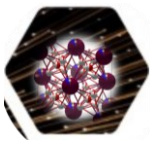

1.6 The Bi_2O_3-Dy_2O_3-WO_3 system

Meng *et al.* [66] used the co-doping strategy to create several ternary oxides. They discovered that the co-doping strategy lowers the total substituent concentration needed to stabilize the δ–phase of Bi_2O_3 to lower temperatures compared to the total substituent concentration needed for singly doped systems. They ascribed the stability to the increased entropy of mixing. Jung *et al.* [67] used the co-doping strategy to fabricate the Bi_2O_3-Dy_2O_3-WO_3 system. The total substituent concentration needed to stabilize the δ–phase to lower temperatures in this system was 12 mol% with respect to the cations [67]. This is significantly lower than the 28.5 mol% total substituent concentration needed in the Bi_2O_3-Dy_2O_3 system. W^{6+} has been shown to not stabilize the δ–phase as a single dopant at ambient temperature [50].

The $(BiO_{1.5})_{0.88}(DyO_{1.5})_{0.08}(WO_3)_{0.04}$ composition had a reported conductivity of 0.098 and 0.569 S cm^{-1} at 500 and 700 °C, respectively [67]. This is one of the highest conductivities ever reported for a solid solution of Bi_2O_3. The conductivity is two orders of magnitude higher than that reported for YSZ at corresponding temperatures. Unfortunately, in the 12 – 21 mol% total substituent concentration range, the Bi_2O_3-Dy_2O_3-WO_3 system exhibited both phase separation and ageing after prolonged annealing at 500 °C for over 100 h [68].

1.7 Aims and Objectives of the Project

This work is aimed at studying comprehensively the relationship between average structure, local structure and conductivity as a function of both temperature and total substituent concentration in new double and triple substituted solid solutions of Bi_2O_3. The insights gained from this work will be used to design systems of Bi_2O_3 with improved conductivity and structural and phase stabilities. The objectives of the work were:

1. To verify if WO_3 within the concentration range 22-28 mol% can stabilize the highly conductive pure δ-phase in the Bi_2O_3-WO_3 system. Powder X-ray diffraction will be used to study independently the average structure and phase evolution as a function of WO_3 and annealing temperature in the Bi_2O_3-WO_3 system. Variable temperature Raman spectroscopy will be used to probe the evolution of the structure as a function of temperature (from ambient temperature to 800 °C) at constant composition. This will be complemented by differential thermal analysis to probe the thermal stability of the phases present from ambient temperature up to 800 °C. Variable temperature impedance

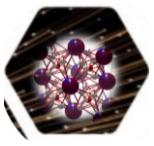

spectroscopy will be used to determine conductivities of the material and compared with those of YSZ at corresponding temperatures.

2. To combine W, Nb, Dy and Er (cations reported to produce systems high conductivity in Bi_2O_3 as discussed earlier) and produce novel systems such as Dy_2O_3-Er_2O_3-Bi_2O_3, Dy_2O_3-Er_2O_3-WO_3-Bi_2O_3 and Dy_2O_3-Er_2O_3-Nb_2O_5-Bi_2O_3 using the co-doping strategy. This is aimed at producing systems with both structural stability and high ionic conductivity. The phase evolution and conductivity will be studied in a similar way to the Bi_2O_3-WO_3 system. In addition, the pair distribution function technique will be used to probe both the local and average structure of phases found in the fabricated systems. Where applicable, symmetry mode-based Rietveld refinement will be employed to follow any phase evolution encountered in the new systems as a function of temperature. Any changes observed will be correlated with changes in conductivity measurements.
3. To probe the ageing phenomenon and establish a link between the conductivity decline and changes in the local structure of the material. This will be achieved by using local structural probes such X-ray absorption spectroscopy, photoluminescence and the pair distribution function technique on materials that exhibited ageing and those that did not. These techniques are able to probe the local environment (coordination numbers, oxidation state, bond lengths and site geometry) of a specific element (W, Er, Dy, Bi). By studying a sample before and after ageing, it is hoped that the changes in the local structure of the material will provide insights into how the ageing phenomenon occurs.

1.8 References

[1] Wachsman, E.D. and Lee, K.T., 2011. Lowering the temperature of solid oxide fuel cells. *Science*, *334*(6058), pp.935-939.

[2] Singhal, S.C., 2000. Science and technology of solid-oxide fuel cells. *MRS Bulletin*, *25*(3), pp.16-21.

[3] Adams, T.A., Nease, J., Tucker, D. and Barton, P.I., 2013. Energy conversion with solid oxide fuel cell systems: A review of concepts and outlooks for the short-and long-term. *Industrial & Engineering Chemistry Research*, *52*(9), pp.3089-3111.

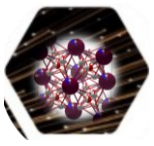

[4] Ormerod, R.M., 2003. Solid oxide fuel cells. *Chemical Society Reviews*, *32*(1), pp.17-28.

[5] Shin, T.H., Ida, S. and Ishihara, T., 2011. Doped CeO_2–$LaFeO_3$ composite oxide as an active anode for direct hydrocarbon-type solid oxide fuel cells. *Journal of the American Chemical Society*, *133*(48), pp.19399-19407.

[6] Adams, T.A., Nease, J., Tucker, D. and Barton, P.I., 2013. Energy conversion with solid oxide fuel cell systems: A review of concepts and outlooks for the short-and long-term. *Industrial & Engineering Chemistry Research*, *52*(9), pp.3089-3111.

[7] Stambouli, A.B. and Traversa, E., 2002. Solid oxide fuel cells (SOFCs): a review of an environmentally clean and efficient source of energy. *Renewable and Sustainable Energy Reviews*, *6*(5), pp.433-455.

[8] Fergus, J.W., 2006. Electrolytes for solid oxide fuel cells. *Journal of Power Sources*, *162*(1), pp.30-40.

[9] West, A.R., 2014. *Solid state chemistry and its applications*. John Wiley & Sons.

[10] Catlow, C.R.A., 1990. Atomistic mechanisms of ionic transport in fast-ion conductors. *Journal of the Chemical Society, Faraday Transactions*, *86*(8), pp.1167-1176.

[11] Abrahams, I. and Krok, F., 2003. A model for the mechanism of low temperature ionic conduction in divalent-substituted γ-BIMEVOXes. *Solid State Ionics*, *157*(1-4), pp.139-145.

[12] Abraham, F., Boivin, J.C., Mairesse, G. and Nowogrocki, G., 1990. The BIMEVOX series: a new family of high performances oxide ion conductors. *Solid State Ionics*, *40*, pp.934-937.

[13] Jiang, N., Wachsman, E.D. and Jung, S.H., 2002. A higher conductivity Bi_2O_3-based electrolyte. *Solid State Ionics*, *150*(3-4), pp.347-353.

[14] Boivin, J.C., 2001. Structural and electrochemical features of fast oxide ion conductors. *International Journal of Inorganic Materials*, *3*(8), pp.1261-1266.

[15] Nakayama, M. and Martin, M., 2009. First-principles study on defect chemistry and migration of oxide ions in ceria doped with rare-earth cations. *Physical Chemistry Chemical Physics*, *11*(17), pp.3241-3249.

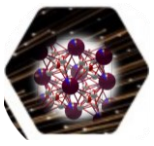

[16] Murray, A.D., Murch, G.E. and Catlow, C.R.A., 1986. A new hybrid scheme of computer simulation based on Hades and Monte Carlo: Application to ionic conductivity in Y^{3+} doped CeO_2. *Solid State Ionics*, *18*, pp.196-202.

[17] Andersson, D.A., Simak, S.I., Skorodumova, N.V., Abrikosov, I.A. and Johansson, B., 2006. Optimization of ionic conductivity in doped ceria. *Proceedings of the National Academy of Sciences*, *103*(10), pp.3518-3521.

[18] Badwal, S.P.S., Ciacchi, F.T. and Milosevic, D., 2000. Scandia–zirconia electrolytes for intermediate temperature solid oxide fuel cell operation. *Solid State Ionics*, *136*, pp.91-99.

[19] Mogensen, M., Sammes, N.M. and Tompsett, G.A., 2000. Physical, chemical and electrochemical properties of pure and doped ceria. *Solid State Ionics*, *129*(1-4), pp.63-94.

[20] Lee, J.G., Park, J.H. and Shul, Y.G., 2014. Tailoring gadolinium-doped ceria-based solid oxide fuel cells to achieve 2 W cm^{-2} at 550 C. *Nature Communications*, *5*(1), pp.1-10.

[21] He, X., Zhu, Y. and Mo, Y., 2017. Origin of fast ion diffusion in super-ionic conductors. *Nature Communications*, *8*(1), pp.1-7.

[22] Cabot, A., Marsal, A., Arbiol, J. and Morante, J.R., 2004. Bi_2O_3 as a selective sensing material for NO detection. *Sensors and Actuators B: Chemical*, *99*(1), pp.74-89.

[23] Bhande, S.S., Mane, R.S., Ghule, A.V. and Han, S.H., 2011. A bismuth oxide nanoplate-based carbon dioxide gas sensor. *Scripta Materialia*, *65*(12), pp.1081-1084.

[24] Li, R., Wang, D., Ge, L., He, S., Chen, H. and Guo, L., 2014. Effect of Bi_2O_3 on the electrochemical performance of $LaBaCo_2O_{5+\delta}$ cathode for intermediate-temperature solid oxide fuel cells. *Ceramics International*, *40*(2), pp.2599-2603.

[25] Won-In, K., Pongkrapan, S. and Dararutana, P., 2011. Eco-glass based on Thailand quartz sands and bismuth oxide. In *Materials Science Forum* (Vol. 695, pp. 223-226). Trans Tech Publications Ltd.

[26] Maeder, T., 2013. Review of Bi_2O_3 based glasses for electronics and related applications. *International Materials Reviews*, *58*(1), pp.3-40.

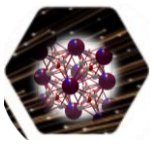

[27] Valant, M. and Suvorov, D., 2004. Dielectric Characteristics of Bismuth Oxide Solid Solutions with a Fluorite-Like Crystal Structure. *Journal of the American Ceramic Society*, *87*(6), pp.1056-1061.

[28] Harwig, H.A. and Gerards, A.G., 1978. Electrical properties of the α, β, γ, and δ phases of bismuth sesquioxide. *Journal of Solid State Chemistry*, *26*(3), pp.265-274.

[29] Sammes, N.M., Tompsett, G.A., Näfe, H. and Aldinger, F., 1999. Bismuth based oxide electrolytes—structure and ionic conductivity. *Journal of the European Ceramic Society*, *19*(10), pp.1801-1826.

[30] Levin, E.M. and Roth, R.S., 1964. Polymorphism of bismuth sesquioxide. I. Pure Bi_2O_3. *Journal of Research of the National Bureau of Standards. Section A, Physics and Chemistry*, *68*(2), p.189.

[31] Harwig, H.A. and Weenk, J.W., 1978. Phase relations in bismuth sesquioxide. *Zeitschrift für Anorganische und Allgemeine Chemie*, *444*(1), pp.167-177.

[32] Harwig, H.A. and Gerards, A.G., 1979. The polymorphism of bismuth sesquioxide. *Thermochimica Acta*, *28*(1), pp.121-131.

[33] Cheng, H., Huang, B., Lu, J., Wang, Z., Xu, B., Qin, X., Zhang, X. and Dai, Y., 2010. Synergistic effect of crystal and electronic structures on the visible-light-driven photocatalytic performances of Bi_2O_3 polymorphs. *Physical Chemistry Chemical Physics*, *12*(47), pp.15468-15475.

[34] Hull, S., 2004. Superionics: crystal structures and conduction processes. *Reports on Progress in Physics*, *67*(7), p.1233.

[35] Wachsman, E.D., Ball, G.R., Jiang, N. and Stevenson, D.A., 1992. Structural and defect studies in solid oxide electrolytes. *Solid State Ionics*, *52*(1-3), pp.213-218.

[36] Hull, S., Norberg, S.T., Tucker, M.G., Eriksson, S.G., Mohn, C.E. and Stølen, S., 2009. Neutron total scattering study of the δ and β phases of Bi_2O_3. *Dalton Transactions*, (40), pp.8737-8745.

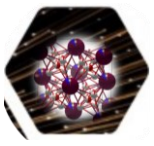

[37] Battle, P.D., Catlow, C.R.A., Drennan, J. and Murray, A.D., 1983. The structural properties of the oxygen conducting δ phase of Bi_2O_3. *Journal of Physics C: Solid State Physics*, *16*(17), p.L561.

[38] Sillén, L.G., 1937. *X-ray studies on bismuth trioxide*. Almqvist & Wiksell.

[39] Aidhy, D.S., Sinnott, S.B., Wachsman, E.D., Phillpot, S.R. and Nino, J.C., 2009. Structure of δ-Bi_2O_3 from density functional theory: A systematic crystallographic analysis. *Journal of Solid State Chemistry*, *182*(5), pp.1222-1228.

[40] Gattow, G. and Schröder, H., 1962. About bismuth oxides. III. The crystal structure of the high-temperature modification of bismuth (III) oxide (δ -Bi_2O_3). *Z. Anorg. Allg. Chem*, *318*, p.14.

[41] Willis, B.T.M., 1965. The anomalous behaviour of the neutron reflexion of fluorite. *Acta Crystallographica*, *18*(1), pp.75-76.

[42] Harwig, H.A., 1978. On the Structure of Bismuth sesquioxide: The α, β, γ, and δ-Phase. *Zeitschrift für Anorganische und Allgemeine Chemie*, *444*(1), pp.151-166.

[43] Mädler, L. and Pratsinis, S.E., 2002. Bismuth oxide nanoparticles by flame spray pyrolysis. *Journal of the American Ceramic Society*, *85*(7), pp.1713-1718.

[44] Radaev, S.F., Simonov, V.I. and Kargin, Y.F., 1992. Structural features of γ-phase Bi_2O_3 and its place in the sillenite family. *Acta Crystallographica Section B: Structural Science*, *48*(5), pp.604-609.

[45] Azad, A.M., Larose, S. and Akbar, S.A., 1994. Bismuth oxide-based solid electrolytes for fuel cells. *Journal of Materials Science*, *29*(16), pp.4135-4151.

[46] Takahashi, T. and Iwahara, H., 1973. High oxide ion conduction in sintered oxides of the system Bi_2O_3-WO_3. *Journal of Applied Electrochemistry*, *3*(1), pp.65-72.

[47] Hoda, S.N. and Chang, L.L., 1974. Phase Relations in the System Bi_2O_3-WO_3. *Journal of the American Ceramic Society*, *57*(7), pp.323-326.

[48] Suzuki, T., Yamazaki, T., Hosaka, E. and Yoshioka, H., 1985. Quenched metastable phases and their transformations on heating in the Bi_2O_3-WO_3 system. *Journal of Materials Science*, *20*(11), pp.4155-4162.

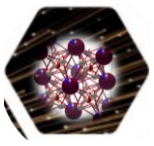

[49] Nespolo, M., Watanabe, A. and Suetsugu, Y., 2002. Re-Investigation of the Structure of $7Bi_2O_3 \cdot 2WO_3$ by Single-Crystal X-ray Diffraction. *Crystal Research and Technology: Journal of Experimental and Industrial Crystallography*, *37*(4), pp.414-422.

[50] Watanabe, A. and Ono, A., 2004. Thermostable region of an oxide ion conductor, $Bi_7WO_{13.5}$ (= $7Bi_2O_3 \cdot 2WO_3$), and the solid solubility extension. *Solid State Ionics*, *174*(1-4), pp.15-18.

[51] Borowska-Centkowska, A., Leszczynska, M., Krok, F., Malys, M., Wrobel, W., Hull, S. and Abrahams, I., 2018. Local structure and conductivity behaviour in Bi 7 WO 13.5. *Journal of Materials Chemistry A*, *6*(13), pp.5407-5418.

[52] Watanabe, A., Ishizawa, N. and Kato, M., 1985. An outline of the structure of $7Bi_2O_3 \cdot 2WO_3$ and its solid solutions. *Journal of Solid State Chemistry*, *60*(2), pp.252-257.

[53] Verkerk, M.J. and Burggraaf, A.J., 1981. High Oxygen Ion Conduction in Sintered Oxides of the Bi_2O_3-Dy_2O_3 System. *Journal of the Electrochemical Society*, *128*(1), p.75.

[54] Wachsman, E.D., Boyapati, S. and Jiang, N., 2001. Effect of dopant polarizability on oxygen sublattice order in phase-stabilized cubic bismuth oxides. *Ionics*, *7*(1), pp.1-6.

[55] Fung, K.Z., Chen, J. and Virkar, A.V., 1993. Effect of aliovalent dopants on the kinetics of phase transformation and ordering in RE_2O_3-Bi_2O_3 (RE= Yb, Er, Y, or Dy) solid solutions. *Journal of the American Ceramic Society*, *76*(10), pp.2403-2418.

[56] Boyapati, S., Wachsman, E.D. and Chakoumakos, B.C., 2001. Neutron diffraction study of occupancy and positional order of oxygen ions in phase stabilized cubic bismuth oxides. *Solid State Ionics*, *138*(3-4), pp.293-304.

[57] Tran, T.B. and Navrotsky, A., 2014. Energetics of disordered and ordered rare earth oxide-stabilized bismuth oxide ionic conductors. *Physical chemistry chemical physics*, *16*(6), pp.2331-2337.

[58] Verkerk, M.J. and Burggraaf, A.J., 1981. High oxygen ion conduction in sintered oxides of the Bi_2O_3-Ln_2O_3 system. *Solid State Ionics*, *3*, pp.463-467.

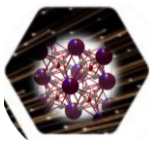

[59] Verkerk, M.J., Van de Velde, G.M.H., Burggraaf, A.J. and Helmholdt, R.B., 1982. Structure and ionic conductivity of Bi_2O_3 substituted with lanthanide oxides. *Journal of physics and chemistry of solids*, *43*(12), pp.1129-1136.

[60] Jiang, N., Buchanan, R.M., Stevenson, D.A., Nix, W.D., Li, J.Z. and Yang, J.L., 1995. Anion ordering in aged stabilized bismuth oxide. *Materials Letters*, *22*(5-6), pp.215-219.

[61] Verkerk, M.J., Keizer, K. and Burggraaf, A.J., 1980. High oxygen ion conduction in sintered oxides of the Bi_2O_3-Er_2O_3 system. *Journal of applied electrochemistry*, *10*(1), pp.81-90.

[62] Shuk, P., Wiemhöfer, H.D., Guth, U., Göpel, W. and Greenblatt, M., 1996. Oxide ion conducting solid electrolytes based on Bi_2O_3. *Solid State Ionics*, *89*(3-4), pp.179-196.

[63] Wachsman, E.D., Jiang, N., Mason, D.M. and Stevenson, D.A., 1989. Solid state oxygen kinetics in Er_2O_3 stabilized Bi_2O_3. *ECS Proceedings Volumes*, *1989*(1), p.15.

[64] Shitara, K., Moriasa, T., Sumitani, A., Seko, A., Hayashi, H., Koyama, Y., Huang, R., Han, D., Moriwake, H. and Tanaka, I., 2017. First-principles selection of solute elements for Er-stabilized Bi_2O_3 oxide-ion conductor with improved long-term stability at moderate temperatures. *Chemistry of Materials*, *29*(8), pp.3763-3768.

[65] Yun, B.H., Lee, C.W., Jeong, I. and Lee, K.T., 2017. Dramatic enhancement of long-term stability of erbia-stabilized bismuth oxides via quadrivalent Hf doping. *Chemistry of Materials*, *29*(24), pp.10289-10293.

[66] Meng, G., Chen, C., Han, X., Yang, P. and Peng, D., 1988. Conductivity of Bi_2O_3-based oxide ion conductors with double stabilizers. *Solid State Ionics*, *28*, pp.533-538.

[67] Jung, D.W., Duncan, K.L. and Wachsman, E.D., 2010. Effect of total substituent concentration and dopant ratio on conductivity of $(DyO_{1.5})_x$–$(WO_3)_y$–$(BiO_{1.5})_{1-x-y}$. *Acta Materialia*, *58*(2), pp.355-363.

[68] Jung, D.W., Duncan, K.L., Camaratta, M.A., Lee, K.T., Nino, J.C. and Wachsman, E.D., 2010. Effect of Annealing Temperature and Dopant Concentration on the Conductivity Behavior in $(DyO_{1.5})_x$–$(WO_3)_y$–$(BiO_{1.5})_{1-x-y}$. *Journal of the American Ceramic Society*, *93*(5), pp.1384-1391.

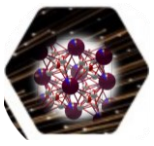

Chapter 2: Experimental Techniques

2.1 Synthetic Methods

The properties of functional materials have been shown to depend heavily on the local, average and microstructure of the material. The local, average and microstructure of the materials such as bond length, site geometry, phases present, particle size, morphology and defects can be controlled to a certain extent by the synthetic method used. Manipulation of parameters such as synthesis temperature, pH, and pressure determine the local, average and microstructure of the material in a chemical reaction and can lead to the design of functional material with enhanced properties. There are various synthetic methods employed in the fabrication of solid inorganic functional materials. In this work, only two synthetic methods were explored, viz: solid-state reactions and the citrate-gel method.

2.1.1 Solid-state Reactions

The solid-state reaction method is the conventional, classic method of fabricating inorganic solids. In a simple case, stoichiometric amounts of powdered reactants X and Y are mixed, ground and heated in a furnace for a prolonged period to form a product XY. X and Y can be elements or compounds. A comprehensive understanding of the atomistic basis of the solid-state reaction was made possible by Frenkel, Wagner and Schottky [1] and was reviewed extensively by Busch [2]. The formation of spinel from two individual oxides is normally used as a prototype reaction to illustrate the reaction mechanism of a solid-state reaction [3, 4]. For a solid-state reaction to occur, the surfaces of the reactants X and Y at the interface between the reactants must have vacancies. These vacancies enable the exchange of atoms between the reactants and lead to the formation of

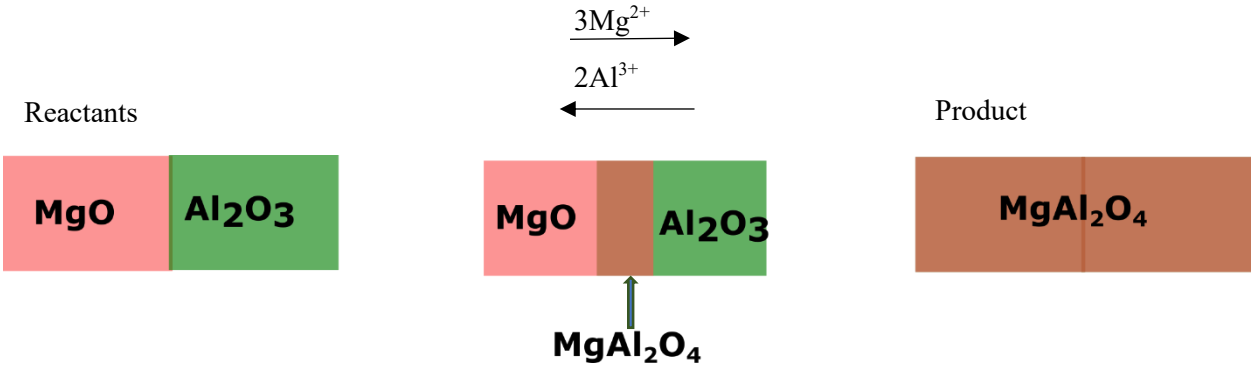

Figure 2.1. Reaction mechanism of the solid-state reaction at the interfaces of MgO and Al_2O_3.

a nucleus of the product XY. This nucleus grows into the new phase and further separates the reactants (Fig. 2.1).

Further reaction is facilitated by higher temperatures which enable the hopping of reactant atoms from one vacant site to another from the two opposite interfacial regions, through the new phase towards the opposite interfaces between the new phase and the reactants (Fig. 2.1). Intermediate grinding and pellet pressing during the reaction increase intimacy between fresh reactants and facilitate further reaction. Solid-state reactions are widely used in the fabrication of bismuth oxide solid solutions. In this work, this method was used as a reference method to fabricate the solid solutions of bismuth oxide and compare the products to those synthesized using the citrate-gel method. There are numerous disadvantages associated with the solid-state reaction method. This method is in general, energy-intensive since it requires high temperatures for prolonged periods. Reaction times can vary from several days to up to a week. Sometimes it does not lead to any product even after heating at high temperatures for up to a month [4, 5]. It is also not entirely suitable for oxides like Bi_2O_3, PbO and Tl_2O that volatilise easily. It is particularly unsuited to very stable, non-reactive reagents and is notorious for forming inhomogeneous samples with large particle sizes. However, in this work, the solid-state reaction method has been used to synthesis some of the materials to study the effect of synthetic route. This also enables direct comparison to materials reported in literature synthesised using this method.

Generally, to synthesis the materials in this work, the oxides were pre-fired to 700 °C to remove any possible bismutite ($Bi_2O_3 \cdot CO_2$) and moisture which has been reported to influence the phase evolution in Bi_2O_3 solid solutions [6]. Since oxides of the rare earths are expensive, and only a small amount was needed for synthesis, some of the rare earth oxides were obtained by thermal decomposition of nitrate salts in a muffle furnace at 700 °C for about 2 hours in a method similar to that employed by Melnikov *et al.* [7]. Stoichiometric amounts of the oxides were mixed in an agate mortar and manually ground for an hour in acetone (the acetone was added for ease of grinding and mixing). The mixture was dried in an oven at 80 °C for 12 hours before being annealed in a muffle furnace at 800°C in air for 24 hours and slow cooled (~1 °C/min) back to room temperature. It was then reground before being annealed at 800°C in air for a further 24 hours and slow cooled again. More specific details will be given in each results chapter.

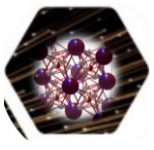

Other soft chemistry methods have been developed to form products of oxides where the solid-state reaction would not give products [5]. In soft chemistry methods, atomic-level mixing of reactants is achieved by the use of complexing agents usually in solution. One example of soft chemistry methods is the citrate-gel method.

2.1.2 Citrate-gel Method

In the citrate-gel method, the carboxylic acid, citric acid is used as a chelating agent in which the carboxylate groups act as ligands to form complexes with metal cations. Citric acid has three carboxylic groups on each acid molecule (Fig. 2.2), so it is a very effective and efficient complexing agent.

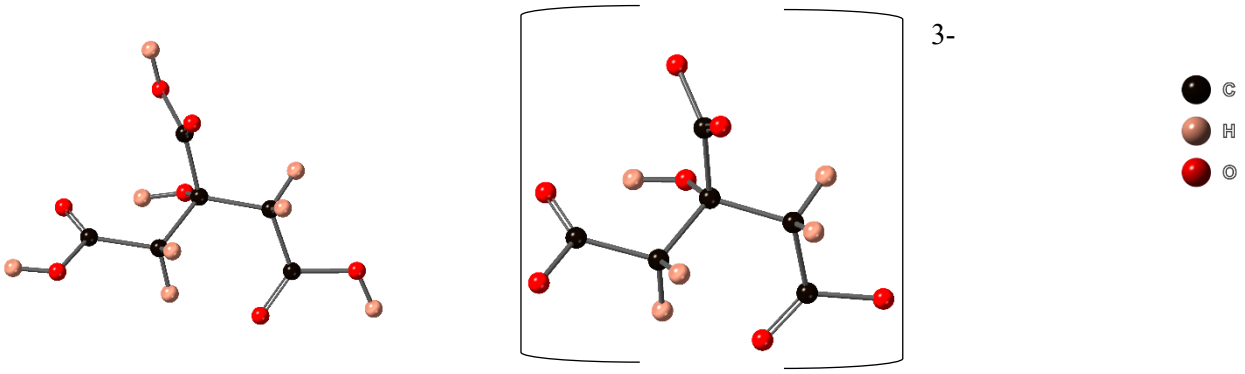

Figure 2.2. Structure of a citric acid molecule and the fully ionized citrate ion.

The citrate ion is a highly branched ligand with seven possible oxygen atoms acting as donor atoms (Fig. 2.2). The solution equilibria of citrate-metal complexes have been reported to be fairly complicated and it is challenging to predict the complex that this ligand forms. For instance, Bi^{3+} has been reported to form dimers, cubes, chains and sheets with citrate ions [8]. Since the exact stoichiometric amount of citrate ions present to complex with the total metal ions added is not known, an excess amount of citric acid is normally added to make sure that the complexing agent is not a limiting reactant. The metals used are normally added in the form of nitrate salt solutions. After the complexing step, the solvent is evaporated at temperatures of about 200 °C to leave behind a viscous gel. The gel is then calcined in air using a furnace at temperatures between 450–500 °C to leave behind the metal oxides. A further annealing step at a higher temperature may be needed to achieve the desired crystalline phase. The citrate-gel method, if successful, can result in improved homogeneity, and controlled particle and crystallite size [9]. In general, products are

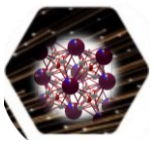

formed at relatively lower temperatures compared to solid-state reactions [9]. Since mixing takes place at the molecular level, ternary and quaternary metal oxides are easy to make [10].

Generally, in this work, stoichiometric amounts (with respect to the metal oxides) of $Bi(NO_3)_3 \cdot 5H_2O$ (99.99% pure, Sigma-Aldrich) and $Er(NO_3)_3 \cdot 5H_2O$ (99.99% pure, Sigma-Aldrich) were completely dissolved in acetic acid at room temperature while stirring. As sources of W and Dy, $(NH_4)_6H_2W_{12}O_{40} \cdot H_2O$ (Sigma-Aldrich) and $DyCl_3 \cdot 6H_2O$ (99.99% pure, Sigma-Aldrich), respectively, were mixed together in acetic acid and heated to ~150°C until all the $DyCl_3 \cdot 6H_2O$ had dissolved. After cooling, 50 ml of 1 M nitric acid was added to dissolve the $(NH_4)_6H_2W_{12}O_{40} \cdot H_2O$ completely under constant stirring. The solutions were then mixed in the presence of citric acid in a 3:1 mole ratio of citric acid to metal ions. The resultant solution was heated at ~250°C under constant stirring until the solvent evaporated and left behind a viscous gel. The gel was dried overnight in an oven at 80°C and then calcined at 500°C in a muffle furnace for ~12 hours. It was slowly cooled in the furnace (the estimated average cooling rate was ~1 °C min^{-1}) back to room temperature and then ground. The ground powder was further annealed at 750°C for a further 24 hours. Any deviations from this procedure applied in this work will be reported in the respective chapters.

2.2 Diffraction

In this work, the diffraction phenomenon was extensively used to characterize the structure of the crystalline materials. Diffraction is the process whereby waves spread out when passing through an aperture with a width comparable to the wavelength of the waves. The distances between arrays of atoms in crystalline materials are in the order of 0.1 nm. This is comparable to the wavelength of X-rays. Max von Laue first suggested that arrays of atoms in a crystalline material could act as a diffraction grating for X-rays in 1912. This was subsequently confirmed by experiments in the same year by Max von Laue, Walter Friedrich and Paul Knipping [11].

2.2.1 Bragg's Law

The diffraction pattern obtained from the passage of X-rays through a crystalline material can be partly explained by using Bragg's analysis. The Fraunhofer approximation is invoked to simplify the Bragg analysis. In this approximation, the distances from the source to the aperture (or sample) and from the aperture (or sample) to the observation plane (or detector) should be far larger than the opening width of the aperture. The waves (from source and diffracted waves) should also be

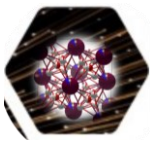

coherent. This means that the waves can be modelled as plane waves and that the waves reaching the detector can be viewed as parallel. In Bragg's analysis, the arrays of atoms are viewed as planes that reflect the monochromatic X-rays (Fig. 2.3).

Suppose that the angle between the incident X-rays and the upper plane is θ, called the Bragg

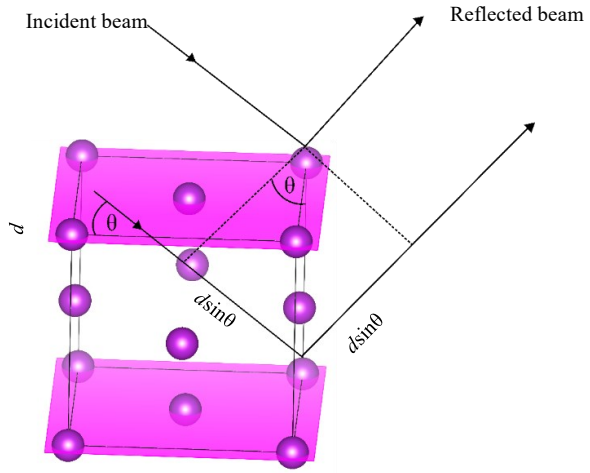

Figure 2.3. Illustration of Bragg's law. The layers of atoms reflect the incident beam. When two layers are parallel and separated by a distance *d*, the incident ray reflected at the layer a distance *d* from the first layer will have travelled a distance 2*d*sinθ by the time they reach an observation point provided they are approximated to be parallel at that point.

angle, the incident ray can be reflected from both the upper plane and the bottom plane. By the time the rays reach the detector, the ray that has been reflected from the bottom plane has travelled a longer distance (called path length) of 2*d*sinθ, where *d* is the interplanar distance. If this path length is an integer multiple of the wavelength of the X-rays and the Fraunhofer approximation is invoked, constructive interference (bright spot) is observed at the detector when $2d\sin\theta = m\lambda$, and m =1, 2, 3, 4… This condition is called Bragg's law. However, when 2*d*sinθ is not an integer multiple of the wavelength, destructive interference (dark region) is observed at the detector. When the sample is a single crystal, the pattern observed on the detector in 2 dimensions appears as an array of spots as shown in Fig. 2.4.

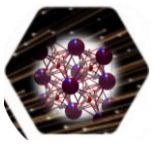

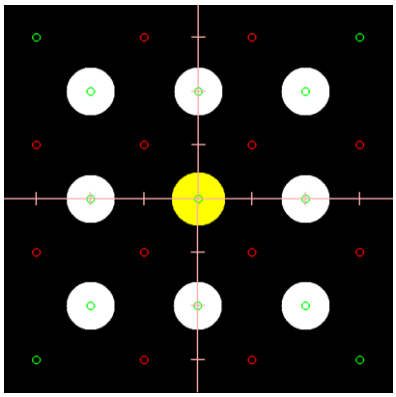

Figure 2.4. A single crystal diffraction pattern. The red, green and white spots are reflections from planes that constitute atoms of different types and/or positions in the crystal.

The distance between the spots has a reciprocal relationship with the width of the aperture or *d*, the distance between the arrays of atoms. The distance *d* between the arrays of atoms, the Bragg angle θ, the identity of the reflecting plane (Miller index) and the angular relationships between the arrays of points can be used to determine the geometry of the unit cell of the material being probed. Further analysis of the intensity of the spots and any observed systematic absences of spots can lead to structure determination. However, *ab initio* structure determination is not a subject of this work. Sources covering Bragg's law, *ab initio* structure determination and diffraction in-depth are listed in the Bibliography.

2.2.2 Crystal Systems and the Crystallographic Lattices

The unit cell is the smallest repeat unit that encloses points in a point lattice. The point lattice can either be in 2 dimensions (2D) or 3 dimensions (3D). Each lattice point can be translated using a translation vector $\mathbf{t} = n_1\mathbf{a_1} + n_2\mathbf{a_2} + n_3\mathbf{a_3}$ where n_1, n_2, n_3 are integers and $\mathbf{a_1}$, $\mathbf{a_2}$ and $\mathbf{a_3}$ are basis vectors to recreate an entire infinite lattice. The infinite set of translation vectors is called a vector lattice **T**. When the vector lattice is used to describe the pattern of spots created by a diffraction lattice from a crystalline material, the lattice is called a crystallographic lattice and the basis vectors are crystallographic basis vectors. When the crystallographic basis vectors ($\mathbf{a_1}$, $\mathbf{a_2}$ and $\mathbf{a_3}$) are chosen such that all the translation vectors are an integral linear combination of the basis vectors, the lattice they describe is called a primitive lattice (P). In general, the basis vectors are chosen to be parallel to rotation axes, and perpendicular to mirror planes, i.e., they are symmetry-adapted. This leads to the seven crystal systems (Table 2.1) obtained from the 32 crystallographic point groups. If the vector lattice that describes the crystal lattice is still a linear combination of the integral multiples of the basis vectors, the lattice they describe remains primitive. The point groups

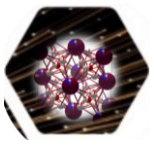

are the group of finite symmetry operations (rotation, reflection, inversion, and roto-inversion) that leave at least one point invariant when applied to a crystallographic object.

Table 2.1. The seven crystal systems.

Crystal System	Lattice parameters
Triclinic 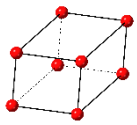	$a \neq b \neq c$ $\alpha = 90° \neq \beta \neq \gamma$
Monoclinic 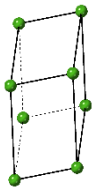	$a \neq b \neq c$ $\alpha = \beta = 90° \neq \gamma$
Orthorhombic 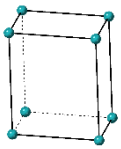	$a \neq b \neq c$ $\alpha = \beta = \gamma = 90°$
Trigonal 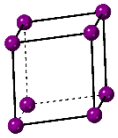	$a = b = c$ $\alpha = \beta = \gamma \neq 90°$
Hexagonal 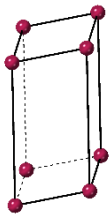	$a = b \neq c$ $\alpha = 120°, \beta = \gamma = 90°$
Tetragonal 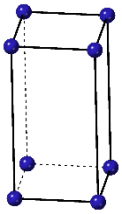	$a = b \neq c$ $\alpha = \beta = \gamma = 90°$

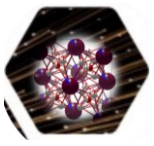

Cubic	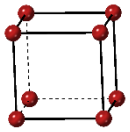	$a = b = c$ $\alpha = \beta = \gamma = 90°$

Symmetry-adapted basis vectors simplify both the matrices that represent the symmetry operations and the formulae for calculating distances and angles of a unit cell. A consequence of this is that the vector lattice might comprise lattice vectors that are no longer integral linear combinations of the basis vectors. When this happens, the lattice described by these vectors is said to be centred and is called the Bravais lattice. The common types of centred lattices are base centred A (b–c plane), base centred B (a–c plane), base centred C (a–b plane), face centring F (a–b, b–c and a–c planes), the inner centring I, and the rhombohedral centring R (along a diagonal). There are infinite types of Bravais lattices. However, when only the seven crystal systems and the common lattices are combined, 14 Bravais lattices emerge as shown in Table 2.2

Table 2.2. The fourteen Bravais lattices*.

Crystal System	P	C	I	F	R	Lattice parameters
Triclinic	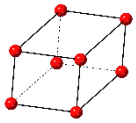					$a \neq b \neq c$ $\alpha = 90° \neq \beta \neq \gamma$
Monoclinic	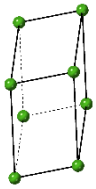	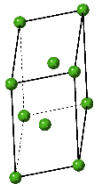				$a \neq b \neq c$ $\alpha = \beta = 90° \neq \gamma$
Orthorhombic	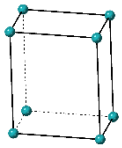	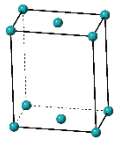	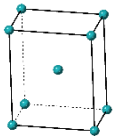	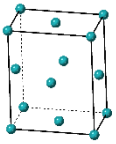		$a \neq b \neq c$ $\alpha = \beta = \gamma = 90°$

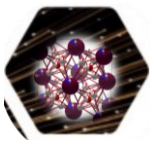

Trigonal		$a = b = c$ $\alpha = \beta = \gamma \neq 90°$
Hexagonal		$a = b \neq c$ $\alpha = 120°,$ $\beta = \gamma = 90°$
Tetragonal		$a = b \neq c$ $\alpha = \beta = \gamma = 90°$
Cubic	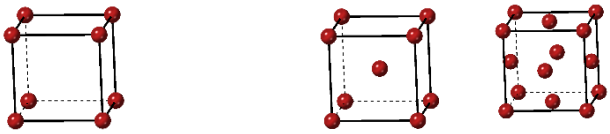	$a = b = c$ $\alpha = \beta = \gamma = 90°$

*The trigonal and hexagonal systems share the same Laue class and cannot be distinguished in a powder diffraction pattern and are normally collapsed into one lattice.

When rotations and reflections are combined with translation vectors, new compound symmetry elements called infinite symmetry elements emerge (screw axes and glide planes). When these infinite symmetry elements are combined with the 32 crystallographic point groups, 230 crystallographic space group types are produced [12, 13]. The 3D crystal symmetry of different crystalline materials are described partly by using the 230 space group types. However, space group types alone are not enough and are different from space group symmetries of a material. The space group symmetry of materials comprises the space group type and the position of the symmetry elements. This means that two materials can have the same space group type but different space group symmetries or crystal structures depending on the position of the symmetry elements. That means that the number of space group symmetries is infinite.

During a phase transition, a material can change from one space group symmetry to another. Depending on the nature of the phase transition, a group–subgroup relationship may exist between

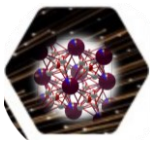

the space group symmetries of the two phases. Symmetry mode analysis can be employed to follow the phase transition and simplify the analysis across the phase transition as discussed in the next section and applied in Chapter 5.

2.2.3 Symmetry Relationships Between Space Groups

In the symmetry mode approach, the symmetry of the low symmetry structure (hettotype) is decomposed and expressed in terms of the distortion modes of the high symmetry structure (aristotype). Distortion modes (specific to displacive modes) are a group of correlated atomic displacements that are symmetry adapted. In the conventional crystallographic description of a crystal structure, the basis of the unit cell could be developed from a cartesian coordinate space. The x, y, and z coordinates and occupancy of a site must be given to describe the crystal structure. In this description, the hettotype is entirely independent of the aristotype. However, in the symmetry mode approach, the structure of the hettotype can be expressed in terms of the structure of the aristotype plus distortion modes that break some of the symmetry constraints of the aristotype.

If the symmetry lowering involves the size of the unit cell without an origin shift, a transformation matrix needs to be calculated to express the basis of the hettotype in terms of the basis of the aristotype. The general equation normally used is given by:

$$\begin{pmatrix} a' \\ b' \\ c' \end{pmatrix} = \begin{pmatrix} a_{11} & b_{12} & c_{13} \\ a_{21} & b_{22} & c_{23} \\ a_{31} & b_{32} & c_{33} \end{pmatrix} \begin{pmatrix} a \\ b \\ c \end{pmatrix} \tag{2.1}$$

where a', $b'$and c' denotes the basis of the hettotype and a, b and c denotes the basis of the aristotype. The 3 × 3 matrix is the transformation matrix relating the two bases. Distortion modes move atoms in a correlated manner to lower symmetry.

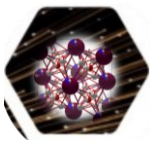

The motion of the atoms can be described by using a vector. Since many atoms can be affected by a single distortion mode, the vector can have high dimensions and operate in a space called carrier space. In this general carrier space, a set of vectors that point in a specific direction and lead to structures of lower symmetry or distortion symmetries is called an order parameter direction (OPD). In this subspace, each member of the set leads to a different distortion symmetry or hettotype. The OPD gives a guide on how distortion modes can lower the symmetry of an aristotype for a given irreducible representation (irrep) at a given k-point. The k-point is the point that describes where superlattice reflections will be observed after a phase transition in reciprocal space in addition to the fundamental reflections from the aristotype. For a given irrep in 3D, a general OPD can be given as (a; b; c) where a, b, and c are called the branches of the OPD. When $a \neq b \neq c$, the structure that results from this distortion mode is called the kernel and has the lowest symmetry possible as illustrated by Fig. 2.5. If $a = b \neq c$, the distortion symmetry is intermediate between the kernel and the parent, i.e. it is a supergroup of the kernel and a subgroup of the parent.

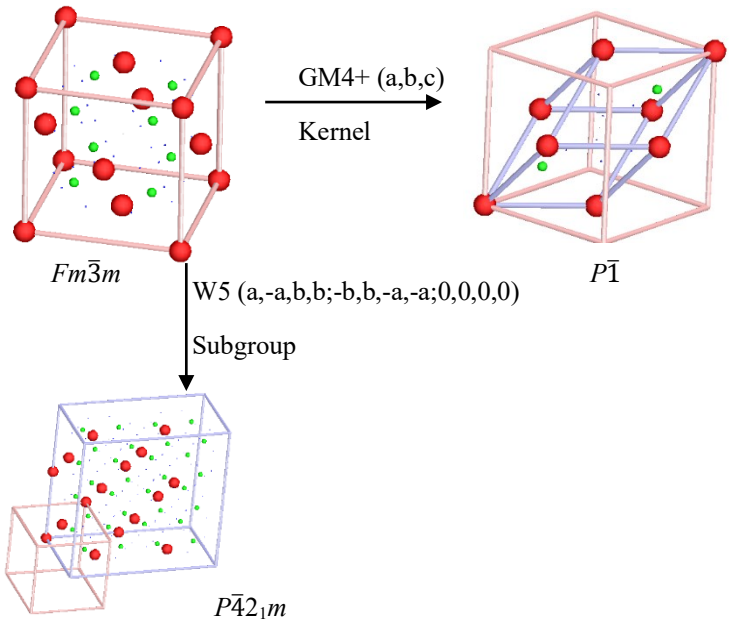

Figure 2.5. A partial subgroup tree showing the relationship between the aristotype ($Fm\bar{3}m$) and its isotropy subgroups ($P\bar{4}2_1m$ and $P\bar{1}$).

To express the structure of the hettotype in terms of the structure of the aristotype plus distortion modes, representation theory is normally used [14]. However, to perform such a decomposition, extensive knowledge of representation and group theory is not a prerequisite. Software packages such as AMPLIMODES [15] and the ISODISTORT suite of programs [16, 17] are used to perform

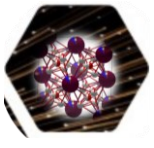

the decomposition. In this work, the ISODISTORT suite of programs was used. Campbell et al. [18] and Dinnebier et al. [19] summarize well the recipe for using ISODISTORT to perform the decomposition. The search over arbitrary k-points method restricted by the space group and basis of the hettotype was employed in this work. An equation similar to (2.1) for changing the basis was used and the specific equation will be discussed further in Chapter 5.

2.2.4 Powder X-ray Diffraction

Many crystalline functional materials are used when they are in their powdered (polycrystalline) form. Therefore, it is beneficial to study the material in the form they are used to gain a deeper understanding of their behaviour when in use. When X-ray diffraction is used to probe polycrystalline materials, the technique is called powder X-ray diffraction (PXRD). Neutrons and to a lesser extent electrons can also be used. The use of PXRD to probe the structure of materials was reported as early as 1916 by Debye and Scherrer and independently by Hull in 1917 [20-22]. Here a polycrystalline material is usually irradiated with coherent X-rays of fixed wavelength (angle dispersive), except in the Laue method where a polychromatic beam is used at a fixed angle (energy dispersive).

If the crystallites in polycrystalline materials are randomly oriented, instead of producing individual spots as observed in Fig. 2.4, the resultant 3D diffraction pattern is a group of nested cones about an origin (called Debye-Scherrer cones) as Fig. 2.6 (a) illustrates. However, since 2D detectors are used and the actual diffraction pattern observed is a group of nested circles about an origin (called Debye-Scherrer rings) as illustrated by Fig. 2.6 (b). When the ring or a portion thereof is integrated and the resulting numerical values of the intensity are plotted as a function of twice the Bragg angle (2θ) as in Fig. 2.6 (c), the information is converted from 2D to 1D. This result in the loss of information due to peak overlap. This peak overlap may be due to high symmetry (as found in cubic structures) or from accidental peak overlap due to low symmetry. Therefore, careful analysis of such data is of paramount importance. The relative intensity of each peak (known as a Bragg peak) or Debye-Scherrer ring is related to the average structure of the material.

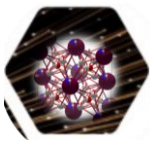

Some of the intensities that appear in between and underneath the Bragg peaks from diffuse coherent scattering are related to the local structure of the material and indicate a deviation from the long-range periodicity of the material. The relationship between the relative intensities measured (Bragg and diffuse intensities) and the structure is discussed in depth in most powder diffraction books (listed in the Bibliography) and will not be discussed further. This work will focus on the methods that extract the information from the powder diffraction data and relate it to both the local and average structure of the material. To relate the Bragg data to the average structure of the material, the Rietveld refinement method is used. To extract information relating to both the local and average structure, both the Bragg and diffuse scattering data (i.e. total scattering data) are analysed by using the technique called the pair distribution function (PDF).

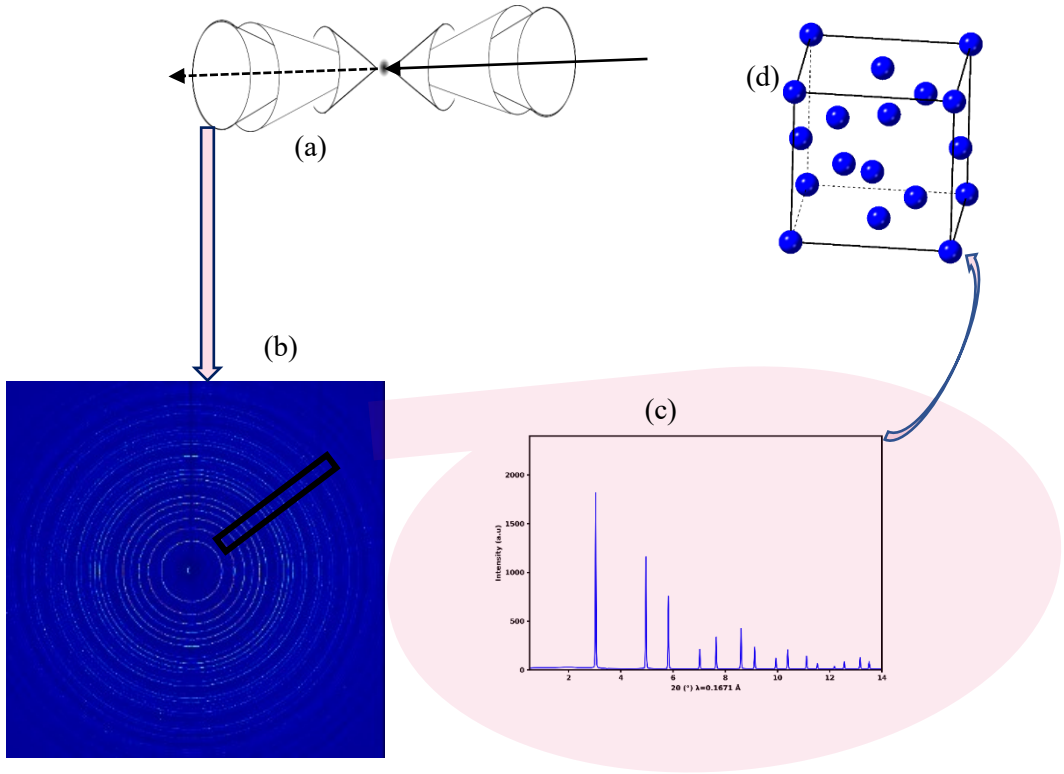

Figure 2.6. The Debye-Scherrer nested cones in 3D **(a)** are shown to transform into nested circles in 2D **(b)**. After integration of the intensity of each circle or part thereof, the 1D intensity is obtained **(c)**. Structure determination methods are employed to obtain a structure from the data **(d)**.

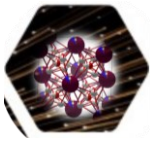

2.2.5 The Rietveld Method

Earlier methods for structure determination from powder diffraction data were adapted from methods used in structure determination from single-crystal data [23]. They relied on the decomposition of the powder diffraction pattern, i.e., the calculation of the integrated intensities from each Bragg peak. However, when there was a significant overlap of the Bragg peaks, these methods gave inaccurate structural solutions and were limited only to solving high symmetry structures. In 1967 and 1969, Rietveld [24, 25] presented a method that utilized the whole profile of the diffraction pattern (each data point in the profile) instead of only the integrated intensities of the Bragg peaks, as shown in Fig. 2.7. This means that the intensity should be digitized into discrete values (y_{obs}) per point. This revolutionized structural solution from powder diffraction data because the inaccuracies due to peak overlap were significantly reduced. However, since this method utilizes the least square fitting procedure, it requires a starting model to calculate the intensity (y_{calc}) at each point. Therefore, it is not a stand-alone method in structure determination but plays a huge role in refining structural parameters.

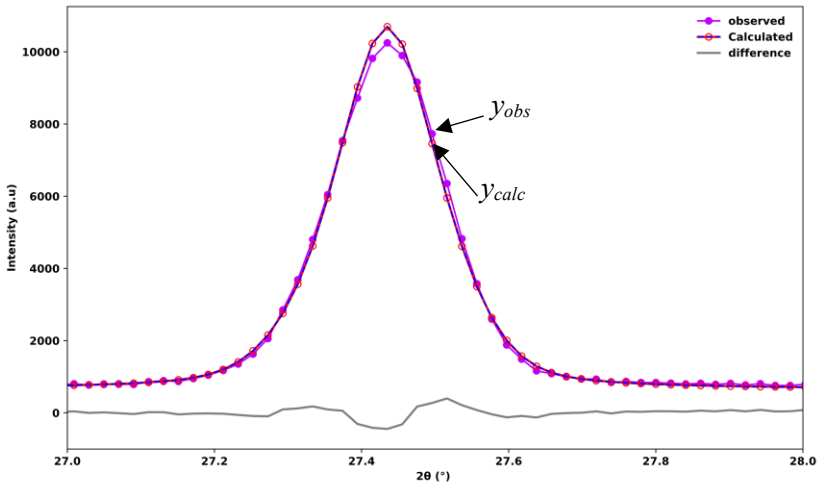

Figure 2.7. A fragment of a diffraction pattern showing the digitized intensity values as a function of 2θ. The open circles represent y_{calc} values and the closed circles represent y_{obs} values.

The quantity minimized in a Rietveld refinement is given by:

$$S = \sum_{i=1}^{N} w_i (y_{obs}^i - y_{calc}^i(\boldsymbol{f}))^2 \qquad (2.2)$$

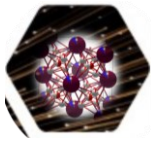

where $w_i = 1/ y^i_{obs}$ is the weight of each data point that is normally used. Other weighting schemes are discussed further by ref. [19]. The variable $\boldsymbol{f}$ represents the fitting parameters in $y^i_{calc(\boldsymbol{f})}$ and S is nonlinear in these parameters therefore good starting values are necessary for the numerical minimization algorithm to converge. The calculated intensities are given by the equation:

$$\boldsymbol{y}^i_{calc}(\boldsymbol{f}) = K \times p_{hkl} \times L_\theta \times P_\theta \times A_\theta \times T_{hkl} \times E_{hkl} \times |F_{hkl}|^2 \qquad (2.3)$$

where, K is the scale factor, p_{hkl} is the multiplicity factor, L_θ is the Lorentz factor, P_θ is the polarization factor, A_θ is the absorption factor, T_{hkl} is the preferred orientation factor, E_{hkl} is the extinction factor and F_{hkl} is the structure factor and hkl denotes the Miller index of a particular Bragg peak. The calculated peak intensities and peak positions are parametrized by both the structure (i.e. atomic coordinates, site occupancies and thermal displacements) in the asymmetric unit and the diffraction experiment (unit cell distances and angles, instrument resolution function, domain size, microstrain etc.). The meaning of each parameter in equation (2.3) is a lengthy subject and is well explained in literature [12, 19].

Agreement factors (R-factors) are used to monitor the progress and merits of a Rietveld refinement. Table 2.3 summarizes the meaning of each factor and its significance to the fitting statistics. These factors should be used with caution. Since a Rietveld refinement utilizes the least square fitting method, it is susceptible to being stuck at local minima. This may result in good agreement factors, however, the fitted values may be physically meaningless. For instance, negative thermal factors have no physical meaning structurally but may indicate dominant absorption effects during data collection.

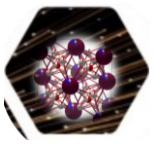

Table 2.3. Table of agreement factors for Rietveld refinement and their meanings [19].

Agreement factor	Meaning
$R_p = \frac{\sum_{i=1}^{N} \lvert y_{obs}^i - y_{calc}^i(\boldsymbol{f}) \rvert}{\sum_{i=1}^{N} y_{obs}^i}$	Measures the difference between observed and calculated profiles. Overemphasises the most intense peaks. No uncertainties used.
$R_{wp} = \sqrt{\frac{\sum_{i=1}^{N} w_i (y_{obs}^i - y_{calc}^i(\boldsymbol{f}))^2}{\sum_{i=1}^{N} w_i {y_{obs}^i}^2}}$	Measures the difference between observed and calculated profiles. Uncertainties are considered. No emphasis on most intense peaks (weighting; w_i is used). Background fitting easily influences this factor.
$R'_p = \frac{\sum_{i=1}^{N} \lvert y_{obs}^i - y_{calc}^i(\boldsymbol{f}) \rvert}{\sum_{i=1}^{N} \lvert y_{obs}^i - Bkg^i \rvert}$	Same as R_p with background (Bkg^i) removed, reveals the influence of background on fitting.
$R'_{wp} = \sqrt{\frac{\sum_{i=1}^{N} w_i (y_{obs}^i - y_{calc}^i(\boldsymbol{f}))^2}{\sum_{i=1}^{N} w_i (y_{obs}^i - Bkg^i)^2}}$	Same as R_{wp} with background removed, reveals the influence of background on fitting.
$R_{exp} = \sqrt{\frac{N - P}{\sum_{i=1}^{N} w_i {y_{obs}^i}^2}}$	The measure of the best possible fit. Heavily relies on counting statistics and the number of fitted parameters. N is the number of data points and P is the number of fitted parameters.
$R'_{exp} = \sqrt{\frac{N - P}{\sum_{i=1}^{N} w_i (y_{obs}^i - Bkg^i)^2}}$	Same as R_{exp} with background removed, reveals the influence of background on the expected best fit.
$\chi = \frac{R_{wp}}{R_{exp}} = \sqrt{\frac{\sum_{i=1}^{N} w_i (y_{obs}^i - y_{calc}^i(\boldsymbol{f}))^2}{N - P}}$	The measure of the goodness of fit (fit quality). For a good fit, this value ranges between 1 and 1.5. A value outside this range warrants further scrutiny of fitting or data quality.
$R_{Bragg} = \frac{\sum_{k=1}^{K} \lvert I_{obs}^k - I_{calc}^k(\boldsymbol{f}) \rvert}{\sum_{k=1}^{K} I_{obs}^k}$	This is for comparison with single-crystal structure refinements. I_{obs}^k and I_{calc}^k are the observed and calculated intensities of the kth reflection out of K reflections.
$d = \frac{\sum_{i=1}^{N} (\Delta y^i - \Delta y^{i-1})}{\sum_{i=1}^{N} (\Delta y^i)^2}$	Durbin-Watson statistic. It measures the serial correlation between adjacent data points in the difference profile. $\Delta y^i = y_{obs}^i - y_{calc}^i(\boldsymbol{f})$.

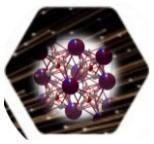

When used in conjunction with the agreement factors, the difference profile plot is a very important indicator of the progress and merit of a Rietveld refinement. Fig. 2.8 illustrates how the difference

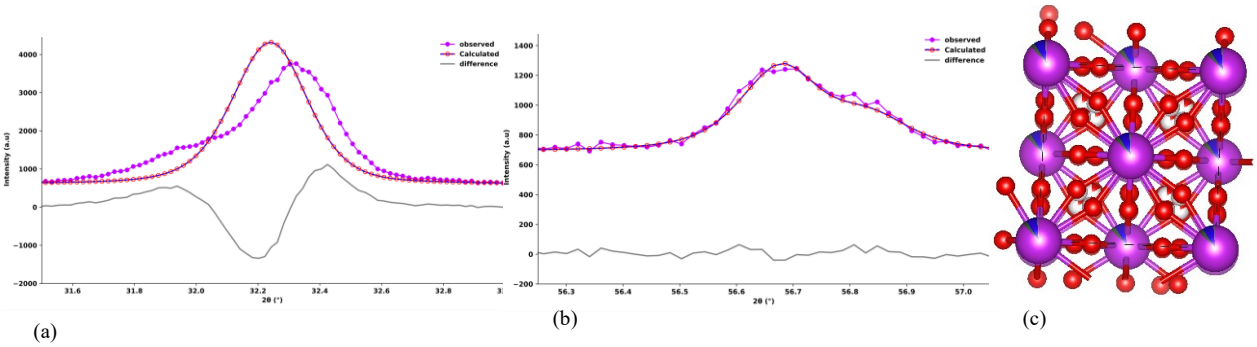

Figure 2.8. The difference profile plot showing the progress and merit of a Rietveld refinement. **(a)** illustrates how a mismatch in lattice parameter appears in the difference profile plot, and **(b)** illustrates an apparent good profile fit, yet the corresponding structure in **(c)** shows atoms are outside the unit cell in positions forbidden by symmetry and have wrong occupancies (more than 1).

profile plot can be used to diagnose the errors that contributed to a poor fit. These diagnoses were provided by McCusker et al. [26] in a form of guidelines for a Rietveld refinement. Viewing the structure after a successful refinement is also a good way of assessing whether the structural values obtained from the fit are physically meaningful. If atoms occupy positions that are forbidden by symmetry (Fig. 2.8 (c)), it might be an indication that the refinement was stuck at a local minimum.

2.2.6 Total Scattering and the PDF Method

The Rietveld method is a powerful method when refining crystal structures from Bragg data. However, only ideal crystals have a perfectly periodic structure. Real crystals or polycrystalline materials exhibit some deviations from perfect periodicity at the local level. These deviations have been reported to correlate with the unique properties of complex materials [27]. Results from a diffraction experiment performed on a polycrystalline material that has local deviations from the average structure results in broad undulating peaks underneath and around the Bragg peaks. Intensities of the Bragg peaks decrease and contribute to the broad undulating peaks convoluted with the background. The δ-Bi_2O_3 phase is very disordered, therefore the Bragg data is insufficient to give a comprehensive solution of the δ-Bi_2O_3 structure since during the refinement the background is fitted and excluded from determining structural parameters.

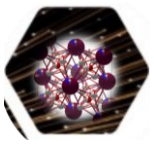

To probe the structure of disordered materials comprehensively, the total scattering data need to be carefully analysed. One of the techniques used to analyse total scattering data is the pair distribution function (PDF) method. The PDF is the measure of the probability of finding an atom centre at a distance r from the centre of an arbitrarily chosen reference atom (Fig. 2.9). This method does not assume periodicity on the material.

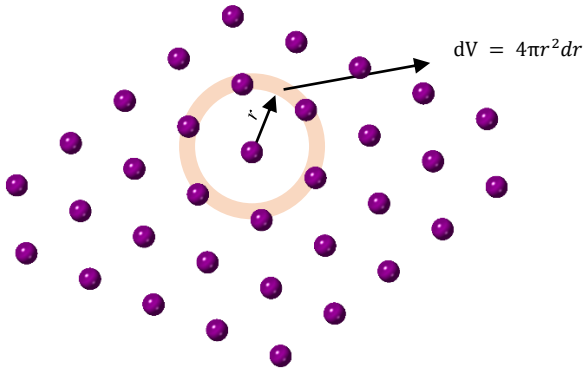

Figure 2.9. Illustration of the PDF as the measure of the probability of finding an atom centre in a given thin spherical shell of volume $dV = 4\pi r^2 dr$ within a radius r from a reference atom.

In statistical thermodynamics, large numbers of thermodynamically equivalent configurations (ensembles) of a system tend to produce ensemble averages that are characteristic of the system as a whole. However, the correlated microscopic deviations from the random ensemble averages can be measured by correlation functions. In a perfectly crystalline material, given the position vector of one atom $\boldsymbol{a_1}$, the position of another atom with position vector $\boldsymbol{a_2}$ can be predicted with very high accuracy. This indicates very high correlations between atomic positions. Given that $g(\boldsymbol{a_2} - \boldsymbol{a_1})$ is the PDF (an example of a correlation function), it is expected that $g(\boldsymbol{a_2} - \boldsymbol{a_1}) = 0$ anywhere else except where $\boldsymbol{a_2} - \boldsymbol{a_1} = \boldsymbol{a}$, the translation vector between atoms in a perfectly crystalline material. However, for disordered crystalline and amorphous materials this "all or nothing" probability does not apply, therefore correlation functions for these materials will differ from those of perfectly crystalline materials. In isotropic materials (polycrystalline and amorphous materials), $g(\boldsymbol{a_2} - \boldsymbol{a_1})$ reduces to $g(a)$, i.e. only the magnitude $|\boldsymbol{a_2} - \boldsymbol{a_1}| = a$ matters. To be consistent with the notation used in literature for the PDF function, $g(r)$ will be used instead of $g(a)$ in this work. $g(r)$ is proportional to the ensemble-averaged number density $\langle\rho\rangle$ of atoms' centres found in a small spherical shell of volume $dV = 4\pi r^2 dr$ as shown in Figure 2.9. Thus,

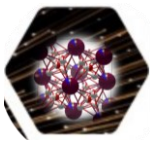

$$\mathrm{g}(r) \propto \rho(r) \propto \langle \frac{Total\ number\ of\ atoms\ in\ dV}{4\pi r^2 dr} \rangle$$

This is the measure of the microscopic or local probability of finding an atom centre at a distance r from a reference atom. This is normalized by the global number density ($\rho_0 = Total\ number\ of\ atoms\ in\ V/V$), i.e.,

$$\mathrm{g}(r) = \rho(r)/\rho_0 \tag{2.4}$$

In an amorphous material as $r \to \infty$, the correlations between atoms die out due to a lack of order at high r, $\rho(r) \to \rho_0$ and $\mathrm{g}(r) \to 1$. However, in an ideal crystalline material, correlations between atoms remain significant over high r values.

Zernike and Prins [28] derived a phenomenological relationship between $\mathrm{g}(r)$ and the measured scattered intensity. When the measured scattered intensity is corrected for effects such as absorption, fluorescence, Compton scattering, the intensity from the sample container and the sample environment, the intensity obtained is called the coherent intensity ($I_{coh}(Q)$). Q (=$4\pi \sin\theta / \lambda$) is the magnitude of the scattering vector in isotropic samples. For a single element material, when $I_{coh}(Q)$ is normalized by the number of scatterers (N) and the average scattering power per atom ($\langle f(Q) \rangle^2$ for X-rays) the scattering intensity per atom is called the total scattering structure function $S(Q)$. It is a dimensionless quantity and when $S(Q)$ is normalized properly $\langle S(Q) \rangle = 1$, that is, $S(Q)$ when averaged in Q space must oscillate closely around 1. In principle, $S(Q)$ can be directly analysed in reciprocal space as in a Rietveld refinement, however, when $S(Q)$ is reduced i.e., $S(Q) - 1$ is obtained, weighted by Q and sine Fourier transformed, $G(r)$, called the reduced total PDF is obtained:

$$G(r) = \left(2/\pi\right) \int_0^\infty Q[S(Q) - 1]\, sin(Qr)\, dQ \tag{2.5}$$

Which, for bulk materials is related to $\mathrm{g}(r)$ by:

$$G(r) = 4\pi r \rho_0 (g(r) - 1) \tag{2.6}$$

In this work, the PDF method was used to analyse selected systems of Bi_2O_3. Therefore, data analysis using the PDF method will be discussed. The PDF is a real space function, and some structural information can be extracted directly without the use of a model. Careful data reduction and correction must be done. In this work, the data reduction was mostly done using the xPDF

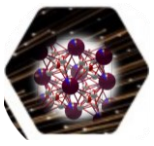

suite of programs [29]. In Fig. 2.10 the reduced total PDF of nickel is provided. Nickel in its crystalline form has a face-centred lattice (Figure 2.10 (a)) and has a lattice parameter a of ~ 3.5 Å. From geometrical arguments and using the hard spheres approximation, the next nearest neighbour distance for nickel is expected to be ~ $1/\sqrt{2}\,a = 2.5$Å. The first nearest neighbour peak in Figure 2.10 (b) is observed at around 2.487Å as expected. This illustrates the power of PDF in revealing structural information in a model-independent way. Some small oscillations observed between peaks can be attributed to termination ripples. These are caused by using the upper limit Q_{max} rather than ∞ as required by the sine Fourier transform in equation (2.4). Measurements cannot be done up to infinity in Q space. The ripples change rapidly with the change in Q_{max} compared to structural features hence they are easily recognized.

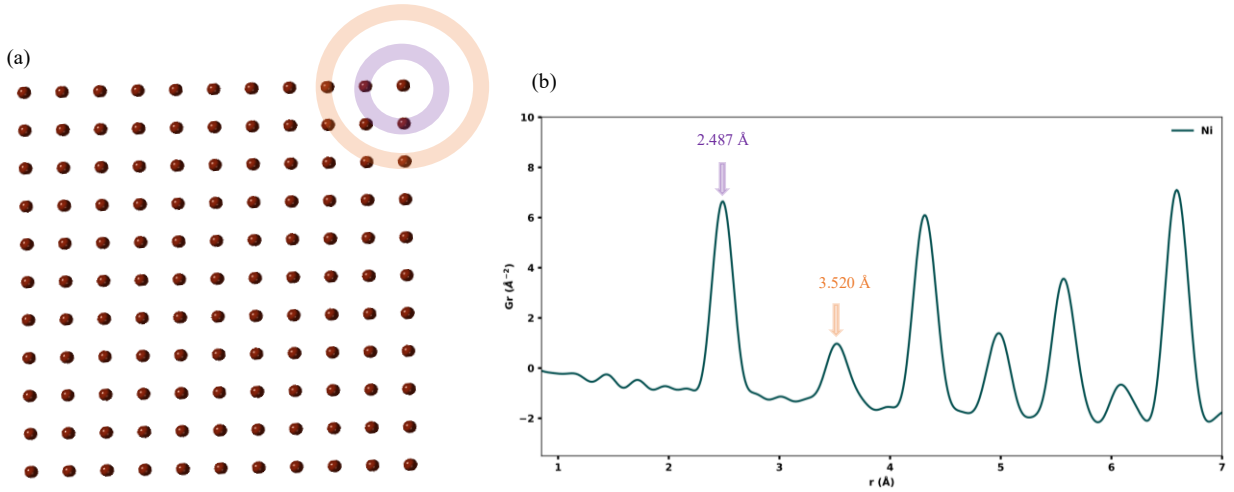

Figure 2.10. Crystal structure of Ni viewed along the $\boldsymbol{a}_1$ axis **(a)** and its reduced total PDF **(b)** The arrows show the peak positions representing the first and second nearest neighbours' distances.

Models can be used to fit the PDF data by implementing full profile refinement algorithms similar to the procedures applied in Rietveld refinements. These are called small-box modelling or real space modelling. In this work, TOPAS Academic v6 & 7 [30-32] and PDFgui [33] were used to perform small-box modelling. An initial structure model is needed to perform this kind of analysis. This is normally obtained from Rietveld refinements and best describes the average structure. To probe the local structure further, big-box modelling is normally used. In this method, a big box is constructed from the unit cell describing the average structure and is used as the initial model. The space group symmetry of the big box can be described as P1 and refinements from this will also reflect the deviation from the average structure. In this work, the RMCProfile code v6.7.9 [34] was

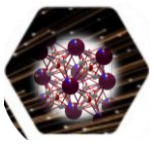

used. TOPAS4RMC [35] was used to obtain the instrument resolution matrix and the Bragg profile for the Bragg data.

2.3 X-ray Absorption Spectroscopy (XAS)

2.3.1 Absorption

In the X-ray energy regime, when photons impinge on matter, they can be reflected, refracted, or absorbed. In this section of the thesis, focus will be given to the absorption process and how it can be used to reveal local structural details that complement the diffraction methods. In the energy range ~ 1-100 keV, the attenuation process consist of Thompson scattering, Compton scattering and photoelectric absorption. The dominant process is photoelectric absorption. In this process, for instance, when a beam of photons impinges on a sample, a photon is annihilated, and a core-level electron is removed from a given shell, resulting in a core-hole formation and an excited atom. When the energy of the X-rays matches or is larger than the characteristic energy of a given shell, the interaction between the photons and the electrons increases abruptly i.e., the absorption coefficient μ of the material becomes discontinuous, forming an edge (Fig. 2.11).

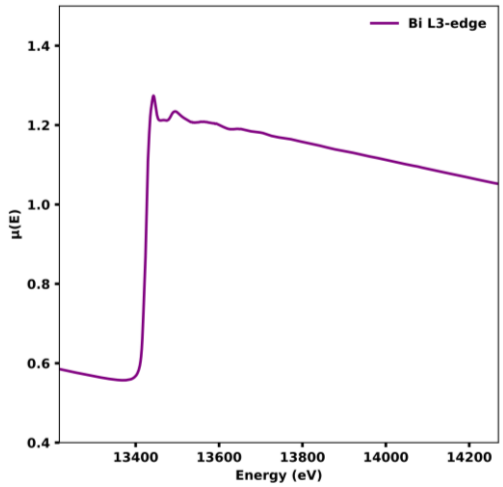

Figure 2.11. The absorption coefficient as a function of energy measured across the Bi L_3-edge in monoclinic Bi_2O_3.

The absorption coefficient is defined as the reciprocal thickness t of the material needed to reduce the intensity of the incident beam I_0 by a factor of 1/e. It is a function of both energy and the proton number Z of a material. For a sample of thickness t, the fraction of the intensity transmitted T is given by:

$$T = \frac{I}{I_0} = e^{-\mu t} \tag{2.7}$$

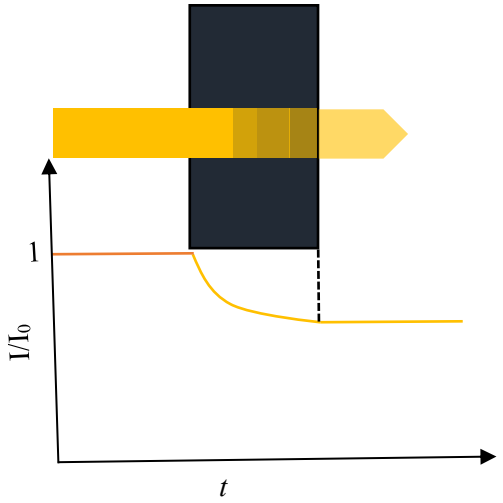

Figure 2.12. The fall in intensity of an X-ray transmitted through a material follows an exponential decay function inside the material of thickness t.

where I is the transmitted intensity. This means that the absorption coefficient can be experimentally measured by measuring the intensity of the incident beam I_0 and I the intensity of the transmitted beam through a sample of known thickness t as shown in Fig. 2.12. Other processes such as fluorescence and Auger emission can be used to measure the absorption coefficient when transmission experiments are not feasible (Fig. 2.13). The photoelectric absorption process and absorption coefficient depend on the electron density and electron binding energy of a material. These are related to the identity of the absorbing element, the local geometry of its site and the nature of the chemical bonding of a material, therefore, measurements of the absorption coefficient as a function of energy can reveal structural and chemical bonding details of a material. These

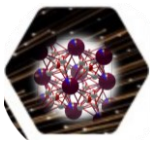

include coordination, formal valences, and the density of states for a given absorber. Hence XAS is a very powerful tool for probing the electronic structure and coordination of a material.

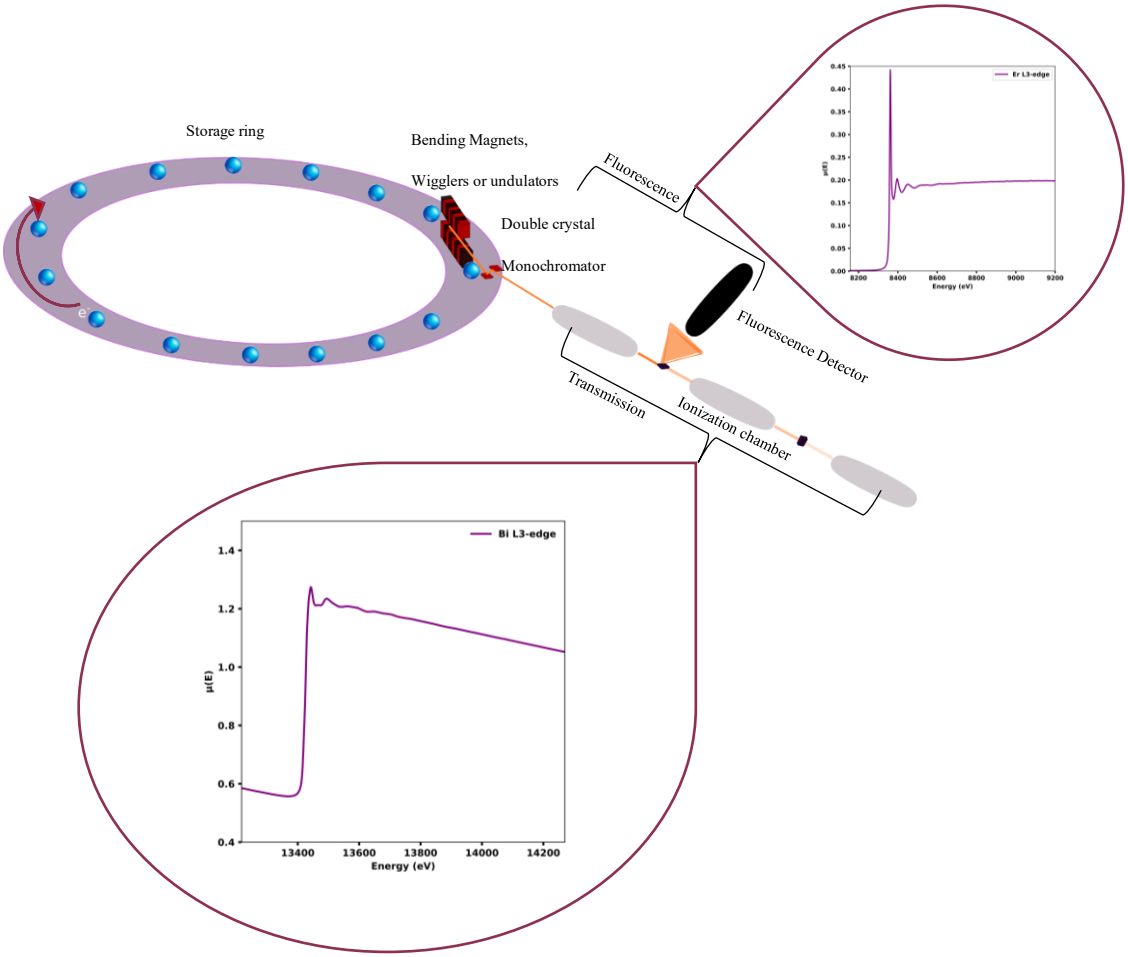

Figure 2.13. A schematic showing a simplified version of the setup in a typical XAS beamline at a third-generation synchrotron. Both transmission and fluorescence detection modes are shown.

2.3.2 X-ray Absorption Fine Structure

When a chemical species (atom or ion) is surrounded by a group of other chemical species, the electron density and bonding environment change the structure of the absorption coefficient compared to that of an isolated atom. Oscillations are observed in this absorption coefficient as a function of energy. These are referred to as the absorption fine structure. The region within 50 eV of the edge is known as the X-ray absorption near edge structure (XANES) region (Fig. 2.14). In this region, when a photoelectron is ejected, it interacts with many surrounding particles due to long escape depth or mean free path, hence data modelling in this region remains a challenge [36, 37]. However, the qualitative analysis still reveals important information about the local geometry of the absorber as demonstrated in Chapters 6 and 7. The fine structure can extend to up to 1000

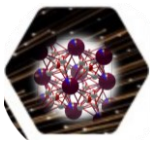

eV from the edge [38]. The region from about 50 – 1000 eV is known as the extended X-ray absorption fine structure (EXAFS) region [38, 39]. However, it should be noted that the XANES can overlap with the EXAFS region. In the EXAFS region, single scattering events dominate, hence, data in this region are amenable to modelling as will be shown in Chapter 7.

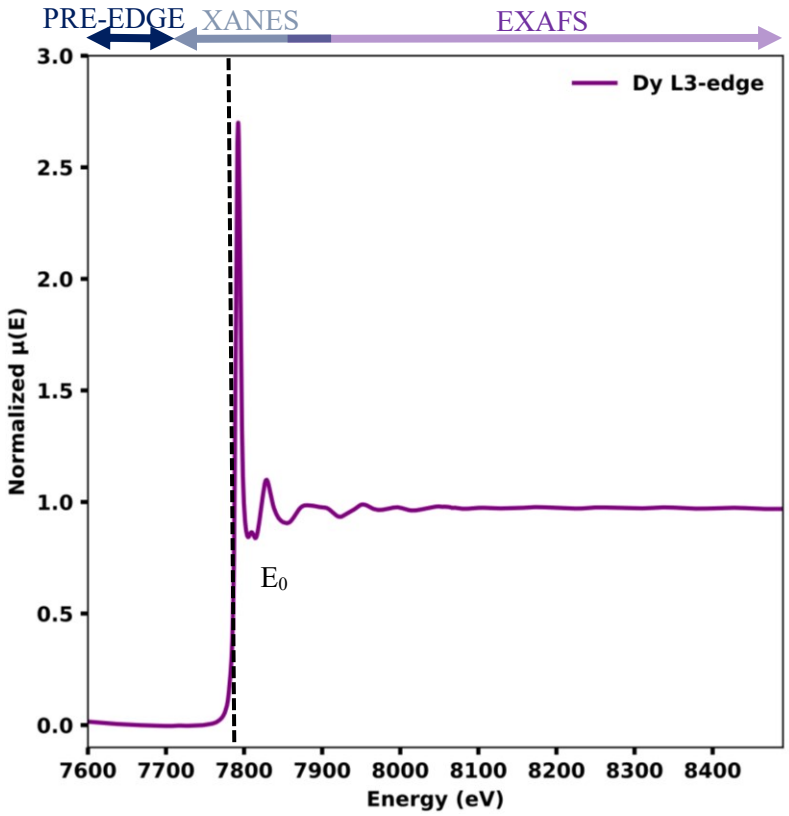

Figure 2.14. A normalized XAFS spectrum of Dy_2O_3 measured in transmission mode and across the Dy L_3-edge showing some of the regions found in an XAFS spectrum.

2.3.3 The XANES region

This region of the absorption spectrum extends to about 50 eV beyond the absorption edge and is dominated by the multiple scattering of the photoelectron ejected. Because of the difficulties in modelling data from this region, this part of the spectrum is used mostly for fingerprinting i.e., comparing measured data to spectra of standard materials. Some advances have been achieved in theoretical XANES such as the work done by Rehr *et al.* [40] using the FEFF code and Green's functions and from linear-response time-dependant density functional theory (LR-TDDFT) as reported by Nascimento and Govind [41]. The spectra of standard materials may be obtained

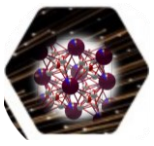

empirically or using theoretical calculations. In a simple case the intensity of an absorption peak or probability of an electronic transition is proportional to the transition moment integral:

$$I \propto |\int_{-\infty}^{+\infty} \psi^* \mu_M \psi \, d\tau \, |^2$$

where ψ^* and ψ are the wave functions of the excited and ground states, respectively. Assuming μ_M is the electric dipole moment operator and $d\tau$ is the volume element. A non-zero value of the integral means the electric dipole transition is allowed and a zero value means that the electric dipole transition is forbidden. The electric dipole moment is antisymmetric. For an electronic transition to be allowed, the $\psi^* \mu_M \psi$ should be symmetric. This means that $\psi^* \psi$ should give an antisymmetric product for the transition to be allowed. This suggests that the nature of the wave functions or in the case of atoms, the atomic orbitals should have opposite parity for the ground and excited states. For instance, a transition involving a K-shell electron will occur between the *s* and *p* or *f* orbitals. The product of any two of these wavefunctions will be antisymmetric. Conservation of momentum will prevent the pure *s* → *f* transition (overall momentum of the photon–excited state system will have to change). A transition from *s* to pure *d* is also forbidden because these orbitals are both symmetric. However, if a ligand provides p orbitals to a metal centre and hybridization takes place with d orbitals and the point group of the site where the metal centre is located is noncentrosymmetric, the electronic transition becomes allowed. The splitting of the *d* orbitals by the ligand field will also be reflected in the spectrum, providing coordination information. This illustrates some examples of how the pre-edge and XANES regions can be used to study the electronic transitions and local environment around the absorber.

2.3.4 The EXAFS region

This is the region of the spectrum starting from around 50 eV and beyond. The energy of the photoelectron is high enough that the electron will escape and scatter off the neighbouring atoms before going back to the absorbing atom. The photoelectron spread out as a spherical wave with wavevector *k* (Fig. 2.15). Upon scattering off neighbouring atoms, the outgoing wave can interfere constructively or destructively with the backscattered wave. Constructive interference increases

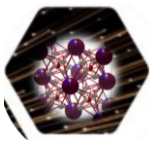

the electron density on the absorbing atom, which increases the probability of an absorption event occurring or the absorption coefficient. Destructive interference reduces the electron density.

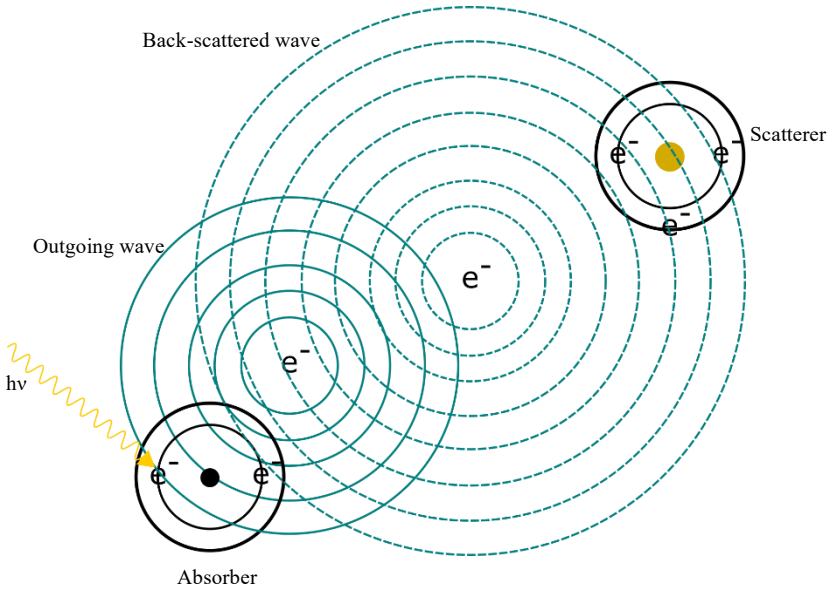

Figure 2.15. A Schematic showing the origin of EXAFS. An electron is ejected from the absorber by a photon. The outgoing electron spherical wave spreads out and scatters from an absorber. The back-scattered electron wave interferes with the outgoing wave either destructively or constructively and modulates the absorption coefficient function.

These interferences manifest themselves as fine oscillations in the spectrum and are referred to as the extended X-ray absorption fine structure. The modulations of the absorption coefficient are represented by the so-called EXAFS function:

$$\chi(k) = \frac{\mu(k) - \mu_0(k)}{\mu_0(k)} \qquad (2.8)$$

Where $\mu_0(k)$ is the absorption coefficient of an isolated absorbing atom. An analytical expression for the $\chi(k)$ known as the EXAFS equation is given by:

$$\chi(k) = \sum_j \frac{S_0^2 N_j f_j(k) e^{-2R_j/\lambda(k)} e^{-2k^2\sigma_j^2}}{kR_j^2} \sin\left[2kR_j + \delta_j(k)\right] \qquad (2.9)$$

Where S_0^2 represent intrinsic losses i.e., the reduction in the amplitude due to the relaxation of the other electrons in the atom after the ejection of the core-level electron. S_0^2 normally ranges between 0.7–1.0. During data fitting, when S_0^2 is outside this range, other fitted parameters might be

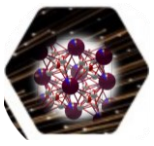

inaccurate. N_j is the coordination number in the jth shell. It is highly correlated with S_0^2. It is advisable to keep one fixed during fitting. $f_j(k)$ is the scattering amplitude function of the neighbouring atoms in the jth shell. For small atoms like H, this function is insignificant. This function is calculated and included in fitting codes.

The $e^{-2R_j/\lambda(k)}$ term models the effect of the magnitude of the mean free path i.e., how far the photoelectron will travel and still participate in the EXAFS. The $e^{-2R_j/\lambda(k)}$ has a universal behaviour in *k* as summarized by Newville [42] and is included in most EXAFS fitting codes. In the EXAFS region, the mean free path is short and hence EXAFS is dominated by single scattering events. The $e^{-2k^2\sigma_j^2}$ term models the damping effects of the disorder from the neighbouring atoms in the jth shell. The σ_j^2 term is the mean-square displacement in the bond distance (R_j) and is a fitted parameter. A positive value 2-3 orders of magnitude smaller than one is common. The $\delta_j(k)$ term represents the phase shift experienced by the waves as they backscatter from the neighbouring atoms in the jth shell. In this work, the Demeter suite of software packages v0.9.26 [43] and Larch v0.9.55 [44] were used to perform the data normalization and EXAFS data fitting.

2.4 Raman and Photoluminescence spectroscopy

As in the case of X-rays, when infrared radiation and /or visible light impinges on a molecule or crystal, the radiation can undergo elastic scattering, inelastic scattering or photoelectric absorption. In the infrared to visible light energy regime, the frequencies of the photons are closer to the vibrational frequencies of atoms in molecules or crystals, and the energy gaps between valence bands and conduction bands.

2.4.1 Raman spectroscopy

A photon can be inelastically scattered such that the molecule is excited from its ground state, *n*, to an excited vibrational state, *m*, via a virtual state, *x*. This type of scattering is called Stokes scattering. However, when a photon is inelastically scattered, such that a molecule is promoted to a virtual excited state *x*, from an already excited state *m*, and the molecule relaxes back to ground state *n* instead of the initially excited state *m*, the scattering is known as anti-Stokes scattering.

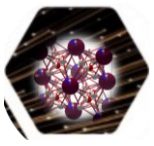

When there is no change in the incident photon energy, the scattering is known as Rayleigh scattering, as Fig. 2.16 shows.

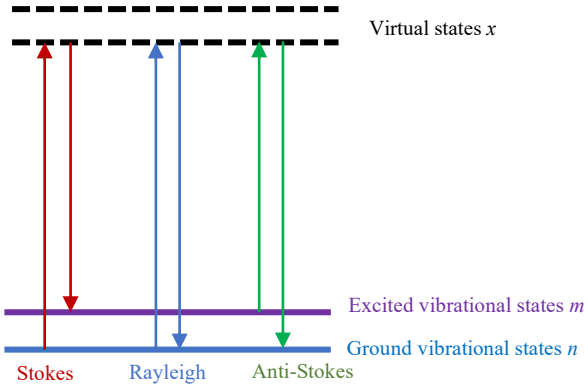

Figure 2.16. An illustration of the Rayleigh and Raman scattering events.

The technique that measures the intensity of scattering events as a function of the energy difference between the incident photon energy and the scattered photon energy (energy shifts) is known as Raman spectroscopy. For a molecule to exhibit Raman spectroscopy, the vibrations must change the polarizability of the electron cloud around a molecule. Some vibrations do not lead to a change in polarizability, i.e., they are Raman-inactive. The symmetry of a molecule plays a significant role in determining the type of vibrational normal modes that are Raman-active. Group Theory helps predict the normal modes that are Raman-active or inactive in a molecule. There are references that deal with this subject in some depth [45, 46]. In this work, focus will only be given to how Raman spectroscopy helps reveal the phases of materials that could not be easily identified from PXRD.

In crystalline materials, Raman-active modes can be calculated using a method called the Correlation Method [47]. In this method, the translational motion of a group of atoms occupying the same Wyckoff position in a structure is correlated with their overall motion in the factor group or the group for the smallest Bravais lattice. The Correlation Method helps predict normal modes that are Raman-active or inactive for a group of atoms in crystalline materials, as opposed to individual molecules [47]. However, extensive knowledge of the Correlation Method is not needed to predict the Raman-active modes, given the space group of the material. The Bilbao Crystallography server provides a tool for calculating normal modes that are Raman-active [48-50]. All that is needed is the space group number and the Wyckoff positions of the atoms. A hurdle

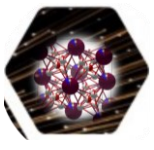

in the use of Raman spectroscopy as a fingerprinting technique and as a local structural probe is that it is difficult to predict which of the Raman-active modes will be observed experimentally and at what waveshifts. Polarized Raman spectroscopy helps with band assignment in that it provides further information on symmetry of vibrational modes [51, 52]. Density Functional Theory (DFT) is normally used to calculate the frequencies of the normal modes, and a library of standard materials is also needed for fingerprinting. For instance, the Correlation Method predicts the following Raman-active modes for a fluorite phase where the metals occupy the 4*a* site, and the anions occupy the 8*c* and 32*f* Wyckoff sites:

$$\Gamma = A_{1g} + E_g + 3T_{2g} \tag{2.10}$$

However, only the T_{2g} modes are observed experimentally for most fluorite phases, such as the δ-Bi_2O_3 like phases obtained from solid solutions of Bi_2O_3 as shown in Fig. 2.17.

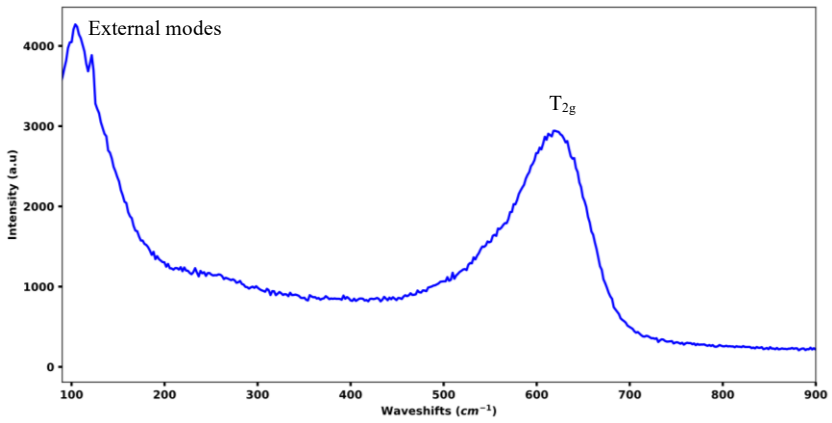

Figure 2.17. Raman spectrum of $Dy_{0.285}Bi_{.715}O_{1.5}$ (28.5DSB) at ambient temperature showing the broad T_{2g} and external modes. This spectrum is typical for most δ-Bi_2O_3 like phases.

In this work, the fingerprinting method was used to determine the phases present in the materials synthesized.

2.4.2 Photoluminescence

When the energy of the photons is enough to promote an electron from the valence band or colour centre to the conduction band, photoelectric absorption takes place. However, each electronic state can be divided into many vibrational levels. If the lifetime of an excited state is longer than the lifetime of a vibration, molecules in their excited state will vibrate and undergo non-radiative processes such that the overall energy of the excited state is decreased before a radiative emission takes place (Fig. 2.18). This normally results in the radiated energy having a longer wavelength

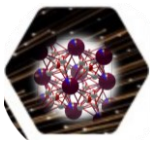

than the exciting radiation, and this process is called luminescence. When the exciting radiation is light, the process is called photoluminescence (PL).

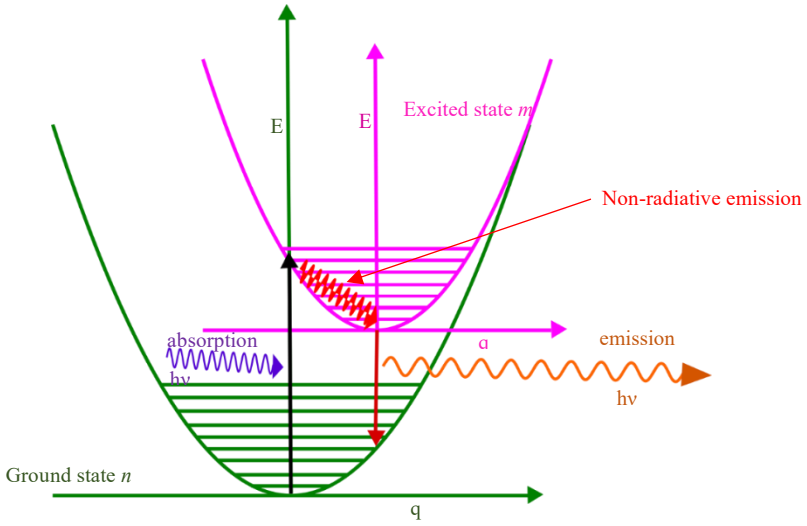

Figure 2.18. Configuration-coordinate diagram illustrating the PL process.

When the exciting radiation (λ_{ex}) is kept constant and the emitted radiation is monitored at various wavelengths, the spectrum produced is called the emission spectrum. However, when the exciting line is varied and the radiation is monitored at a single line (λ_{em}), the spectrum is called the excitation spectrum as Figure 2.19 illustrates.

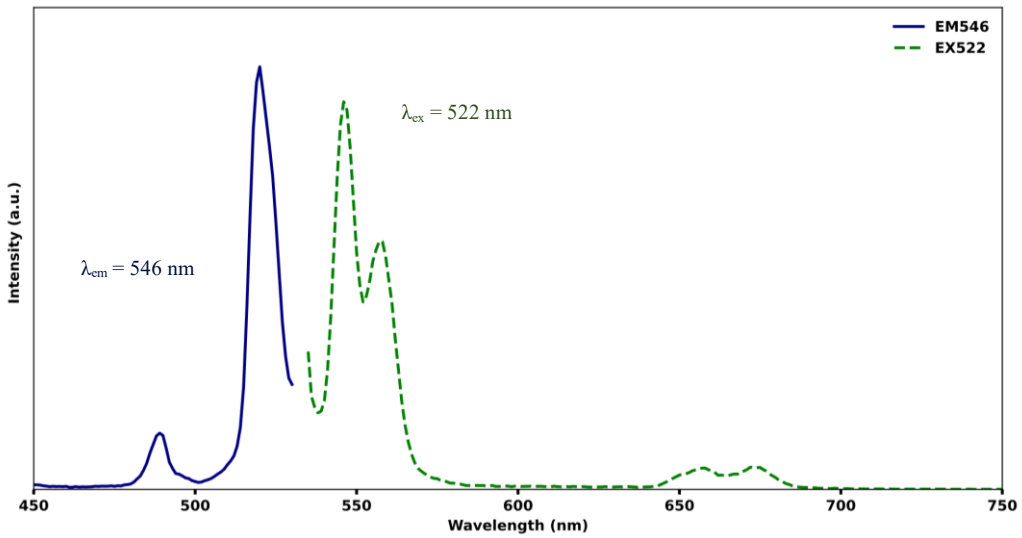

Figure 2.19. Excitation spectrum (solid line) and emission spectrum (dashed line) of $Er_{0.2}Bi_{0.8}O_{1.5}$ (20ESB).

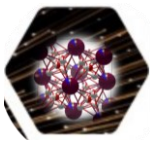

The exciting radiation normally used is in the UV-vis region, therefore, the *valence electrons*, electrons trapped in vacancies and/or atom-vacancy clusters are probed. This means that *photoluminescence* can be used to monitor the changes in: electronic structure, local environment around an emitting centre and the concentration of a chemical species in a given site symmetry in a crystalline material. For instance, the Er^{3+} cations in 20ESB have been shown to emit two lines at 545 and 558 nm when the λ_{ex} ranges between 489 to 521 nm [53]. This emission should be forbidden if Er^{3+} is occupying a centrosymmetric environment in the solid solution of Bi_2O_3. In this work, these two lines will be monitored to determine the distribution of Er^{3+} cation in the solid solution of Bi_2O_3.

2.5 Electrochemical Impedance Spectroscopy (EIS)

The conductivity of a solid electrolyte is the bulk property that was correlated with some average and local structural changes in this work. Conductivity, σ, is given by:

$$\sigma = 1/\rho = l/RA \qquad (2.11)$$

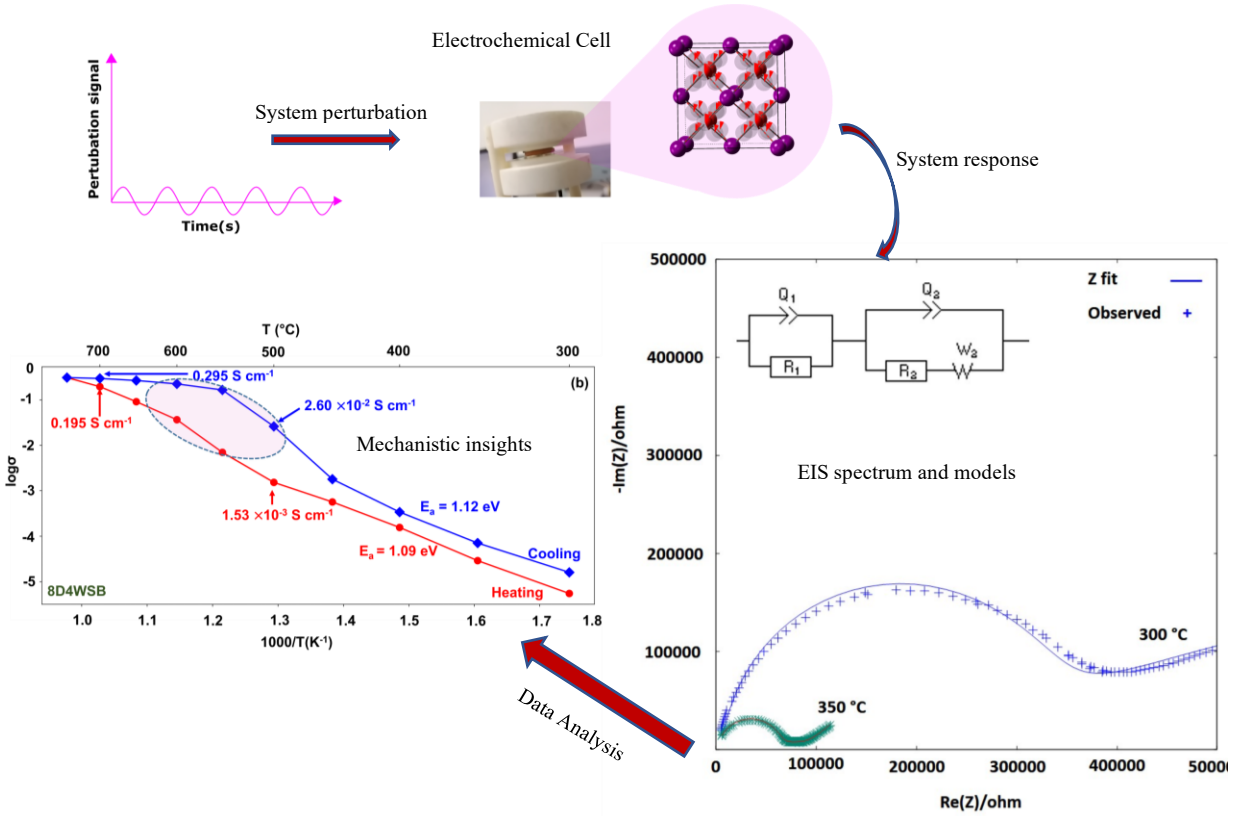

Figure 2.20. A Flow diagram showing the process involved in EIS. This involves the perturbation of an electrochemical system at equilibrium and measuring its response. Data analysis is usually done by using equivalent circuits and mechanistic insights are correlated with structural changes.

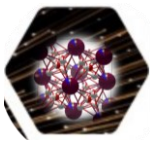

where ρ is the resistivity of the material, l is the thickness, A is the surface area and $R$is the resistance of the material. In this work, the material was pressed into pellets/cylindrical disks of thickness l and surface area A on each side. The resistance R of the material was obtained from EIS. EIS involves the perturbation of a system that should be in a steady state with sinusoidal signals of either current or voltage (Fig. 2.20).

To ensure that the system is linear or pseudo-linear during the measurements, the signal amplitude should be smaller than the thermal voltage which is ~ 25 mV at 25 °C [54] and is given by:

$$V = \mathrm{R}T/F = kT/e \tag{2.12}$$

where R is the gas constant, T is the absolute temperature, F is the Faraday constant, k is the Boltzmann constant and e is the elementary charge. After each perturbation, the output signal is measured. This response signal should also be sinusoidal and have the same frequency as the input signal but can be shifted in phase. The impedance of the system, Z, is calculated from:

$$Z(\omega, t) = \frac{V_0 e^{-i\omega t}}{I_0 e^{-i\omega t+\phi}} \tag{2.13}$$

where V_0 is the maximum voltage amplitude, I_0, is the maximum current amplitude, $\omega = 2\pi f$ is the angular frequency, t is the time, and ϕ is the phase angle. The impedance can also be written as:

$$Z(\omega, t) = Z_0[cos\phi - isin\phi] \tag{2.14}$$

$$\text{and } Z_0 = \frac{V_0}{I_0} \tag{2.15}$$

The real component is normally denoted as Z′, and the imaginary component as Z′′. The real component is the normal resistance, and the imaginary component is the contribution from the capacitive and inductive reactances. Impedance is a function of time, but Fourier transforms are used to convert it to the frequency domain. For the transformation to be valid, the response should be measured from a linear system. The system should also be causal, i.e. should withstand extraneous signal perturbations, and should be stable, i.e. show no or negligible drift during excitation.

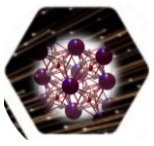

Results from EIS can be correlated with many complex material variables: from mass transport, rates of chemical reactions, corrosion, and dielectric properties to defects and microstructure [54, 55]. Different regions of polycrystalline solid electrolytes are characterized by resistive (R) and capacitive (C) reactances usually placed in parallel [54]. The characteristic relaxation time or time constant τ of each parallel RC circuit is given by the product of R and C, i.e.:

$$\tau = RC \tag{2.16}$$

At the maximum value of Z'', $\omega_m RC = 1$, where ω_m is called the frequency of maximum loss [54]. Equation (2.16) makes it possible to identify different RC elements and assign them to appropriate regions of the sample like grain, grain boundaries and electrode-electrolyte interfaces as Table 2.4 illustrates.

Table 2.4. Capacitance values and the associated mechanism or regions in an electrochemical cell [55]

Capacitance [F]	Process and/or region
10^{-12}	Bulk
10^{-11}	Minor, secondary phase
10^{-11} - 10^{-8}	Grain boundary
10^{-10} - 10^{-9}	Bulk ferroelectric
10^{-9} - 10^{-7}	Surface layer
10^{-7} - 10^{-5}	Sample-electrode interphase
10^{-5}	Electrochemical reaction

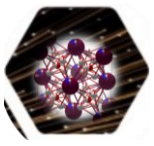

Impedance data can be presented in the form of imaginary component Z'' (reactive) plotted against the real component Z' (resistive) in a plot called Nyquist or impedance plane plot (Fig. 2.21). In this plot, resistance (R) values are obtained from Z' intercepts and capacitance (C) values are obtained by applying equation (2.16) to the frequency at the maximum of each semicircle present

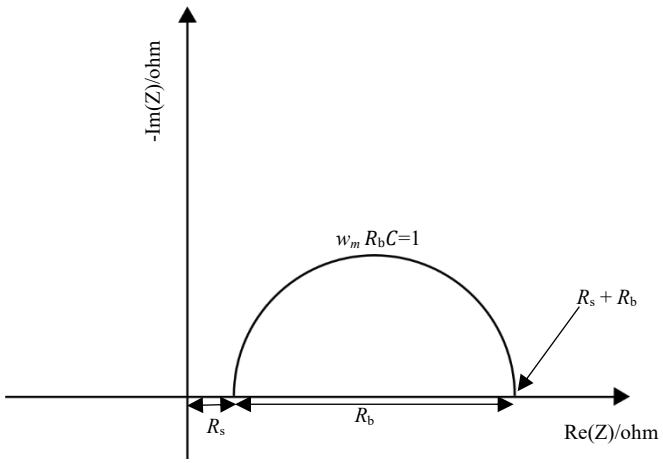

Figure 2.21. An impedance plane plot showing the parameters normally used as initial starting values in data fitting. R_s represents the uncompensated resistance of the setup of the system, R_b is the bulk resistance of the material being probed.

(Fig. 2.21). These values serve as initial estimates during data fitting.

A disadvantage of a Nyquist plot is that frequency is implicit. To circumvent this problem, the Bode plot is used to supplement the Nyquist plot. The Bode plot is a pair of graphs of log|Z| and ϕ as a function of frequency [54]. The Bode plot reveals the number of different semicircles present, especially if they are not apparent in the Nyquist plot and their time constant is about 1 decade apart [54]. It also reveals the frequency range at which capacitive behaviour dominates resistive behaviour.

Different models are used in experimental data interpretation, such as mathematical models, based on a plausible physical theory that predicts impedance. Empirical equivalent circuits whose

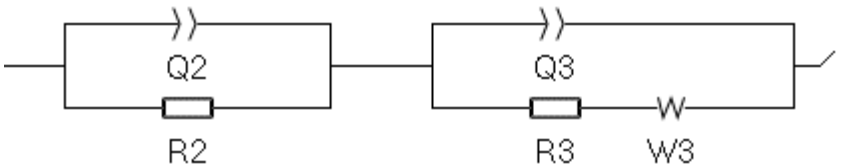

Figure 2.22. An equivalent circuit used in data fitting. Q represent a constant phase element; R is the resistance and W is the Warburg diffusion.

impedance matches that of the data and has physical meaning are also used and were the method of choice in this work. Equivalent circuit models are employed in data fitting to generate a calculated function that is minimized in the complex non-linear least squares (CNLS) fitting procedure. In this work, the circuit that was employed predominantly is given in Figure 2.22. In cases where this circuit was not applied, the relevant circuit will be given. The R2/Q2 component of the circuit is attributed to the bulk processes (intragrain conductivity) and the (R3+W3)/Q3 is attributed to the electrolyte-electrode interfaces in the materials explored in this work.

2.6 References

[1] Wagner, C. and Schottky, W., 1930.Theory of ordered solid solutions. *Z. Phys. Chem.*, (*11)*, pp.163.

[2] Busch, G. and Schade, H., 2013. *Lectures on Solid State Physics: International Series in Natural Philosophy* (Vol. 79). Elsevier.

[3] Dufour, L.C., 1996. *Chemical kinetics of solids*. Hermann Schmalzried, VCH, Weinheim 1995, XVI, pp.233-265.

[4] West, A.R., 2014. *Solid state chemistry and its applications*. John Wiley & Sons, p. 187-194.

[5] Segal, D., 1998. Soft chemistry routes to zirconia ceramics. In *Key Engineering Materials* (Vol. 153, pp. 241-250). Trans Tech Publications Ltd.

[6] Levin, E.M. and Roth, R.S., 1964. Polymorphism of bismuth sesquioxide. I. Pure Bi_2O_3. *Journal of Research of the National Bureau of Standards. Section A, Physics and Chemistry*, *68*(2), p.189.

[7] Melnikov, P., Arkhangelsky, I.V., Nascimento, V.A., Silva, A.F., de Oliveira, L.C.S., Consolo, L.Z. and Herrero, A.S., 2015. Thermolysis mechanism of dysprosium hexahydrate nitrate $Dy(NO_3)_3 \cdot 6H_2O$ and modeling of intermediate decomposition products. *Journal of Thermal Analysis and Calorimetry*, *122*(2), pp.571-578.

[8] Parkinson, J., 1998. New approach to the solution chemistry of bismuth citrate antiulcer complexes. *Chemical Communications*, (8), pp.881-882.

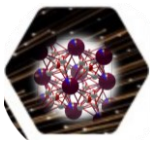

[9] Zhang, L.E., Zhou, L.U., Jinzhen, Z.H.U., Hao, Y.A.N.G., Pengde, H.A.N., Yan, C.H.E.N. and Zhang, Q., 2012. Citrate sol-gel combustion preparation and photoluminescence properties of YAG: Ce phosphors. *Journal of Rare Earths*, *30*(4), pp.289-296.

[10] Danks, A.E., Hall, S.R. and Schnepp, Z.J.M.H., 2016. The evolution of 'sol–gel'chemistry as a technique for materials synthesis. *Materials Horizons*, *3*(2), pp.91-112.

[11] Friedrich, W., Knipping, P. and von Laue, M., 1912. Sitzungsberichte der Math. Phys. Klasse (Kgl.), Bayerische Akademie der Wissenschaften.

[12] Pecharsky, V. and Zavalij, P., 2008. *Fundamentals of powder diffraction and structural characterization of materials*. Springer Science & Business Media.

[13] Hahn, T. eds., 2005. *International Tables for Crystallography: Volume A Space-Group Symmetry*. International Union of Crystallography.

[14] Bradley, C. and Cracknell, A., 2010. *The mathematical theory of symmetry in solids: representation theory for point groups and space groups*. Oxford University Press.

[15] Orobengoa, D., Capillas, C., Aroyo, M.I. and Perez-Mato, J.M., 2009. AMPLIMODES: symmetry-mode analysis on the Bilbao Crystallographic Server. *Journal of Applied Crystallography*, *42*(5), pp.820-833.

[16] H. T. Stokes, D. M. Hatch, and B. J. Campbell, ISODISTORT, ISOTROPY Software Suite, iso.byu.edu

[17] Stokes, H.T., Hatch, D.M., Campbell, B.J. and Tanner, D.E., 2006. ISODISPLACE: a web-based tool for exploring structural distortions. *Journal of Applied Crystallography*, *39*(4), pp.607-614.

[18] Campbell, B.J., Evans, J.S., Perselli, F. and Stokes, H.T., 2007. Rietveld refinement of structural distortion-mode amplitudes. *IUCr Comput. Comm. Newsl*, *8*, pp.81-95.

[19] Dinnebier, R.E., Leineweber, A. and Evans, J.S.O., 2019. *Rietveld Refinement: Practical Powder Diffraction Pattern Analysis using TOPAS*. De Gruyter.

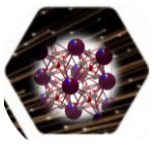

[20] Debye, P. and Scherrer, P., 1916. Interferenzen an regellos orientierten Teilchen im Röntgenlicht. I. *Nachrichten von der Gesellschaft der Wissenschaften zu Göttingen, Mathematisch-Physikalische Klasse*, *1916*, pp.1-15.

[21] Hull, A.W., 1917. A new method of X-ray crystal analysis. *Physical Review*, *10*(6), p.661.

[22] Hull, A.W., 1917. The crystal structure of iron. *Journal of the Franklin Institute*, *184*(3), pp.447-448.

[23] Will, G., 2006. *The Rietveld Method and the Two Stage Method to Determine and Refine Crystal Structures from Powder Diffraction Data*. Springer.

[24] Rietveld, H.M., 1967. Line profiles of neutron powder-diffraction peaks for structure refinement. *Acta Crystallographica*, *22*(1), pp.151-152.

[25] Rietveld, H.M., 1969. A profile refinement method for nuclear and magnetic structures. *Journal of Applied Crystallography*, *2*(2), pp.65-71.

[26] McCusker, L.B., Von Dreele, R.B., Cox, D.E., Louër, D. and Scardi, P., 1999. Rietveld refinement guidelines. *Journal of Applied Crystallography*, *32*(1), pp.36-50.

[27] Egami, T. and Billinge, S.J., 2003. *Underneath the Bragg peaks: structural analysis of complex materials*. Elsevier.

[28] Zernike, F.T. and Prins, J.A., 1927. Die beugung von röntgenstrahlen in flüssigkeiten als effekt der molekülanordnung. *Zeitschrift für Physik A Hadrons and nuclei*, *41*(2), pp.184-194.

[29] Yang, X., Juhas, P., Farrow, C.L. and Billinge, S.J., 2014. xPDFsuite: an end-to-end software solution for high throughput pair distribution function transformation, visualization and analysis. *arXiv preprint arXiv:1402.3163*.

[30] Coelho, A.A., Chater, P.A. and Kern, A., 2015. Fast synthesis and refinement of the atomic pair distribution function. *Journal of Applied Crystallography*, *48*(3), pp.869-875.

[31] Coelho, A.A., Evans, J., Evans, I., Kern, A. and Parsons, S., 2011. The TOPAS symbolic computation system. *Powder Diffraction*, *26*(S1), pp.S22-S25.

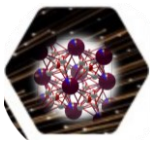

[32] Coelho, A.A., 2018. TOPAS and TOPAS-Academic: an optimization program integrating computer algebra and crystallographic objects written in C++. *Journal of Applied Crystallography*, *51*(1), pp.210-218.

[33] Farrow, C.L., Juhas, P., Liu, J.W., Bryndin, D., Božin, E.S., Bloch, J., Proffen, T. and Billinge, S.J.L., 2007. PDFfit2 and PDFgui: computer programs for studying nanostructure in crystals. *Journal of Physics: Condensed Matter*, *19*(33), p.335219.

[34] Tucker, M.G., Keen, D.A., Dove, M.T., Goodwin, A.L. and Hui, Q., 2007. RMCProfile: reverse Monte Carlo for polycrystalline materials. *Journal of Physics: Condensed Matter*, *19*(33), p.335218.

[35] Zhang, Y., Eremenko, M., Krayzman, V., Tucker, M.G. and Levin, I., 2020. New capabilities for enhancement of RMCProfile: instrumental profiles with arbitrary peak shapes for structural refinements using the reverse Monte Carlo method. *Journal of Applied Crystallography*, *53*(6), pp.1509-1518.

[36] Rehr, J.J. and Albers, R.C., 2000. Theoretical approaches to x-ray absorption fine structure. *Reviews of Modern Physics*, *72*(3), p.621.

[37] Rehr, J.J. and Ankudinov, A.L., 2005. Progress in the theory and interpretation of XANES. *Coordination Chemistry Reviews*, *249*(1-2), pp.131-140.

[38] Garino, C., Borfecchia, E., Gobetto, R., van Bokhoven, J.A. and Lamberti, C., 2014. Determination of the electronic and structural configuration of coordination compounds by synchrotron-radiation techniques. *Coordination Chemistry Reviews*, *277*, pp.130-186.

[39] Willmott, P., 2019. *An introduction to synchrotron radiation: techniques and applications*. John Wiley & Sons.

[40] Rehr, J.J., Kas, J.J., Vila, F.D., Prange, M.P. and Jorissen, K., 2010. Parameter-free calculations of X-ray spectra with FEFF9. *Physical Chemistry Chemical Physics*, *12*(21), pp.5503-5513.

[41] Nascimento, D.R. and Govind, N., 2022. Computational approaches for XANES, VtC-XES, and RIXS using linear-response time-dependent density functional theory based methods. *Physical Chemistry Chemical Physics*, *24*(24), pp.14680-14691.

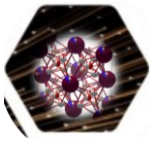

[42] Newville, M., 2014. Fundamentals of XAFS. *Reviews in Mineralogy and Geochemistry*, *78*(1), pp.33-74.

[43] Ravel, B. and Newville, M., 2005. ATHENA, ARTEMIS, HEPHAESTUS: data analysis for X-ray absorption spectroscopy using IFEFFIT. *Journal of Synchrotron Radiation*, *12*(4), pp.537-541.

[44] Newville, M., 2013, April. Larch: an analysis package for XAFS and related spectroscopies. *Journal of Physics: Conference Series* (Vol. 430, No. 1, p. 012007). IOP Publishing.

[45] Vincent, A., 2013. *Molecular symmetry and group theory: a programmed introduction to chemical applications*. John Wiley & Sons.

[46] Maurya, R.C. and Mir, J.M., 2019. Molecular Symmetry and Group Theory. In *Molecular Symmetry and Group Theory*. De Gruyter.

[47] Fateley, W.G., 1972. *Infrared and Raman selection rules for molecular and lattice vibrations: the correlation method*. Krieger Publishing Company.

[48] Aroyo, M.I., Perez-Mato, J.M., Orobengoa, D., Tasci, E.M.R.E., de la Flor, G. and Kirov, A., 2011. Crystallography online: Bilbao crystallographic server. *Bulg. Chem. Commun*, *43*(2), pp.183-197.

[49] Aroyo, M.I., Perez-Mato, J.M., Capillas, C., Kroumova, E., Ivantchev, S., Madariaga, G., Kirov, A. and Wondratschek, H., 2006. Bilbao Crystallographic Server: I. Databases and crystallographic computing programs. *Zeitschrift für Kristallographie-Crystalline Materials*, *221*(1), pp.15-27.

[50] Aroyo, M.I., Kirov, A., Capillas, C., Perez-Mato, J.M. and Wondratschek, H., 2006. Bilbao Crystallographic Server. II. Representations of crystallographic point groups and space groups. *Acta Crystallographica Section A: Foundations of Crystallography*, *62*(2), pp.115-128.

[51] Tanaka, M. and Young, R.J., 2006. Review Polarised Raman spectroscopy for the study of molecular orientation distributions in polymers. *Journal of Materials Science*, *41*, pp.963-991.

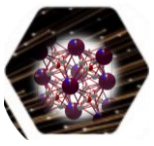

[52] Maczka, M., Hanuza, J., Hermanowicz, K., Fuentes, A.F., Matsuhira, K. and Hiroi, Z., 2008. Temperature-dependent Raman scattering studies of the geometrically frustrated pyrochlores $Dy_2Ti_2O_7$, $Gd_2Ti_2O_7$ and $Er_2Ti_2O_7$. *Journal of Raman Spectroscopy*, *39*(4), pp.537-544.

[53] Wachsman, E.D., Jiang, N., Frank, C.W., Mason, D.M. and Stevenson, D.A., 1990. Spectroscopic investigation of oxygen vacancies in solid oxide electrolytes. *Applied Physics A*, *50*(6), pp.545-549.

[54] Barsoukov, E. and Macdonald, J.R., 2005. *Impedance Spectroscopy Theory, Experiment, and Applications, 2nd ed.* John Wiley &Sons.

[55] Irvine, J.T., Sinclair, D.C. and West, A.R., 1990. Electroceramics: characterization by impedance spectroscopy. *Advanced Materials*, *2*(3), pp.132-138.

2.7 Bibliography

1. West, A.R., 2022. *Solid state chemistry and its applications*. John Wiley & Sons.

2. Brinker, C.J. and Scherer, G.W., 2013. *Sol-gel Science: the physics and chemistry of sol-gel processing*. Academic press.

3. Pecharsky, V.K. and Zavalij, P.Y., 2005. *Fundamentals of powder diffraction and structural characterization of materials*. Springer US.

4. Hammond, C., 2009. *The basics of crystallography and diffraction*. International Union of Crystallography (Vol. 12). OUP Oxford.

5. David, W.I., Shankland, K., McCusker, L.B. and Baerlocher, C. eds., 2006. *Structure determination from powder diffraction data* (Vol. 13). OUP Oxford.

6. Müller, U., 2013. *Symmetry relationships between crystal structures: applications of crystallographic group theory in crystal chemistry* (Vol. 18). OUP Oxford.

7. Müller, U. and Wondratschek, H. eds., 2005. *International Tables for Crystallography: Volume A1 Symmetry Relations Between Space Groups*. International Union of Crystallography.

8. Dinnebier, R.E., Leineweber, A. and Evans, J.S.O., 2019. *Rietveld refinement: practical powder diffraction pattern analysis using TOPAS*. De Gruyter.

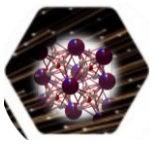

9. Young, R.A., 1993. *The Rietveld method*. International union of crystallography (Vol. 5). OUP Oxford.

10. Will, G., 2006. *Powder diffraction: The Rietveld method and the two-stage method to determine and refine crystal structures from powder diffraction data*. Springer Science & Business Media.

11. Dinnebier, R.E. and Billinge, S.J. eds., 2008. *Powder diffraction: theory and practice*. Royal society of chemistry.

12. Egami, T. and Billinge, S.J., 2003. *Underneath the Bragg peaks: structural analysis of complex materials*. Elsevier.

13. Calvin, S., 2013. *XAFS for everyone*. CRC press.

14. Bunker, G., 2010. *Introduction to XAFS: a practical guide to X-ray absorption fine structure spectroscopy*. Cambridge University Press.

15. Teo, B.K., 2012. *EXAFS: basic principles and data analysis* (Vol. 9). Springer Science & Business Media.

16. McMorrow, D. and Als-Nielsen, J., 2011. *Elements of modern X-ray physics*. John Wiley & Sons.

17. Willmott, P., 2019. *An introduction to synchrotron radiation: techniques and applications*. John Wiley & Sons.

18. Smith, E. and Dent, G., 2005. *Modern Raman spectroscopy: a practical approach*. John Wiley & Sons.

19. William, G.F., Francis, R.D., Neil, T.M. and Freeman, F.B., 1972. *Infrared and Raman selection rules for molecular and lattice vibration: the correlation method.* Wiley Inter Science.

20. de Bettencourt-Dias, A. ed., 2014. *Luminescence of lanthanide ions in coordination compounds and nanomaterials*. John Wiley & Sons.

21. Maurya, R.C. and Mir, J.M., 2019. *Molecular symmetry and group theory: approaches in spectroscopy and chemical reactions*. Walter de Gruyter GmbH & Co KG.

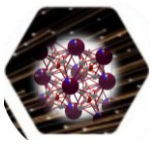

22. Vij, D.R. ed., 1998. *Luminescence of solids*. Springer Science & Business Media.

23. Macdonald, J.R. and Barsoukov, E. eds., 2018. *Impedance spectroscopy: theory, experiment, and applications*. John Wiley & Sons.

24. Orazem, M.E. and Tribollet, B., 2008. *Electrochemical impedance spectroscopy*. John Wiley & Sons.

25. Lasia, A., 2014. *Electrochemical impedance spectroscopy and its applications*. Springer.

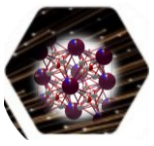

Chapter 3: Insights on the phase transitions, stability and conductivity in the Bi_2O_3-WO_3 system

Sikhumbuzo M. Masina[a], Caren Billing[a,*], Rudolph M. Erasmus[b,c], David G. Billing[a,c]

[a]Molecular Science Institute, School of Chemistry, University of the Witwatersrand, Private Bag X3, Johannesburg, 2050, South Africa

[b]Material Physics Research Institute, Microscopy and Microanalysis Unit, University of the Witwatersrand, Private Bag X3, Johannesburg, 2050, South Africa.

[c]DST-NRF Centre of Excellence in Strong Materials, University of the Witwatersrand, Private Bag X3, Johannesburg, 2050, South Africa.

Correpsonding author* email: caren.billing@wits.ac.za

ORCIDs:

S.M. Masina 0000-0002-9806-8403,
Caren Billing 0000-0001-5462-1150,
Rudolph M. Erasmus 0000-0001-7455-766X,
David G. Billing 0000-0001-8995-924X

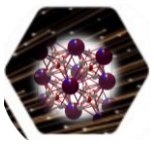

Abstract

Equilibrium phases of the Bi_2O_3-WO_3 system, synthesized using the citrate-gel method with slow cooling, have been systematically investigated for samples with 22-27 mol% WO_3. Annealing temperature and content of WO_3 were shown to play a significant role in the phases present. Both powder X-ray diffraction and Raman spectroscopy revealed that the room temperature equilibrium phases were $7Bi_2O_3 \cdot WO_3$ and $7Bi_2O_3 \cdot 2WO_3$, with the latter being dominant. Variable temperature Raman spectroscopy showed that both these phases were present up to 850°C, with the possible formation of a third unidentified phase at higher temperatures. The ionic conductivities of the mixed-phase materials were between that for the pure $7Bi_2O_3 \cdot WO_3$ and $7Bi_2O_3 \cdot 2WO_3$ phases and at 700°C was only about three times lower than that of the pure defect fluorite phase of the 22 mol% WO_3 samples. The Arrhenius plots showed no sudden increase in conductivity between 300-750°C providing evidence that no major phase change occurred in this temperature range.

Keywords: Tungsten substituted bismuth oxide; sillenite phase; mixed phases; oxide electrolyte; variable temperature Raman spectroscopy; ionic conductivity.

3.1 Introduction

Solid solutions based on the Bi_2O_3-WO_3 system have shown remarkable versatility. The W-rich phases are used to produce photocatalysts of technological importance and the Bi-rich phases function as O^{2-} ion conducting solid electrolytes displaying high stability under low O_2 partial pressures and high ionic conductivities [1-4]. Bi_2O_3 in its defect fluorite δ-phase (space group $Fm\bar{3}m$) was found to have ionic conductivities around 1 S cm^{-1} at 730°C, the highest of any oxide ion conductor reported to date at that temperature [5, 6]. δ-Bi_2O_3 has a highly disordered oxide ion sublattice. This is due to 25% of the oxygen sites being inherently vacant. The Bi^{3+} $6s^2$ lone pair of electrons is stereochemically active and occupies a similar volume to an oxide ion. Additionally, Bi^{3+} is a highly polarizable cation [7, 8]. All these factors contribute immensely to the reported high oxide ion conductivity of Bi_2O_3 in this phase.

Unfortunately, δ-Bi_2O_3 is only stable in the narrow temperature range of 729-824°C [9, 10]. Below this range, the ordered monoclinic α-phase (space group $P2_1/c$) exists and is predominantly an electronic conductor and above this range, Bi_2O_3 melts [11, 12]. However, the δ-phase can be

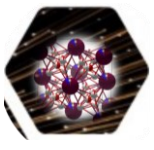

stabilized at lower temperatures, including room temperature, by substitution of Bi^{3+} by various transition metal cations such as W^{6+} and most of the rare earth elements [13-18].

Takahashi *et al*. [4] reported that Bi_2O_3 substituted with 22 mol% WO_3 stabilized the cubic phase at ambient temperature and showed conductivities of 0.062 S cm^{-1} at 700°C which is higher than that for yttria-stabilized zirconia (YSZ) (around 0.010 S cm^{-1}), the current state of the art electrolyte used in commercial solid oxide fuel cells (SOFCs) [19]. They used solid-state reactions to fabricate their materials which require higher temperatures and long heating times ranging from 20 hours to several days. They also quenched their samples, consequently, producing a phase that is metastable as suggested by Watanabe [20].

When cooled slowly, Watanabe and Ono [21] reported that in the composition 22.22 mol% WO_3, two tetragonal phases, $7Bi_2O_3{\cdot}WO_3$ and $7Bi_2O_3{\cdot}2WO_3$, start to co-exist below 670°C and persist to room temperature. They reported these two phases to be the true equilibrium phases for the given composition. Borowska-Centkowska *et al*. [22, 23] reported relatively high ionic conductivities of these two phases (~0.058 S cm^{-1} for $7Bi_2O_3{\cdot}2WO_3$ and ~3.7×10^{-3} S cm^{-1} for $7Bi_2O_3{\cdot}WO_3$ at 700°C) when investigated as pure phases.

Interestingly, in trying to solve the energy crisis by studying fast oxide ion conductors for application in intermediate temperature SOFCs, the energy intensive solid-state reactions is widely used to fabricate the electrolytes. This generally involves at least two grinding and high temperature (≥800°C) annealing steps, and total annealing times of several days. Very few studies use synthetic methods which are less energy intensive. For example, the citrate gel method requires a lower temperature calcination step (at 400-500°C) for a few hours immediately followed by the higher temperature annealing step with a reduced time as compared to the solid state-method. In addition, slow cooling is reported to often produce a mixture of phases, which might be the true equilibrium phases depending on the thermal history at certain compositions [21]. However, there is a dearth of knowledge on how the conductivity of a mixture compares to that of the pure phases which are usually metastable and degrade with prolonged heating at intermediate temperatures. Considering these gaps and the previous findings, this work uses the citrate-gel method to fabricate ambient temperature equilibrium phases of the Bi_2O_3-WO_3 system at various compositions and compares the average structure composition and conductivity of these materials with phases obtained via solid-state reactions.

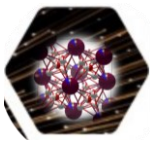

3.2 Experimental

3.2.1 Synthetic procedures and materials

3.2.1.1 Citrate-gel method

Samples of $(Bi_2O_3)_{1-x}(WO_3)_x$, where $0.22 \leq x \leq 0.27$, were synthesized using the citrate-gel method. These will be referred to as 22%-27% WO_3 nominal compositions. Stoichiometric amounts of $BiONO_3$ (Merck) and $(NH_4)_6H_2W_{12}O_{40}.H_2O$ (Sigma-Aldrich) were dissolved in 100 ml 2 M nitric acid under constant stirring for 15 minutes using a magnetic stirrer. Citric acid was added as a complexing agent in a 1:3 mole ratio of total metal ions to citric acid while stirring. The solvent was evaporated at 200°C to form a gel. The gel was dried in an oven overnight at 80°C and calcined in a furnace at 500°C for 12 hours to form a powder. These powders were then annealed at 50°C intervals from 500-650°C for 20 hours at each step and quenched in air to room temperature (by simply removing the samples from the furnace at the annealing temperature) to study the effects of annealing temperature. Powders of identical compositions were also annealed at 800°C for 24 hours and slowly cooled back to room temperature in the furnace (by simply turning the furnace off and allowing it to cool, where the average cooling rate is estimated at ~1°C min^{-1}) to obtain the equilibrium phases. To verify if the phases were equilibrium phases, the same samples were also annealed at 800°C for 3 days and slowly cooled to ambient temperatures.

3.2.1.2 Solid-state reactions

For reference purposes, solid-state reactions were used to fabricate similar composition as those made via the citrate-gel method. Stoichiometric amounts of Bi_2O_3 (99% pure, British Drug House) and WO_3 (99% pure, Acros Organics) were mixed in an agate mortar and manually ground for an hour in acetone (99.56% pure, KEM*i*CAL). The mixture was dried in air for 24 hours before being annealed at 800°C for 24 hours and slow cooled back to room temperature in the furnace as before. It was then reground before being annealed at 800°C for a further 24 hours and slow cooled again.

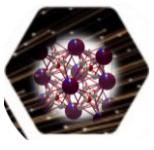

3.2.2 Characterization techniques

3.2.2.1 Powder X-ray Diffraction

A Bruker D2 phaser in Bragg-Brentano configuration, equipped with a sealed Co radiation tube, secondary beam Fe K_β filter, Bruker Lynxeye PSD detector, and primary and secondary Soller slits was used to obtain diffraction patterns for phase identification from the powders. The K_β filtration methodology applied is never 100% effective and hence some K_β radiation is detected in the measured diffraction pattern.. Phase identification was done using DIFFRAC.SUITE EVA linked to the crystallography open database (COD) [24]. Rietveld refinements were done using DIFFRAC.TOPAS (V.5) [25] and a Pearson VII function to model the experimental peak profiles. Four Inorganic Crystal Structure Database (ICSD) [26] entries; 97481 for $7Bi_2O_3{\cdot}WO_3$, 88840 for $7Bi_2O_3{\cdot}2WO_3$, 171327 for $Bi_2O_3{\cdot}WO_3$ (S.G. *B*2*cb*) and 67647 for $Bi_2O_3{\cdot}WO_3$ (S.G. *Pca*2$_1$) were used as initial structural models in the refinements. In addition to scale factors, selected corrections, lattice and positional parameters were refined for both phases. Rietveld refinements confirm the phase identification and primary results from the refinements are included in the Supporting Information sections (Tables S1-3, Fig.'s S1-2).

3.2.2.2 Variable temperature Raman spectroscopy

Raman spectroscopy (RS) measurements were obtained using a Horiba LabRAM HR Raman system equipped with an argon ion laser of emission line 514.532 nm, a Symphony CCD detector cooled to –129°C using liquid nitrogen and a 600 lines/mm grating. An Olympus optical microscope attachment with a 50× LWD objective lens and a Linkham TS1500 sample stage were used for the *in situ* variable temperature measurements. The sample stage was purged with high purity argon gas and the spectra were measured between ambient temperature and 850°C at 170°C increments using a heating rate of 10°C min^{-1}. The maximum acquisition time was 2 minutes and the powder form of the samples was analysed.

3.2.2.3 Variable temperature impedance spectroscopy

Electrochemical impedance spectroscopy (EIS) was done using a MTZ-35 frequency response analyser from BioLogic. It was equipped with a HF-1100 furnace and a HTSH-1100 sample holder to do the variable temperature measurements. The measurements were done in air, with both heating and cooling cycles in the range 300-750°C at 50°C increments using a heating/cooling rate

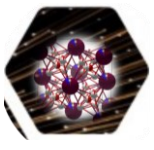

of 10°C min^{-1}. The system was allowed to equilibrate for 30 minutes before each measurement. The frequency range was from 1 Hz to 1 MHz with an A.C. amplitude of 10 mV.

The powders were mixed with a minimum amount 0.3 wt% polyvinyl alcohol (PVA) as a binder and pressed into pellets using a uniaxial cold press at a constant pressure of 500 MPa with a 5 mm diameter die to produce pellets of about 1 mm in thickness. The green bodies were first heated to 300°C in 6 hours and soaked at this temperature for 4 hours to remove the binder. The temperature was then ramped up to 820°C and the pellets were sintered at this temperature for 14 hours and cooled slowly in the furnace back to room temperature. Higher sintering temperatures improve both the sinterability and the density of the pellets which are important for accurate conductivities. Pellets were directly inserted between the two platinum disks from the cell-holder without additional coatings.

The Nyquist plots were modelled using the equivalent circuit approach and the EC-Lab v11.21 software. Fitted parameters are given in the Supporting Information sections (Fig. S3, Tables S4-7). Solid solutions of bismuth oxide have been reported to exhibit negligible grain boundary resistances [27, 28] and for these samples only a single high frequency semi-circle was measured for the low temperature data. The resistance, described as R1 in Fig. S3, thus most likely represents the bulk resistance of the electrolyte, as also denoted by the capacitance values of the order of 10^{-12} F typical for a bulk electrolyte process.

3.2.2.4 Differential thermal analysis

Differential thermal analysis (DTA) was conducted using a Perkin Elmer STA 6000 with alumina crucibles. Powdered samples of ~19 mg were analysed. Temperature calibration was performed by melting an indium standard in an alumina crucible. The instrument was operated in the simultaneous thermogravimetric analysis (TGA)-DTA mode. The measurements were done between 30 and 800°C for both heating and cooling cycles at a heating/cooling rate of 10°C min^{-1}. Nitrogen was used as the purging gas at a flow rate of 20 ml min^{-1}.

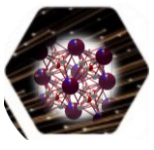

3.3 Results and discussion

3.3.1 Ambient temperature phase studies

3.3.1.1 Effects of annealing on phase transitions

For samples prepared via the citrate-gel method, a stepwise annealing process from 500°C to 650°C at 50°C intervals (followed by quenching in air at each stage) enabled the study of the effects of annealing temperature on phase composition by analysing the quenched samples using PXRD at ambient temperature at each interval. Figure 3.1 illustrates that for both the 22% and 25% samples annealed to 500°C, there is a mixture of three phases present: a tetragonal sillenite phase $7Bi_2O_3{\cdot}WO_3$ (COD 2003105) with space group $I4/m$, another tetragonal phase $7Bi_2O_3{\cdot}2WO_3$ (COD 1531949) with space group $I4_1$ and a minor orthorhombic russellite phase Bi_2WO_6 (COD 1528730) with space group $Pca2_1$. Interestingly, the russellite phase is said to be refractory with no phase transition occurring up to 850°C for the pure phase [29]. Here it is seen that the russellite phase disappears as the sample is annealed from 500°C to 650°C, while the $7Bi_2O_3{\cdot}2WO_3$ and sillenite phases persist. This suggests that the russellite phase has a low conversion temperature when mixed with other phases. The same behaviour was observed for the 23% and 24% samples. It was also observed that as the annealing temperature increased from

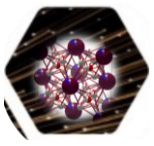

500°C to 650°C, the $7Bi_2O_3 \cdot 2WO_3$ phase became more dominant and the sillenite phase diminished.

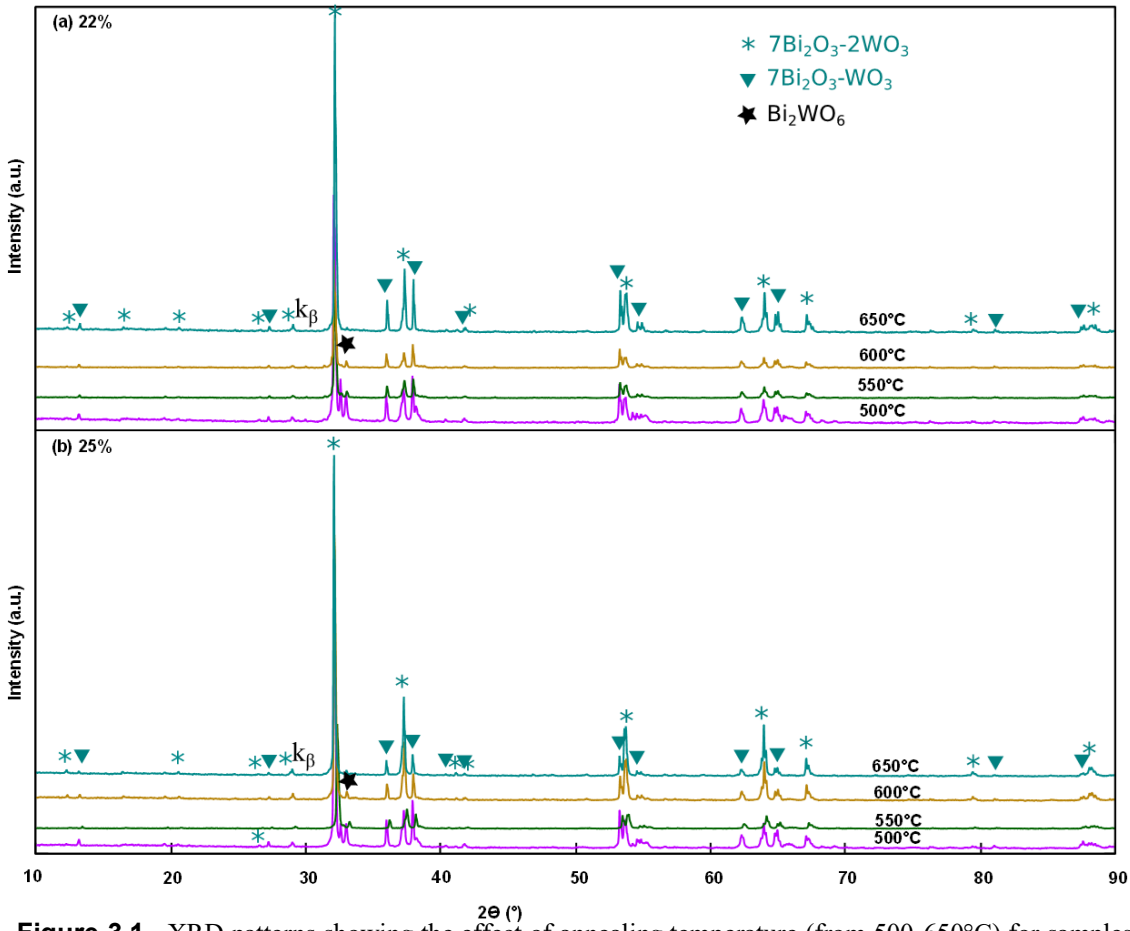

Figure 3.1. XRD patterns showing the effect of annealing temperature (from 500-650°C) for samples with **(a)** 22% and **(b)** 25% WO_3.

After annealing at 800°C followed by slow cooling to room temperature, a mixture of $7Bi_2O_3 \cdot 2WO_3$ and the sillenite phase persisted (Fig. 3.2), but with $7Bi_2O_3 \cdot 2WO_3$ becoming the more dominant phase. The samples were further annealed for 72 hours at 800°C and then slow cooled to ambient temperature to verify whether these phases were equilibrium phases. In Figure 3.2 it can be seen that no observable phase change occurred. More resolved peaks were seen due to improved crystallinity of the $7Bi_2O_3 \cdot 2WO_3$ phase as confirmed by the Rietveld refinement results in Figure S3.1(f) and Figure S3.1(g) in the Supporting Information section.

According to the phase diagram by Hoda and Chang [24], a pure $7Bi_2O_3 \cdot 2WO_3$ phase exists for samples containing ~20-25% mole fraction WO_3 prepared by quenching samples from 800°C.

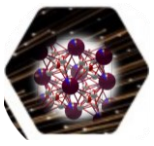

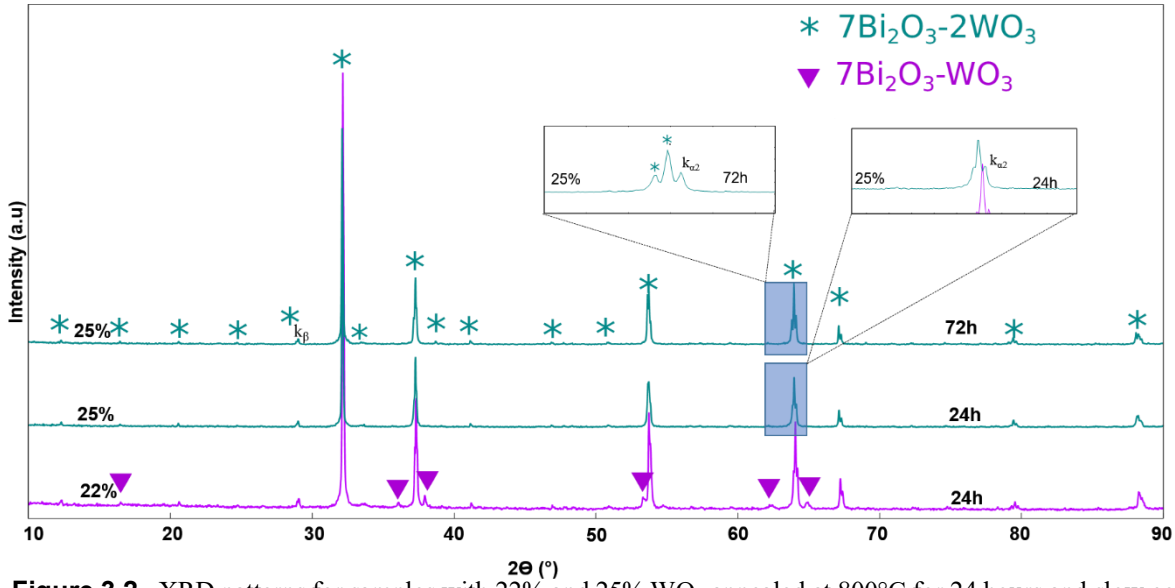

Figure 3.2. XRD patterns for samples with 22% and 25% WO_3 annealed at 800°C for 24 hours and slow cooled back to room temperature. The 25% sample was also annealed for a further 72 hours. The insets show more pronounced peak splitting due to improved crystallinity of the $7Bi_2O_3 \cdot 2WO_3$ phase upon further annealing.

This stability range was also confirmed by Watanabe and Ono [21], who also showed that for samples containing 23% mole fraction WO_3 soaked at 550°C, the $7Bi_2O_3 \cdot 2WO_3$ degraded to an extent to produce a phase containing 12.5% mole fraction of WO_3 which corresponds to the sillenite phase ($7Bi_2O_3 \cdot WO_3$). This suggests that for the compositions used in this work when synthesised using the citrate-gel method, these two phases may be the true equilibrium state at ambient temperature. This agrees with Watanabe and Ono's [21] findings that, when using the solid-state method, these two phases coexisted below 670°C up to ambient temperature. In the case of slow cooling the samples, it is not unexpected then that both phases are present even when annealed at 800°C.

3.3.1.2 Effects of concentration on phase formation

The annealing temperature is not the only parameter that influences the phases formed in the Bi_2O_3-WO_3 system, but the stoichiometric concentration ratio of the initial metal ions used predictably plays a significant role as can be seen in the phase diagram by Hoda and Chang [24]. In the present work, the concentration of WO_3 was systematically increased from 22 mol% to 27 mol% in 1 mol% increments and all samples were directly annealed at 800°C. This is within the solubility range of WO_3 (22-28 mol%) reported by Takahashi and Iwahara [4]. It was observed that generally as the concentration of WO_3 was increased, the $7Bi_2O_3$-$2WO_3$ phase became more dominant and the sillenite phase diminished as depicted in Fig.'s 3a and 3b. This agrees well with

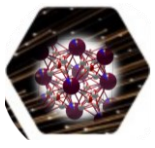

the observation made by Hoda and Chang [24] that the onset of decomposition of the sillenite phase is favoured by the amount of soluble WO_3, with higher WO_3 concentrations leading to the stabilisation of phases with higher W content.

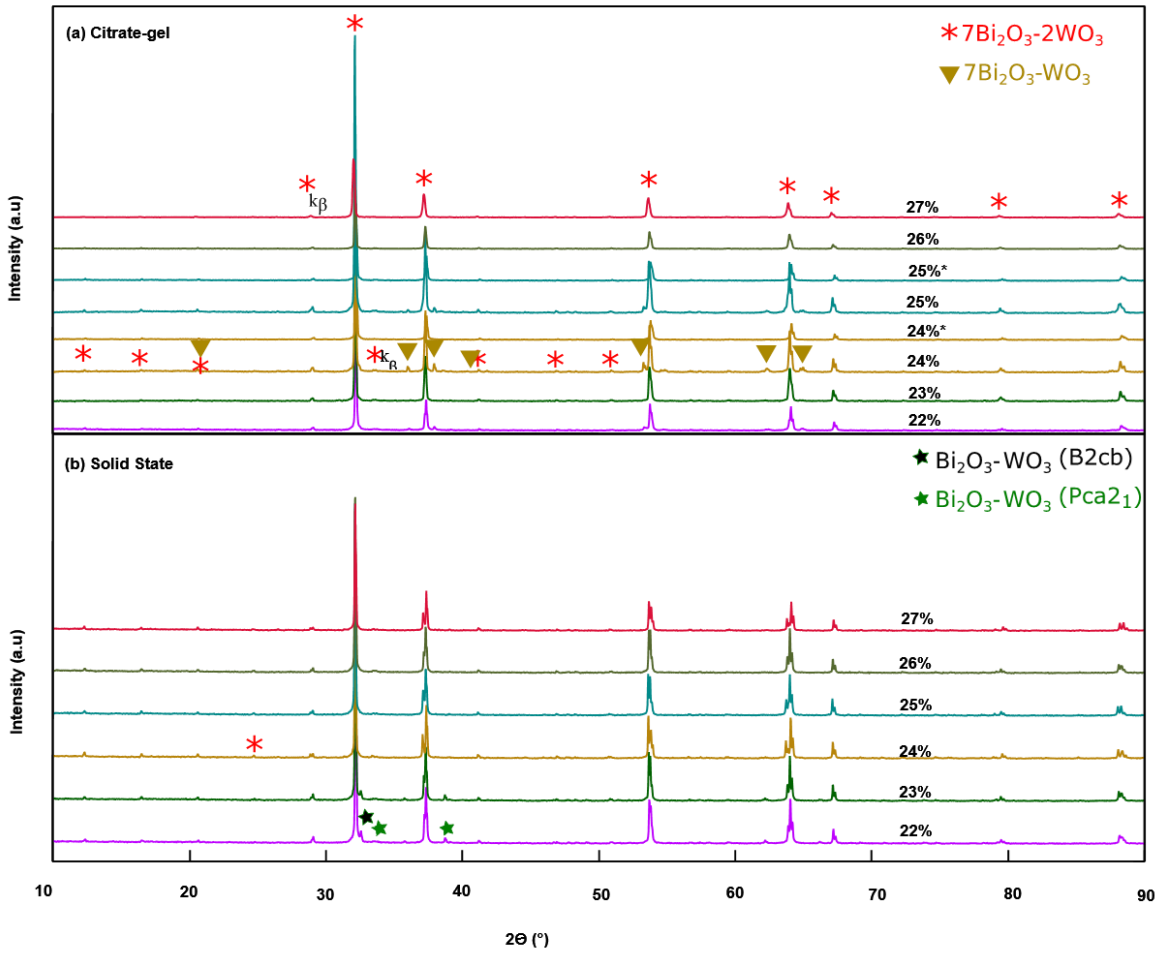

Figure 3.3. XRD patterns showing the influence of concentration on phase composition for samples fabricated using **(a)** the citrate-gel method and **(b)** solid-state reactions, all annealed at 800°C. The * represents the resynthesised samples.

Initially the 24% and 25% compositions showed peculiar behaviour where the sillenite phase remained to a greater extent (Fig. 3.3(a)). From Rietveld refinements it was established that only about 84% of the 24% composition was made up of the $7Bi_2O_3{\cdot}2WO_3$ phase. This was not observed when using solid-state reactions to synthesize the solid solutions of the same composition (Fig. 3.3(b)). On remaking these samples using the citrate-gel method, however, the sillenite phase was lower and in line with the other samples (Fig. 3.3(a)) and Table S3.1 in the Supporting

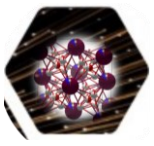

Information section). This intimates that side reactions might have occurred during the initial synthesis [30, 31] which might have inhibited the conversion of the sillenite phase. In general it was found that as the amount of WO_3 increased the extent of $7Bi_2O_3{\cdot}2WO_3$ phase formation increased, with a maximum of 97% of the sample existing as the $7Bi_2O_3{\cdot}2WO_3$ phase for the 26% WO_3 composition.

For the 22% and 23% compositions made using solid-state reactions, two additional $Bi_2O_3{\cdot}WO_3$ phases (with space groups *B*2*cb* and *Pca*2$_1$) were observed (Fig. 3b), be it the total percentage to which they were present was ≤~2%. According to the phase diagram of Watanabe and Ono [21], the $Bi_2O_3{\cdot}WO_3$ phases are only expected to start forming at compositions above 50% WO_3 content. Since this phase was only produced in these two samples synthesised using the solid-state method, it is highly likely that this phase formed due to local regions in the initial mixtures having higher WO_3 content. None of the samples made via the citrate-gel method contained this phase after annealing at 800 °C.

Raman spectroscopy was used to verify the XRD results and to determine whether other minor or amorphous phases that are not detectable by XRD but Raman active were present. Raman spectroscopy probes the local structure of Raman active materials and can be a very good complementary technique to conventional XRD which probes only the average structure. Fig. 4 compares the spectra for the 22% sample prepared by the citrate-gel method and solid-state reactions. Peak fitting using Gaussian functions was done to obtain accurate Raman shifts. The results were comparable to those obtained by Hardcastle and Wachs [32] who specifically studied the Raman spectroscopy of bismuth tungstates.

In Fig. 4, the Raman bands at 895 cm^{-1}, 840 cm^{-1}, 817 cm^{-1} and 718 cm^{-1} are assigned to the $7Bi_2O_3{\cdot}2WO_3$ phase and those at 914 cm^{-1}, 620 cm^{-1}, 534 cm^{-1}, 505 cm^{-1}, 350 cm^{-1} and 312 cm^{-1} are assigned to the sillenite phase. Bands below 200 cm^{-1} are difficult to assign to any particular phase because they overlap with the very intense characteristic lattice vibration bands. All bands above 200 cm^{-1} were assigned to the two main phases identified by XRD thereby confirming that no other main phases were present.

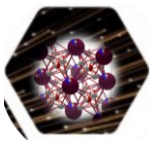

The Raman spectrum of the sample fabricated via the citrate-gel method shows similar results to that synthesised using solid-state reactions. Of particular importance is the fact that no additional phases were detected for samples fabricated using the citrate-gel method.

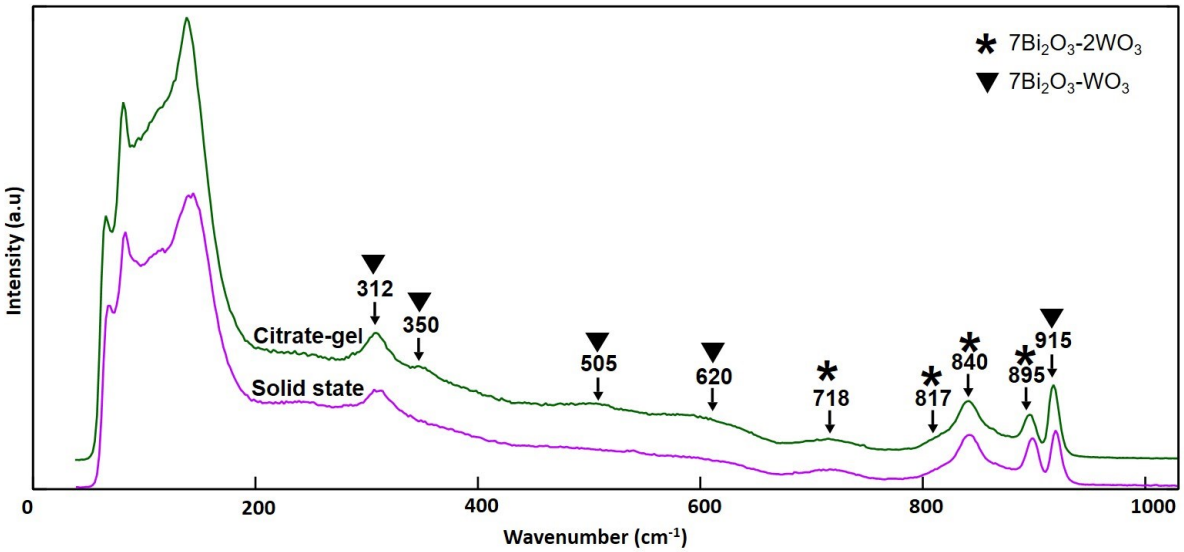

Figure 3.4. Raman spectra of the 22% WO_3 composition synthesised using the citrate-gel method and solid-state reactions where both samples were annealed at 800°C.

3.3.2 Variable temperature phase studies

For high temperature applications, it is important to understand the phase stability of these materials upon heating. Since most literature concerning the study of the Bi_2O_3-WO_3 system involves materials synthesised via solid-state reactions, only samples synthesized via the citrate-gel method were investigated further in this work. Variable temperature Raman spectroscopy (VT-RS) was run on powdered samples with the lowest (22%) and highest (27%) WO_3 content. Unfortunately for the 22% sample, a significant intensity loss with increasing temperature made it very difficult to extract any structural features from the data beyond 25°C. The results for the 27% sample are presented in Figure 3.5 where only data above 200 cm^{-1} are depicted. It is seen that as the temperature increased the peaks at higher Raman shifts assigned to the $7Bi_2O_3 \cdot 2WO_3$ phase became broader and shifted more significantly to lower wavenumbers as compared to those assigned to the sillenite phase. The peak broadening indicates that the disorder in the structure of $7Bi_2O_3 \cdot 2WO_3$ increased more at higher temperatures compared to the sillenite phase. The greater peak shift also indicates a higher expansion rate for the $7Bi_2O_3 \cdot 2WO_3$ phase.

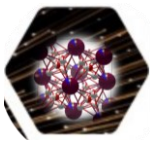

Focusing on the most intense peaks, the spectrum at 680°C shows the broad band from $7Bi_2O_3 \cdot 2WO_3$ at around 890 cm^{-1} and the sillenite peak at around 915 cm^{-1}, indicating that both phases exist beyond 670°C for the 27% composition. This mixture of phases was not observed beyond 670°C by Watanabe and Ono [21]. Even at 850°C where the intensities are very low, the presence of both phases is evident. There does appear to possibly be the formation of another unidentified phase from 680°C with the emergence of a very broad peak at about 860 cm^{-1} which was initially thought to simply be the overlap of the two $7Bi_2O_3 \cdot 2WO_3$ peaks in that region. At no stage does a band at around 600 cm^{-1} appear which means that the defect fluorite phase of Bi_2O_3 ($Fm\bar{3}m$) was not observed at any temperature.

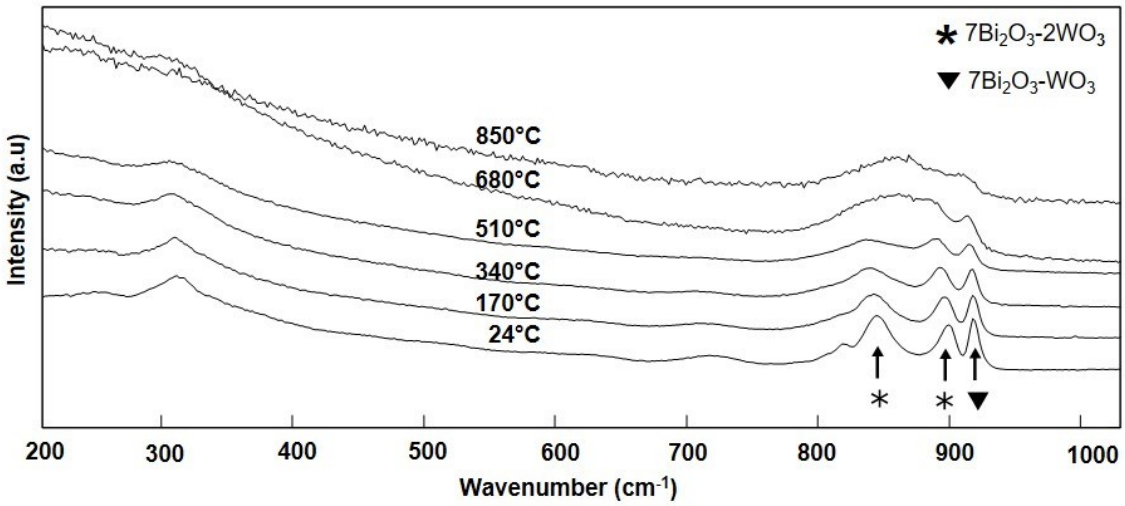

Figure 3.5. VT-Raman spectra from 200 cm^{-1} of the 27% WO_3 sample (fabricated via the citrate-gel method) showing phase stability up to 850°C. Intensities at 680°C were doubled and at 850°C were multiplied by a factor of twelve to enhance features.

3.3.3 Conductivity studies

The conductivities of mixed-phase materials are seldom reported, yet these mixtures have been found to be the true equilibrium phases for the Bi_2O_3-WO_3 system [22]. In this work temperature dependant conductivities of the mixed-phase materials were determined from variable temperature electrochemical impedance spectroscopy (VT-EIS) measurements. Fig. 6 shows the Arrhenius plots of the bulk electrolyte conductivities of samples with 23%-26% WO_3 content. It was observed that generally, as the concentration of WO_3 increased, the conductivity decreased especially at lower temperatures. This trend has been widely reported in literature for any impurity in the host Bi_2O_3. In this case it is ascribed to a decrease in unit cell volume, an increase in the

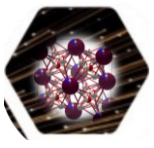

average strength of cation-oxide ion bond, vacancies being trapped in the WO_6 coordination spheres and a decrease in intrinsic vacancies [23,33].

The 25% composition does not follow the same trend, but has lower conductivities across the temperature range. The sample analysed in this case was the original sample with the higher sillenite content (see Fig. 3.3(a)). From Table 1 it can clearly be seen that the sillenite phase ($7Bi_2O_3 \cdot WO_3$) exhibits inferior conductivities compared to $7Bi_2O_3 \cdot 2WO_3$ in the temperature range studied here. It thus appears that the structural differences override the impurity cation concentration effects when comparing the conductivities of the 25% and 26% samples.

As can be seen from Table 3.1, in the lower temperature range (300°C to 400°C) the conductivity of the 23% composition in this work lies between that for the sillenite and the $7Bi_2O_3$-$2WO_3$ phases, indicating the influence of a mixture of phases. From around 550°C and above, the conductivities for the 23%, 24% and 26% compositions were very similar (Fig. 3.6(a)). The highest conductivity obtained at 700°C was 0.018 S cm^{-1} (for 23% composition) which is just slightly lower than that for the $7Bi_2O_3 \cdot 2WO_3$ phase (~0.058 S cm^{-1}). Again, this is probably due to the small amount of sillenite still present in these samples. The increased contact resistance between the sample and the two platinum disks from the cell holder (especially at the lower temperatures) might have also played a role since no coating was applied. Surprisingly the conductivity for the 22% composition was found to be only slightly higher (0.062 S cm^{-1} at 700°C) for the pure δ-Bi_2O_3 phase ($Fm\bar{3}m$) as reported by Takahashi and Iwahara [4] compared to that found in this work.

Further from literature, Borowska-Centkowska *et al.* [23] observed a massive jump in conductivity just before 800°C for the pure sillenite phase corresponding to the formation of the cubic defect fluorite phase. A similar phase change from $7Bi_2O_3 \cdot 2WO_3$ to the cubic phase was noted above 850°C, but the conductivities were not measured to such high temperatures in this work [22]. Neither the VT-RS data nor the VT-EIS data reflected any phase transitions to the cubic phase in this work, even with RS measurements up to 850°C. Watanabe and Ono [21] reported the conductivities for the 23% WO_3 composition synthesised by solid-state reactions, which was predominantly the tetragonal $7Bi_2O_3$-$2WO_3$ phase, and these were only slightly lower than that for the pure $7Bi_2O_3 \cdot 2WO_3$ phase [22] (see Table 3.1).

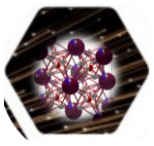

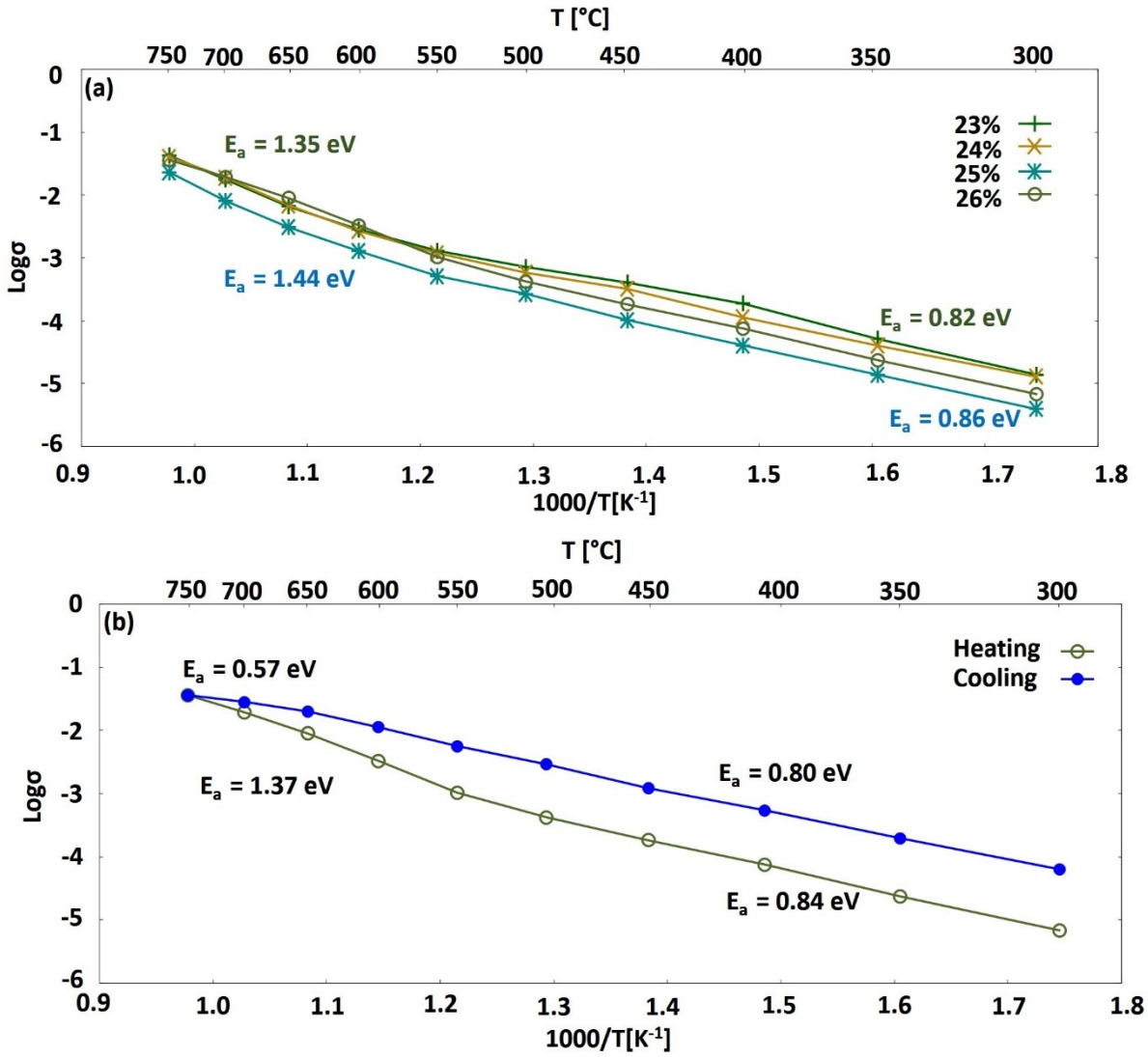

Figure 3.6. Arrhenius plots showing the temperature dependant bulk conductivities (in units of S cm^{-1}) for **(a)** 23%-26% WO_3 content samples for the heating cycle and **(b)** the 26% WO_3 content sample for both the heating and cooling cycles.

The Arrhenius plots (Fig. 3.6(a)) showed a moderate increase in slope and activation energy in the 550-750°C temperature range as compared to the 300-550°C range. These changes in activation energy are thermally induced and can either be due to a change in the oxygen sublattice or it could be due to the emergence of the unidentified phase as suggested from the Raman data. The former justification more readily substantiates the cooling cycle (Fig. 3.6(b)) being far more linear. It should be noted that the activation energies quoted were rather calculated from the plot of ln(σT) versus 1/T due to the theoretical justification associated with this relationship which is derived from the random walk theory.

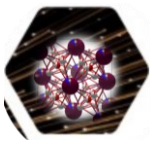

Table 3.1. Comparison of temperature related bulk conductivities for related materials*.

Temperature /°C	Conductivity /S cm^{-1}				
	23% WO_3	23% WO_3	22% WO_3	$7Bi_2O_3$-$2WO_3$	$7Bi_2O_3$-WO_3
300	1.4×10^{-5}	~2.8×10^{-4}	-	3.01×10^{-4}	3.4×10^{-6}
400	1.87×10^{-4}	~1.8×10^{-3}	~2.7×10^{-3}	~7.4×10^{-3}	~1.1×10^{-5}
700	0.018	~0.047	0.062	~0.058	~3.7×10^{-3}
800	-		~0.14	~0.11	~1.1
Reference	This work	[21]	[4]	[22]	[23]

*Values indicated as ~ were extracted from the graphs in the publications.

DTA thermographs showed no significant displacements during the heating and cooling cycles as can be seen from Fig. 3.7. Only a slight endothermic displacement is observed between 550-650°C mainly during the heating cycle which again could either be attributed to the characteristic of minor disordering occurring in the oxygen sublattice or to the formation of the unidentified phase.

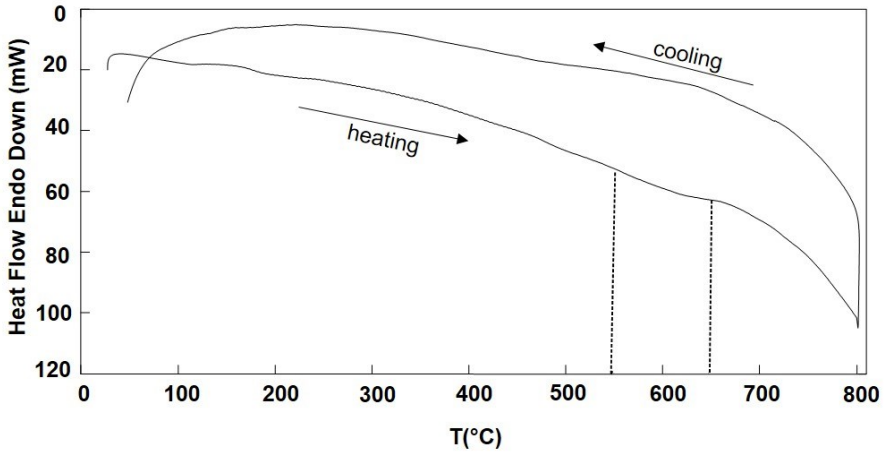

Figure 3.7. A DTA thermograms for the 23% WO_3 content sample (mass = 18.478 mg) showing only a slight endothermic displacement between 550-650 °C in the heating cycle. No baseline subtraction was done.

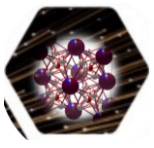

3.4 Conclusion

In the Bi_2O_3-WO_3 system, the citrate-gel method combined with slow cooling produced a mixture of russellite, sillenite and $7Bi_2O_3 \cdot 2WO_3$ phases for WO_3 concentrations of 22%-27% at lower annealing temperatures (500-650°C). After annealing at 800°C the russellite phase had disappeared and the sillenite phase was significantly reduced, but a mixture of both the sillenite and $7Bi_2O_3 \cdot 2WO_3$ phases was retained in the temperature range studied. Unlike the work by Watanabe and Ono [21] who showed that a pure $7Bi_2O_3 \cdot 2WO_3$ phase exists above 670°C (when using the solid-state method), here VT-RS data confirmed that the sillenite phase was clearly still present beyond 670 °C. Both the DTA and VT-EIS data were inconclusive as to whether the slight changes observed at higher temperatures were due to disordering in the oxygen sublattice or the emergence of an unidentified phase as inferred from the Raman data.

The magnitude of the conductivities measured were between that for the pure $7Bi_2O_3 \cdot 2WO_3$ and sillenite phases, especially in the lower temperature range. As expected, the sample containing a high sillenite content displayed a lower conductivity at all temperatures. At 700°C, the conductivity of the mixture was only three times lower than that of the supposed pure δ-phase for the 22% WO_3 content [4] that was obtained by quenching and was also still slightly higher than that for YSZ (at the same temperature).

The appreciable conductivity for this mixture of phases provides a different perspective into the study of solid oxide ion conductors. Rather than focusing on a pure, quenched phase which is metastable, a mixture of phases might offer the desired conductivities and stabilities at a lower energy cost. Therefore, efforts should be made to study the conductivities of the mixtures before they are discarded in favour of these pure metastable phases that degrade with long term annealing.

3.5 Acknowledgements

National Research Foundation (Grant Numbers 78555; 99003; 105852), the DST/NRF Centre of Excellence in Strong Materials and the University of the Witwatersrand.

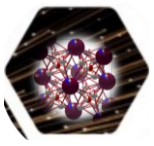

3.6 References

[1] S.P. Adhikari, H. Dean, Z.D. Hood, R. Peng, K.L. More, I. Ivanov, Z. Wu, and A. Lachgar, Visible-light-driven Bi_2O_3/WO_3 composites with enhanced photocatalytic activity. RSC Adv. **5**(111), 91094-91102 (2015)

[2] X.F.Cao, L. Zhang, X.T. Chen, Z.L. Xue, Microwave-assisted solution-phase preparation of flower-like Bi_2WO_6 and its visible-light-driven photocatalytic properties. CrystEngComm **13**(1), 306-311 (2011)

[3] A.M. Azad, S. Larose, S.A. Akbar, Bismuth oxide-based solid electrolytes for fuel cells. J. Mater. Sci. **29**(16), 4135-4151 (1994)

[4] T. Takahashi, H. Iwahara, High oxide ion conduction in sintered oxides of the system Bi_2O_3 -WO_3. J. Appl. Electrochem. **3**(1), pp.65-72 (1973)

[5] T. Takahashi, H. Iwahara, Oxide ion conductors based on bismuth sesquioxide. Mater. Res. Bull, **13**(12), 1447-1453 (1978)

[6] P.Shuk, H.D. Wiemhöfer, U. Guth, W. Göpel, M. Greenblatt, Oxide ion conducting solid electrolytes based on Bi_2O_3. Solid State Ion. **89**(3-4), 179-196 (1996)

[7] A. Laarif, F.Theobald, The lone pair concept and the conductivity of bismuth oxides Bi_2O_3. Solid State Ion. **21**(3), 183-193 (1986)

[8] J.C. Boivin, Structural and electrochemical features of fast oxide ion conductors. Int. J. Inorg. Mater. **3**(8), 1261-1266 (2001)

[9] C.R. Rao, G.S. Rao, S. Ramdas, Phase transformations and electrical properties of bismuth sesquioxide. J. Phys. Chem. **73**(3), 672-675 (1969)

[10] A.M. Azad, S. Larose, S.A. Akbar, Bismuth oxide-based solid electrolytes for fuel cells. J. Mater. Sci. **29**(16), 4135-4151 (1994)

[11] M. Drache, P. Roussel, J.P. Wignacourt, Structures and oxide mobility in Bi− Ln− O materials: heritage of Bi_2O_3. Chem. Rev. **107**(1), 80-96 (2007)

[12] E.M. Levin, R.S. Roth,. Polymorphism of bismuth sesquioxide. II. Effect of oxide additions on the polymorphism of Bi_2O_3. J. Res. Natl Inst. Stand. Technol. **68**(2), 197-206 (1964)

[13] N. Jiang, E.D. Wachsman, S.H. Jung, A higher conductivity Bi_2O_3-based electrolyte. Solid State Ion. **150**(3-4), 347-353 (2002)

[14] A. Watanabe, M. Sekita, Stabilized δ-Bi_2O_3 phase in the system Bi_2O_3–Er_2O_3–WO_3 and its oxide-ion conduction. Solid State Ion. **176**(31-34), 2429-2433 (2005)

[15] D. Mercurio, M. El Farissi, B. Frit, J.M. Reau, J. Senegas, Fast ionic conduction in new oxide materials of the Bi_2O_3–Ln_2O_3–TeO_2 systems (Ln= La, Sm, Gd, Er). Solid State Ion. **39**(3-4), 297-304 (1990)

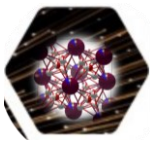

[16] N. Portefaix, P. Conflant, J.C. Boivin, J.P. Wignacourt, M. Drache, New Bi–Ln–V–O Anionic Conductors with δ-Bi_2O_3 Fluorite-Type Structure (Ln= Y, Sm, Eu, Gd, Tb, Dy, Er, Yb). J. Solid State Chem. **134**(2), 219-226 (1997)

[17] K. Shitara, T. Moriasa, A. Sumitani, A. Seko, H. Hayashi, Y. Koyama, R. Huang, D. Han, H. Moriwake, I. Tanaka, First-principles selection of solute elements for Er-stabilized Bi_2O_3 oxide-ion conductor with improved long-term stability at moderate temperatures. Chem. Mater. **29**(8), 3763-3768 (2017)

[18] S. Bandyopadhyay, A. Dutta, A structural insight into the electrical properties of Dy-Ho co-doped phase stabilized Bismuth Oxide based electrolytes. J. Electroanal. Chem. **817**, 55-64 (2018)

[19] E.D. Wachsman, K.T. Lee,. Lowering the temperature of solid oxide fuel cells. Science, **334**(6058), 935-939 (2011)

[20] A. Watanabe, Polymorphic transformation of δ-Bi_2O_3 stabilized with Ln_2O_3 (Ln= Sm, Eu, Gd, Tb and Dy) into a new phase with a C-type rare-earth oxide-related structure. Solid State Ion. **79**, 84-88 (1995)

[21] A. Watanabe, A. Ono, Thermostable region of an oxide ion conductor, $Bi_7WO_{13.5}$ (= $7Bi_2O_3 \cdot 2WO_3$), and the solid solubility extension. Solid State Ion. **174**(1-4), 15-18 (2004)

[22] A. Borowska-Centkowska, M. Leszczynska, F. Krok, M. Malys, W. Wrobel, S. Hull, I. Abrahams, Local structure and conductivity behavior in $Bi_7WO_{13.5}$. J. Mater. Chem. A **6**(13), 5407-5418 (2018)

[23] A. Borowska-Centkowska, F. Krok, I. Abrahams, W. Wrobel, J.R. Dygas, S. Hull, Thermal variation of structure and electrical conductivity in $Bi_{14}WO_{24}$. Solid State Ion. **202**(1), 14-21 (2011)

[24] S. Gražulis, D. Chateigner, R.T. Downs, A.F.T. Yokochi, M. Quirós, L. Lutterotti, E. Manakova, J. Butkus, P. Moeck, A. Le Bail, Crystallography Open Database–an open-access collection of crystal structures. J. Appl. Crystallogr. **42**(4), 726-729 (2009)

[25] Bruker, TOPAS, version 5. Bruker AXS Inc., Madison, Wisconsin, USA, 2014.

[26] G. Bergerhoff, I.D. Brown, in Crystallographic databases, ed. By F. Allen, G. Bergerhoff, R. Sievers (International Union of Crystallography, Chester, 1987), 77-95

[27] D.W. Jung, J.C. Nino, K.L. Duncan, S.R. Bishop, E.D. Wachsman, Enhanced long-term stability of bismuth oxide-based electrolytes for operation at 500 °C. Ionics, **16**(2), 97-103 (2010)

[28] H. Jung, S. Y. Chung, Absence of Distinctively High Grain-Boundary Impedance in Polycrystalline Cubic Bismuth Oxide. Journal of the Korean Ceramic Society, **54**(5), 413-421(2017)

[29] S.N. Hoda, L.L. Chang, Phase Relations in the System Bi_2O_3-WO_3. J. Am. Ceram. Soc. **57**(7), 323-326 (1974)

[30] A.E. Danks, S.R. Hall, Z.J.M.H. Schnepp, The evolution of 'sol–gel'chemistry as a technique for materials synthesis. Mater. Horiz. **3**(2), 91-112 (2016)

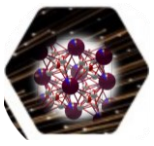

[31] A.R West, Solid State Chemistry and its Applications. (John Wiley & Sons. 2014)

[32] F.D. Hardcastle, I.E. Wachs, Raman spectroscopy of bismuth tungstates. J. Raman Spectrosc. **26**(6), 407-412 (1995)

[33] V.V. Kharton, F.M.B. Marques, A. Atkinson, Transport properties of solid oxide electrolyte ceramics: a brief review. Solid State Ion. **174**(1-4), 135-149 (2004)

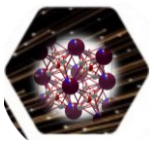

3.7 Supporting Information

Insights on the phase transitions, stability and conductivity in the Bi_2O_3-WO_3 system

Sikhumbuzo M. Masina[a], Caren Billing[a,*], Rudolph M. Erasmus[b,c], David G. Billing[a,c]

[a]Molecular Science Institute, School of Chemistry, University of the Witwatersrand, Private Bag X3, Johannesburg, 2050, South Africa

[b]Material Physics Research Institute, Microscopy and Microanalysis Unit, University of the Witwatersrand, Private Bag X3, Johannesburg, 2050, South Africa.

[c]DST-NRF Centre of Excellence in Strong Materials, University of the Witwatersrand, Private Bag X3, Johannesburg, 2050, South Africa.

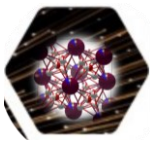

3.7.1 Rietveld Refinements

Table S3.1. Quantitative phase composition from Rietveld refinement for samples annealed at 800 °C.

	Weight % $7Bi_2O_3$-WO_3	**Weight % $7Bi_2O_3$-$2WO_3$**
22% WO_3 sol-gel	20.3(39)	79.7(39)
23% WO_3 sol-gel	8.1(9)	91.9(9)
24% WO_3 sol-gel	16.1(2)	83.9(9)
24% WO_3 sol-gel repeat	13.7(2)	86.3(9)
25% WO_3 sol-gel	11.4(1)	88.6(1)
25% WO_3 sol-gel repeat	9.9(3)	90.1(3)
26% WO_3 sol-gel	2.1(2)	97.9(2)
27% WO_3 sol-gel	4.3(16)	95.7(16)

	Weight % $7Bi_2O_3$-WO_3	**Weight % $7Bi_2O_3$-$2WO_3$**	**Weight % Bi_2O_3-WO_3(B2cb)**	**Weight % Bi_2O_3-WO_3($Pca2_1$)**
22% WO_3 solid state	20.3(8)	77.7(6)	0.6(1)	1.4(9)
23% WO_3 solid state	20.1(9)	78.3(5)	0.9(2)	0.7(7)
24% WO_3 solid state	12.9(2)	87.1(2)		
25% WO_3 solid state	14.9(1)	85.1(2)		
26% WO_3 solid state	16.5(9)	83.5(16)		
27% WO_3 solid state	15.0(11)	85.0(11)		

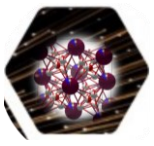

Table S3.2. Crystallographic data – Sol-gel samples.

Mol% WO_3	**22**	**23**	**24**	**25**	**26**	**27**
Whole Pattern						
Rexp	5.30	4.59	4.15	3.95	8.95	8.22
Rwp	6.63	6.89	6.79	7.31	10.18	10.03
Rp	5.07	5.35	5.17	5.47	7.77	7.96
GOF	1.20	1.50	1.64	1.85	1.14	1.22
$7Bi_2O_3 \cdot WO_3$						
R-Bragg	1.181	0.993	1.824	1.93	4.882	3.705
Weight %	20.3(39)	8.1(9)	16.1(9)	11.4(1)	2.1(2)	4.3(16)
Space group	*I*4/*m*	*I*4/*m*	*I*4/*m*	*I*4/*m*	*I*4/*m*	*I*4/*m*
a / Å	8.7096(7)	8.73(18)	8.701(6)	8.703(1)	8.704(1)	8.69(1)
c / Å	17.340(2)	17.2(5)	17.367(1)	17.366(3)	17.352(2)	17.366(3)
Cell Vol / $Å^3$	1315.4(2)	1313(68)	1315(2)	1315.6(4)	1314.6(3)	1312.1(3)
Crystal Density /$g.cm^{-3}$	8.820(2)	8.8(4)	8.822(15)	8.818(2)	8.825(2)	8.842(3)
$7Bi_2O_3 \cdot 2WO_3$						
R-Bragg	2.640	3.260	1.056	2.133	1.504	1.488
Weight %	79.7(39)	91.9(9)	83.9(9)	88.6(1)	97.9(2)	95.7(16)
Space group	$I4_1$	$I4_1$	$I4_1$	$I4_1$	$I4_1$	$I4_1$
a / Å	12.5099(2)	12.5176(4)	12.5161(2)	12.5216(1)	12.5251(2)	12.5210(5)
c / Å	11.2168(2)	11.2108(5)	11.2107 (2)	11.2278 (2)	11.2204(3)	11.2246(5)
Cell Vol / $Å^3$	1755.4(7)	1756.64(14)	1756.2(8)	1760.43 (6)	1760(1)	1760.0 (1)
Crystal Density /$g.cm^{-3}$	8.81039(3)	8.8042(7)	8.8063(3)	8.7852 (3)	8.7862(5)	8.7874 (8)

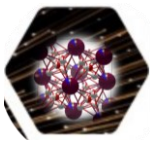

Table S3.3. Crystallographic data – Solid state samples.

Mol% WO_3	**22**	**23**	**24**	**25**	**26**	**27**
Whole Pattern						
Rexp	5.37	5.41	5.57	5.33	5.42	5.91
Rwp	6.90	7.20	6.83	6.12	6.47	6.65
Rp	5.41	5.63	5.43	4.92	5.16	5.23
GOF	1.29	1.33	1.23	1.15	1.19	1.13
$7Bi_2O_3 \cdot WO_3$						
R-Bragg	0.729	0.720	1.016	0.854	0.929	1.363
Weight %	20.3(8)	20.1(9)	12.9(2)	14.9(1)	16.5(9)	15.0(11)
Space group	*I*4/*m*	*I*4/*m*	*I*4/*m*	*I*4/*m*	*I*4/*m*	*I*4/*m*
a / Å	8.707(8)	8.707(6)	8.854(7)	8.867(5)	8.8571(16)	8.8348(5)
c / Å	17.36(2)	17.36(2)	16.817(2)	16.813(1)	16.838(6)	16.8643(12)
Cell Vol / $Å^3$	1317(3)	1316(3)	1318(2)	1321.7(18)	1320.9(7)	1316.4(1)
Crystal Density /$g.cm^{-3}$	8.81(2)	8.812(17)	8.800(18)	8.778(12)	8.783(5)	8.8140(9)
$7Bi_2O_3 \cdot 2WO_3$						
R-Bragg	1.200	1.475	1.460	2.5412	2.234	1.302
Weight %	77.7(6)	78.3(5)	87.1(2)	85.1(2)	83.5(16)	85.0(11)
Space group	$I4_1$	$I4_1$	$I4_1$	$I4_1$	$I4_1$	$I4_1$
a / Å	12.5206 (1)	12.52198(18)	12.5060(16)	12.5196(2)	12.520(14)	12.49459(1)
c / Å	11.2329(1)	11.2389(2)	11.2618(13)	11.2553(2)	11.238(18)	11.2418(2)
Cell Vol / $Å^3$	1760.95(5)	1762.27(4)	1761.34(3)	1764.22(7)	1761.93(5)	1755.02(5)
Crystal Density /$g.cm^{-3}$	8.7827(2)	8.7761(2)	8.7807(3)	8.7664(4)	8.7778(2)	8.8123(2)
$Bi_2O_3 \cdot WO_3$ (*B2cb*)						
R-Bragg	10.157	5.853				
Weight %	0.6(1)	0.9(2)				
Space group	B2cb	B2cb				
a / Å	5.596(1)	5.598(2)				
b / Å	5.482(1)	5.481(2)				
c / Å	16.621(3)	16.614(5)				

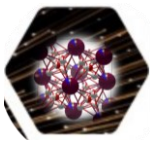

Cell Vol / Å^3	509.9(2)	509.8(3)				
Crystal Density /g.cm^{-3}	9.088(4)					
$Bi_2O_3 \cdot WO_3$ (*Pca*2$_1$)						
R-Bragg	7.921	8.716				
Weight %	1.4(9)	0.7(7)				
Space group	*Pca*2$_1$	*Pca*2$_1$				
a / Å	5.404(1)	5.404(1)				
b / Å	16.209(2)	16.209(3)				
c / Å	5.4036(6)	5.4041(9)				
Cell Vol / Å^3	473.3(1)	473.4(1)				
Crystal Density /g.cm^{-3}	9.791(3)	9.789(3)				

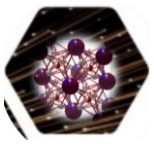

Figure S3.1. Rietveld plots for sol-gel samples.

a) 22% WO_3

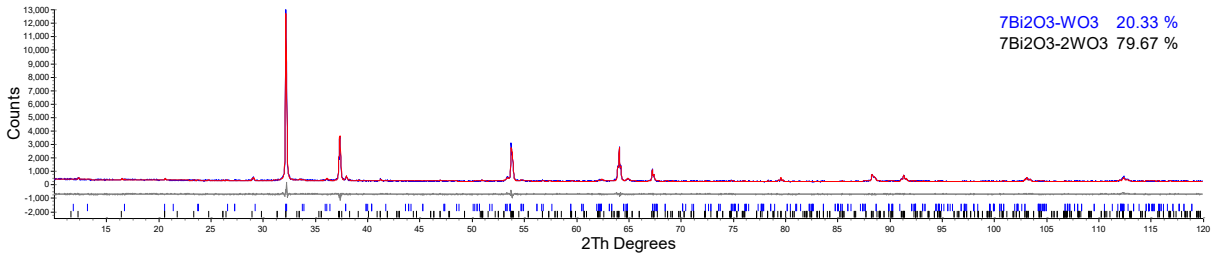

b) 23% WO_3

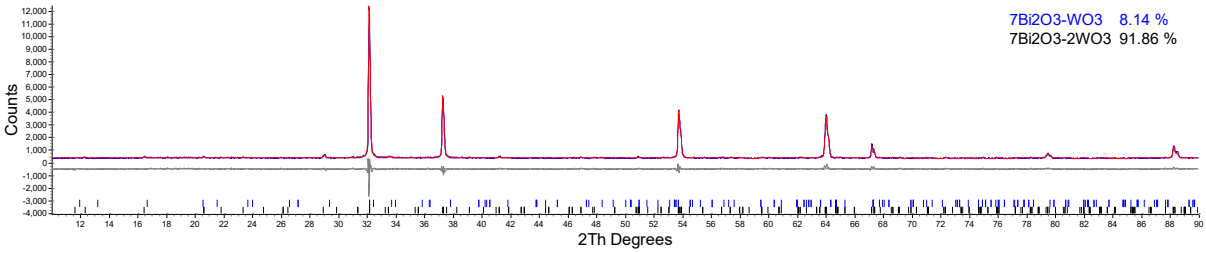

c) 24% WO_3

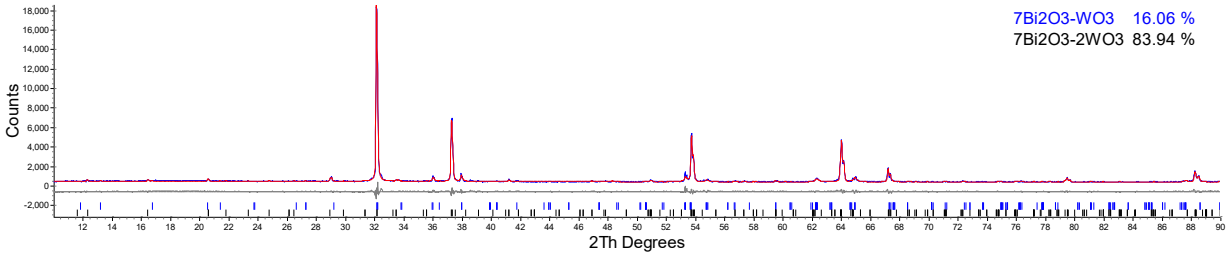

d) 24% WO_3 repeat

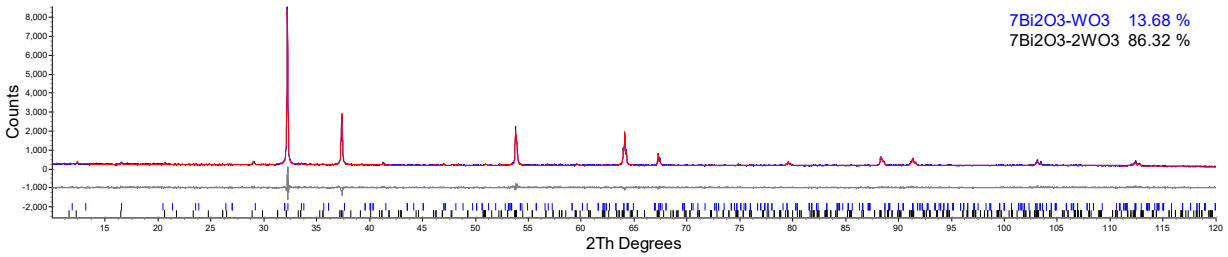

e) 25% WO_3

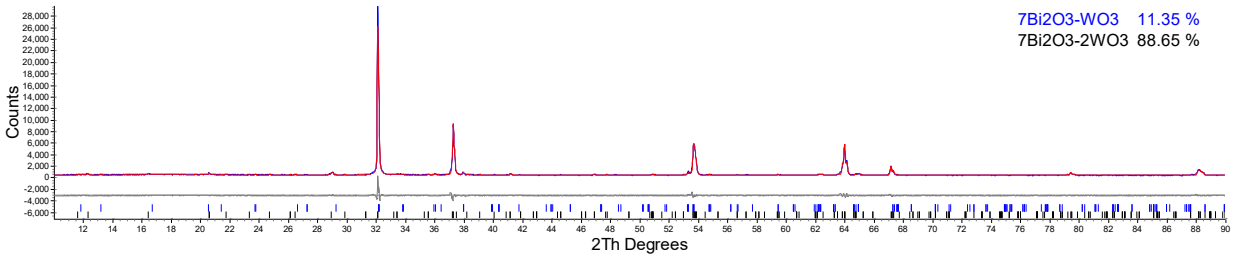

f) 25% WO_3 repeat

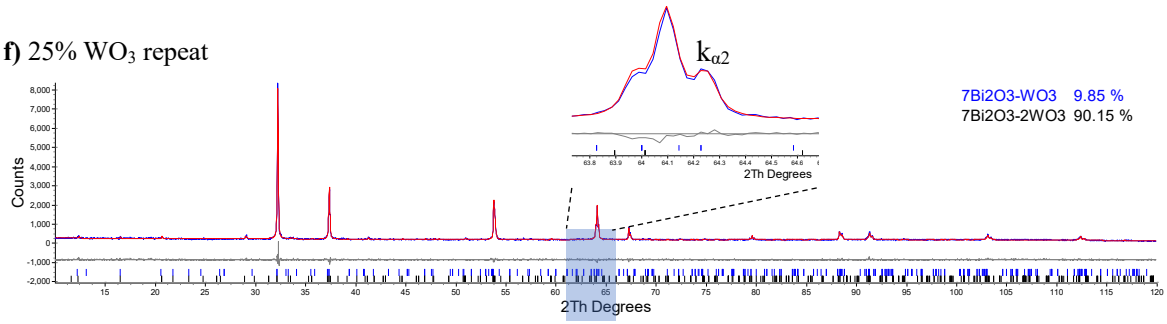

g) 25% WO_3 72 h of annealing at 800 °C

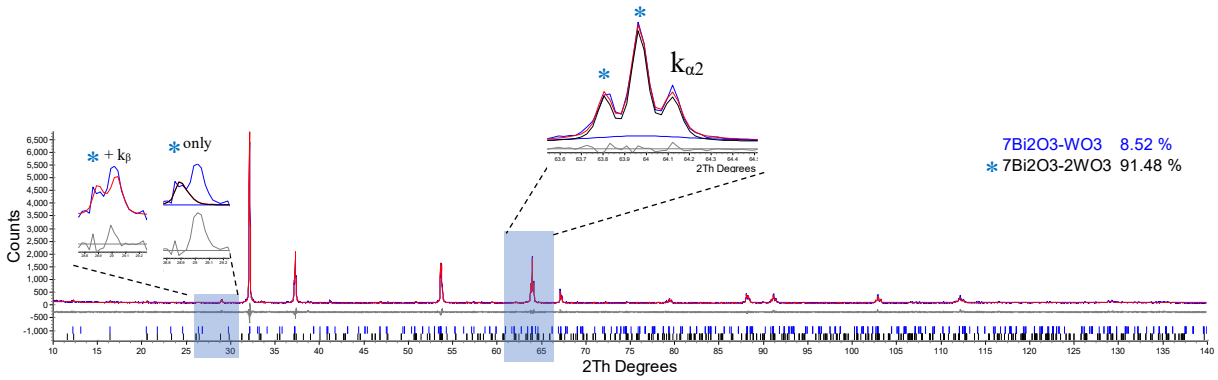

h) 26% WO_3

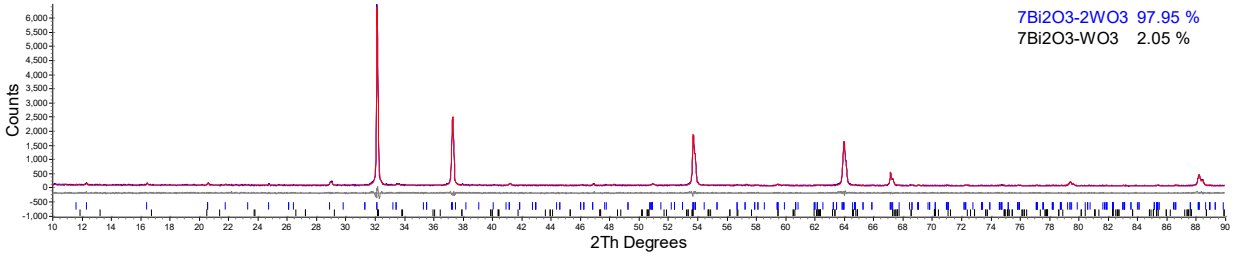

i) 27% WO_3

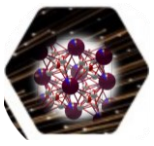

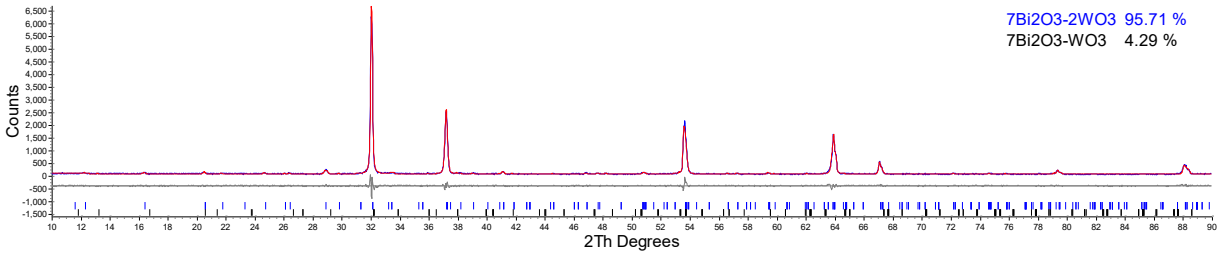

Figure S3.2. Rietveld plots for Solid State samples

a) 22% WO_3

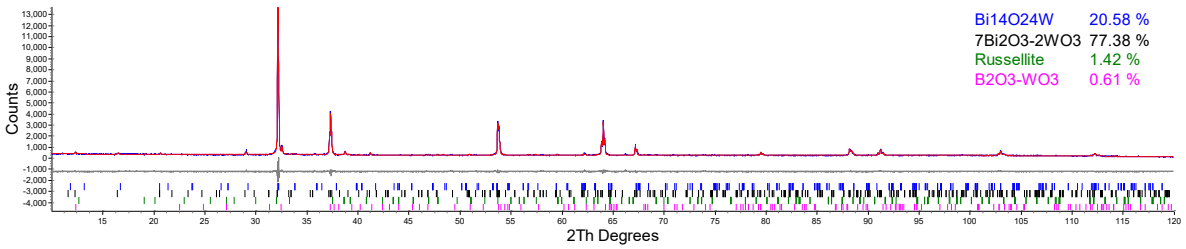

b) 23% WO_3

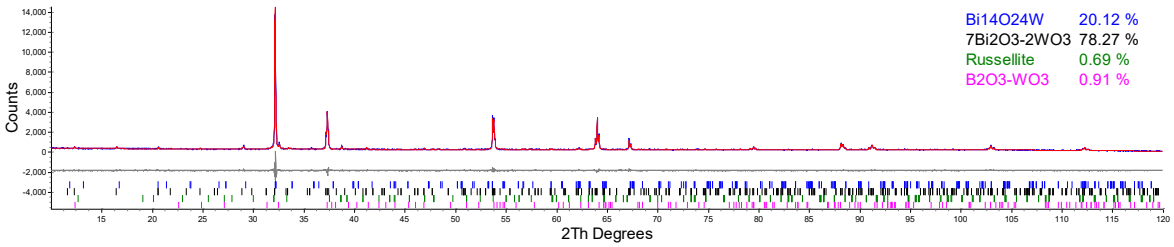

c) 24% WO_3

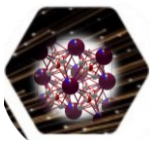

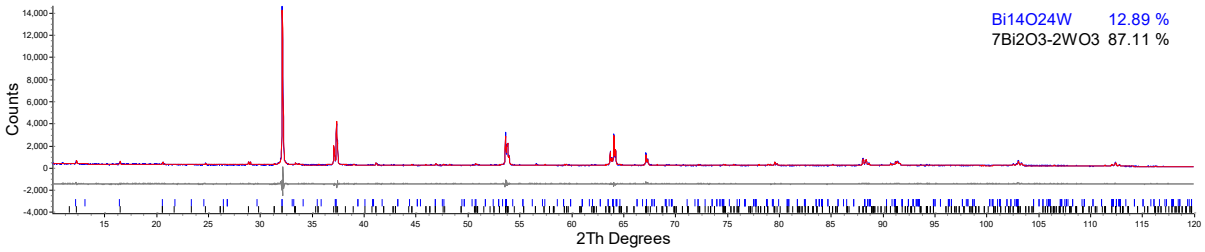

d) 25% WO_3

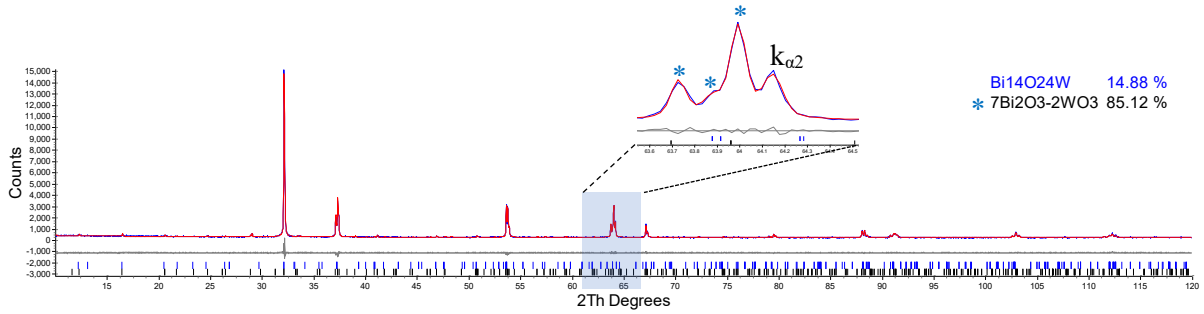

e) 26% WO_3

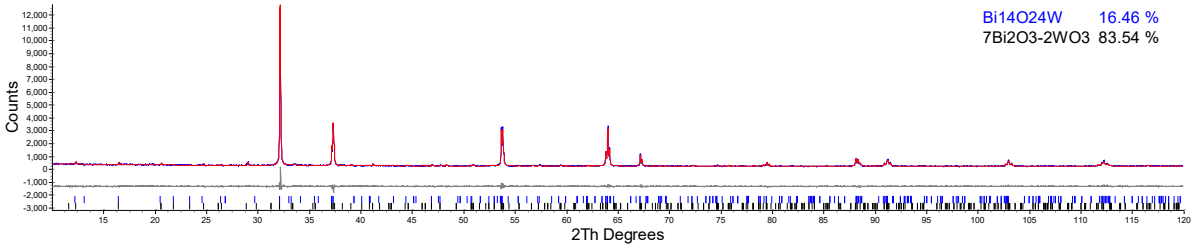

f) 27% WO_3

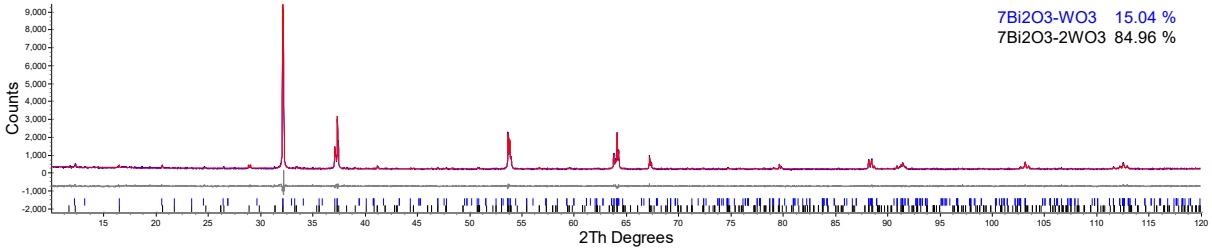

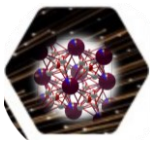

3.7.2 Equivalent Circuit Fitting

Figure S3.3. An example of the equivalent circuit fitting of VT-EIS Nyquist plots: the 26% WO_3 sol-gel sample on heating. Q represent a constant phase element modelling a non-ideal capacitor and W is the Warburg diffusion element.

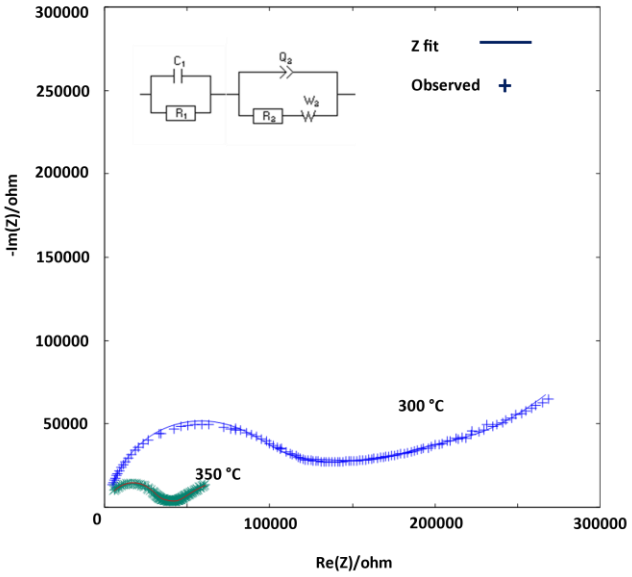

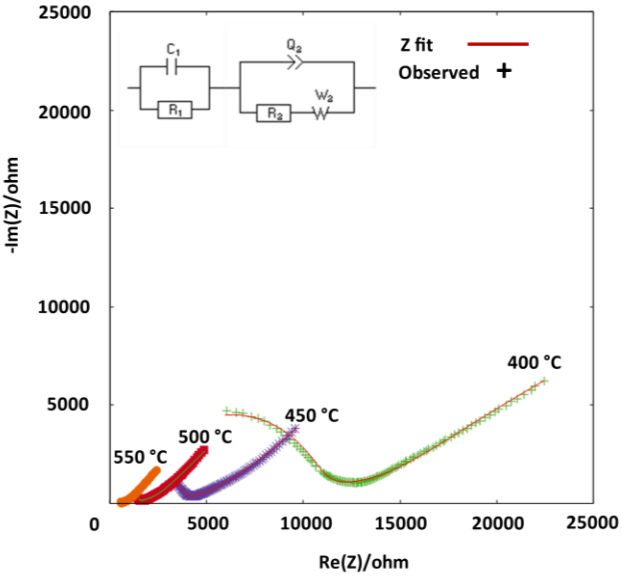

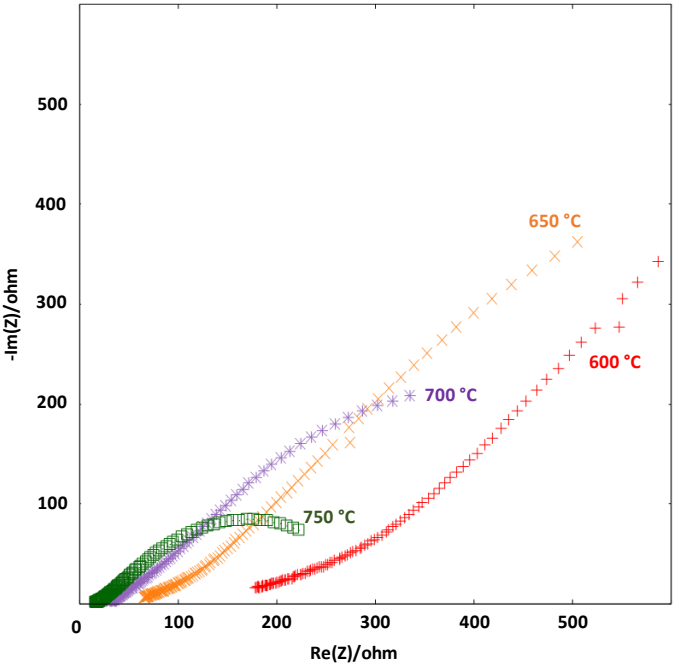

The high temperature plots were not fitted. Instead the values for R1 were taken from the highest frequency point along the Re(Z)-axis. For plots where the graph has no Re(Z)-axis intercept, the R1 values were taken to be the Re(Z) value of the last point in the graph. For the lower temperature plots, the low frequency data were fitted where possible. However, it is only the bulk resistance (R1) which is further scrutinised in this work.

Table S3.4. VT-EIS data for 23% WO_3 sol-gel sample.

Temperature (°C) - heating	**300**	**350**	**400**	**450**	**500**
R1/ Ω	45229	12335	3380	1563	880
C1/ F	19.07×10^{-12}	18.99×10^{-12}	27.16×10^{-12}	20.29×10^{-12}	14.5×10^{-12}
R2/ Ω	392321	51 292	15 411	5 695	2 970
Q2/ $F.s^{(a2-1)}$	86.32×10^{-9}	0.399×10^{-6}	5.163×10^{-6}	24.74×10^{-6}	45.32×10^{-6}
a2	0.884	0.843	0.873	0.837	0.897
s2/ $\Omega.s^{-0.5}$	1.182×10^{6}	2.053×10^{5}	1.390×10^{5}	1.321×10^{5}	1.133×10^{5}
Temperature (°C) - cooling	**500**	**450**	**400**	**350**	**300**
R1/ Ω	141	334	992	3120	9652
C1/ F	-	-	25.23×10^{-12}	26.98×10^{-12}	41.54×10^{-12}
R2/ Ω	-	-	1 606	18 014	7 250
Q2/ $F.s^{(a2-1)}$	-	-	5.503×10^{-6}	5.749×10^{-6}	3.819×10^{-6}
a2	-	-	0.831	0.826	0.870
s2/ $\Omega.s^{-0.5}$	-	-	2.361×10^{4}	5.902×10^{4}	1.204×10^{6}

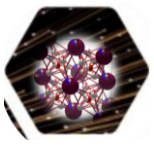

Table S3.5. VT-EIS data for 24% WO_3 sol-gel sample.

Temperature (°C) - heating	**300**	**350**	**400**	**450**	**500**
R1/ Ω	46623	14946	5294	1869	1036
C1/ F	17.57×10^{-12}	15.57×10^{-12}	14.87×10^{-12}	16.12×10^{-12}	20.01×10^{-12}
R2/ Ω	1.284×10^{6}	73614	11198	3601	4260
Q2/ $F.s^{(a2-1)}$	59.33×10^{-9}	0.105×10^{-6}	0.266×10^{-6}	3.729×10^{-6}	8.917×10^{-6}
a2	0.820	0.848	0.827	0.877	0.629
s2/ $\Omega.s^{-0.5}$	3.785×10^{6}	6.528×10^{5}	3.010×10^{5}	2.104×10^{5}	2.215×10^{5}
Temperature (°C) - cooling	**500**	**450**	**400**	**350**	**300**
R1/ Ω	129	258	622	1634	4709
C1/ F	-	-	-	25.56×10^{-12}	47.23×10^{-12}
R2/ Ω	-	-	-	12043	1414
Q2/ $F.s^{(a2-1)}$	-	-	-	6.111×10^{-6}	0.497×10^{-6}
a2	-	-	-	0.545	0.778
s2/ $\Omega.s^{-0.5}$	-	-	-	2.568×10^{4}	2.007×10^{5}

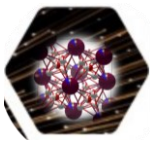

Table S3.6. VT-EIS data for 25% WO_3 sol-gel sample. The (–) means no fitting was done. Resistance values were taken from the highest frequency point along the Re(Z) axis.

Temperature (°C) - heating	**300**	**350**	**400**	**450**	**500**
R1/ Ω	149846	42643	14543	5723	2201
C1/ F	9.41×10^{-12}	10.81×10^{-12}	12.12×10^{-12}	11.78×10^{-12}	23.42×10^{-12}
R2/ Ω	705707	40901	9223	2966	781
Q2/ $F.s^{(a2-1)}$	0.198×10^{-6}	0.484×10^{-6}	4.59×10^{-6}	6.667×10^{-6}	9.937×10^{-6}
a2	0.898	0.778	0.854	0.861	0.500
s2/ $\Omega.s^{-0.5}$	3.87×10^{6}	1.859×10^{5}	9.315×10^{4}	5.411×10^{4}	3.427×10^{4}
Temperature (°C) - cooling	**500**	**450**	**400**	**350**	**300**
R1/ Ω	348	791	1992	4362	13102
C1/ F	-	-	20.00×10^{-12}	30.03×10^{-12}	30.42×10^{-12}
R2/ Ω	-	-	16063	3506	10381
Q2/ $F.s^{(a2-1)}$	-	-	14.67×10^{-6}	5.749×10^{-6}	3.819×10^{-6}
a2	-	-	0.890	0.873	0.324
s2/ $\Omega.s^{-0.5}$	-	-	2.537×10^{5}	3.822×10^{5}	6.875×10^{5}

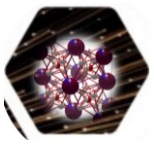

Table S3.7. VT-EIS data for 26% WO_3 sol-gel sample. The (–) means no fitting was done. Resistance values were taken from the highest frequency point along the Re(Z) axis.

Temperature (°C) - heating	**300**	**350**	**400**	**450**	**500**
R1/ Ω	86179	25018	7816	3243	1400
C1/ F	15.82×10^{-12}	17.19×10^{-12}	21.66×10^{-12}	16.61×10^{-12}	16.78×10^{-12}
R2/ Ω	137390	22886	13131	4555	1349
Q2/ $F.s^{(a2-1)}$	98.12×10^{-9}	0.522×10^{-6}	16.31×10^{-6}	25.36×10^{-6}	16.32×10^{-6}
a2	0.478	0.394	0.195	0.272	0.387
s2/ $\Omega.s^{-0.5}$	5.733×10^{5}	1.262×10^{5}	1.511×10^{5}	8.125×10^{4}	3.257×10^{4}
Temperature (°C) - cooling	**500**	**450**	**400**	**350**	**300**
R1/ Ω	203	484	1085	3005	9304
C1/ F	-	-	19.87×10^{-12}	23.34×10^{-12}	47.84×10^{-12}
R2/ Ω	-	-	3.476×10^{15}	3442	14393
Q2/ $F.s^{(a2-1)}$	-	-	13.58×10^{-6}	4.395×10^{-6}	1.261×10^{-6}
a2	-	-	0.405	0.402	0.323
s2/ $\Omega.s^{-0.5}$	-	-	7.039×10^{18}	1.008×10^{6}	1.442×10^{6}

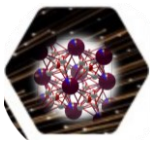

Chapter 4: A Temperature Dependent Phase Evolution Study of a Quaternary Bi_2O_3 Solid Electrolyte

Sikhumbuzo M. Masina[a], Caren Billing[a,c*], Rudolph M. Erasmus[b,c], David G. Billing[a,c]

[a]Molecular Science Institute, School of Chemistry, University of the Witwatersrand, Private Bag X3, Johannesburg, 2050, South Africa

[b]Material Physics Research Institute, School of Physics, University of the Witwatersrand, Private Bag X3, Johannesburg, 2050, South Africa.

[c]DST-NRF Centre of Excellence in Strong Materials, University of the Witwatersrand, Private Bag X3, Johannesburg, 2050, South Africa.

Abstract

A triply substituted system $(Bi_2O_3)_{0.88}(Dy_2O_3)_{0.08}(Er_2O_3)_{0.03}(WO_3)_{0.01}$ (8D3E1WSB) was designed to improve phase stability in the system $(Bi_2O_3)_{0.88}(Dy_2O_3)_{0.08}(WO_3)_{0.04}$ (8D4WSB). 8D3E1WSB showed remarkable stability after annealing for 100 hours at 500°C compared to the doubly substituted 8D4WSB which showed significant phase separation under the same conditions. Its total conductivity at 700°C was 0.273 S cm^{-1}, comparable to 0.295 S cm^{-1} obtained from 8D4WSB and an order of magnitude greater than that of yttria-stabilized zirconia at the same temperature. Arrhenius plots of the total conductivity of both systems exhibited discontinuities between 550-600°C characteristic of phase changes. Variable temperature Raman spectroscopy and variable temperature powder X-ray diffraction showed phase transitions in these materials in the same temperature range that conductivity discontinuities were observed.

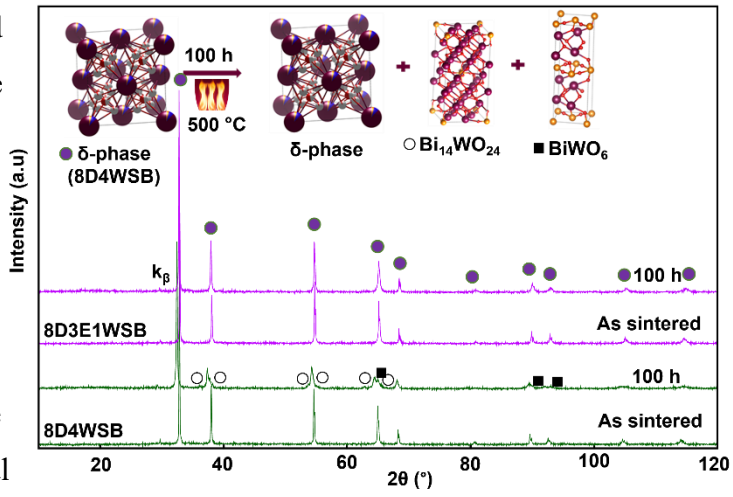

Keywords: Bismuth oxide, variable temperature, triple substitution, Rietveld refinement, phase transition, conductivity

4.1 Introduction

Solid oxide fuel cells (SOFCs) are electrochemical devices that convert chemical energy directly to electrical energy with reduced CO_2, SO_2 and NO_x emissions as compared to internal combustion engines [1]. They are highly efficient and when operated in combined heat and power mode they can reach efficiencies above 80% [2]. Although these devices have been known since Bauer and Preis reported their first use to produce electricity in 1937 [3], no large-scale production has been achieved. The main problem stems from the high temperature at which SOFCs operate (800-1000°C) [4], which is mainly determined by the electrolyte's conductivity. The electrolyte consists of an oxide ion conducting ceramic that relies mainly on the thermally activated oxide ion hopping mechanism (vacancy mechanism) for ionic transport, especially for cubic systems. The state-of-the-art electrolyte, yttria-stabilized zirconia (YSZ), has conductivities ranging from ~0.01 S cm^{-1} at 800°C to ~0.1 S cm^{-1} at 1000°C [5,6]. These high temperatures require the use of expensive materials (such as substituted $LaCrO_3$) with high melting points for interconnects in a SOFC stack which drives up both the capital and operational costs [7].

Numerous studies have been conducted on other potential ceramic electrolytes to reduce the operating temperature of SOFCs to the intermediate range (500-800°C) [8-11]. A group of electrolytes of interest are the solid solutions of Bi_2O_3. Bi_2O_3 in its fluorite δ-phase is highly defective, with 25% of the oxygen sites vacant and displays conductivities of ~1 S cm^{-1} at 730°C, the highest for an oxide ion conducting ceramic reported thus far [12-16]. However, the δ-Bi_2O_3 phase is only stable within a narrow high temperature range (730-824°C) – below 730°C the monoclinic α-Bi_2O_3 phase exists which is predominantly an electronic conductor and at 824°C Bi_2O_3 melts [17-20].

To stabilize the highly conductive defect fluorite-type phases (henceforth referred to as the δ-phases), isovalent and aliovalent cations have been used to substitute the Bi^{3+} cation in the structure, albeit resulting in reduced ionic conductivity [21-26]. The diminished conductivity is attributed to vacancy-impurity cation association, increased average cation-anion bond strength, vacancies being trapped in coordination spheres of aliovalent cations such as W^{6+} and reduced average polarizability of cations compared to the unsubstituted material [27-30]. The so-called stabilised δ-phase in certain solid solutions of Bi_2O_3 is, however, only metastable and undergoes phase decomposition and ageing (degradation of the conductivity due to oxide ion and vacancy

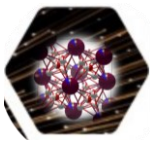

ordering) when annealed at temperatures ≤600°C for 100 hours or more [31-34]. This is the target temperature for operating intermediate temperature SOFCs (IT-SOFCs) and oxygen sensors for which these materials are fabricated.

Takahashi *et al*. [35] and Verkerk *et al*. [36,37] reported that $(Bi_2O_3)_{0.88}(WO_3)_{0.22}$ and $(Bi_2O_3)_{0.80}(Er_2O_3)_{0.20}$, and $(Bi_2O_3)_{0.715}(Dy_2O_3)_{0.285}$, respectively, showed superior conductivities to that for YSZ at intermediate temperatures. Jung *et al*. [38] reported that $(BiO_{1.5})_{0.88}(DyO_{1.5})_{0.08}(WO_3)_{0.04}$ (which can also be written as $(Bi_2O_3)_{0.846}(Dy_2O_3)_{0.077}(WO_3)_{0.077}$) exhibited a conductivity of 0.098 S cm^{-1} at 500°C, the highest of any substituted Bi_2O_3 reported thus far at this temperature. Unfortunately, this material undergoes phase decomposition and ageing when annealed at 500 and 600 °C for over 100 hours, therefore it might not be suitable for use in IT-SOFCs. Watanabe and Sekita [22] found that $(Bi_2O_3)_{0.705}(Er_2O_3)_{0.245}(WO_3)_{0.05}$ showed no phase decomposition or ageing when annealed at 600°C for 1100 hours, but at such high dopant concentrations, the conductivity was about 6 times lower (~0.015 S cm^{-1}) [22] than that for the material made by Jung *et al*. [38]

Based on these reports, it was endeavoured to produce a new solid solution of Bi_2O_3 that combined the sought-after properties, i.e. a material that retained the high conductivity displayed by $(BiO_{1.5})_{0.88}(DyO_{1.5})_{0.08}(WO_3)_{0.04}$ [38], as well as exhibiting the phase stability of $(Bi_2O_3)_{0.705}(Er_2O_3)_{0.245}(WO_3)_{0.05}$ [22]. To this end a Bi_2O_3 solid solution substituted with all three impurity cations (Er^{3+}, Dy^{3+}, W^{6+}) was investigated, namely, $(Bi_2O_3)_{0.88}(Dy_2O_3)_{0.08}(Er_2O_3)_{0.03}(WO_3)_{0.01}$ (8D3E1WSB). For comparison purposes, the double-substituted system, $(Bi_2O_3)_{0.88}(Dy_2O_3)_{0.08}(WO_3)_{0.04}$ (8D4WSB) was also fabricated to check whether the incorporation of Er does indeed lead to better stability.

4.2 Experimental

4.2.1 Synthetic procedures

The citrate gelation method was the synthetic procedure used. Stoichiometric amounts, with respect to the metal oxides, of $Bi(NO_3)_3 \cdot 5H_2O$ (99.99% pure, Sigma-Aldrich) and $Er(NO_3)_3 \cdot 5H_2O$ (99.99% pure, Sigma-Aldrich) were completely dissolved in acetic acid at room temperature while stirring. $(NH_4)_6H_2W_{12}O_{40} \cdot H_2O$ (Sigma-Aldrich) and $DyCl_3 \cdot 6H_2O$ (99.99% pure, Sigma-Aldrich) were mixed together in acetic acid and heated to 150°C until all the $DyCl_3 \cdot 6H_2O$ had dissolved. After cooling, 50 ml of 1 M nitric acid was added to dissolve the $(NH_4)_6H_2W_{12}O_{40} \cdot H_2O$ completely

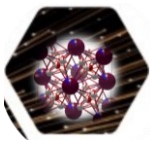

under constant stirring. The two solutions were then mixed in the presence of citric acid in a 3: 1 mole ratio of citric acid to metal ions. The resultant solution was heated at 250°C under constant stirring until the solvent evaporated and left behind a viscous white gel. The gel was dried overnight in an oven at 80°C and then calcined at 500°C in a muffle furnace for 12 hours. It was slowly cooled in the furnace (the estimated average cooling rate was ~1 °C min^{-1}) back to room temperature and then ground. The ground powder was further annealed at 750°C for a further 24 hours. A similar procedure was used for the double-substituted system without the addition of $Er(NO_3)_3 \cdot 5H_2O$.

4.2.2 Characterization techniques

4.2.2.1 Powder X-ray Diffraction (PXRD)

A Bruker D2 PHASER in Bragg-Brentano configuration, equipped with a sealed Co K_α radiation tube (λ = 1.7903 Å), secondary beam Fe K_β filter, Bruker Lynxeye PSD detector, and primary and secondary Soller slits was used to obtain scans for phase identification from the powders. Phase identification was done using DIFFRAC.SUITE EVA linked to the crystallography open database (COD) [39].

Variable temperature (VT)-PXRD was used to study phase changes as a function of temperature. A Bruker D8 Advance in Bragg-Brentano configuration, equipped with a sealed Cu K_α radiation tube (λ = 1.5419 Å), secondary beam Ni K_β filter, Bruker Vantec detector, and primary and secondary Soller slits was used to obtain scans from the powders. The samples were heated and cooled in air at a rate of 6 °C min^{-1} from 30°C to 810°C and back to 30°C using an Anton Paar XRK900 reaction chamber. Scans were taken at 30°C intervals in both heating and cooling cycles. Rietveld refinements were done using TOPAS Academic (v.6) [40]. The instrument resolution function was obtained from a silicon standard reference material (Si SRM 640d), by modelling the data using the Pseudo-Voigt TCHZ peak shape function as implemented in TOPAS Academic (v.6) [40]. The different phases were modelled from initial structural models obtained from the Inorganic Crystal Structure Database (ICSD) [41]. Entries 189995 and 189996 were used for the β- and δ-phases and entries 97481 and 88840 were used for the $7Bi_2O_3$-WO_3 and $7Bi_2O_3$-$2WO_3$ phases, respectively. Details of the refinements and parameters refined are found in Figure S4.1 and S4.2, Table S4.1 and S4.2 in the Supporting Information.

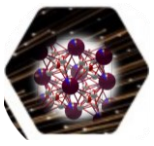

4.2.2.2 Raman Spectroscopy (RS)

Raman spectroscopy measurements were obtained using a Horiba LabRAM HR Raman system equipped with an argon-ion laser of emission line 514.532 nm, a Symphony CCD detector cooled to −129°C using liquid nitrogen and a 600 lines/mm grating. An Olympus optical microscope attachment with a 50× LWD objective lens and a Linkham TS1500 sample stage were used for the *in situ* variable temperature measurements. The sample stage was purged with high purity argon gas and the spectra were measured between ambient temperature and 850°C at 170°C increments using a heating rate of 10°C min^{-1}. The maximum acquisition time was 2 minutes and the powder form of the samples was analysed.

4.2.2.3 Electrochemical Impedance Spectroscopy (EIS)

Variable temperature (VT)-EIS was done using a MTZ-35 frequency response analyser from BioLogic. It was equipped with an HF-1100 furnace and HT-1100 sample holder. The measurements were done in air, with both heating and cooling cycles in the range 300-750°C at 50°C increments using a heating/cooling rate of 10° C min^{-1}. The system was allowed to equilibrate for 30 minutes at each temperature before measurement. The frequency range was from 10 Hz to 1 MHz with an A.C. amplitude of 10 mV. The pellets were prepared by mixing the powder samples with an aqueous solution of 0.3 wt% polyvinyl alcohol (PVA) as a binder and pressed into pellets using a uniaxial cold press at a constant pressure of 500 MPa and a 5 mm die. The pellets had a thickness of about 1 mm. Although the sintering process will be elaborated on in the discussion, the general process used was to first heat the pellets to 300°C over 6 hours and then soak at this temperature for 4 hours to remove the binder. The temperature was then ramped to 820°C and the pellets were sintered at this temperature for 14 hours. Data collected from 300-500°C were modelled using equivalent circuits (see Figures S4.3-S4.8 in the Supporting Information) as implemented in the EC-Lab software v11.21. Fitted parameters are shown in Tables S4.3 and S4.4. The semicircles at high frequencies that represent the total conductivity could not be resolved at high temperatures (Figures S4.4, S4.5, S4.7 and S4.8 in the Supporting Information), therefore the real impedance value of the last high frequency point was used to approximate R1, the total resistance. A similar approach was used by Jiang *et al*. [42]. Although values are quoted as total conductivities, it is expected that these should not differ much from the bulk conductivities as solid solutions of Bi_2O_3 have been shown to exhibit negligible grain boundary resistance [32, 43].

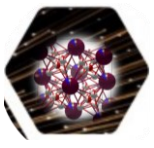

4.3 Results and discussion

4.3.1 Initial phase assessment

In designing the triply substituted system (8D3E1WSB), the amount of tungsten oxide and total substituent concentration were first optimised in the doubly substituted system (8D4WSB). The strategy adopted by Jung *et al*. [38] when optimising the Dy^{3+}:W^{6+} ratio for their doubly substituted system was to initially find that at least 12 mol% total metal ion dopant concentration in a 2:1 ratio of Dy^{3+}:W^{6+} was needed to obtain a dominant δ-phase. This corresponds to about 15 mol% total metal oxide dopant concentration and this appeared to also produce a dominant δ-phase when using a 2:1 ratio of Dy_2O_3:WO_3 instead (Fig. 4.1(a)). When using a different ratio of 1:1 Dy_2O_3:WO_3, a prominent mixture of phases was formed because of the limited solubility of WO_3 in Bi_2O_3. During this optimisation stage, all the compositions were annealed at 750°C for 72 hours and slow cooled to ambient temperature to ensure the equilibrium phases were obtained. The WO_3 content was then reduced and Er_2O_3 introduced in a ratio of 8:3:1 for Dy_2O_3:Er_2O_3:WO_3 and the

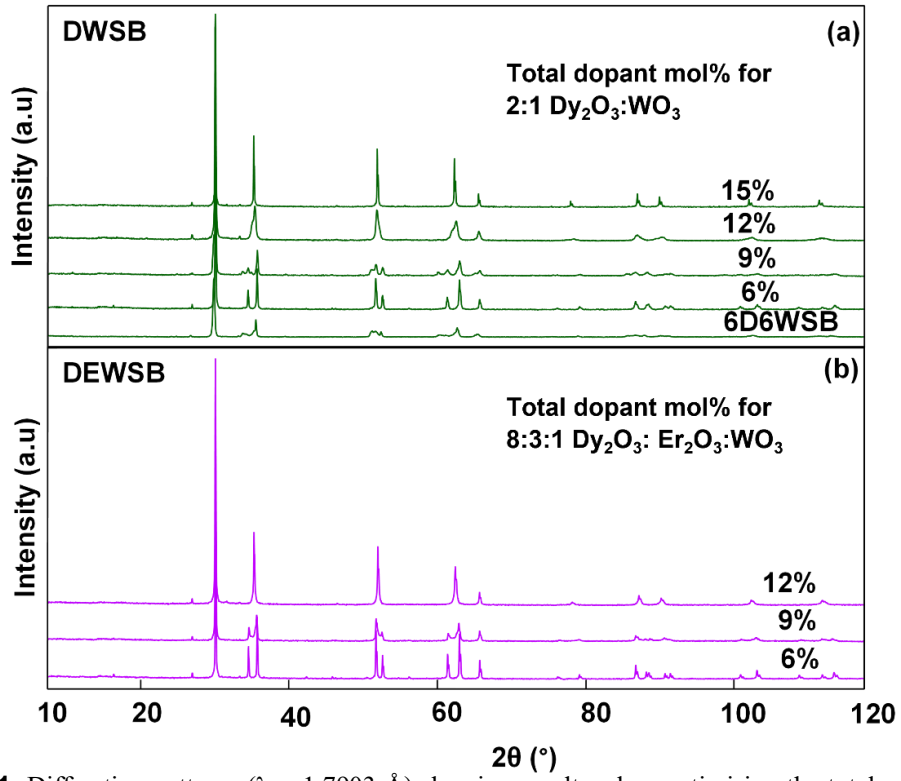

Figure 4.1. Diffraction patterns (λ = 1.7903 Å) showing results when optimising the total metal oxide dopant concentration. **(a)** The doubly substituted DWSB system employing a 2:1 ratio of Dy_2O_3:WO_3 showed the dominant δ-phase only for the 15 mol% total dopant concentration. The 6D6WSB with a 1:1 ratio clearly showed mixed phases. **(b)** The triply substituted DEWSB system needed 12 mol% total metal oxide dopant concentration for 8:3:1 Dy_2O_3:Er_2O_3:WO_3 for the δ-phase to appear dominant.

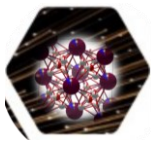

minimum total metal oxide dopant concentration needed to yield what appeared to be a pronounced δ-phase was 12 mol% (Fig. 4.1(b)). In this work the 8D4WSB material with a 12 mol% total metal oxide dopant concentration was used for comparison to establish the effect of the Er_2O_3 and triple substitution in the 8D3E1WSB system.

An interesting result arose from the initial attempts at preparing pellets for EIS measurements. This involved heating the pellets slowly to 300°C over 50 hours to remove the binder and then sintering at 820°C for a further 20 hours to densify the pellets (a total time of 70 hours) before being slowly cooled to ambient temperature. The slow heating rate at temperatures below 300°C is reported to be key for effective debinding and limiting formation of stubborn carbonaceous residues [44]. PXRD scans of the sintered pellets were taken to check whether the phase integrity was maintained. The triply substituted system effectively remained unchanged (Fig. 4.2(a)), but the doubly substituted system showed phase degradation to form a mixture of the δ-phase, a tetragonal $Bi_{4.5}W_{1.6}O_{16}$ phase (space group *I4₁/amd*) and some unknown phase (Fig. 4.2(b)). A reduction in the total sintering time of the pelletised green bodies was thus implemented. The

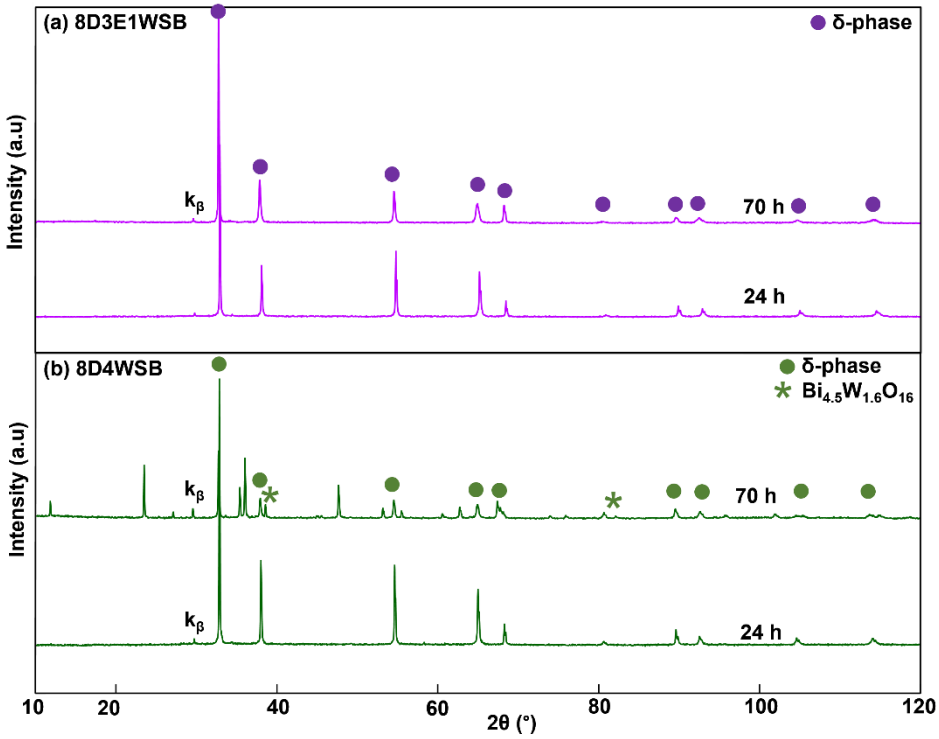

Figure 4.2. Diffraction patterns (λ = 1.7903 Å) of the pellets sintered for a total time of 70 h or 24 h for **(a)** 8D3E1WSB and **(b)** 8D4WSB. Unmarked peaks indicate unknown phases.

pellets were first heated to 300°C in 6 hours and soaked at this temperature for 4 hours to remove

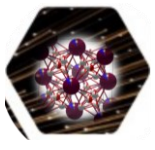

the binder. The temperature was then ramped to 820°C and the pellets were sintered at this temperature for 14 hours (a total time of 24 hours). No phase degradation was observed in either system in this case (Fig. 4.2).

These preliminary results suggested that 8D3E1WSB might possess some of the phase stability reported by Watanabe and Sekita [22] for the Bi_2O_3-Er_2O_3-WO_3 system, but with half the total substituent concentration in this case. To verify these observations, both 8D3E1WSB and 8D4WSB powders that were synthesised using the procedure described in the experimental section were further heat treated to obtain equilibrium phases and reduce impurity phases. This was done by heating the powders to 300°C in 56 hours to effectively remove organic impurities and moisture [44], soaked at this temperature for 4 hours and then annealed at 820°C for 20 hours. Pellets were fabricated (sintering for the 24-hour time period as discussed) and then further annealed at 500°C for 50 hours and 100 hours. Again 8D3E1WSB appeared to maintain its structural integrity with only minor peak broadening occurring (Fig. 4.3(a)), whereas 8D4WSB exhibited anisotropic peak broadening and peak splitting after 50 hours (Fig. 4.3(b)) with phase degradation taking place to form a mixture of the δ-phase, a tetragonal phase $Bi_{14}WO_{24}$ (space group *I*4/*m*) and an orthorhombic phase Bi_2WO_6 (space group *B*2*cb*), especially upon further annealing. This was also observed by Jung *et al.* [32] when investigating the long-term stability of bismuth oxide-based electrolytes for operation at 500°C. This highlights the stabilising effects obtained by reducing the tungsten content, incorporating Er^{3+} and by implementing triple substitution.

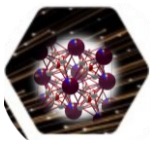

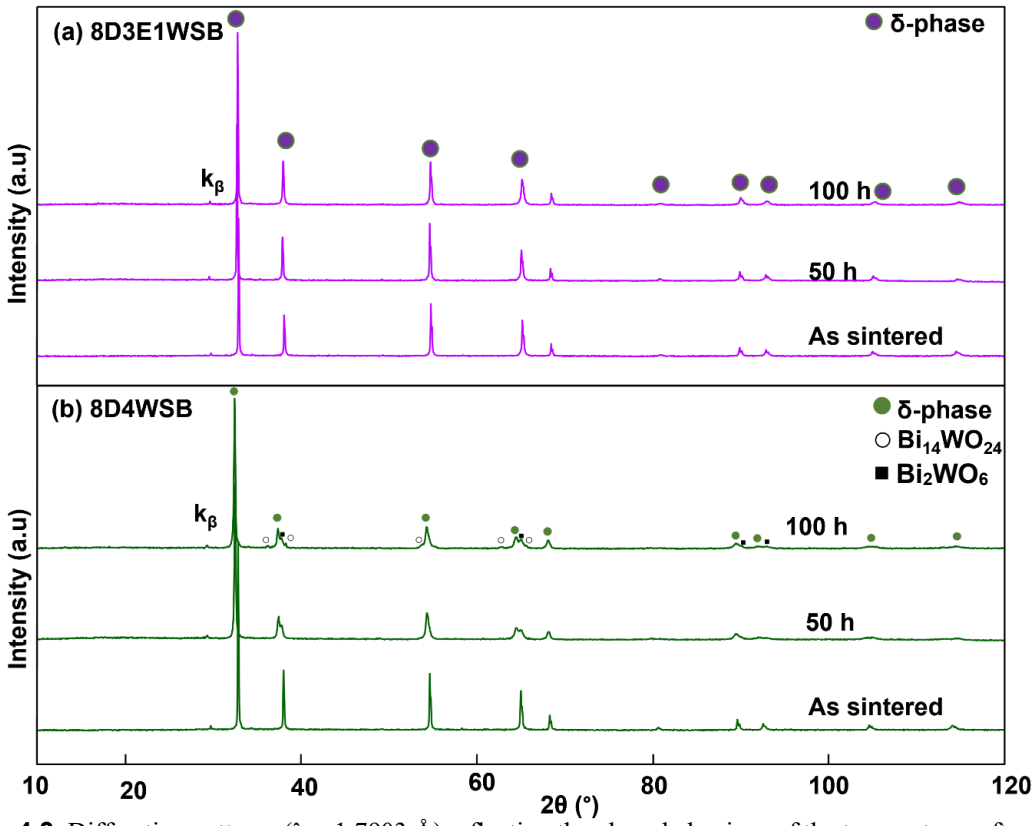

Figure 4.3. Diffraction patterns (λ = 1.7903 Å) reflecting the phase behaviour of the two systems after annealing at 500°C for 50 hours and 100 hours. **(a)** 8D3E1WSB exhibited minor peak broadening while **(b)** 8D4WSB showed anisotropic peak broadening and peak splitting characteristic of phase separation.

4.3.2 Conductivity measurements

The total conductivities for the heating and cooling cycles for both 8D3E1WSB and 8D4WSB as shown in the Arrhenius plots (Fig. 4.4) display a step up in conductivities in the 500-600°C temperature range. This was more pronounced for the triple-substituted system and is normally associated with a phase change. This was unexpected as 8D3E1WSB appeared to be the more stable material. At 700°C the total conductivities of 0.273 S cm^{-1} and 0.295 S cm^{-1} for 8D3E1WSB and 8D4WSB, respectively, were slightly lower than the value of 0.59 S cm^{-1} reported for the $(BiO_{1.5})_{0.88}$ $(DyO_{1.5})_{0.08}$ $(WO_3)_{0.04}$ system by Jung *et al*. [38]. It should be noted that in this work no electrodes were coated directly onto the pellet for the conductivity measurements. The pellet was directly placed between two solid platinum disc electrodes (with a similar diameter to the pellet) in the spring-loaded cell holder. This appears to provide less intimate contact and resulted in the slightly lower values especially during the first heating cycle, thus values for the cooling cycle are referred to here. That being said, the conductivity at 700°C is still an order of magnitude

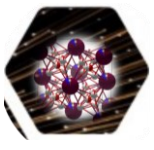

higher than that of YSZ at the same temperature [45]. The conductivities at 500°C for both 8D3E1WSB (6.69×10^{-3} S cm^{-1}, Fig. 4.4(a)) and 8D4WSB (2.60×10^{-2} S cm^{-1}, Fig. 4.4(b)) during the cooling cycle were, however, almost 1-2 orders of magnitude lower than the reported value of 9.8×10^{-2} S cm^{-1} for the $(BiO_{1.5})_{0.88}$ $(DyO_{1.5})_{0.08}$ $(WO_3)_{0.04}$ system of Jung *et al*. [38]. This is most likely due to the presence of secondary phases with more ordered oxygen sublattices as compared to the pure δ-phase at low temperatures. This will be elaborated on when looking at the variable temperature Raman spectroscopy results. The activation energy below 500°C for 8D3E1WSB and 8D4WSB were effectively the same for both heating and cooling cycles, but the ~4-5 times lower conductivity for 8D3E1WSB seems to indicate that the two systems have slightly different phases in the lower temperature range.

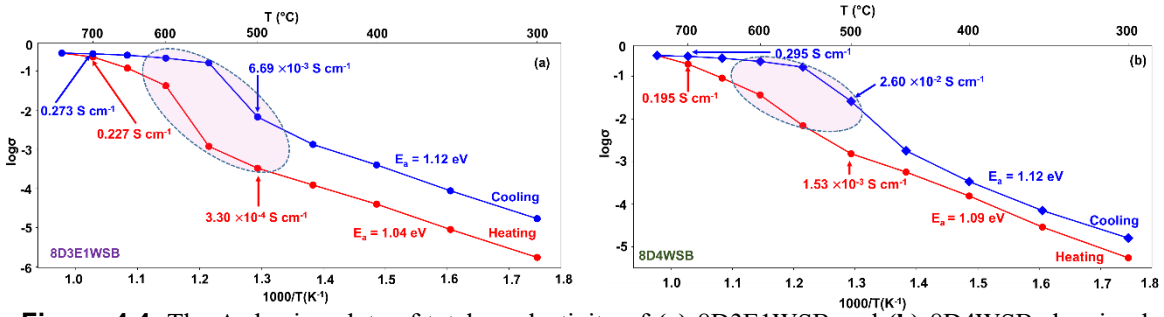

Figure 4.4. The Arrhenius plots of total conductivity of **(a)** 8D3E1WSB and **(b)** 8D4WSB showing both the heating and cooling cycles. Both systems show hysteresis on the onset of the phase transition evident from the step change at around 500-600°C as highlighted.

4.3.3 Variable temperature-PXRD and Rietveld studies

To probe the cause of the step in total conductivity, VT-PXRD was employed. From Fig. 4.5(a) and 4.5(b) for 8D3E1WSB and 8D4WSB, respectively, it is clearly seen that phase changes occur upon heating. The temperature range (around 500 to 600°C) in which the prominent phase changes occurred in the PXRD measurements corresponds to the range where the steps in conductivity were observed, providing evidence that these dramatic changes in conductivity are due to phase changes. Furthermore, the discrepancy in magnitude of the conductivity at these steps between the two solid solutions reinforces the idea that the phase transitions are different for these materials during heating. For 8D3E1WSB (Fig. 4.5(a)) a clear mixture of the tetragonal β-phase and the defect fluorite-type δ-phase becomes discernible around 500 to 600°C. For 8D4WSB (Fig. 4.5(b)) the prominent phase change involves a mixture of two tetragonal phases, $Bi_{14}WO_{24}$ and $Bi_{14}W_2O_{27}$, and the desired δ-phase.

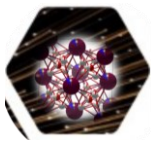

Closer inspection of the diffraction patterns for both systems at lower temperatures revealed subtle peak broadness (particularly for 8D3E1WSB) and peak asymmetry, suggesting the presence of a mixture of phases at ambient temperature already. However, looking at the ambient temperature patterns alone it was not immediately obvious.

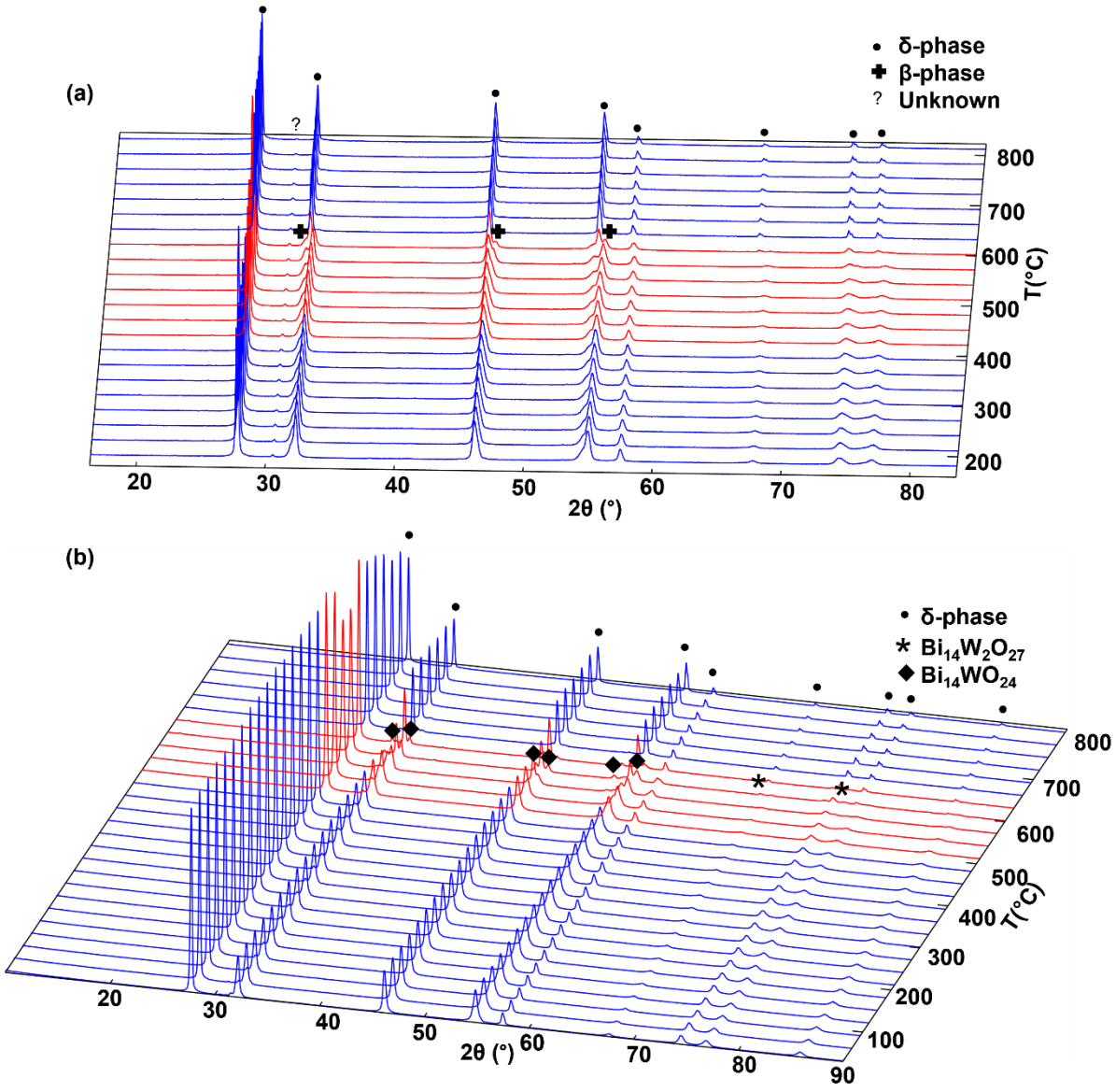

Figure 4.5. Stacked diffraction patterns (λ = 1.5419 Å) for VT-PXRD measurements of **(a)** 8D3E1WSB and **(b)** 8D4WSB showing phase changes during the heating cycle.

Rietveld refinement of the diffraction pattern for 8D4WSB at 30°C showed intensity mismatch and a poor fit when the δ-phase alone was used (Fig. 4.6(a)). The results improved when a multiphase fitting of $Bi_{14}W_2O_{27}$ and the δ-phase was done (Fig. 4.6(b)). When $Bi_{14}WO_{24}$ was

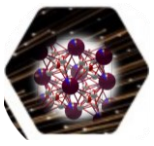

added as the third phase, however, a significantly better overall fit of the shoulder on the peak at around 31.8° 2θ was obtained as Fig 4.6(c) and Fig S4.2 (in the Supporting Information) illustrate. The refinement of these data suggested a ~51% δ-phase content of the crystalline material. It was also interesting to note the additional tungsten-containing phases had formed even with such a low tungsten content. At 750°C, the single δ-phase was enough to produce an excellent fit (Fig. 4.6(d)). This corroborated the results obtained from VT-EIS that the composition 8D4WSB consisted of a mixture of phases at temperatures less than 600°C.

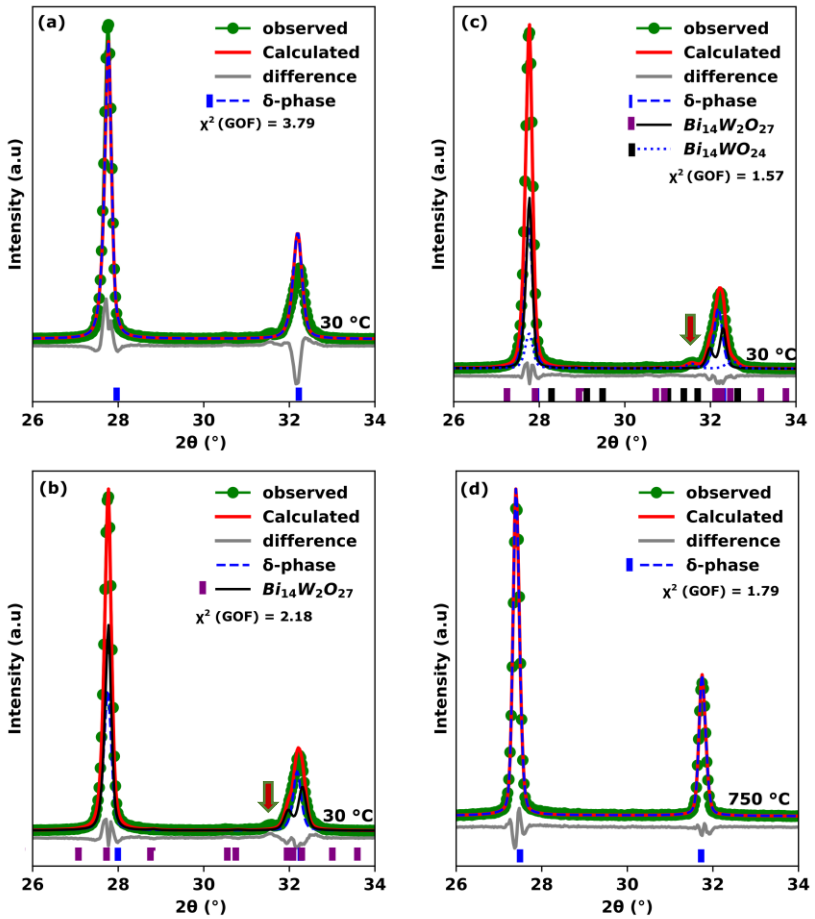

Figure 4.6. Rietveld refinements of the diffraction patterns (λ = 1.5419 Å) for 8D4WSB where the dots represent observed data, the red line shows the fit and grey line is the difference curve. This was done by incorporating **(a)** the δ-phase at 30°C, **(b)** the δ-phase and the $Bi_{14}W_2O_{27}$ phase at 30°C, **(c)** the δ-, $Bi_{14}WO_{24}$ and $Bi_{14}W_2O_{27}$ phases at 30°C and **(d)** only the δ-phase at 750°C. The red arrows show how the $Bi_{14}WO_{24}$ phase improves the fit on the peak at 31.8° 2θ.

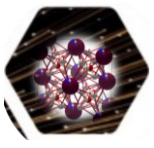

Similarly, Rietveld refinement of the diffraction pattern for 8D3E1WSB at 30°C confirmed the presence of a second phase. When only the defect fluorite-type δ-phase was used to fit the pattern at ambient temperature, a very poor fit was obtained (Fig. 4.7(a)). Incorporating the secondary β-phase for a multiphase Rietveld refinement, produced a much better overall fit (Fig. 4.7(b)) which also indicated that about 62% of the crystalline material consisted of the β-phase. A poor fit was obtained when it was attempted to incorporate $Bi_{14}WO_{24}$ as the secondary phase instead. Once again the defect fluorite-type δ-phase on its own was sufficient to give an excellent fit at high temperatures (Fig. 4.7(c)). The fact that the single δ-phase was present at high temperatures for both systems also reflects why their conductivities were so similar in this range. In the 510-600°C temperature range where the phase evolution is more pronounced, peak "reorientation" occurs for some of the peaks – shoulders become the main peaks and the main peaks become shoulders (Fig. 4.7(d)). Eventually, the new shoulders vanish at high temperatures. This is highly likely due to the dominant β-phase transitioning to the δ-phase as the temperature increases.

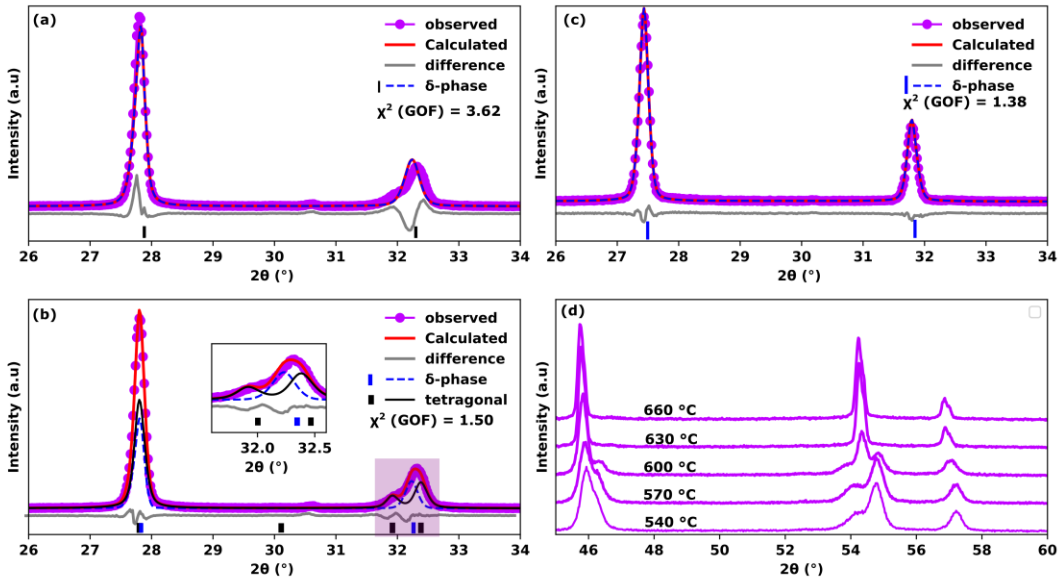

Figure 4.7. Rietveld refinements of the diffraction patterns (λ = 1.5419 Å) for 8D3E1WSB where the dots represent observed data, the red line shows the fit and grey line is the difference curve. This was done by including **(a)** the δ-phase only at 30°C, **(b)** the mixture of δ- and β-phases at 30°C and **(c)** the single δ-phase at 810°C. **(d)** An enlarged view depicting how the shoulders transform to become the main peaks.

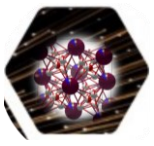

As further evidence, Fig. 4.8 shows the diffraction pattern for the tetragonal β-phase that was obtained during the synthesis process after the gel was merely calcined at 500°C for 8D3E1WSB. Once the sample was annealed at 750°C, in the mixture the β- and δ-phases are present. Comparing these two patterns illustrates how the peak asymmetry arises when the δ-phase starts forming.

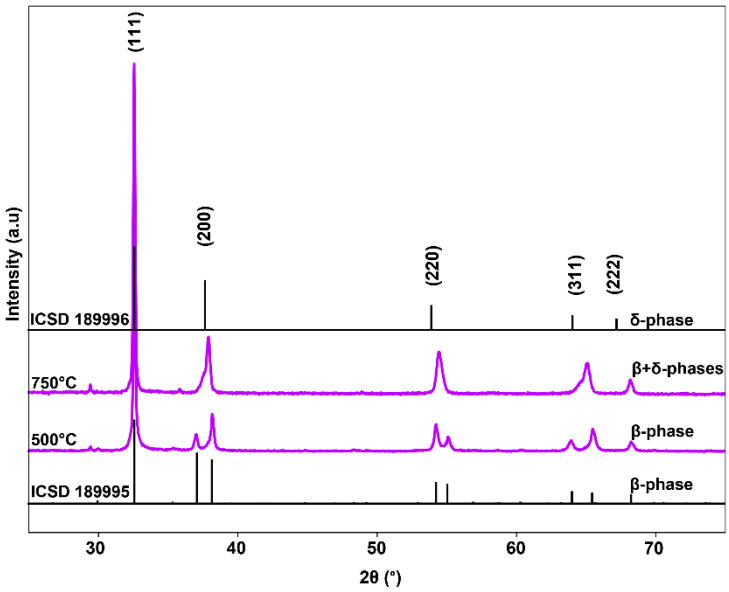

Figure 4.8. Comparison of diffraction patterns (λ = 1.7903 Å) for the tetragonal β-phase obtained from the 8D3E1WSB sample calcined at 500°C and then after further annealing at 750°C a mixture of the β and δ phases results. ICSD 189995 and 189996 are the collection codes of the β- and δ-phases from the Inorganic Crystal structure Database (ICSD).

During the VT-PXRD cooling run for 8D3E1WSB, the observed change in the diffraction patterns were less dramatic with only anisotropic peak broadening being noticeable from around 510°C (Fig. 4.9). The (111) and (222) peaks, showed no broadening but instead the intensities of these peaks increased. This indicates an almost complete overlap of these peaks for the δ- and β-phases as was clearly illustrated by the Rietveld analysis in Fig. 4.7(b) and Fig. S4.1 in the Supporting Information. Additionally, Fig. 4.8 shows all peaks of the tetragonal β-phase split into two except for those coinciding with the peaks indexed as (111) and (222) in the δ-phase. It is suspected that the observed anisotropic peak broadening at 510°C (Fig. 4.9), might be due to distortions caused by phase separation of the δ- and β-phases. Verkerk *et al*. [36] also observed anisotropic peak broadening when using a high-temperature Guinier camera during a heating run for the Bi_2O_3-Er_2O_3 system. Unfortunately, the resolution of the conventional diffractometers used was too low

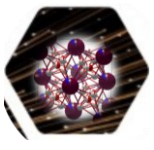

to resolve the peaks from the different phases, but from examining the overall stacked plot it is clear that a mixture of phases form upon cooling again.

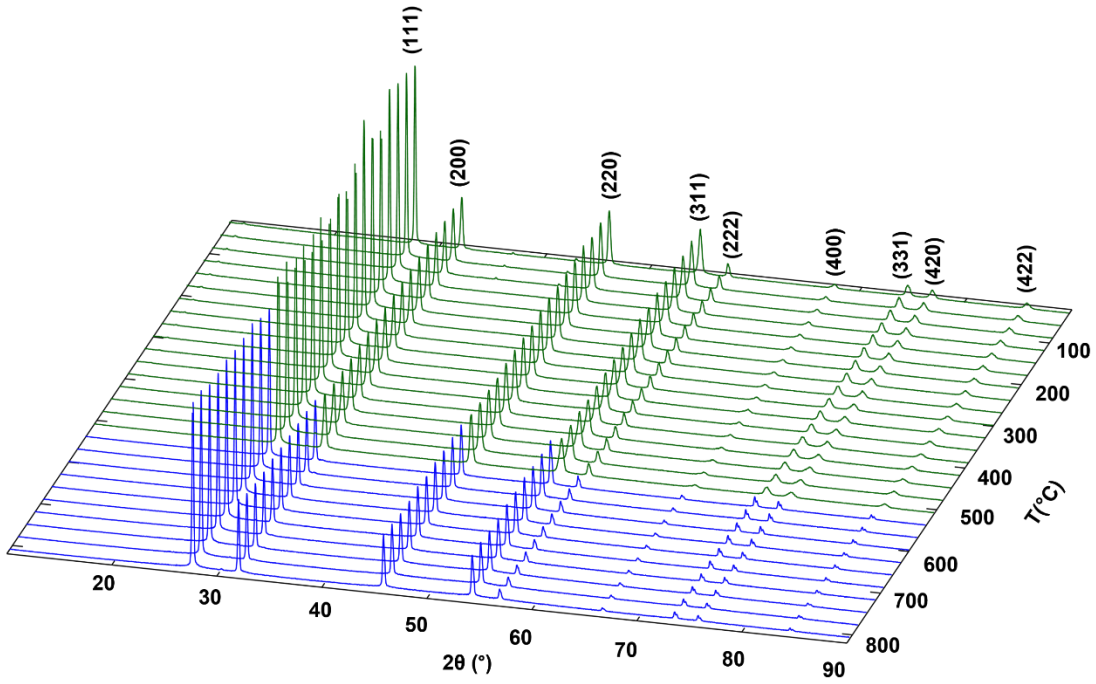

Figure 4.9. Stacked diffraction patterns (λ = 1.5419 Å) for VT-PXRD measurements of 8D3E1WSB showing anisotropic peak broadening from 510°C during the cooling cycle. All peaks exhibited broadening except those with Miller indices (111) and (222). Green colour indicates onset of anisotropic peak broadening. Indexing only applies to the pure δ-phase above 510°C.

The delayed peak broadening which appears from ~510°C also coincides with the delayed step decrease in conductivity in the Arrhenius plot during the cooling cycle (Fig. 4.4(a)), thereby again confirming a phase change. This hysteresis, with higher conductivities for the cooling cycle in the temperature range 600-550°C, which denotes the δ- to β-phase transition during cooling here, is an occurrence also normally observed during the δ-Bi_2O_3 transition to the β-Bi_2O_3 [13].

4.3.4 Raman spectroscopy

To further investigate the structure and cause for the conductivity behaviour observed, Raman spectroscopy (RS) was used. Unlike conventional XRD which looks at the average structure, RS probes the local structure and is very sensitive to a mixture of phases. Factor group theory predicts one Raman active band for an ideal fluorite structure, the T_{2g} band from the M-O-M vibrations (with the oxygen in the 8*c* sites). One Raman band for a defect fluorite-type structure of substituted

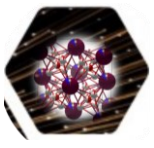

and unsubstituted bismuth oxide has been reported before. For example, Lee *et al*. [46] observed a single peak at 600 cm^{-1} for erbia substituted bismuth oxide in a ratio of 4:1 B_2O_3:Er_2O_3 for the defect fluorite-type δ-phase when using an excitation line of 532 nm. The band below 200 cm^{-1} wavenumbers is attributed to external lattice vibrations. [47]

The spectra for both the doubly and triply substituted systems exhibited Raman bands additional to that for the defect fluorite-type δ-phase at lower temperatures as shown in Fig. 4.10. This reinforces the idea that there is a mixture of phases and that the cubic phase was not truly stabilized at ambient temperature. As a check, it was found that similar results were obtained whether using the citrate-gel method or the ceramic method to synthesise the material.

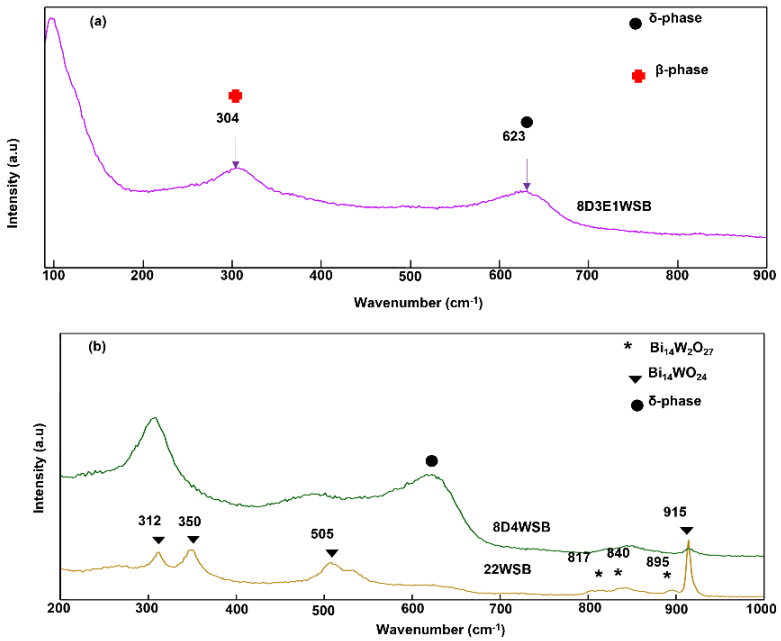

Figure 4.10. Raman spectra of **(a)** 8D3E1WSB at 170°C and **(b)** 8D4WSB and 22WSB at 22°C. Intensities from 22WSB were doubled to enhance features.

Hardcastle and Wachs [48] observed peaks at 124 cm^{-1}, 311 cm^{-1} and 462 cm^{-1} for the β-phase using the same excitation line of 514.5 nm as in this work. Thus the peak at 304 cm^{-1} for 8D3E1WSB (Fig. 4.10(a)) seems to indicate that the β-phase is present. The very low intensity peaks at ~124 cm^{-1} (which appears as a shoulder on the band below 200 cm^{-1}) and ~462 cm^{-1} for the β-phase could not be resolved here. The spectrum at 170°C is shown since at ambient temperatures the spectrum was dominated by photoluminescence from Er. This may also have caused the lower intensities for the ~124 cm^{-1} and ~462 cm^{-1} bands, together with the loss in intensity at higher temperature.

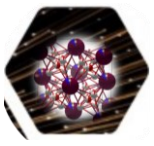

To identify the additional phases present in 8D4WSB, the spectrum was compared to that obtained for the $(Bi_2O_3)_{0.78}(WO_3)_{0.22}$ (22WSB) system (Fig. 4.10(b)). The 22WSB system consisted of a mixture of $Bi_{14}WO_{24}$ and $Bi_{14}W_2O_{27}$ which was verified using XRD and RS results obtained by Hardcastle and Wachs [48]. Most of the bands observed coincided with those from the $Bi_{14}WO_{24}$ and $Bi_{14}W_2O_{27}$ phases exhibiting wave shifts at 914 cm^{-1}, 840 cm^{-1}, 505 cm^{-1} and 305 cm^{-1}. These results agree well with those obtained using VT-PXRD and would explain the lower conductivity at lower temperatures since these two phases are reported to have a relatively ordered oxygen sublattice compared to the δ-phase.

As for VT-PXRD and VT-EIS results, phase changes were also observed from VT-RS spectra as Fig. 4.11 illustrates. By 680°C, the spectra of the two systems were similar, showing the presence of the pure δ-phase. For the spectra measured at 570°C for 8D3E1WSB and 510°C for 8D4WSB, bands for the secondary phases were still present, but were far less intense relative to the band at ~620 cm^{-1}. This supports the temperature ranges in which the phase transitions occurred as

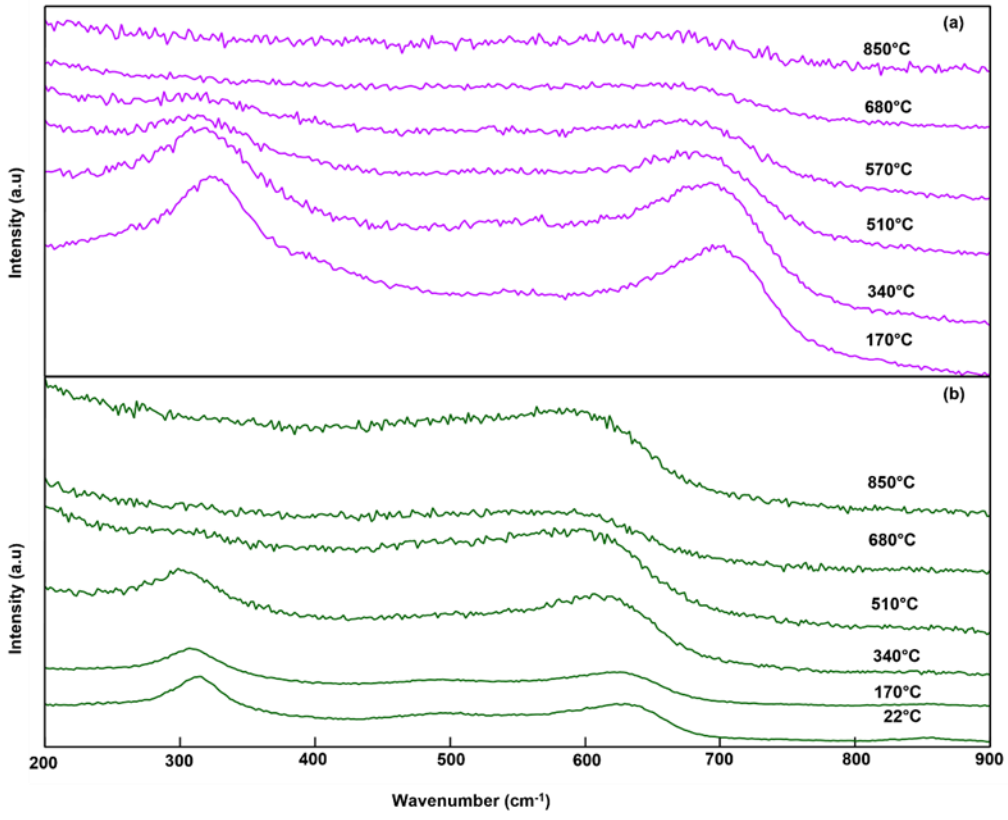

Figure 4.11. VT-Raman spectra of **(a)** 8D3E1WSB and **(b)** 8D4WSB. Intensities above 170°C were increased by a factor of five to enhance features in both systems.

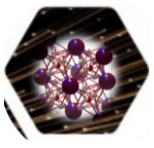

determined by VT-PXRD and inferred from VT-EIS measurements. The fact that both systems comprised a pure δ-phase at high temperatures would also explain why the two systems have almost the same conductivity at 750°C (Fig. 4.4). 8D4WSB and 8D3E1WSB have different phases at low temperatures. 8D4WSB has the δ-phase and $7Bi_2O_3$-$2WO_3$ as one of the phases at low temperatures (Table S4.2) while 8D3E1WSB has the β-phase as the predominant phase (Table S4.1). $7Bi_2O_3$-$2WO_3$ is more conductive (~0.1 S cm^{-1} at 500°C) [28] than the β-phase at low temperatures (~0.0001 S cm^{-1} at 500°C) [13], this explains the significant difference in conductivities at low temperatures between the two compositions.

4.4 Conclusion

Two Bi_2O_3 systems substituted with 12% total metal oxides were synthesised and characterised in this work. The $(Bi_2O_3)_{0.88}(Dy_2O_3)_{0.08}$ $(WO_3)_{0.04}$ (8D4WSB) system, comprised a mixture of phases at room temperature, namely, $Bi_{14}WO_{24}$, $Bi_{14}W_2O_{27}$ and the δ-phases. The triple substituted $(Bi_2O_3)_{0.88}(Dy_2O_3)_{0.08}(Er_2O_3)_{0.03}(WO_3)_{0.01}$ (8D3E1WSB) system consisted of a mixture of the δ- and β-phases at ambient temperature. Both materials converted fully to the δ-phase above 600°C. The conductivity of the two materials were comparable from 600°C, but at lower temperatures the conductivity for 8D4WSB was almost four times higher than that for 8D3E1WSB. Pellets of the materials annealed at 500°C for up to 100 hours showed far more degradation for 8D4WSB than for 8D3E1WSB. Thus at 500°C there is a trade-off between stability and conductivity. This also indicates that combining metal oxide dopants displaying various properties does produce materials with improved properties thereby supporting the further investigation of triple substituted materials. Increasing the total metal oxide dopant concentration to ~15% may produce more phase pure materials, however, and the effect of the ratio of the substituents on the stability and conductivity need further investigation.

What was evident from this work was the wealth of information revealed by the variable temperature studies of the materials, be it PXRD, RS or EIS, and further with the combination of these techniques, each different in the physics they employ, complementing each other. It also highlighted that simply confirming phases by peak positions in XRD is far from adequate. The phase evolution, as initially hinted by the VT-EIS data, only became obvious from the VT-XRD

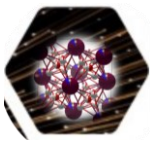

data which resulted in more rigorous analysis of the lower temperature data using Rietveld refinement and with phase confirmation coming from RS.

4.5 Acknowledgements

The authors acknowledge financial support for their research from the National Research Foundation (NRF, South Africa) and Department of Science and Innovation (DSI, South Africa), as well as the University of the Witwatersrand. S.M. Masina also acknowledges the ICDD for a Ludo Frevel scholarship.

4.6 References

[1] Stambouli, A.B. and Traversa, E., 2002. Solid oxide fuel cells (SOFCs): a review of an environmentally clean and efficient source of energy. *Renewable and Sustainable Energy Reviews*, *6*(5), pp.433-455.

[2] Ormerod, R.M., 2003. Solid oxide fuel cells. *Chemical Society Reviews*, *32*(1), pp.17-28.

[3] Huang, K. and Goodenough, J.B., 2009. *Solid oxide fuel cell technology: principles, performance and operations*. Woodhead Publishing Limited, Cambridge.

[4] Singhal, S.C., 2000. Science and technology of solid-oxide fuel cells. *MRS Bulletin*, *25*(3), pp.16-21.

[5] Kim, N. and Grey, C.P., 2002. Probing oxygen motion in disordered anionic conductors with ^{17}O and ^{51}V MAS NMR spectroscopy. *Science*, *297*(5585), pp.1317-1320.

[6] Fergus, J.W., 2006. Electrolytes for solid oxide fuel cells. *Journal of Power Sources*, *162*(1), pp.30-40.

[7] Brandon, N.P., Skinner, S. and Steele, B.C., 2003. Recent advances in materials for fuel cells. *Annual Review of Materials Research*, *33*(1), pp.183-213.

[8] Tsoga, A., Gupta, A., Naoumidis, A. and Nikolopoulos, P., 2000. Gadolinia-doped ceria and yttria stabilized zirconia interfaces: regarding their application for SOFC technology. *Acta Materialia*, *48*(18-19), pp.4709-4714.

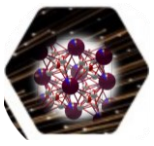

[9] Marina, O.A., Bagger, C., Primdahl, S. and Mogensen, M., 1999. A solid oxide fuel cell with a gadolinia doped ceria anode: preparation and performance. *Solid State Ionics*, *123*(1-4), pp.199-208.

[10] Atkinson, A., 1997. Chemically-induced stresses in gadolinium-doped ceria solid oxide fuel cell electrolytes. *Solid State Ionics*, *95*(3-4), pp.249-258.

[11] Fuentes, R.O. and Baker, R.T., 2008. Synthesis and properties of Gadolinium-doped ceria solid solutions for IT-SOFC electrolytes. *International Journal of Hydrogen Energy*, *33*(13), pp.3480-3484.

[12] Takahashi, T., Iwahara, H. and Nagai, Y., 1972. High oxide ion conduction in sintered Bi_2O_3 containing SrO, CaO or La_2O_3. *Journal of Applied Electrochemistry*, *2*(2), pp.97-104.

[13] Harwig, H.A. and Gerards, A.G., 1978. Electrical properties of the α, β, γ, and δ phases of bismuth sesquioxide. *Journal of Solid State Chemistry*, *26*(3), pp.265-274.

[14] Takahashi, T. and Iwahara, H., 1978. Oxide ion conductors based on bismuth sesquioxide. *Materials Research Bulletin*, *13*(12), pp.1447-1453.

[15] Gambino, M., Giannici, F., Longo, A., Di Tommaso, S., Labat, F. and Martorana, A., 2015. Dopant clusterization and oxygen coordination in Ta-doped bismuth oxide: A structural and computational insight into the mechanism of anion conduction. *The Journal of Physical Chemistry C*, *119*(47), pp.26367-26373.

[16] Shuk, P., Wiemhöfer, H.D., Guth, U., Göpel, W. and Greenblatt, M., 1996. Oxide ion conducting solid electrolytes based on Bi_2O_3. *Solid State Ionics*, *89*(3-4), pp.179-196.

[17] Rao, C.R., Rao, G.S. and Ramdas, S., 1969. Phase transformations and electrical properties of bismuth sesquioxide. *The Journal of Physical Chemistry*, *73*(3), pp.672-675.

[18] Jung, D.W., Duncan, K.L. and Wachsman, E.D., 2010. Effect of total substituent concentration and dopant ratio on conductivity of $(DyO_{1.5})_x$–$(WO_3)_y$–$(BiO_{1.5})_{1-x-y}$. *Acta Materialia*, *58*(2), pp.355-363.

[19] Azad, A.M., Larose, S. and Akbar, S.A., 1994. Bismuth oxide-based solid electrolytes for fuel cells. *Journal of Materials Science*, *29*(16), pp.4135-4151.

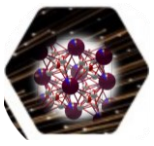

[20] Drache, M., Roussel, P. and Wignacourt, J.P., 2007. Structures and oxide mobility in Bi− Ln− O materials: heritage of Bi_2O_3. *Chemical Reviews*, *107*(1), pp.80-96.

[21] Jiang, N., Wachsman, E.D. and Jung, S.H., 2002. A higher conductivity Bi_2O_3-based electrolyte. *Solid State Ionics*, *150*(3-4), pp.347-353.

[22] Watanabe, A. and Sekita, M., 2005. Stabilized δ-Bi_2O_3 phase in the system Bi_2O_3–Er_2O_3–WO_3 and its oxide-ion conduction. *Solid State Ionics*, *176*(31-34), pp.2429-2433.

[23] Mercurio, D., El Farissi, M., Frit, B., Reau, J.M. and Senegas, J., 1990. Fast ionic conduction in new oxide materials of the Bi_2O_3–Ln_2O_3–TeO_2 systems (Ln= La, Sm, Gd, Er). *Solid State Ionics*, *39*(3-4), pp.297-304.

[24] Portefaix, N., Conflant, P., Boivin, J.C., Wignacourt, J.P. and Drache, M., 1997. New Bi–Ln–V–O Anionic Conductors with δ-Bi_2O_3 Fluorite-Type Structure (Ln= Y, Sm, Eu, Gd, Tb, Dy, Er, Yb). *Journal of Solid State Chemistry*, *134*(2), pp.219-226.

[25] Shitara, K., Moriasa, T., Sumitani, A., Seko, A., Hayashi, H., Koyama, Y., Huang, R., Han, D., Moriwake, H. and Tanaka, I., 2017. First-principles selection of solute elements for Er-stabilized Bi_2O_3 oxide-ion conductor with improved long-term stability at moderate temperatures. *Chemistry of Materials*, *29*(8), pp.3763-3768.

[26] Bandyopadhyay, S. and Dutta, A., 2018. A structural insight into the electrical properties of Dy-Ho co-doped phase stabilized Bismuth Oxide based electrolytes. *Journal of Electroanalytical Chemistry*, *817*, pp.55-64.

[27] Kharton, V.V., Marques, F.M.B. and Atkinson, A., 2004. Transport properties of solid oxide electrolyte ceramics: a brief review. *Solid State Ionics*, *174*(1-4), pp.135-149.

[28] Borowska-Centkowska, A., Leszczynska, M., Krok, F., Malys, M., Wrobel, W., Hull, S. and Abrahams, I., 2018. Local structure and conductivity behaviour in $Bi_7WO_{13.5}$. *Journal of Materials Chemistry A*, *6*(13), pp.5407-5418.

[29] Laarif, A. and Theobald, F., 1986. The lone pair concept and the conductivity of bismuth oxides Bi_2O_3. *Solid State Ionics*, *21*(3), pp.183-193.

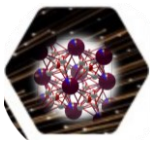

[30] Boyapati, S., Wachsman, E.D. and Jiang, N., 2001. Effect of oxygen sublattice ordering on interstitial transport mechanism and conductivity activation energies in phase-stabilized cubic bismuth oxides. *Solid State Ionics*, *140*(1-2), pp.149-160.

[31] Fung, K.Z., Chen, J. and Virkar, A.V., 1993. Effect of Aliovalent Dopants on the Kinetics of Phase Transformation and Ordering in RE_2O_3-Bi_2O_3 (RE= Yb, Er, Y, or Dy) Solid Solutions. *Journal of the American Ceramic Society*, *76*(10), pp.2403-2418.

[32] Jung, D.W., Nino, J.C., Duncan, K.L., Bishop, S.R. and Wachsman, E.D., 2010. Enhanced long-term stability of bismuth oxide-based electrolytes for operation at 500 °C. *Ionics*, *16*(2), pp.97-103.

[33] Jiang, N., Buchanan, R.M., Henn, F.E.G., Marshall, A.F., Stevenson, D.A. and Wachsman, E.D., 1994. Aging phenomenon of stabilized bismuth oxides. *Materials Research Bulletin*, *29*(3), pp.247-254.

[34] Jiang, N. and Wachsman, E.D., 1999. Structural stability and conductivity of phase-stabilized cubic bismuth oxides. *Journal of the American Ceramic Society*, *82*(11), pp.3057-3064.

[35] Takahashi, T. and Iwahara, H., 1973. High oxide ion conduction in sintered oxides of the system Bi_2O_3-WO_3. *Journal of Applied Electrochemistry*, *3*(1), pp.65-72.

[36] Verkerk, M.J., Keizer, K. and Burggraaf, A.J., 1980. High oxygen ion conduction in sintered oxides of the Bi_2O_3-Er_2O_3 system. *Journal of Applied Electrochemistry*, *10*(1), pp.81-90.

[37] Verkerk, M.J. and Burggraaf, A.J., 1981. High Oxygen Ion Conduction in Sintered Oxides of the Bi_2O_3-Dy_2O_3 System. *Journal of the Electrochemical Society*, *128*(1), pp.75-82.

[38] Jung, D.W., Duncan, K.L., Camaratta, M.A., Lee, K.T., Nino, J.C. and Wachsman, E.D., 2010. Effect of Annealing Temperature and Dopant Concentration on the Conductivity Behavior in $(DyO_{1.5})_x$–$(WO_3)_y$–$(BiO_{1.5})_{1-x-y}$. *Journal of the American Ceramic Society*, *93*(5), pp.1384-1391.

[39] Gražulis, S., Chateigner, D., Downs, R.T., Yokochi, A.F.T., Quirós, M., Lutterotti, L., Manakova, E., Butkus, J., Moeck, P. and Le Bail, A., 2009. Crystallography Open Database–an

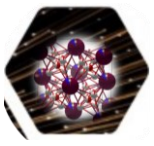

open-access collection of crystal structures. *Journal of Applied Crystallography*, 42(4), pp.726-729.

[40] A. Coelho, "Topas Academic v6," Coelho Software, Brisbane, Australia, 2016.

[41] G. Bergerhoff, I.D. Brown, in *Crystallographic databases*, ed. by F. G. Allen, R. Bergerhoff, Sievers (International Union of Crystallography, Chester, 1987), pp. 77–95

[42] Jiang, N., Wachsman, E.D. and Jung, S.H., 2002. A higher conductivity Bi_2O_3-based electrolyte. *Solid State Ionics,* 150(3-4), pp.347-353.

[43] Jung, H.J. and Chung, S.Y., 2017. Absence of distinctively high grain-boundary impedance in polycrystalline cubic bismuth oxide. *Journal of the Korean Ceramic Society*, 54(5), pp.413-421.

[44] Boch, P. and Niepce, J.C. eds., 2007. *Ceramic Materials: Processes, Properties, and Applications*. ISTE, Newport Beach, pp.183-187.

[45] Wachsman, E.D. and Lee, K.T., 2011. Lowering the temperature of solid oxide fuel cells. *Science*, *334*(6058), pp.935-939.

[46] Lee, K.T., Lidie, A.A., Jeon, S.Y., Hitz, G.T., Song, S.J. and Wachsman, E.D., 2013. Highly functional nano-scale stabilized bismuth oxides via reverse strike co-precipitation for solid oxide fuel cells. *Journal of Materials Chemistry A*, *1*(20), pp.6199-6207.

[47] Hardcastle, F.D. and Wachs, I.E., 1992. The molecular structure of bismuth oxide by Raman spectroscopy. *Journal of Solid State Chemistry*, 97(2), pp.319-331.

[48] Hardcastle, F.D. and Wachs, I.E., 1995. Raman spectroscopy of bismuth tungstates. *Journal of Raman Spectroscopy*, *26*(6), pp.407-412.

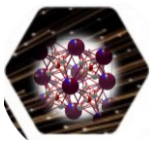

4.7 Supporting Information

A Temperature Dependent Phase Evolution Study of a Quaternary Bi_2O_3 Solid Electrolyte

Sikhumbuzo M. Masina[a], Caren Billing[a,c*], Rudolph M. Erasmus[b,c], David G. Billing[a,c]

[a]Molecular Science Institute, School of Chemistry, University of the Witwatersrand, Private Bag X3, Johannesburg, 2050, South Africa

[b]Material Physics Research Institute, School of Physics, University of the Witwatersrand, Private Bag X3, Johannesburg, 2050, South Africa.

[c]DST-NRF Centre of Excellence in Strong Materials, University of the Witwatersrand, Private Bag X3, Johannesburg, 2050, South Africa.

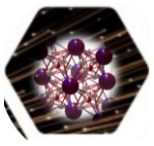

4.7.1 Diffraction Data

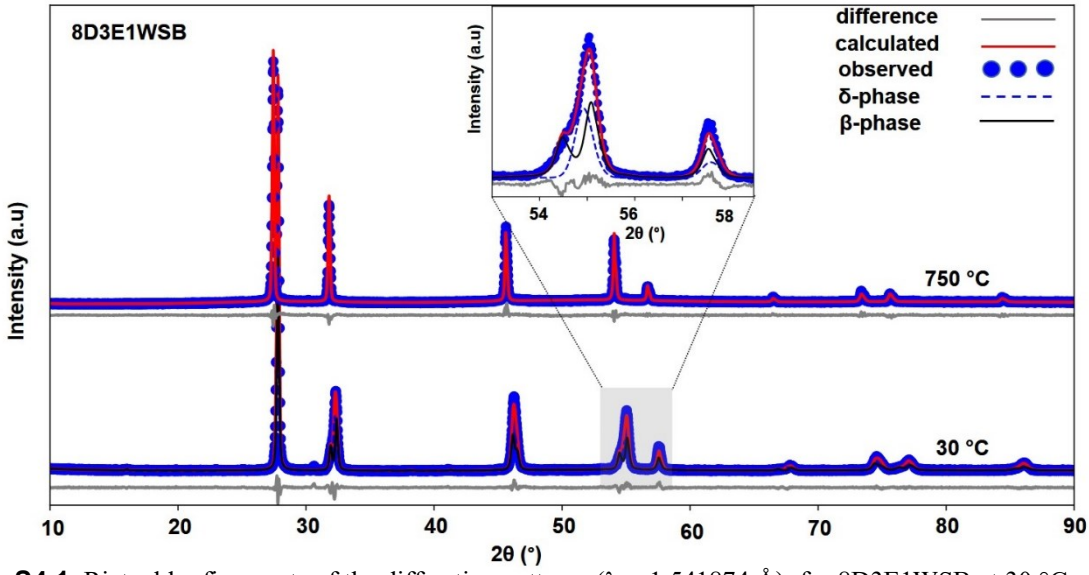

Figure S4.1. Rietveld refinements of the diffraction patterns (λ = 1.541874 Å) for 8D3E1WSB at 30 °C and 810 °C. The insert illustrates how the individual phases contribute to the anisotropic peak broadening observed at 30 °C and reinforce the idea that even at ambient temperature there is a mixture of phases.

Table S4.1. Crystallographic data for 8D3E1WSB. The R-factors obtained from Rietveld Refinement were: Rwp = 10.05%, Rexp = 6.70% and GOF = 1.50 at 30°C; Rwp = 9.81 %, Rexp = 7.10 % and GOF = 1.38 at 810°C.

Phases	δ-phase (30°C)	β-phase (30°C)	δ-phase (810°C)
R-Bragg	2.64	1.97	3.38
Weight %	40 (1)	60(1)	100
Space group	*Fm*-3*m*	*P*-42$_1$*c*	*Fm*-3*m*
a /Å	5.528(31)	7.790(64)	5.616(20)
c /Å	-	5.586(50)	-
Cell volume /Å^3	168.9(28)	338.9(63)	177.1(19)
Crystal density /g.cm^{-3}	9.05(15)	8.97(17)	8.542(92)

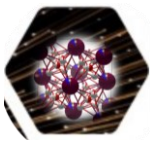

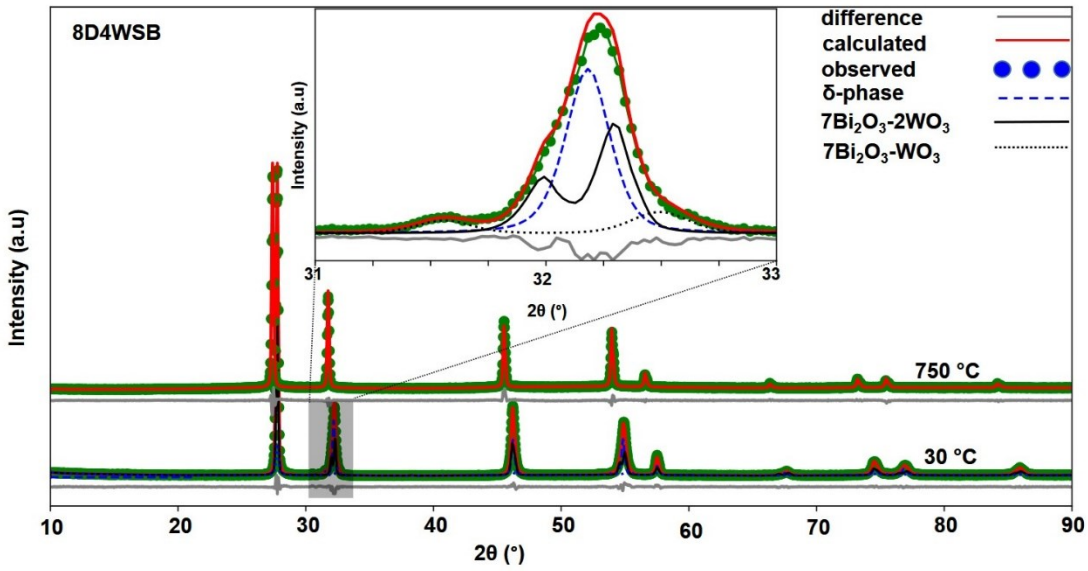

Figure S4.2. Rietveld refinements of the diffraction patterns (λ = 1.541874 Å) for 8D4WSB at 30 °C and 750 °C. The insert illustrates the deconvolution of the calculated pattern into individual phases and how they contribute to the anisotropic peak broadening and shoulders observed.

Table S4.2. Crystallographic data for 8D4WSB. The R-factors obtained from Rietveld Refinement were: Rwp = 6.98%, Rexp = 4.44% and GOF = 1.57 at 30°C; Rwp = 8.28%, Rexp = 4.63% and GOF = 1.79 at 750°C.

Phases	δ-phase (30°C)	$7Bi_2O_3$-$2WO_3$ (30°C)	$7Bi_2O_3$-WO_3 (30°C)	δ-phase (750°C)
R-Bragg	2.43	2.78	2.32	3.44
Weight %	51(1)	41(2)	8(1)	100
Space group	*Fm*-3*m*	*I*41	*I*4/*m*	*Fm*-3*m*
a /Å	5.535(30)	12.336(93)	8.67 (15)	5.626(35)
c /Å	-	11.137(93)	16.92(31)	-
Cell volume /$Å^3$	169.5(28)	1694.9(11)	1271.7(5)	178.1(33)
Crystal density /$g.cm^{-3}$	8.92(15)	9.10 (16)	9.12(36)	8.49(16)

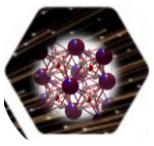

4.7.2 Electrochemical Impedance Data

In the equivalent circuits, R represents a resistor, the Q element represents a real capacitor and W represents Warburg diffusion.

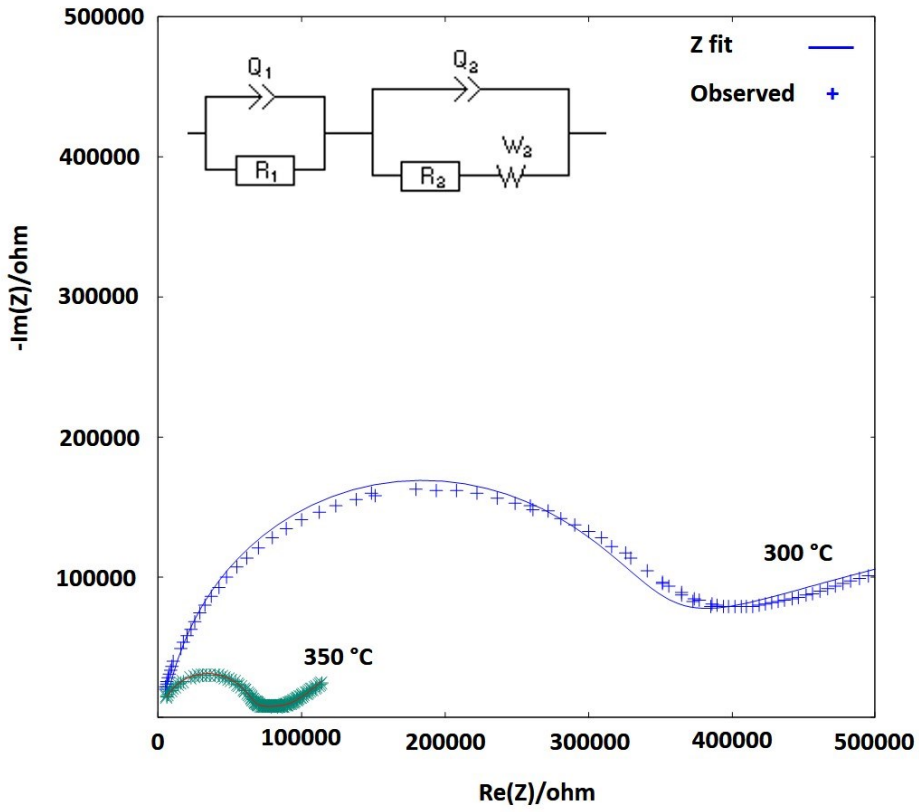

Figure S4.3. Nyquist plots of 8D3E1WSB during a heating cycle between 300 and 350 °C.

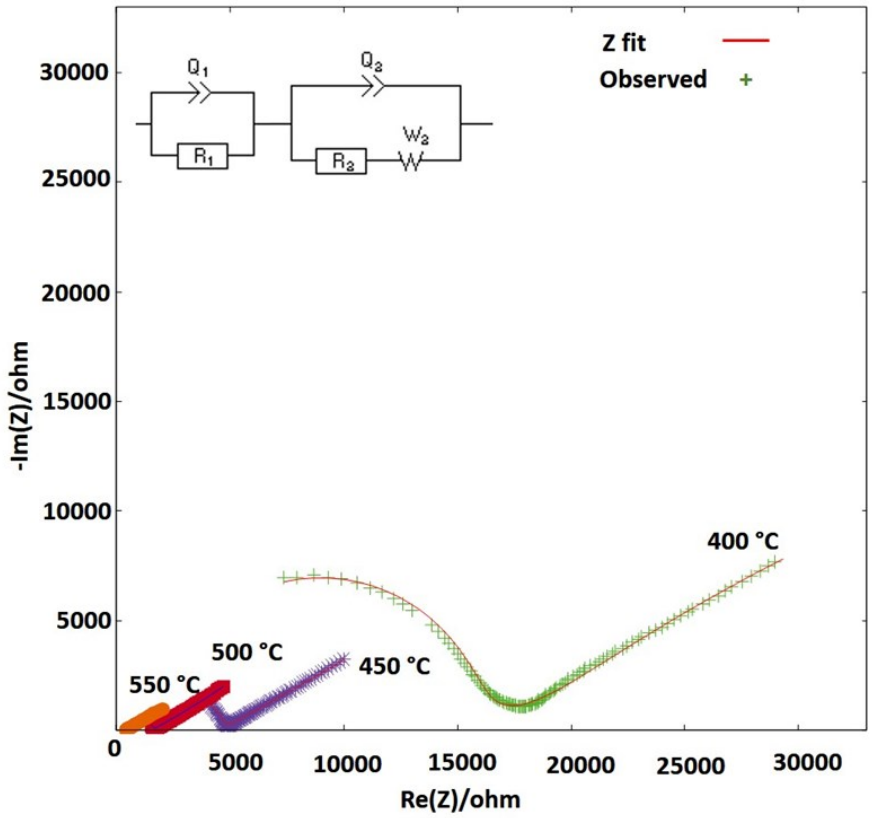

Figure S4.4. Nyquist plots of 8D3E1WSB during a heating cycle between 400 and 550 °C

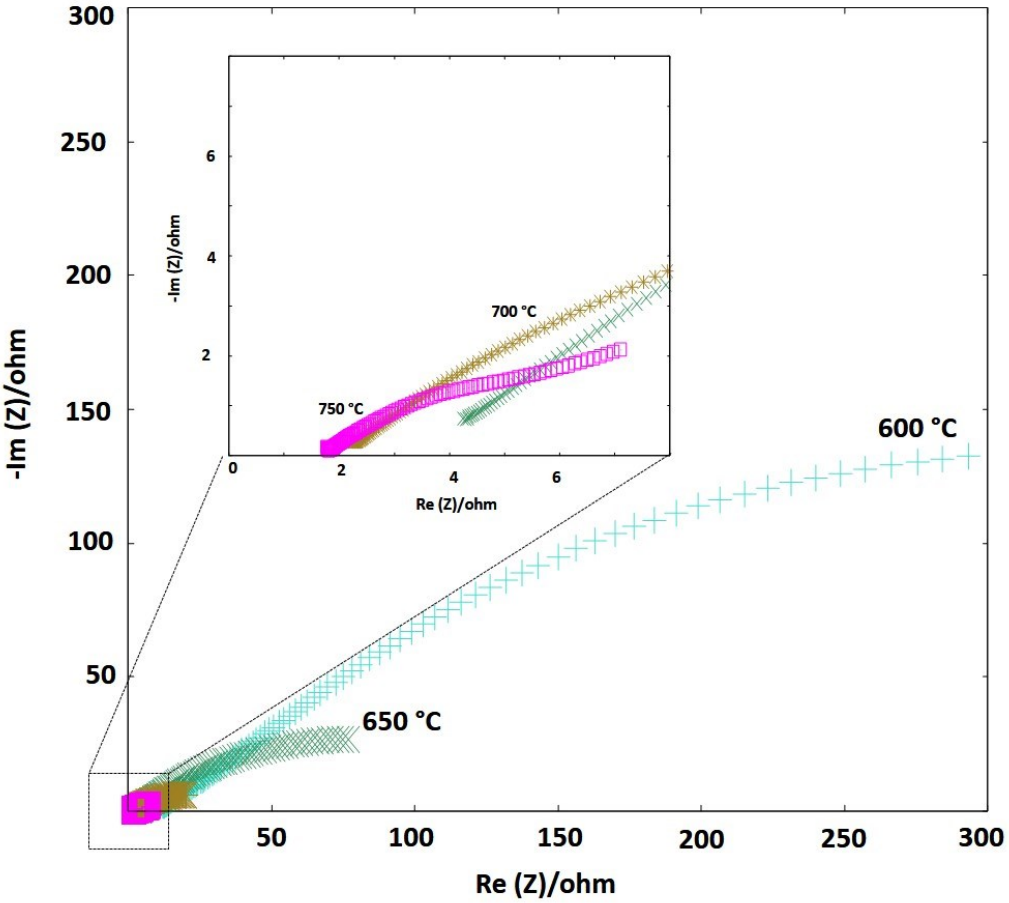

Figure S4.5. Nyquist plots of 8D3E1WSB during a heating cycle between 600 and 750 °C.

Table S4.3. VT-EIS data for 8D3E1WSB on both heating and cooling cycles from 300 to 500 °C.

Temperature /°C Heating	300	350	400	450	500
R1 /Ω	290922	56371	12710	4133	1540
Q1 /F.s$^{(a1-1)}$	13.08 x 10^{-12}	12.13 x 10^{-12}	15.80 x 10^{-12}	13.34 x 10^{-12}	14.65 x 10^{-12}
a1	0.930	0.820	0.990	0.844	0.980
R2 /Ω	977803	42505	10134	2680	5156
Q2 /F.s$^{(a2-1)}$	0.218 x 10^{-6}	0.568 x 10^{-6}	13.88 x 10^{-6}	38.24 x 10^{-6}	59.11 x 10^{-6}
a2	0.367	0.387	0.196	0.257	0.341
s2 /Ω.s$^{-0.5}$	1.551 x 10^{6}	2.227 x 10^{5}	1.912 x 10^{5}	1.343 x 10^{5}	2.085x 10^{5}
Temperature /°C Cooling	500	450	400	350	300
R1 /Ω	76	382	1268	5805	29871
Q1 /F.s$^{(a1-1)}$	-	10.42 x 10^{-12}	82.67 x 10^{-12}	55.57 x 10^{-12}	46.68 x 10^{-12}
a1	-	0.739	0.843	0.987	0.927
R2 /Ω	-	15241	1921	8271	53694
Q2 /F.s$^{(a2-1)}$	-	52.39 x 10^{-9}	83.06 x 10^{-6}	1.27x 10^{-6}	93.8 x 10^{-9}
a2	-	0.368	0.14	0.350	0.471
s2 /Ω.s$^{-0.5}$	-	301	4.7 10 x 10^{4}	4.680 x 10^{4}	1.305 x 10^{5}

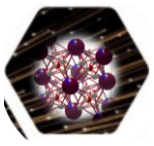

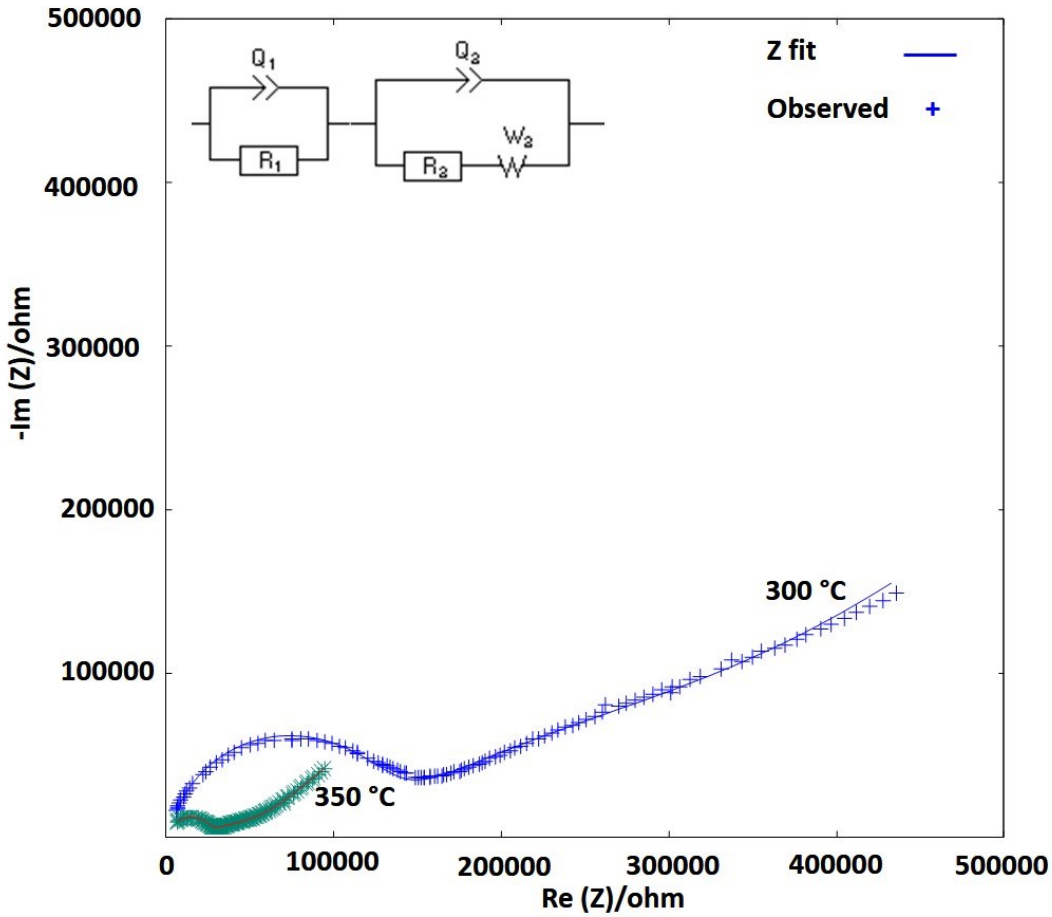

Figure S4.6. Nyquist plots of 8D4WSB during a heating cycle between 300 and 350 °C.

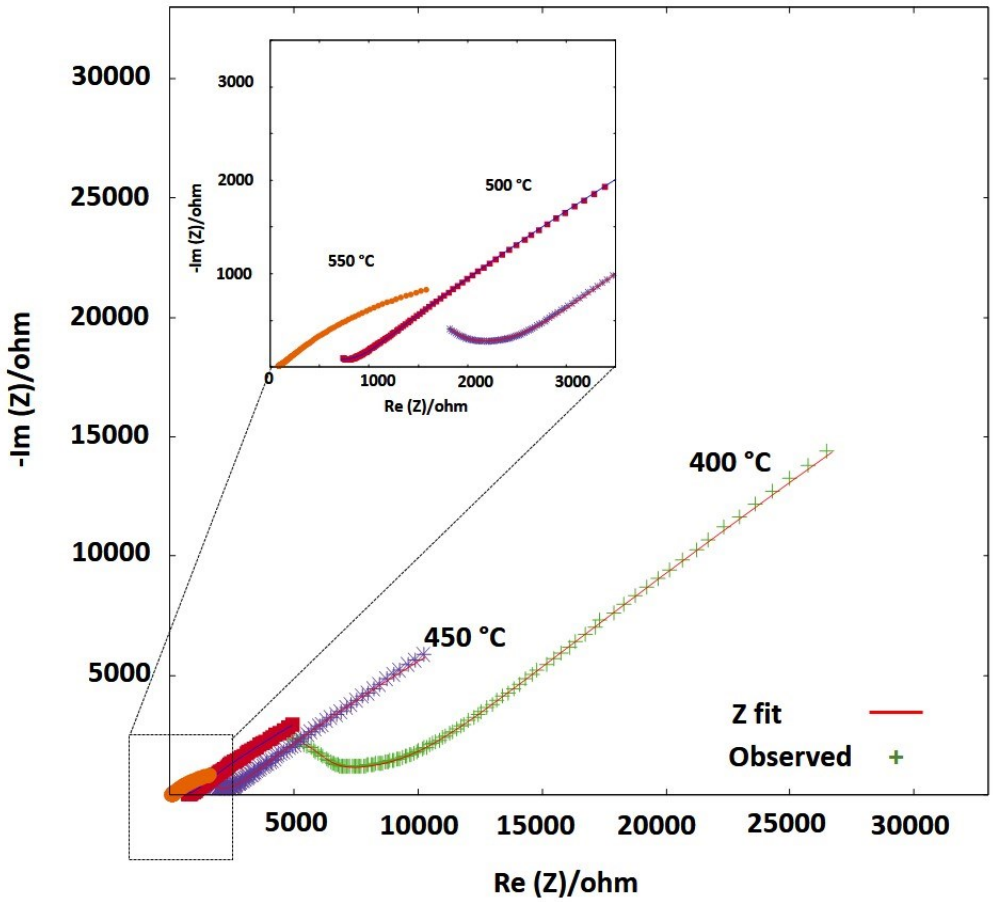

Figure S4.7. Nyquist plots of 8D4WSB during a heating cycle between 400 and 550 °C.

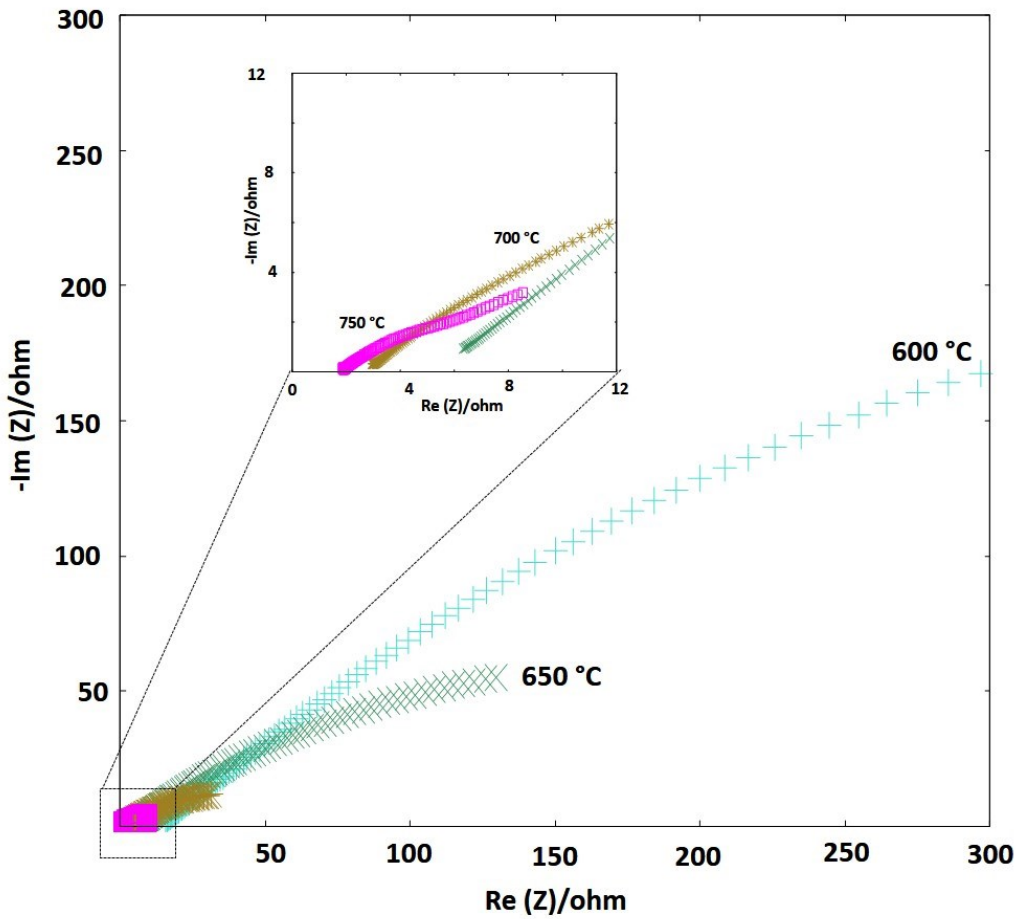

Figure S4.8. Nyquist plots of 8D4WSB during a heating cycle between 600 and 750 °C.

Table S4.4. VT-EIS data for 8D4WSB on both heating and cooling cycles from 300 to 500 °C.

Temperature /°C Heating	300	350	400	450	500
R1 /Ω	104913	19878	3705	1018	378
Q1 /F.s$^{(a1-1)}$	14.31 x 10^{-12}	17.54 x 10^{-12}	27.67 x 10^{-12}	20.29 x 10^{-12}	5.289 x 10^{-12}
a1	0.942	0.995	0.982	0.901	0.882
R2 /Ω	357278	56924	9223	5 695	730
Q2 /F.s$^{(a2-1)}$	0.183 x 10^{-6}	0.991x 10^{-6}	5.163 x 10^{-6}	24.74 x 10^{-6}	31.92 x 10^{-6}
a2	0.423	0.352	0.264	0.837	0.248
s2 /Ω.s$^{-0.5}$	1.484 x 10^{6}	4.977 x 10^{5}	2.309 x 10^{5}	1.321 x 10^{5}	5.382 x 10^{4}

Temperature (°C) Cooling	500	450	400	350	300
R1 /Ω	22	321	1700	8146	36000
Q1 /F.s$^{(a1-1)}$	-	11.93 x 10^{-9}	4.569 x 10^{-9}	79.12x 10^{-12}	0.345 x 10^{-12}
a1	-	0.652	0.683	0.971	0.823
R2 /Ω	-	86	659	4 644	34535
Q2 /F.s$^{(a2-1)}$	-	28.6 x 10^{-5}	84.04 x 10^{-6}	4.467 x 10^{-6}	3.297x 10^{-6}
a2	-	0.291	0.269	0.277	0.302
s2 /Ω.s$^{-0.5}$	-	2.815 x 10^{4}	4.540 x 10^{4}	3.190 x 10^{4}	4.878 x 10^{4}

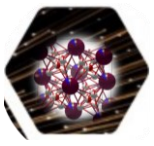

Chapter 5: Symmetry Mode Analysis: Uncovering the Ambiguities and Complexities Between Related Phases in the Bi_2O_3-Dy_2O_3-Er_2O_3 System

Sikhumbuzo M. Masina[a], Caren Billing[a], Daniel Olds[b], Rudolph M. Erasmus[c,d], David G. Billing[a,c]

[a]Molecular Science Institute, School of Chemistry, University of the Witwatersrand, Private Bag X3, Johannesburg, 2050, South Africa

[b]National Synchrotron Light Source II, Brookhaven National Laboratory, Upton 11973, New York, United States

[c]DSI-NRF Centre of Excellence in Strong Materials, University of the Witwatersrand, Private Bag X3, Johannesburg, 2050, South Africa.

[d]Material Physics Research Institute, School of Physics, University of the Witwatersrand, Private Bag X3, Johannesburg, 2050, South Africa.

Abstract:

A new system of the general formula $Dy_{2x}Er_xBi_{1-3x}O_{1.5}$ (DESB, $0.04 \leq x \leq 0.08$) was investigated. The phase evolution as a function of temperature for the $Dy_{0.08}Er_{0.04}Bi_{0.88}O_{1.5}$ composition was studied in-depth. A tetragonal phase (β*-phase), which is a distorted version of the δ-phase obtained through symmetry mode decomposition, was found to describe the phase present below ~400°C. Raman spectroscopy and the pair distribution function technique (including variable temperature measurements) revealed the subtle difference between local structures of the β-Bi_2O_3, the δ-Bi_2O_3-like phase and the proposed β*-phase. With a phase transition to the δ-phase occurring at higher temperatures, symmetry mode analysis with parametric Rietveld refinement was used to obtain the linear coefficient of thermal expansion of $\sim 2.2 \times 10^{-5}$/°C in the temperature range 475–654 °C for the δ-phase. The phase fractions of the β*- and δ-phases were found to be highly correlated with the total conductivity.

Keywords: Symmetry mode analysis; Pair distribution function; Conductivity; Local structure; Phase transition.

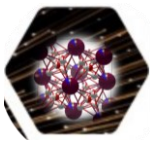

5.1 Introduction

Bi_2O_3 and its chemical derivatives continue to show huge potential for use in devices of technological importance [1-5]. This is due, in part, to the ability of Bi_2O_3 to dissolve many oxides and elements across the periodic table to form a plethora of different solid solutions as summarized by Valant and Suvorov [6] and its ability to exist as many different polymorphs [7,8]. Among the first discovered Bi_2O_3 polymorphs, the monoclinic α-Bi_2O_3 phase ($P2_1/c$) is stable from ambient temperature to 729 °C after which it transitions into the defect fluorite δ-Bi_2O_3 phase ($Fm\bar{3}m$) and Bi_2O_3 melts at 825 °C [9]. With controlled cooling, the δ-Bi_2O_3 phase exhibits hysteresis and can transition into a metastable tetragonal β-Bi_2O_3 phase ($P\bar{4}2_1c$) or a cubic γ-Bi_2O_3 phase ($I23$) at around 645 °C before it reverts to the α-Bi_2O_3 again between 500 and 550 °C [9]. With slow cooling the γ-Bi_2O_3 phase can persist to ambient temperatures. The δ-Bi_2O_3 phase is reported to have conductivities above 1 S cm^{-1} between 730 – 824°C [10-12], the highest conductivity of any solid oxide at this temperature range and is comparable to the conductivities of most molten salts [13]. However, this phase is only stable within a narrow range at high temperatures.

The local structure of the δ-Bi_2O_3 phase has proven to be elusive, with earlier models inadequately describing some experimental observations and theoretical results. The Sillen model described the δ-Bi_2O_3 phase using a simple cubic structure model (space group (SG) $Pn\bar{3}m$) [14, 15]. This structure is similar to the defect fluorite structure, however, the vacant oxygen sites would be ordered along the <111> direction in the defect fluorite phase. This model is inconsistent with the high conductivity observed for the δ-Bi_2O_3 phase and the DFT calculations reported by Aidhy *et al.* [16]. In the DFT study, they found the vacancies to be ordered along the <110> and <111> directions with space group $Fm\bar{3}$. Gattow and Schroder proposed the defect fluorite structure (SG $Fm\bar{3}m$) for the δ-Bi_2O_3 phase with Bi occupying the $4a$ (0 0 0) sites and O statistically occupying 3/4 of the $8c$ (0.25 0.25 0.25) sites [17]. This suggested a completely random distribution of the oxide ions which is consistent with the high conductivity observed, but failed to explain the occupancy of the interstitial ($32f$) sites observed from neutron diffraction experiments [18, 19]. The Willis model described a defect fluorite structure with only the $32f$ (x x x) sites statistically occupied by the oxide ions (3/16 occupancy, $x \approx 0.316$) [8, 20]. This describes a completely random arrangement of the oxide ions and positional disorder and is consistent with the remarkably high conductivity of the material, however, neutron data showed that the $8c$ sites are also occupied

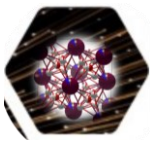

[18, 19]. Models from Battle *et al.* [18] and Hull *et al.* [19] proposed a defect fluorite structure with the oxide ions distributed between the 8*c* and 32*f* sites which agrees well with total scattering data from neutron diffraction and is consistent with the high conductivity observed. The model by Battle *et al.* [18] proposed almost equal occupancy for the 8*c* and 32*f* sites whereas Hull *et al.* [19] proposed a different occupancy for these two sites – two oxide ions randomly occupy the 8*c* sites while the remaining four are randomly distributed among the 32*f* sites in this model. Hull *et al.* [19] also compared the local structures of the α-Bi_2O_3 and β-Bi_2O_3 phases to that of the δ-Bi_2O_3 phase and observed that the Bi–O bonds are asymmetric in all three structures. The structure of the β-Bi_2O_3 phase shows a group-subgroup relationship with that of the δ-Bi_2O_3 phase.

Substituting Bi^{3+} with isovalent and aliovalent cations to stabilise the δ-Bi_2O_3-like phase to ambient temperatures has been extensively reviewed elsewhere [21-24]. The co-doping strategy has produced some systems with the lowest total substituent concentration needed to stabilise the δ-phase to ambient temperatures and the highest conductivities for any substituted systems of Bi_2O_3 so far [25,26]. This is ascribed to the reduced total substituent concentration needed to stabilize the δ-phase, reported to emanate from the stabilising configurational entropy introduced by doping with two or more impurity cations [27, 28]. However, polyphasic materials are a common occurrence in this strategy and very little information is provided on the conductivities of these mixtures and the relationship between the co-existing phases. In this work, Dy^{3+} and Er^{3+} were used to produce a new system with general formula $Dy_{2x}Er_xBi_{1-3x}O_{1.5}$ (DESB, $0.04 \leq x \leq 0.08$) that produces a mixture of a distorted δ-Bi_2O_3-like phase (henceforth referred to as the β*-phase) and an undistorted δ-Bi_2O_3-like phase (henceforth simply referred to as the δ-phase). Variable temperature (VT) synchrotron powder X-ray diffraction (VT-SXRD), VT pair distribution function technique (VT-PDF) and VT electrochemical impedance spectroscopy (VT-EIS) were used to follow the phase evolution and conductivities in this system. Symmetry mode analysis and parametric Rietveld refinements were used to extract information that provided insights into the evolution of the β*- and δ-phases and the correlation between relative phase composition and conductivity is made.

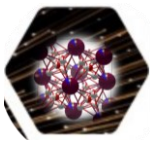

5.2 Experimental methods

5.2.1 Synthetic method

The ceramic method was used to fabricate the different compositions in the $Dy_{2x}Er_xBi_{1-3x}O_{1.5}$ system (where x= 0.04, 0.05, 0.06, 0.07, 0.08). Bi_2O_3 (Sigma-Aldrich, nano, 99.999% pure) and Er_2O_3 (Sigma-Aldrich, 99.999% pure) were pre-fired to 700 °C to remove any possible bismutite ($Bi_2O_3 \cdot CO_2$) and moisture which has been reported to influence the phase evolution in Bi_2O_3 solid solutions as well as the final product [9]. Dy_2O_3 was obtained by thermal decomposition of $Dy(NO_3)_3 \cdot 6H_2O$ (Sigma-Aldrich, 99.999% pure) using the method employed by Melnikov *et al.* [29]. Stoichiometric amounts of Bi_2O_3, Er_2O_3 and Dy_2O_3 were mixed in an agate mortar and manually ground for an hour in acetone (99.56% pure, KEM*i*CAL). The mixture was dried in an oven at 80 °C for 12 hours before being annealed at 800°C in air for 24 hours and slow cooled (∼1 °C/min on average) back to room temperature. It was then reground before being annealed at 800°C in air for a further 24 hours and slow cooled again.

5.2.2 Data collection and analysis

5.2.2.1 Bragg and total scattering data

The PDF beamline 28-ID-1 at NSLS II at Brookhaven National Laboratory was used to collect both the total scattering and Bragg data. The X-ray source is a damping wiggler and the beam is focused horizontally and vertically by a Side Bounce Monochromator (SBM) and a Vertically Focusing Mirror (VFM), respectively. A monochromatic wavelength of 0.1671 Å in Debye-Scherrer geometry was used. The diffractometer employs a PerkinElmer area detector (200 × 200 μm pixels) which was mounted at a direct distance of 530 mm for total scattering data and is capable of fast exchangeability to collect Bragg data at a direct distance of 1528 mm. The detector was offset such that the centre of the beam was in one of the detector corners to increase the reciprocal space range (maximum was 22 $Å^{-1}$ for total scattering data). Kapton capillaries with an outside diameter (OD) of 0.9 mm were used for ambient temperature and 1 mm OD quartz capillaries for VT-data collection. A hot air blower was used to heat the samples from 60 – 810 °C in 30 °C intervals for both heating and cooling cycles and scans were taken at every 30 °C interval. LaB_6 and CeO_2 were used as external calibrants for the ambient temperature measurements and Si (NIST SRM 640d) was used as an external calibrant for the VT measurements. Total scattering data were reduced using xPDFsuite [30] and Bragg data were analysed using TOPAS Academic

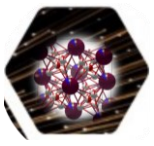

[31]. The scale factor, background factors, lattice constants, some fractional coordinates, mode amplitudes, capillary displacement and temperature calibration factors were the general parameters refined from the Bragg data. The refined data and some parameters are included in the Supplementary Information (Fig. S5.1-S5.5, Fig. S5.14-S5.18, Table S5.1-S5.5 and Table S5.8-S5.9).

5.2.2.2 Raman spectroscopy

Raman spectroscopy measurements were obtained using a Horiba LabRAM HR Raman system equipped with an argon-ion laser of emission line 514.532 nm, a Symphony CCD detector cooled to −129 °C using liquid nitrogen and a 600 lines/mm grating. An Olympus optical microscope attachment with a 50× LWD objective lens and a Linkham TS1500 sample stage was used for the *in situ* variable temperature measurements. The sample stage was purged with high purity argon gas and the spectra were measured between ambient temperature and 850 °C at 170 °C increments using a heating rate of 10 °C min^{-1}. The maximum acquisition time was 2 minutes and the powder form of the samples was analysed.

5.2.2.3 VT-EIS measurements

VT-EIS was done using an MTZ-35 frequency response analyser from BioLogic. It was equipped with an HTF-1100 furnace and HTSH-1100 sample holder. The measurements were done in air, with both heating and cooling cycles in the range of 300-750 °C at 50 °C increments using a heating/cooling rate of 10 °C min^{-1}. The system was allowed to equilibrate for 30 minutes at each temperature before measurement. The frequency range was from 10 Hz to 1 MHz with an A.C. amplitude of 10 mV. The pellets were prepared by mixing the powder samples with an aqueous solution of 0.3 wt% polyvinyl alcohol (PVA) as a binder and pressed into pellets using a uniaxial cold press at a constant pressure of ∼500 MPa and a 5 mm die. The green bodies were first heated to 300 °C over a 6-hour period and then soaked at this temperature for 4 hours to remove the binder. The temperature was then ramped up to 820°C and the pellets were sintered at this temperature for 14 hours before letting the furnace cool with the samples back to room temperature. The pellets had a thickness of ∼1 mm and were directly placed between the smooth platinum disks from the sample holder that were then tightly clamped to ensure good contact. The data fitting procedure applied was the same as that described in Ref. [32]. Fitted data, equivalent

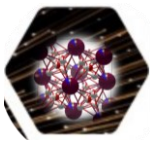

circuits and parameters are included in the Supplementary Information (Fig. S5.8-S5.13, Tables S5.6 and S5.7).

5.1 Results and Discussion

5.1.1 Preliminary Phase Analysis and Conductivity Measurements

SXRD was used to verify the phases present in the DESB materials. All the compositions had an apparent δ-phase as the dominant phase. The lattice constant a as a function of total substituent concentration showed a linear behaviour, obeying Vegard's law (Fig. 5.1(a)) and this suggested that solid solutions were being formed. The decrease in lattice constant a as a function of total substituent concentration is as expected because Er^{3+}(0.89 Å) and Dy^{3+}(0.912 Å) have smaller ionic radii than that of Bi^{3+}(1.03 Å), assuming a coordination number of six in all cases [33].

A closer look at Fig. 5.1(b) indicates that compositions $Dy_{0.1}Er_{0.05}Bi_{0.85}O_{1.5}$ (10D5ESB) and $Dy_{0.12}Er_{0.06}Bi_{0.82}O_{1.5}$ (12D6ESB) had more impurity phases present and were confirmed by Rietveld refinement results shown in Table 5.1 (and Figures S5.2, S5.3) as the bismutite phase (SG *Imm*2), as well as a rhombohedral phase (SG $R\bar{3}mH$) only in 10D5ESB.

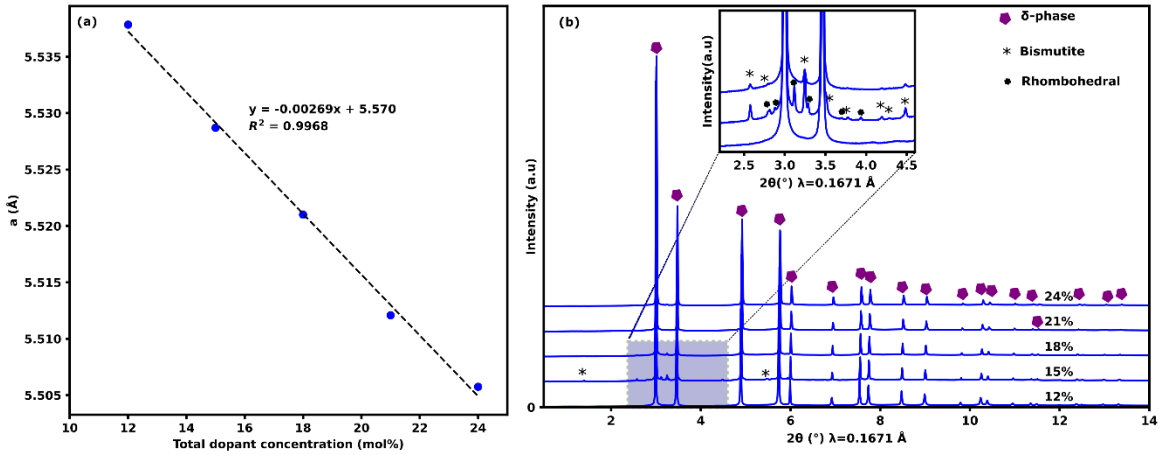

Figure 5.1. **(a)** Plot of the lattice constant a as a function of total substituent concentration showing how the DESB system closely obeyed Vegard's law. Error bars were included and are smaller than symbols used **(b)** Diffractograms of the DESB system; the 10D5ESB and 12D6ESB compositions had the highest impurity phases (inset).

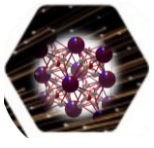

Table 5.1. Relative weight percent of each phase in each composition as obtained from Rietveld refinement of SXRD data[a].

Composition	Abbreviation	δ-phase (%)	Bismutite phase (%)	Rhombohedral phase (%)
$Dy_{0.08}Er_{0.04}Bi_{0.88}O_{1.5}$	8D4ESB	100	0	0
$Dy_{0.1}Er_{0.05}Bi_{0.85}O_{1.5}$	10D5ESB	93.8(2)	3.18(7)	2.9(2)
$Dy_{0.12}Er_{0.06}Bi_{0.82}O_{1.5}$	12D6ESB	98.58(6)	1.42(6)	0
$Dy_{0.14}Er_{0.07}Bi_{0.79}O_{1.5}$	14D7ESB	99.29(7)	0.71(7)	0
$Dy_{0.16}Er_{0.08}Bi_{0.76}O_{1.5}$	16D8ESB	99.12(6)	0.88(6)	0

Composition of the rhombohedral phase was assumed to be $Dy_{0.1}Er_{0.05}Bi_{0.85}O_{1.5}$

The high signal to noise ratio of SXRD data made it possible to pick up even the trace impurity phases (bismutite and rhombohedral) which can be easily missed by conventional XRD as they would be indistinguishable from the background. These impurity phases were not present immediately after synthesis, however, and were found about 12-18 months after synthesis (Fig. S5.6). This suggests that the apparent δ-phase is a metastable phase as reported by Watanabe [34]. Levin and Roth reported that the bismutite phase formed after storing samples of pure Bi_2O_3 under ambient conditions for six months in their work [9]. When the graph in Fig. 5.1(a) was extrapolated to 0% total substituent concentration corresponding to pure Bi_2O_3, the lattice constant a obtained was 5.570 Å. This is lower than the 5.661 Å reported by Hull *et al.* [19] and 5.654 Å reported by Yashima and Ishimura [35] for the pure δ-Bi_2O_3 phase, but their measurements were conducted at temperatures above 730 °C where the pure δ-Bi_2O_3 phase is stable. Extrapolated graphs similar to Fig. 5.1 (a) of ESB and DWSB systems reported by Jung *et al.* [25] at ambient temperatures gave 5.581 and 5.612 Å, respectively, which are comparable to the 5.570 Å obtained in this work.

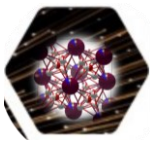

The Arrhenius plot obtained from the VT-EIS results of 8D4ESB showed a discontinuity between 500 and 600 °C which was indicative of a phase transition (Fig. 5.2) and unexpected since preliminary SXRD results suggested the material was phase pure. When compared to VT-EIS results of $Er_{0.20}Bi_{0.80}O_{1.5}$ (20ESB) – measured under virtually identical conditions and confirmed to have the pure δ-phase as shown in later sections (thus exhibiting no phase transition) – the notion that the discontinuity in EIS results is from a phase transition was reinforced (Fig. 5.2). To investigate this discontinuity in conductivity, Raman spectroscopy, VT-PDF and VT-SXRD were used to investigate the phases present at ambient temperature as well as phase evolution as a function of temperature for the 8D4ESB composition.

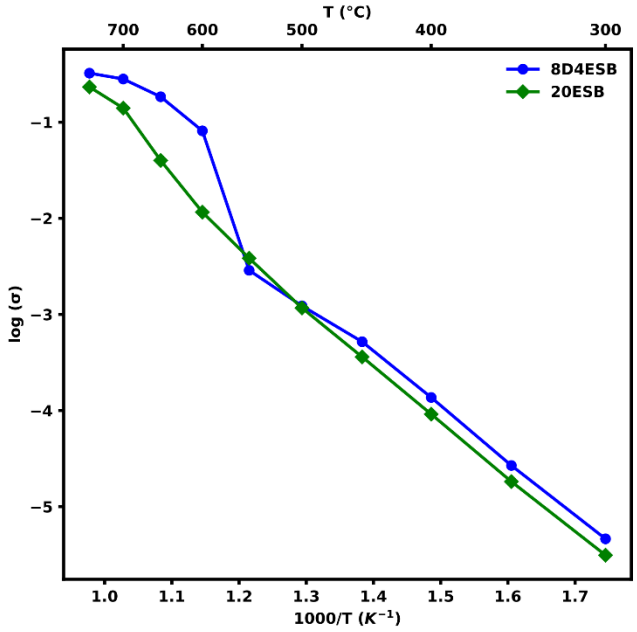

Figure 5.2. The Arrhenius plot of 8D4ESB shows a discontinuity indicative of a phase change during the heating cycle, which is absent in the Arrhenius plot of 20ESB measured under similar conditions.

The presence of a δ-Bi_2O_3 phase exhibits two bands in a Raman spectrum. The intense band below 200 cm^{-1} is attributed to external modes and the band at around 600 cm^{-1} is the T_{2g} mode from the M-O-M vibrations [36]. The metal ions in the 4*a* sites (O-M-O) in the space group $Fm\bar{3}m$ are expected to not show any Raman activity because of the site symmetry of their Wyckoff position ($m\bar{3}m$). However, the Raman spectrum of 8D4ESB (Fig. 5.3(a)) showed at least three bands.

The intense band at ~100 cm^{-1} was attributed to external modes and the T_{2g} band was observed at 623 cm^{-1}. The extra band at 304 cm^{-1} might be attributed to the intense band normally

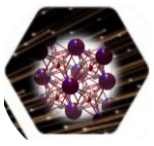

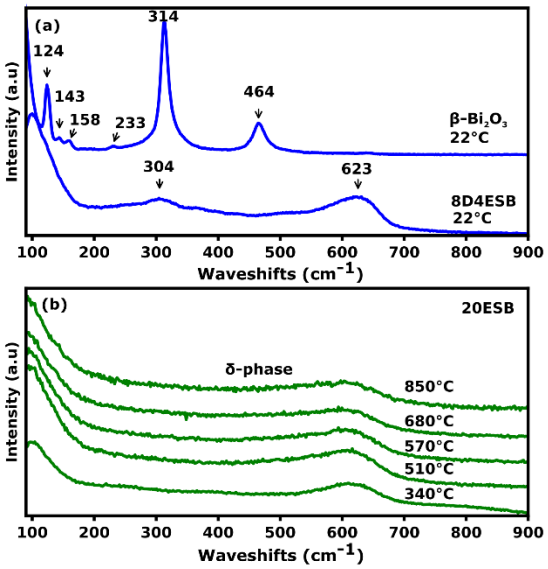

Figure 5.3. **(a)** Raman spectra of 8D4ESB and commercial pure β-Bi_2O_3 at ambient temperature showing that the peak at 304 cm^{-1} for 8D4ESB could be from the β-Bi_2O_3 phase. This is compared to **(b)** the Raman spectra of 20ESB for the pure δ-phase.

observed in the β-Bi_2O_3 phase at around 313 cm^{-1} as reported by Pereira *et al.* [7] and shown in Fig. 5.3(a) at 314 cm^{-1} for β-Bi_2O_3 as measured in this work. The relative intensity of this band would also suggest a substantial percentage of the β-phase would be present, but this was not observed in the SXRD data of 8D4ESB shown in Fig. 5.1(b) and will be discussed further in later sections. In addition, the Raman spectra of 20ESB showed only the two expected bands for the pure δ-phase in the temperature range where the conductivity measurements were made (Fig. 5.3(b)). This reinforced the idea that indeed, only two bands are expected for the pure δ-phase in the measured range. This meant that for 8D4ESB there was either a mixture of phases or a phase that could not be detected by ambient temperature SXRD that Raman spectroscopy was sensitive to. However, the information from Raman spectroscopy of 8D4ESB was not enough to unambiguously identify the other phase as the β-phase.

When the β-phase was incorporated into a Rietveld refinement, relative weight percentages of ~6 and 94 of the β- and δ-phases were obtained (Fig. 5.4(a)). A closer look at the calculated results (Fig. 5.4(a) inset) reveals unaccounted for small peaks from an overestimation of the β-phase. This overestimation is not surprising because the major peaks of the β- and δ-phases overlap making it difficult to clearly resolve the two phases. However, this also suggested that the β-phase at ~6% should have been detected by SXRD as the rhombohedral and bismutite phases were present at

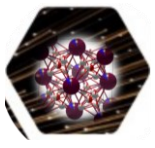

lower relative weight percentages (see Table 5.1 and Fig. 5.1(b)). When the diffraction patterns of a mixture of the two phases was simulated with relative weights of 20% β-phase and 80% δ-phase, the small peaks become more prominent (Fig. 5.4(b)). This shows that if present at higher relative

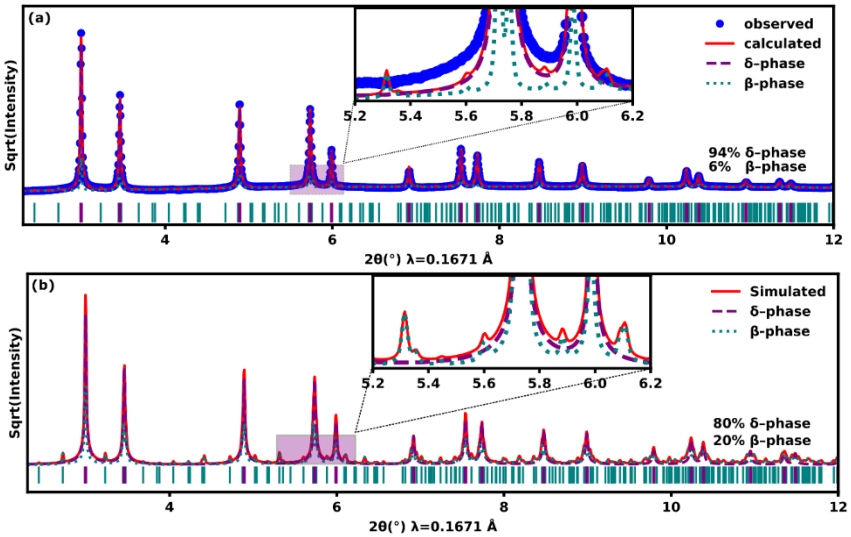

Figure 5.4. **(a)** Shows a plot of the fit obtained from a Rietveld refinement of the experimental Bragg data of 8D4ESB measured at room temperature presented as a square root of the intensity to accentuate the low intensity peaks from the calculated plot (as highlighted in the inset). **(b)** Shows a plot of the calculated Bragg data (red) from a weighted sum of the β- (20%) and δ- (80%) phases.

weights the β-phase should be more visible in the experimental Bragg data of 8D4ESB, but it is not.

The discontinuity in conductivity indicated in the Arrhenius plot for 8D4ESB (Fig. 5.2) would most likely be due to a change in the bulk material. This is because bismuth oxide solid solutions have been shown to have negligible grain boundary effects [37, 38], therefore, a significant jump in conductivity means a change in the structure of the bulk material. The change in conductivity of almost two orders of magnitude between 550 and 600 °C would suggest a significant change in phase and is not expected from a material that contains ~94% δ-phase. The apparent contradiction between the VT-EIS and SXRD (Rietveld refinement) results suggest that a mixture of the β- and δ-phases where the δ-phase (with high ionic conductivity) is present in large proportions is also highly unlikely. This prompted further analysis and is described in the subsequent sections.

From the Raman spectrum and SXRD results for 8D4ESB, it was suspected that the other phase/s present at room temperature could have a structure with symmetry intermediate between that of the β-Bi_2O_3 phase and the δ-phase. The results from Raman spectroscopy, a technique sensitive to

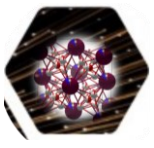

the local structure, prompted further probing of 8D4ESB by the PDF technique to assess the structure more clearly.

5.1.2 The Local Structure from X-ray Total Scattering

The total PDF technique confirmed a close relationship between the measured PDF of 8D4ESB and those from both β-Bi_2O_3 and 20ESB (δ-phase) as shown in Fig. 5.5(a). It is apparent that the PDF measured for 8D4ESB is not exactly the same as either that for the β-Bi_2O_3 or the δ-phase, but rather intermediate between the two. Since there is a group-subgroup relationship between the β-Bi_2O_3- and δ-phases [19], symmetry mode analysis (SMA) was used to decompose the structure of the β-Bi_2O_3 phase (the child structure). This phase is henceforth, referred to as the β^*-phase (SG $P\bar{4}2_1c$). The ISODISTORT server [39, 40] was used to decompose the symmetry of the child structure (β^*-phase) into the symmetry of the parent structure (δ-phase) plus modes that reduce the symmetry using:

$$\begin{pmatrix} a_{\beta^*} \\ b_{\beta^*} \\ c_{\beta^*} \end{pmatrix} = \begin{pmatrix} 1 & 1 & 0 \\ -1 & 1 & 0 \\ 0 & 0 & 1 \end{pmatrix} \begin{pmatrix} a_{\delta} \\ b_{\delta} \\ c_{\delta} \end{pmatrix}$$

for the basis change with no origin change as determined by Hull *et al.* [19] and confirmed in this work. Only one distortion or structure was obtained after the decomposition. The unit cell volume of the β^*-phase obtained after decomposition was smaller than that reported by Hull *et al.* [19] and Blower and Greaves [41] for the β-Bi_2O_3 phase (Fig. 5.6), but the space group type was the same.

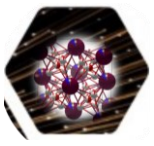

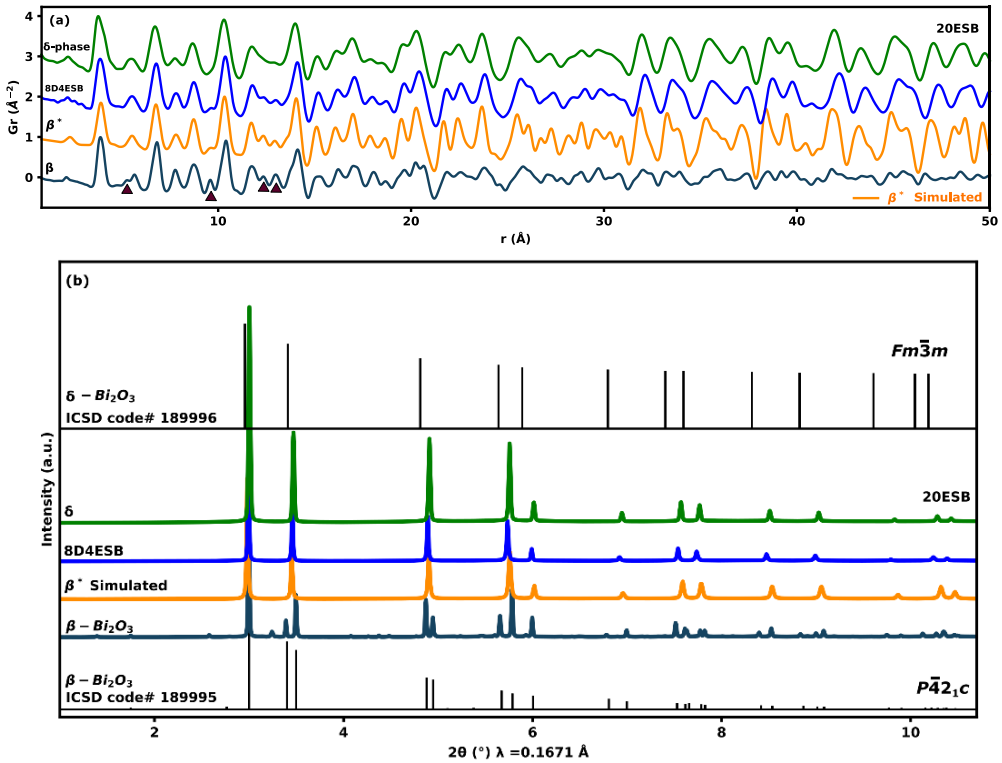

Figure 5.5. **(a)** The total PDFs of pure β-Bi_2O_3- and the δ-phase show a close relationship in the local structure of these two phases. It is also illustrated how the simulated total PDF (Q_{max} = 22 $Å^{-1}$) of the β*-phase resembles that of 8D4ESB. (b) The Bragg data of the pure β-Bi_2O_3- and the δ-phases are totally distinguishable, yet the Bragg data of the β*- and δ-phases, as well as 8D4ESB, are all virtually the same.

The simulated total PDF of the resultant structure was very similar to the measured total PDF of 8D4ESB (Fig. 5.5(a)). The symmetry of this resultant structure was intermediate between that of the β-Bi_2O_3 and the δ-phases. There are striking similarities between the local structures of β-Bi_2O_3, 8D4ESB and the δ-phase, i.e., the region where $r < 6$ Å in the total PDFs, meaning the first M–O (Bi/Dy/Er–O) and M–M (Bi/Dy/Er – Bi/Dy/Er) peaks for the three phases could not be distinguished. For r > ~6 Å, the differences started to manifest as indicated by the arrows in Fig. 5.5(a). The peaks at 9.59, 12.34, and 12.99 Å are more intense for the β-Bi_2O_3 phase than for 8D4ESB and they had virtually vanished for the δ-phase, yet their relative intensity in the β*-phase and in 8D4ESB are comparable. These peaks are predominantly from the M–M and O–O partial PDFs in the β-Bi_2O_3 phase shown by Hull *et al*. [19] and are predominantly from the M–M partials in this work as Bi, Dy and Er have far more electrons than O, therefore the total PDF is dominated by the M–M partials (Fig. S5.7). It should be noted that all the experimental PDFs were reduced using the same parameters, including the maximum magnitude of the scattering vector, Q_{max}. The

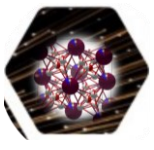

intensities were normalised by dividing by the intensity of the tallest peak in each PDF to put the experimental and simulated PDFs in a similar scale.

Interestingly, the Bragg data of the monophasic β-Bi_2O_3 and δ-phases are completely distinguishable (Fig. 5.5(b)), despite their total PDFs being more similar. However, the simulated Bragg data of the β*-phase is virtually indistinguishable from that of the δ-phase, which could explain why it would be difficult to discern this phase from SXRD data of 8D4ESB. The presence of the β-Bi_2O_3 phase could have been easily picked up from the Bragg data if it were present in high enough percentages. The nuanced differences in the total PDFs and Bragg data are enough to show that the dominant structure in 8D4ESB is closer to that of the β*- and δ-phases than it is to that of the β-Bi_2O_3 phase. The three structures are illustrated by the unit cells shown in Fig. 5.6. The c lattice constants of the β*- and δ-phases are equal and the $a_\delta = a_{\beta^*}\sqrt{2}$. The c lattice constants of the β- and δ-phases are approximately equal and $a_\delta \approx a_\beta/\sqrt{2}$. This shows that there is indeed a relationship between all 3 structures. However, the small differences in unit cell size, shape, atomic positions, and occupancies are enough to show that the phase in 8D4ESB is predominantly the β*-phase when the PDFs and Bragg data are compared and was assumed for further analysis.

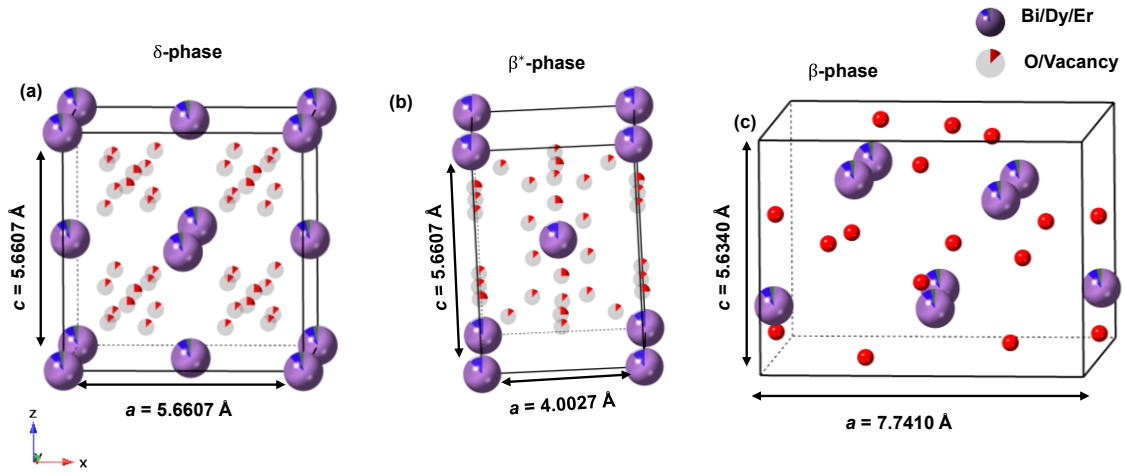

Figure 5.6. **(a)** Illustrates a model unit cell of the structure of the δ-phase (8D4ESB) adapted from that of Hull *et. al* [19], **(b)** shows a model unit cell of the structure of the β*-phase obtained by exploiting the group-subgroup relationship between the δ- and β*-phases, and **(c)** is a model unit cell of the structure for the β-phase adapted from that reported by Blower and Greaves [41].

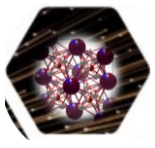

The total PDFs of the compositions explored in this work (Fig. 5.7) also indicated that an increase in total substituent concentration resulted in the total PDFs looking more like those of the monophasic δ-phase – the intensity of the peaks at ~9.59, 12.34, and 12.99 Å (indicated by the arrow and shaded rectangle in Fig. 5.7) decreased. This is expected because the pure δ-phases are obtained at higher substituent concentrations for the solid solutions incorporating individual substituents (17.5 mol% for Er^{3+} and 28.5 mol% for Dy^{3+}) [11,42]. This means that an increase in total substituent concentration stabilises the δ-phase more.

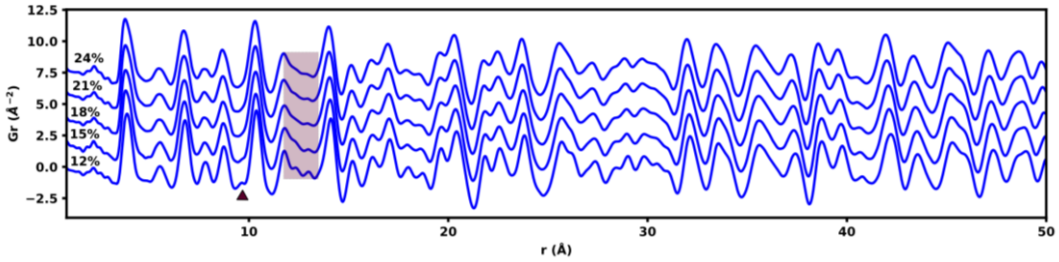

Figure 5.7. Total PDFs of all the compositions explored (8D4ESB, 10D5ESB, 12D6ESB, 14D7ESB, 16D8ESB) illustrating how an increase in total substituent concentration results in a better stabilisation of the δ-phase. Measurements were all done at ambient temperatures.

VT-PDF of 8D4ESB showed that the peaks at ~9.59, 12.34, and 12.99 Å had vanished by ~654 °C upon heating in the same way they did with an increase in total substituent concentration (Fig. 5.8), indicating a stabilisation of the δ-phase. Upon cooling at a similar rate as heating, the intensity of the peaks at ~9.59, 12.34, and 12.99 Å started increasing again. This suggested that the phase transition was reversible upon cooling. These results also suggest that the initial phase of 8D4ESB at ambient temperatures is not predominantly the δ-phase, but most likely the β^*-phase which transitions into the δ-phase at high temperatures.

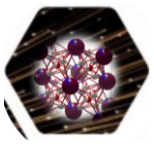

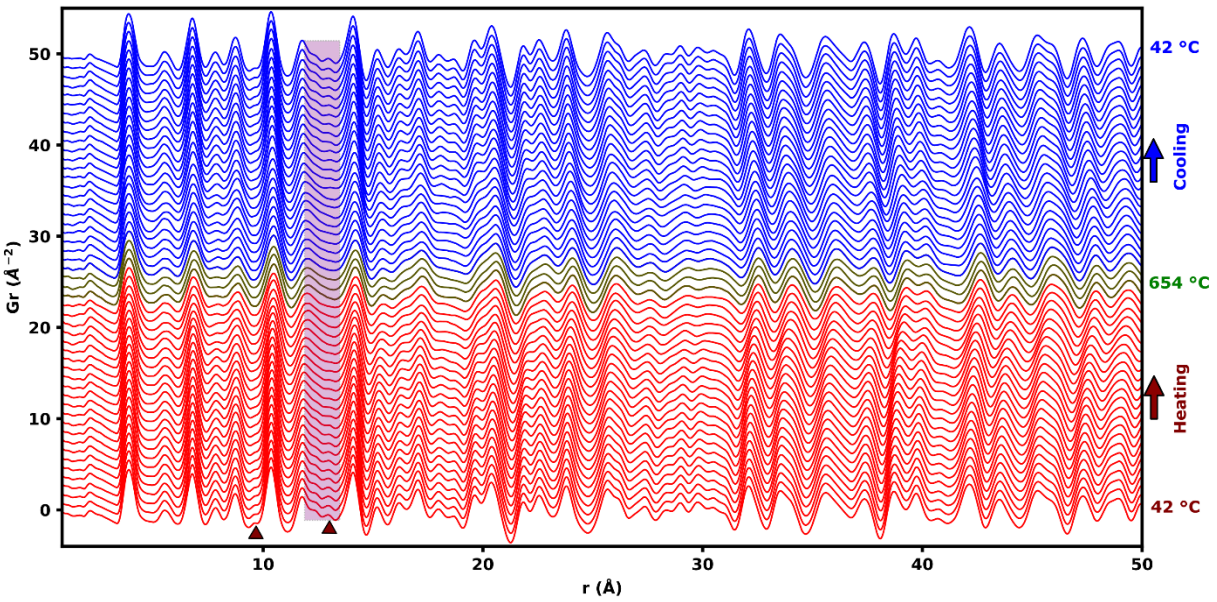

Figure 5.8. VT-PDF of 8D4ESB showing changes in the medium-range structure as a function of temperature. Green total PDFs highlight a section where the phase changes are essentially complete at higher temperatures. The rectangle and the red arrows at 9.59 and 12.34 Å highlight the features from the β*-phase and illustrate how these evolve with changes in temperature.

5.1.3 Symmetry Mode Based Parametric Rietveld Refinement

Since the 8D4ESB composition exhibited a temperature dependent phase transition between structurally closely related phases, extraction of information from the Bragg data also needed careful analysis. To this end, a parametric Rietveld refinement approach combined with SMA was employed [43-45].

The SMA approach is a natural choice when modelling data with phase transitions involving parent (high symmetry) and child (low symmetry) structures. The SMA combined with the parametric Rietveld refinement became even more important because subtle peak splitting was observed on the Bragg data in this work during the heating cycle (Fig. 5.9) and it has been reported that this refinement procedure can handle such intricacies well [44]. It is evident from the anisotropic peak broadening in Fig. 5.9(b-d) that during the phase change, the δ-phase, which is a minor phase, grows at the expense of the initial dominant β*-phase as the temperature is increased. This contradicts the preliminary Rietveld refinement results (see Table 5.1 and Fig. 5.4(a)) where the δ-phase was found to be dominant at room temperature but agrees very well with the VT-EIS and VT-PDF results that indicated a phase change and illustrated how the β*-phase resembles the δ-phase, respectively. Fig. 5.9(b-d) shows a co-existence of the β*- and δ-phases which is a common occurrence for first-order phase transitions.

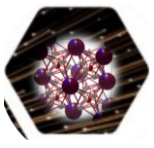

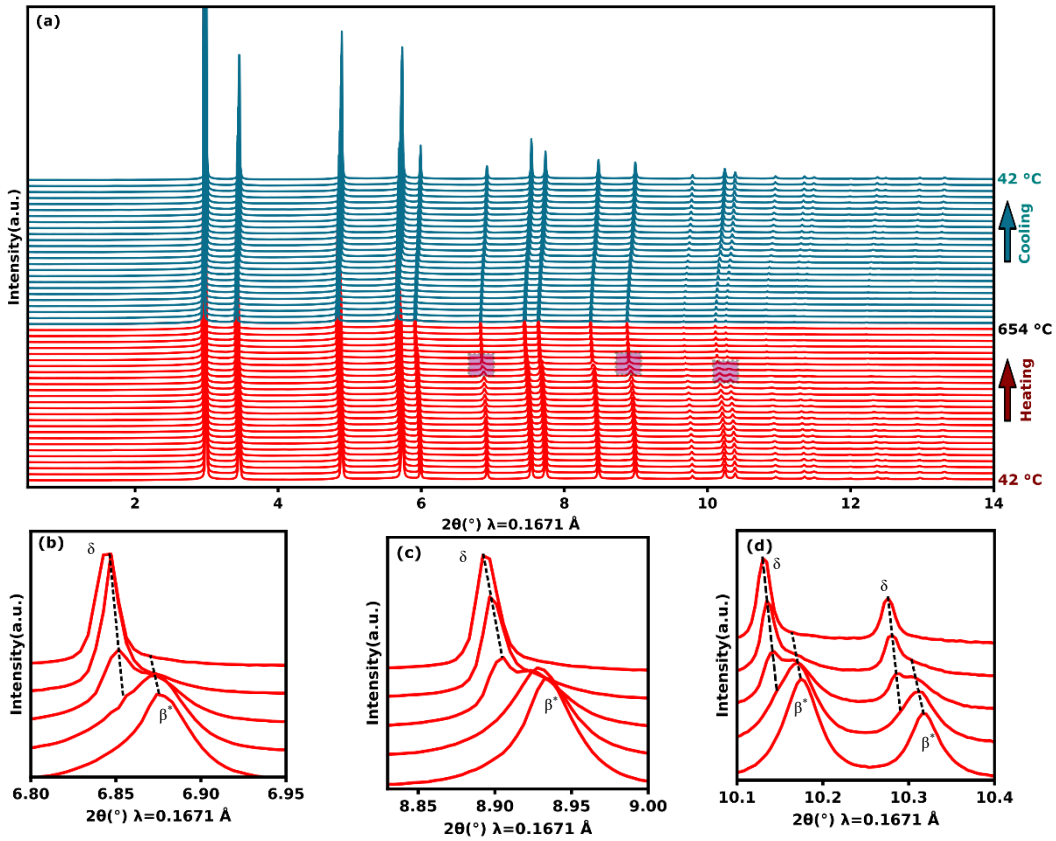

Figure 5.9. **(a)** VT-SXRD Bragg data showing a phase transition and subtle anisotropic peak broadening as highlighted for certain peaks **(b-d)**. Extraction of information from these Bragg data required a joint parametric and symmetry mode Rietveld refinement using both the β*- and δ-phases.

The sudden anisotropic peak broadening can be rationalised by group theoretical calculations of strain using the IsovizQ software [46]. The GM3+ is one of the modes that describes lattice strain and the displacement of the oxygens from the 8*e* site of the β*-phase into the 32*f* site of the δ-phase during a phase transition. Increasing the GM3+ mode amplitude which increases the lattice strain along the *c* axis of the β*-phase more than the *a* and *b* axes causes a more prominent anisotropic peak broadening in the calculated diffraction pattern (Fig. 5.10). The movement of oxygens from the 8*e* site of the β*-phase into the 32*f* site of the δ-phase during growth of the δ-phase will inevitably cause a relaxation of the metal atoms and a sudden increase in lattice distortion causing the observed sudden anisotropic peak broadening (Fig. 5.9) as the δ-phase grows.

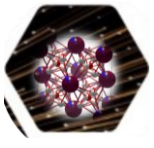

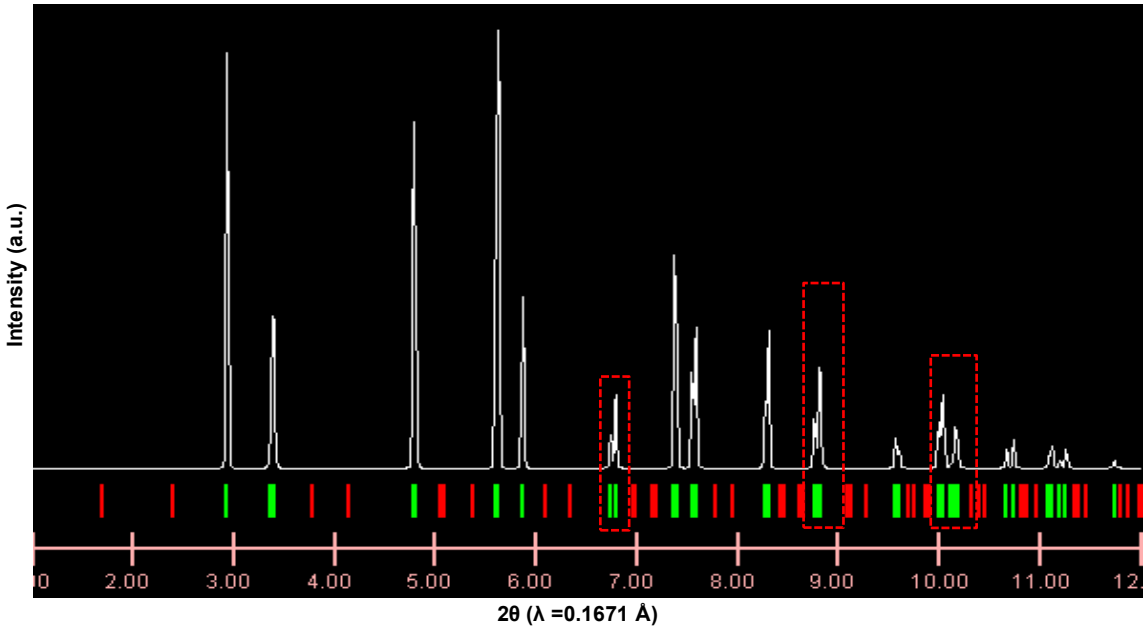

Figure 5.10. A calculated diffraction pattern of the β*-phase showing how the GM3+ strain mode leads to anisotropic peak broadening during a phase transition. Red rectangles highlight peaks with prominent peak broadening. Red and green tick marks signify weak and strong reflections respectively.

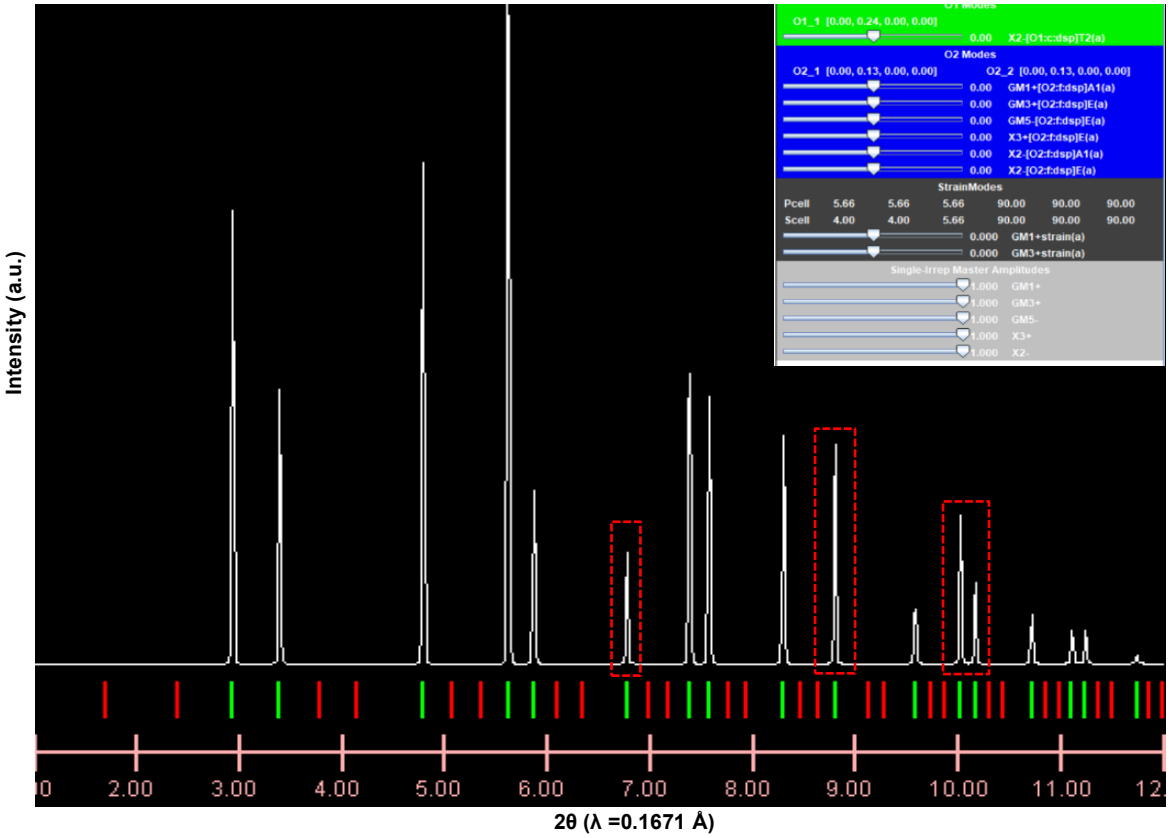

Figure 5.11. A calculated diffraction pattern of the β*-phase illustrating the absence of anisotropic peak broadening when the amplitude of the GM3+ strain mode is zero and the β*-phase is essentially the δ-phases. Red and green tick marks signify weak and strong reflections respectively.

Peaks from the β*-phase vanish once the oxygens are in the 32*f* sites and the phase transition is

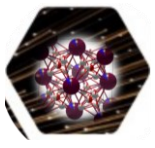

essentially complete as illustrated in Fig. 5.11 These are all observed from the calculated diffraction patterns, but moreover, compare very well with the phenomenon observed in the VT-Bragg data in Fig. 5.9 during the heating cycle. During the cooling cycle, only minor anisotropic broadening of the Bragg peaks was observed. However, VT-PDF showed that the δ-phase reverts to the initial β^*-phase in 8D4ESB upon cooling (Fig. 5.8). The SMA-based parametric Rietveld refinements were done using both structures of the β^*- and δ-phases as a mixture of phases across the whole temperature range on both heating and cooling.

The lattice constants $(a_\delta, a_{\beta^*}, c_{\beta^*})$ for both structures were parametrized using:

$$a = a_0 + {k\Theta_E} \Big/ \left(\left(e^{\left(\frac{\Theta_E}{T-\Delta T}\right)}\right) - 1\right)$$

where a_0 is the lattice constant at 0 K, Θ_E is the Einstein temperature, k is a fitted parameter, T is the hot air blower temperature and ΔT is the difference between the hot air blower and the actual sample temperatures [43]. ΔT was obtained by using Si as a calibrant (Fig. S5.14 and Fig. S5.15) and the equation used by Ref. [43] to describe ΔT. All these parameters, except for T, were refined against the whole data set simultaneously. The model to describe the lattice parameters was chosen following the simple Einstein-like model that is applicable to most materials over a wide temperature range as implemented by Ref. [43]. Since a danger in doing a parametric Rietveld refinement is to impose a physical model that may not describe the data, the changes in lattice

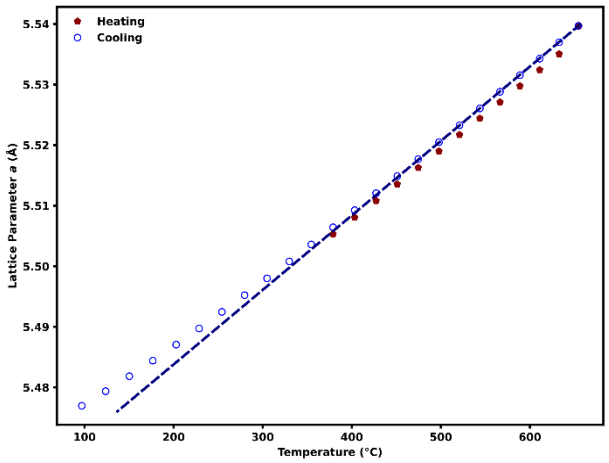

Figure 5.12. The lattice parameter a as a function of temperature of the δ-phase during the heating and cooling cycles obtained via the SMA-based parametric Rietveld refinement. The dotted straight line merely indicates deviation from linearity in the range 97–451 °C during the cooling cycle.

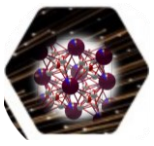

constant a_δ were compared to reported cell variation as a function of temperature for monophasic solid solutions of bismuth oxide where this model was not employed [47-50].

During cooling, the lattice constant a of the δ-phase obtained using SMA-based parametric Rietveld refinement as a function of temperature can be divided into two regions: the region between 97 and 451 °C is non-linear and the region above 451 °C is linear (Fig. 5.12). This behaviour has been reported in many solid solutions of Bi_2O_3 and is ascribed to subtle second-order transitions or disordering/ordering of the oxide ions as the temperature is increased/decreased [47-50]. This gives confidence on the results obtained and the suitability of the model used even if a lower percentage of the δ-phase is present in the 97-451 °C range which may lead to some inaccuracy in the values.

The linear coefficient of thermal expansion for the δ-phase upon heating and cooling in the temperature range 475–654 °C (where the change in lattice constant a was linear) was found to be ~2.2 × 10^{-5}/°C. These values are comparable to the 1.8 × 10^{-5}/°C obtained by Verkerk *et al*. [11] for 15ESB using a dilatometer (in the ~450-650 °C range) and 2.4 × 10^{-5}/°C for pure δ-Bi_2O_3 phase reported by Levin and Roth [9] using XRD (in the ~650-800 °C range). These results indicate that the model used to describe the lattice constants in this work is justified because it

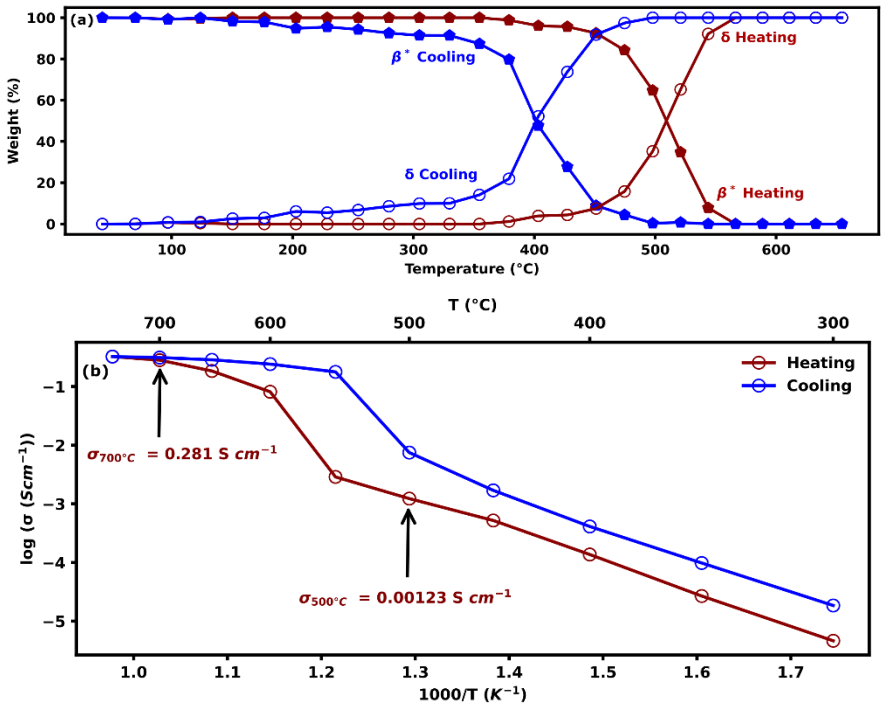

Figure 5.13. The weight fraction of the β*- and δ-phases in **(a)** shows a strong correlation with the total conductivity of the 8D4ESB composition shown in the Arrhenius plots in **(b)** during the heating and cooling cycles.

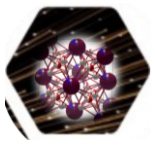

captures well the linear coefficient of thermal expansion when compared to similar results in other Bi_2O_3 materials determined using different experimental and analysis techniques.

The relative weight fraction of the phases obtained from the SMA-based parametric Rietveld refinement showed correlations with the conductivity of the material on both heating and cooling cycles (Fig. 5.13). Between 60 and 500 °C on heating, the average weight percent shows the β^*-phase dominates, with insignificant changes up to ~450 °C. The β^*-phase has an ordered oxygen sublattice compared to the δ-phase and is thus expected to have lower conductivities than the pure δ-phase. These weight fractions partly explain why the conductivities of the material in this work are lower by almost two orders of magnitude before the phase transition (Fig. 5.13(b)). A sudden increase in weight percent of the δ-phase observed between 475 and 566°C coincides with the region where a discontinuity in conductivity was observed. After the phase transition, the weight percent of the δ-phase is about 100% on average, explaining the high conductivity measurements (0.281 S cm^{-1} at 700 °C) observed in this region and is comparable to the 0.37 S cm^{-1} observed for 20ESB at 700 °C [11] and 0.57 S cm^{-1} reported by Jung *et al.* [25] for the system $(BiO_{1.5})_{0.88}(DyO_{1.5})_{0.08}(WO_3)_{0.04}$ at 700 °C with a pure δ-phase. On cooling, a hysteresis was observed in both conductivity and weight percent. Evidence from VT-PDF data also suggests that the δ-phase does revert to the β^*-phase.

5.2 Conclusion

In this work, a new system with the general formula $Dy_{2x}Er_xBi_{1-3x}O_{1.5}$ (DESB, $0.04 \leq x \leq 0.08$) was fabricated using the ceramic method. The phase evolution as a function of temperature was studied in detail for $Dy_{0.08}Er_{0.04}Bi_{0.88}O_{1.5}$ (8D4ESB), the composition with the lowest substituent concentration. It was established that a tetragonal phase, a distorted version of the δ-phase, was stabilised at ambient temperature for 8D4ESB. This tetragonal phase (called the β^*-phase here) has the same space group type as the β-Bi_2O_3 phase ($P\bar{4}2_1c$), but its structure is intermediate between that of the β-Bi_2O_3 and δ-Bi_2O_3 phases. This structure displays virtually the same Bragg pattern as the δ-phase in XRD and was essentially undiscernible at ambient temperatures using SXRD. It was only after using additional probes such as Raman spectroscopy, PDF, VT-PDF, VT-SXRD and VT-EIS that the differences started to manifest and subtle phase transitions were observed. Correlations between the changes in total conductivities and phase fractions as a function of temperature confirmed that the predominant phase at ambient temperature was not the δ-phase for

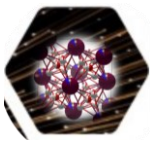

the 8D4ESB composition. This work highlighted the importance of using advanced analysis techniques such as symmetry mode analysis and parametric Rietveld refinement to distinguish between closely related structures that would otherwise not be differentiated using conventional methods.

5.3 Acknowledgements

The authors acknowledge financial support for their research from the National Research Foundation (NRF, South Africa) and Department of Science and Innovation (DSI, South Africa), as well as the University of the Witwatersrand. S.M. Masina also acknowledges the ICDD for a Ludo Frevel scholarship. This research used beamline 28-ID-1 of the National Synchrotron Light Source II, a U.S. Department of Energy (DOE) Office of Science User Facility operated for the DOE Office of Science by Brookhaven National Laboratory under Contract No. DE-SC0012704.

5.4 References

[1] Cabot, A., Marsal, A., Arbiol, J. and Morante, J.R., 2004. Bi_2O_3 as a selective sensing material for NO detection. *Sensors and Actuators B: Chemical*, *99*(1), pp.74-89.

[2] Bhande, S.S., Mane, R.S., Ghule, A.V. and Han, S.H., 2011. A bismuth oxide nanoplate-based carbon dioxide gas sensor. *Scripta Materialia*, *65*(12), pp.1081-1084.

[3] Li, R., Wang, D., Ge, L., He, S., Chen, H. and Guo, L., 2014. Effect of Bi_2O_3 on the electrochemical performance of $LaBaCo_2O_5$+ δ cathode for intermediate-temperature solid oxide fuel cells. *Ceramics International*, *40*(2), pp.2599-2603.

[4] Won-In, K., Pongkrapan, S. and Dararutana, P., 2011. Eco-glass based on Thailand quartz sands and bismuth oxide. In *Materials Science Forum* (Vol. 695, pp. 223-226). Trans Tech Publications Ltd.

[5] Maeder*, T., 2013. Review of Bi_2O_3 based glasses for electronics and related applications. *International Materials Reviews*, *58*(1), pp.3-40.

[6] Valant, M. and Suvorov, D., 2004. Dielectric Characteristics of Bismuth Oxide Solid Solutions with a Fluorite-Like Crystal Structure. *Journal of the American Ceramic Society*, *87*(6), pp.1056-1061.

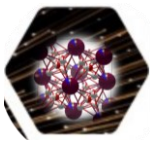

[7] Pereira, A.L., Sans, J.A., Vilaplana, R., Gomis, O., Manjón, F.J., Rodriguez-Hernandez, P., Muñoz, A., Popescu, C. and Beltrán, A., 2014. Isostructural second-order phase transition of β-Bi_2O_3 at high pressures: an experimental and theoretical study. *The Journal of Physical Chemistry C*, *118*(40), pp.23189-23201.

[8] Harwig, H.A., 1978. On the Structure of Bismuth sesquioxide: The α, β, γ, and δ-Phase. *Zeitschrift für Anorganische und Allgemeine Chemie*, *444*(1), pp.151-166.

[9] Levin, E.M. and Roth, R.S., 1964. Polymorphism of bismuth sesquioxide. I. Pure Bi_2O_3. *Journal of Research of the National Bureau of Standards. Section A, Physics and Chemistry*, *68*(2), p.189.

[10] Harwig, H.A. and Gerards, A.G., 1978. Electrical properties of the α, β, γ, and δ-phases of bismuth sesquioxide. *Journal of Solid State Chemistry*, *26*(3), pp.265-274.

[11] Verkerk, M.J., Keizer, K. and Burggraaf, A.J., 1980. High oxygen ion conduction in sintered oxides of the Bi_2O_3-Er_2O_3 system. *Journal of Applied Electrochemistry*, *10*(1), pp.81-90.

[12] Takahashi, T. and Iwahara, H., 1978. Oxide ion conductors based on bismuth sesquioxide. *Materials Research Bulletin*, *13*(12), pp.1447-1453.

[13] Hull, S., 2004. Superionics: crystal structures and conduction processes. *Reports on Progress in Physics*, *67*(7), p.1233.

[14] Harwig, H.A., 1978. On the Structure of Bismuth sesquioxide: The α, β, γ, and δ-Phase. *Zeitschrift für Anorganische und Allgemeine Chemie*, *444*(1), pp.151-166.

[15] Medernach, J.W. and Snyder, R.L., 1978. Powder diffraction patterns and structures of the bismuth oxides. *Journal of the American Ceramic Society*, *61*(11-12), pp.494-497.

[16] Aidhy, D.S., Nino, J.C., Sinnott, S.B., Wachsman, E.D. and Phillpot, S.R., 2008. Vacancy-Ordered Structure of Cubic Bismuth Oxide from Simulation and Crystallographic Analysis. *Journal of the American Ceramic Society*, *91*(7), pp.2349-2356.

[17] Gattow, G. and Schröder, H., 1962. About bismuth oxides III. The crystal structure of the high-temperature modification of bismuth (III) oxide (δ-Bi_2O_3). *Zeitschrift für Anorganische und Allgemeine Chemie* , *318*, p.14.

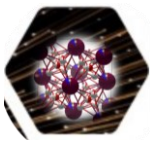

[18] Battle, P.D., Catlow, C.R.A., Heap, J.W. and Moroney, L.M., 1986. Structural and dynamical studies of δ-Bi_2O_3 oxide ion conductors: I. The structure of $(Bi_2O_3)_{1-x}$ $(Y_2O_3)_x$ as a function of x and temperature. *Journal of Solid State Chemistry*, *63*(1), pp.8-15.

[19] Hull, S., Norberg, S.T., Tucker, M.G., Eriksson, S.G., Mohn, C.E. and Stølen, S., 2009. Neutron total scattering study of the δ and β phases of Bi_2O_3. *Dalton Transactions*, (40), pp.8737-8745.

[20] Willis, B.T.M., 1965. The anomalous behaviour of the neutron reflexion of fluorite. *Acta Crystallographica*, *18*(1), pp.75-76.

[21] Sammes, N.M., Tompsett, G.A., Näfe, H. and Aldinger, F., 1999. Bismuth based oxide electrolytes—structure and ionic conductivity. *Journal of the European Ceramic Society*, *19*(10), pp.1801-1826.

[22] Shuk, P., Wiemhöfer, H.D., Guth, U., Göpel, W. and Greenblatt, M., 1996. Oxide ion conducting solid electrolytes based on Bi_2O_3. *Solid State Ionics*, *89*(3-4), pp.179-196.

[23] Azad, A.M., Larose, S. and Akbar, S.A., 1994. Bismuth oxide-based solid electrolytes for fuel cells. *Journal of Materials Science*, *29*(16), pp.4135-4151.

[24] Kharton, V.V., Marques, F.M.B. and Atkinson, A., 2004. Transport properties of solid oxide electrolyte ceramics: a brief review. *Solid State Ionics*, *174*(1-4), pp.135-149.

[25] Jung, D.W., Duncan, K.L. and Wachsman, E.D., 2010. Effect of total substituent concentration and dopant ratio on conductivity of $(DyO_{1.5})_x$–$(WO_3)_y$–$(BiO_{1.5})_{1-x-y}$. *Acta Materialia*, *58*(2), pp.355-363.

[26] Yun, B.H., Kim, K.J., Joh, D.W., Chae, M.S., Lee, J.J., Kim, D.W., Kang, S., Choi, D., Hong, S.T. and Lee, K.T., 2019. Highly active and durable double-doped bismuth oxide-based oxygen electrodes for reversible solid oxide cells at reduced temperatures. *Journal of Materials Chemistry A*, *7*(36), pp.20558-20566.

[27] Meng, G., Chen, C., Han, X., Yang, P. and Peng, D., 1988. Conductivity of Bi_2O_3-based oxide ion conductors with double stabilizers. *Solid State Ionics*, *28*, pp.533-538.

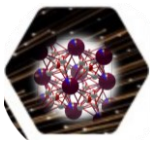

[28] Bandyopadhyay, S. and Dutta, A., 2018. A structural insight into the electrical properties of Dy-Ho co-doped phase stabilized Bismuth Oxide based electrolytes. *Journal of Electroanalytical Chemistry*, *817*, pp.55-64.

[29] Melnikov, P., Arkhangelsky, I.V., Nascimento, V.A., Silva, A.F., de Oliveira, L.C.S., Consolo, L.Z. and Herrero, A.S., 2015. Thermolysis mechanism of dysprosium hexahydrate nitrate $Dy(NO_3)_3 \cdot 6H_2O$ and modeling of intermediate decomposition products. *Journal of Thermal Analysis and Calorimetry*, *122*(2), pp.571-578.

[30] Juhás, P., Davis, T., Farrow, C.L. and Billinge, S.J., 2013. PDFgetX3: a rapid and highly automatable program for processing powder diffraction data into total scattering pair distribution functions. *Journal of Applied Crystallography*, *46*(2), pp.560-566.

[31] Coelho, A.A., 2018. TOPAS and TOPAS-Academic: an optimization program integrating computer algebra and crystallographic objects written in C++. *Journal of Applied Crystallography*, *51*(1), pp.210-218.

[32] Masina, S.M., Billing, C., Erasmus, R.M. and Billing, D.G., 2021. Insights on the phase transitions, stability and conductivity in the Bi_2O_3-WO_3 system. *Journal of Electroceramics*, *46*(2), pp.47-56.

[33] Shannon, R.D., 1976. Revised effective ionic radii and systematic studies of interatomic distances in halides and chalcogenides. *Acta Crystallographica Section A: Crystal Physics, Diffraction, Theoretical and General Crystallography*, *32*(5), pp.751-767.

[34] Watanabe, A., 1995. Polymorphic transformation of δ-Bi_2O_3 stabilized with Ln_2O_3 (Ln= Sm, Eu, Gd, Tb and Dy) into a new phase with a C-type rare-earth oxide-related structure. *Solid State Ionics*, *79*, pp.84-88.

[35] Yashima, M. and Ishimura, D., 2003. Crystal structure and disorder of the fast oxide-ion conductor cubic Bi_2O_3. *Chemical Physics Letters*, *378*(3-4), pp.395-399.

[36] Hardcastle, F.D. and Wachs, I.E., 1992. The molecular structure of bismuth oxide by Raman spectroscopy. *Journal of Solid State Chemistry*, 97(2), pp.319-331.

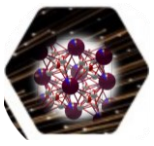

[37] Jung, D.W., Nino, J.C., Duncan, K.L., Bishop, S.R. and Wachsman, E.D., 2010. Enhanced long-term stability of bismuth oxide-based electrolytes for operation at 500° C. *Ionics*, *16*(2), pp.97-103.

[38] Jung, H.J. and Chung, S.Y., 2017. Absence of distinctively high grain-boundary impedance in polycrystalline cubic bismuth oxide. *Journal of the Korean Ceramic Society*, *54*(5), pp.413-421.

[39] Ivantchev, S., Kroumova, E., Madariaga, G., Perez-Mato, J.M. and Aroyo, M.I., 2000. SUBGROUPGRAPH: a computer program for analysis of group–subgroup relations between space groups. *Journal of Applied Crystallography*, *33*(4), pp.1190-1191.

[40] Stokes, H.T., Orden, S.V. and Campbell, B.J., 2016. ISOSUBGROUP: an internet tool for generating isotropy subgroups of crystallographic space groups. *Journal of Applied Crystallography*, *49*(5), pp.1849-1853.

[41] Blower, S.K. and Greaves, C., 1988. The structure of β-Bi_2O_3 from powder neutron diffraction data. *Acta Crystallographica Section C: Crystal Structure Communications*, *44*(4), pp.587-589.

[42] Verkerk, M.J. and Burggraaf, A.J., 1981. High Oxygen Ion Conduction in Sintered Oxides of the Bi_2O_3-Dy_2O_3 System. *Journal of the Electrochemical Society*, *128*(1), p.75.

[43] Stinton, G.W. and Evans, J.S., 2007. Parametric Rietveld refinement. *Journal of Applied Crystallography*, *40*(1), pp.87-95.

[44] Campbell, B.J., Evans, J.S., Perselli, F. and Stokes, H.T., 2007. Rietveld refinement of structural distortion-mode amplitudes. *Ed Newsl*, *8*, p.81.

[45] Müller, M., Dinnebier, R.E., Dippel, A.C., Stokes, H.T. and Campbell, B.J., 2014. A symmetry-mode description of rigid-body rotations in crystalline solids: a case study of $Mg(H_2O)_6RbBr_3$. *Journal of Applied Crystallography*, *47*(2), pp.532-538.

[46] Stokes, H.T., Hatch, D.M., Campbell, B.J. and Tanner, D.E., 2006. ISODISPLACE: a web-based tool for exploring structural distortions. *Journal of Applied Crystallography*, *39*(4), pp.607-614.

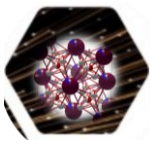

[47] Abrahams, I., Liu, X., Hull, S., Norberg, S.T., Krok, F., Kozanecka-Szmigiel, A., Islam, M.S. and Stokes, S.J., 2010. A combined total scattering and simulation approach to analyzing defect structure in Bi_3YO_6. *Chemistry of Materials*, *22*(15), pp.4435-4445.

[48] Leszczynska, M., Liu, X., Wrobel, W., Malys, M., Dygas, J.R., Norberg, S.T., Hull, S., Krok, F. and Abrahams, I., 2014. Oxide ion distribution, vacancy ordering and electrical behaviour in the Bi_3NbO_7–Bi_3YbO_6 pseudo-binary system. *Journal of Materials Chemistry A*, *2*(43), pp.18624-18634.

[49] Leszczynska, M., Holdynski, M., Krok, F., Abrahams, I., Liu, X. and Wrobel, W., 2010. Structural and electrical properties of $Bi_3Nb_{1-x}Er_xO_{7-x}$. *Solid State Ionics*, *181*(17-18), pp.796-811.

[50] Abrahams, I., Kozanecka-Szmigiel, A., Krok, F., Wrobel, W., Chan, S.C.M. and Dygas, J.R., 2006. Correlation of defect structure and ionic conductivity in δ-phase solid solutions in the Bi_3NbO_7–Bi_3YO_6 system. *Solid State Ionics*, *177*(19-25), pp.1761-1765.

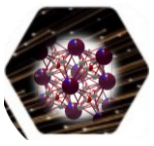

5.5 Supporting Information

Symmetry Mode Analysis: Uncovering the Ambiguities and Complexities Between Related Phases in the Bi_2O_3-Dy_2O_3-Er_2O_3 System

Sikhumbuzo M. Masina[a], Caren Billing[a], Daniel Olds[b], Rudolph M. Erasmus[c,d], David G. Billing[a,c]

[a]Molecular Science Institute, School of Chemistry, University of the Witwatersrand, Private Bag X3, Johannesburg, 2050, South Africa

[b]National Synchrotron Light Source II, Brookhaven National Laboratory, Upton 11973, New York, United States

[c]DSI-NRF Centre of Excellence in Strong Materials, University of the Witwatersrand, Private Bag X3, Johannesburg, 2050, South Africa.

[d]Material Physics Research Institute, School of Physics, University of the Witwatersrand, Private Bag X3, Johannesburg, 2050, South Africa.

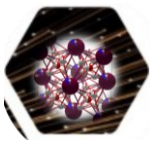

5.5.1 Rietveld Refinement

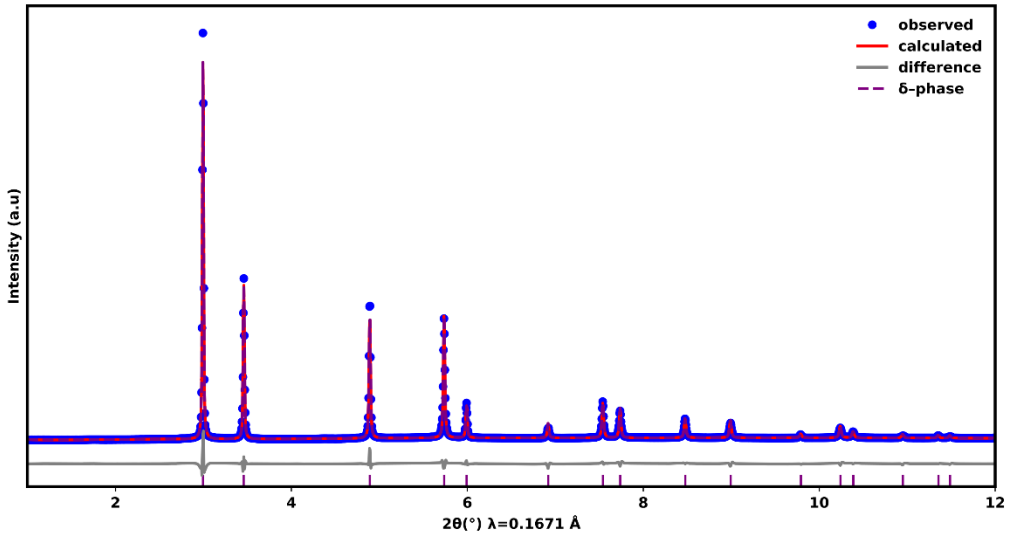

Figure S5.1. Bragg data and Rietveld refinement of the $Dy_{0.08}Er_{0.04}Bi_{0.88}O_{1.5}$ (8D4ESB) composition at ambient temperature. The fit was done using the δ-phase as the structural model modified from that of Webster *et al.* [1].

Table S5.1. Crystallographic data of the $Dy_{0.08}Er_{0.04}Bi_{0.88}O_{1.5}$ composition at ambient temperature.

Phases	δ-phase
R_{wp} (%)	9.14
Weight %	100
Space group	*Fm*-3*m*
a /Å	5. 5378(1)
Cell volume /Å^3	169.83(1)
Crystal density /g.cm^{-3}	8.9011(7)

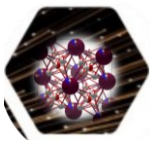

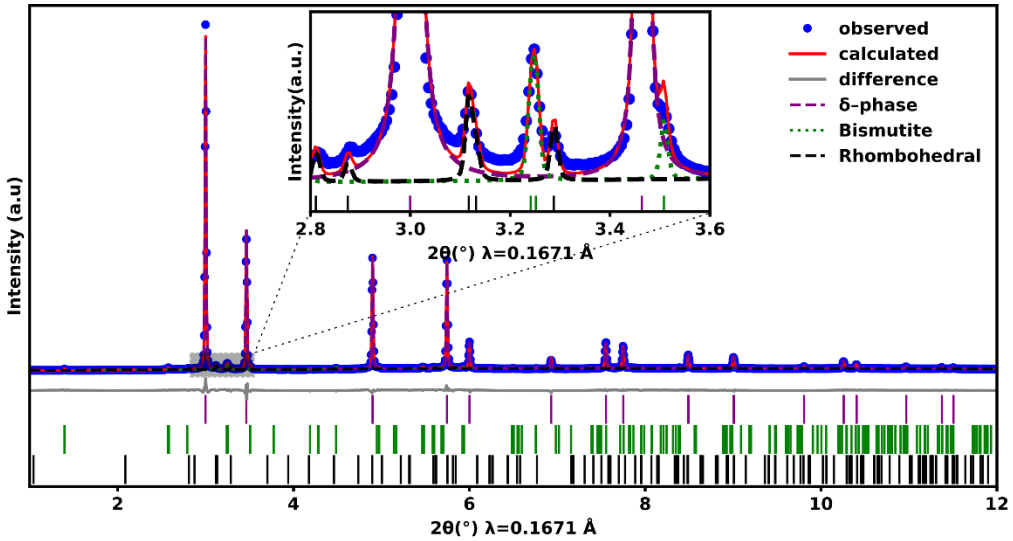

Figure S5.2. Bragg data and Rietveld refinement of the $Dy_{0.1}Er_{0.05}Bi_{0.85}O_{1.5}$ (10D5ESB) composition at ambient temperature. The fit was done using the δ-phase as the structural model modified from that of Webster *et al.* [1]. The inset shows the contributions from the bismutite and rhombohedral phases.

Table S5.2. Crystallographic data of the $Dy_{0.1}Er_{0.05}Bi_{0.85}O_{1.5}$ composition at ambient temperature.

Phases	δ-phase	Bismutite	Rhombohedral
R_{wp} (%)	7.80	7.80	7.80
Weight %	93.8(2)	3.18(7)	2.9(2)
Space group	*Fm*-3*m*	*Imm2*	*R*-3*mH*
a /Å	5.5288(1)	3.8497(7)	3.9640(5)
b /Å	-	3.8708(6)	-
c /Å	-	13.718(2)	27.518(7)
Cell volume /Å^3	169.00(1)	203.8(2)	522.3(1)
Crystal density /g.cm^{-3}	8.8921(5)	8.285(2)	6.667(2)

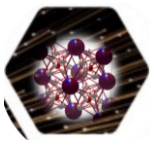

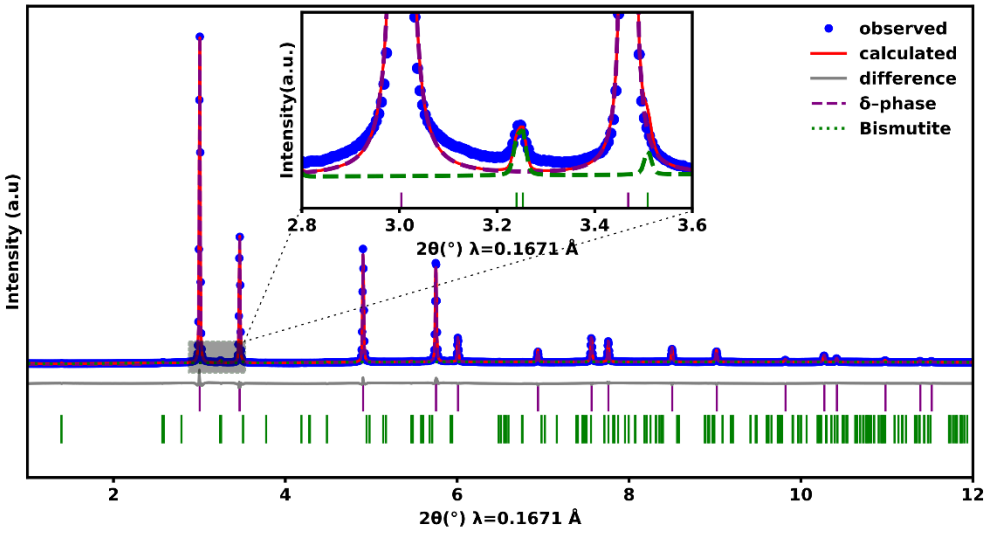

Figure S5.3. Bragg data and Rietveld refinement of the $Dy_{0.12}Er_{0.06}Bi_{0.82}O_{1.5}$ (12D6ESB) composition at ambient temperature. The fit was done using the δ-phase as the structural model modified from that of Webster *et al.* [1]. The inset shows the contribution from the bismutite phase.

Table S5.3. Crystallographic data of $Dy_{0.12}Er_{0.06}Bi_{0.82}O_{1.5}$ composition at ambient temperature.

Phases	δ-phase	Bismutite
R_{wp} (%)	8.09	8.09
Weight %	98.58(6)	1.42(6)
Space group	*Fm*-3*m*	*Imm*2
a /Å	5.5210(1)	3.846(1)
b /Å	-	3.872(1)
c /Å	-	13.721(5)
Cell volume /Å^3	168.29(1)	203.8(2)
Crystal density /g.cm^{-3}	9.1331(5)	8.287(5)

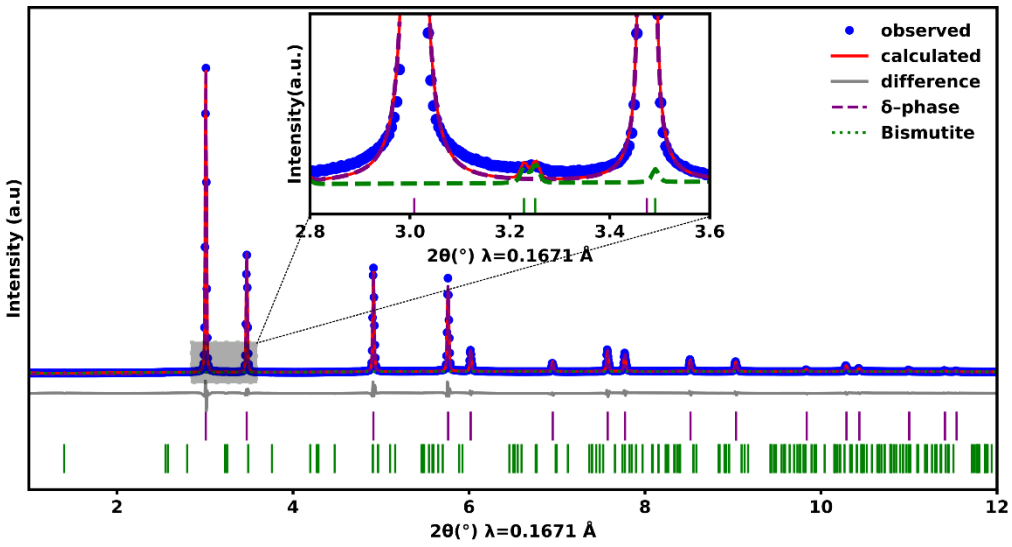

Figure S5.4. Bragg data and Rietveld refinement of the $Dy_{0.14}Er_{0.07}Bi_{0.79}O_{1.5}$ (14D7ESB) composition at ambient temperature. The fit was done using the δ-phase as the structural model modified from that of Webster *et al.* [1]. The inset shows the contribution from the bismutite phase.

Table S5.4. Crystallographic data of $Dy_{0.14}Er_{0.07}Bi_{0.79}O_{1.5}$ composition at ambient temperature.

Phases	δ-phase	Bismutite
R_{wp} (%)	9.22	9.22
Weight %	99.29(7)	0.71(7)
Space group	*Fm*-3*m*	*Imm*2
a /Å	5.5121(1)	3.856(3)
b /Å	-	3.903(3)
c /Å	-	13.69(1)
Cell volume /Å^3	167.48(1)	203.8(2)
Crystal density /g.cm^{-3}	8.8660(8)	8.22(1)

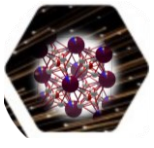

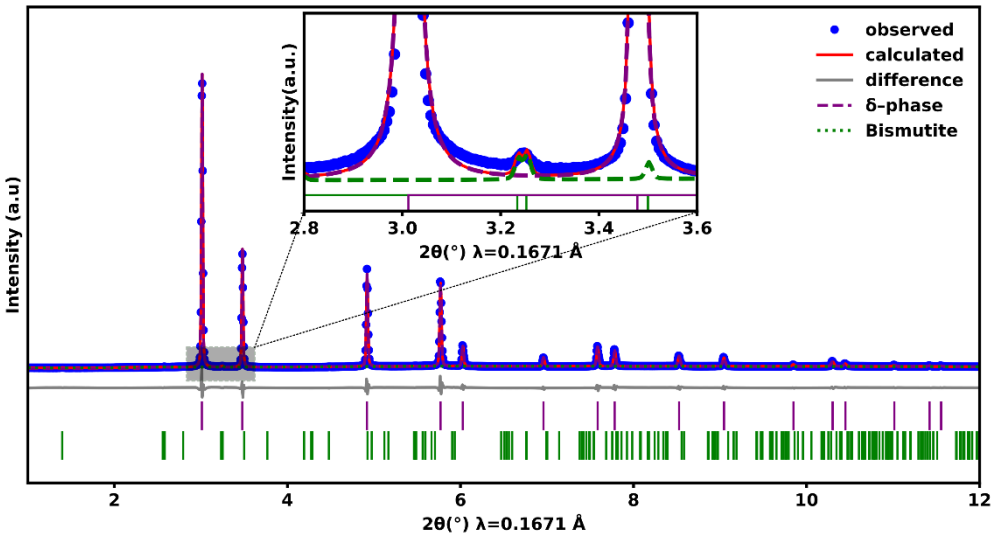

Figure S5.5. Bragg data and Rietveld refinement of the $Dy_{0.16}Er_{0.08}Bi_{0.76}O_{1.5}$ (16D8ESB) composition at ambient temperature. The fit was done using the δ-phase as the structural model modified from that of Webster *et al.* [1]. The inset shows the contribution from the bismutite phase.

Table S5.5. Crystallographic data of $Dy_{0.16}Er_{0.08}Bi_{0.76}O_{1.5}$ composition at ambient temperature.

Phases	δ-phase	Bismutite
R_{wp} (%)	8.74	8.74
Weight %	99.12(6)	0.88(6)
Space group	*Fm*-3*m*	*Imm*2
a /Å	5.5058(1)	3.851(2)
b /Å	-	3.888(2)
c /Å	-	13.703(9)
Cell volume /Å^3	166.90(1)	203.8(2)
Crystal density /g.cm^{-3}	8.8433(9)	8.255(9)

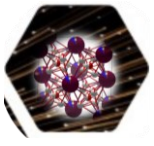

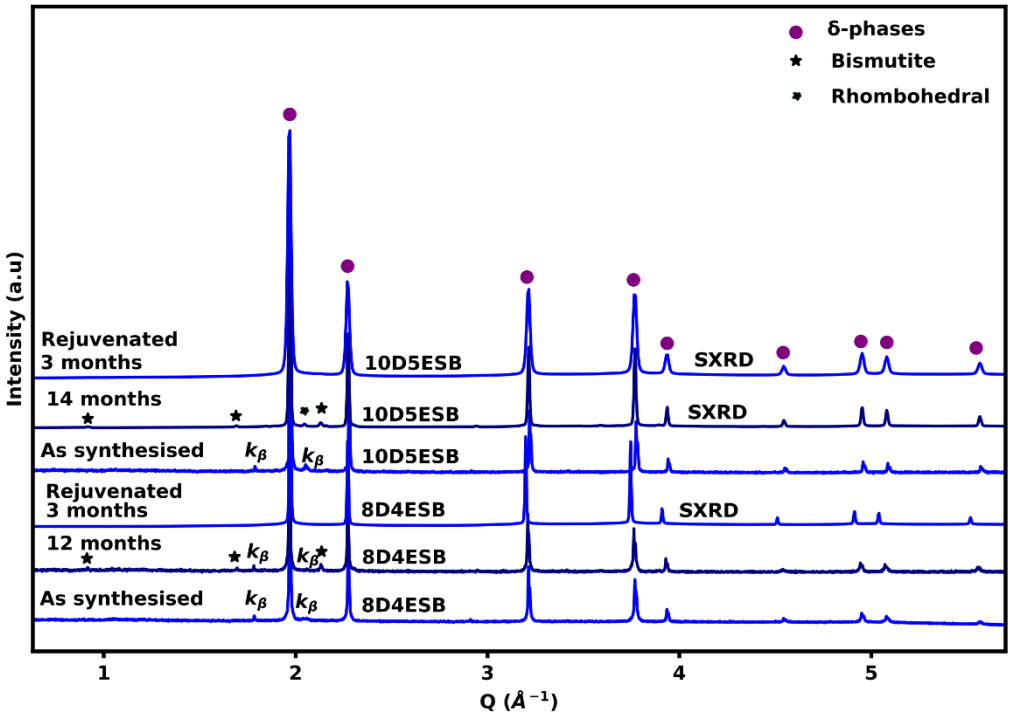

Figure S5.6. Bragg data showing the phase separation in the solid solutions of the Bi_2O_3-Dy_2O_3-Er_2O_3 system at ambient conditions with time. The rejuvenated samples were reheated at 850 °C to recover the initial phase that was obtained directly after synthesis and were measured 3 months after being reheated by SXRD.

The data in Fig. S5.6 were collected by using both in house and synchrotron diffractometers. For easier comparison across the data, the intensity was rather plotted against the magnitude of the scattering vector Q (where $Q = (4\pi \sin\theta)/\lambda$) which normalises the effect of the wavelength on peak positions. The peaks labelled k_β are remnants of unfiltered k_β radiation from the Co sealed tube that passed through the Fe k_β-filter that was used on the laboratory instrument.

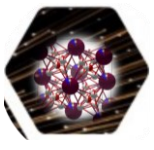

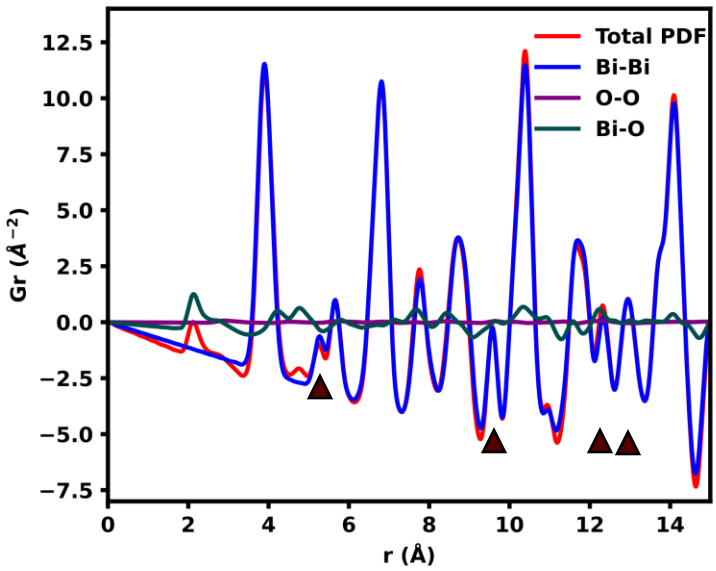

Figure S5.7. **(a)** Simulated X-ray total PDFs and partials of pure β-Bi_2O_3 phase (Q_{max} = 22 Å^{-1}) showing the contribution of the partials to the total PDF. The red triangles show the peaks that distinguish the Total PDF of β-Bi_2O_3 from that of the δ-phase, 8D4ESB and β*-phase. Model used to simulate the PDF was taken from Hull *et al.*[2].

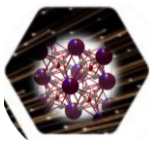

5.5.2 EIS data

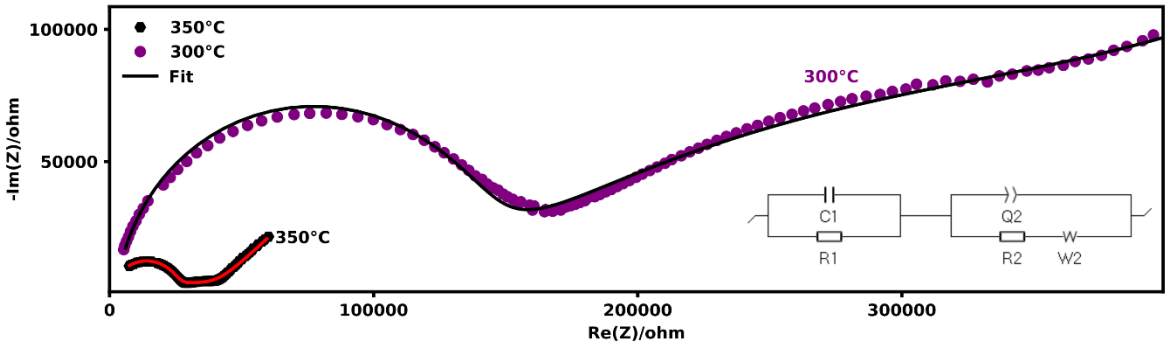

Figure S5.8. Complex impedance plot for 8D4ESB system during a heating cycle from 300-350 °C. Solid and dotted lines represent the fit from the given model in the equivalent circuit. C represent a pure capacitor, R a resistor, Q a constant phase element and W a Warburg diffusion.

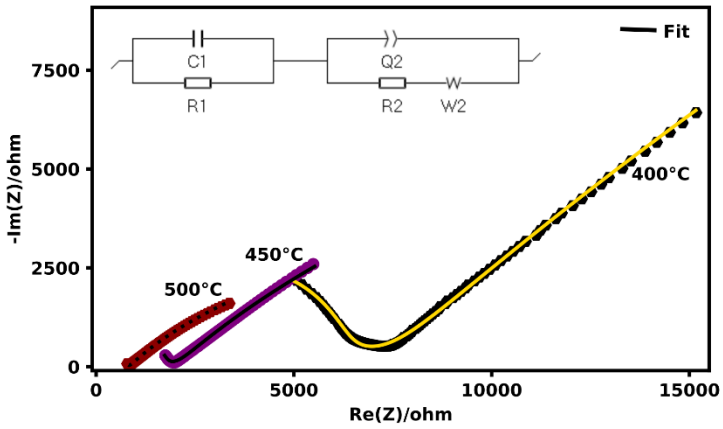

Figure S5.9. Complex impedance plots for 8D4ESB composition during a heating cycle from 400-500 °C. Solid and dotted lines represent the fit from the given model in the equivalent circuit.

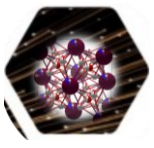

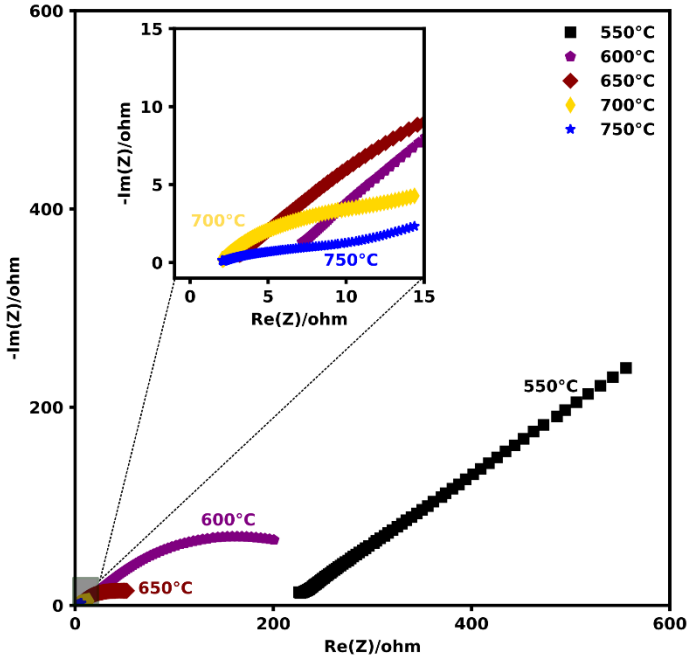

Figure S5.10. Complex impedance plots for the 8D4ESB composition during a heating cycle from 750-500 °C. No fitting was done in this temperature range. Bulk resistances were estimated by taking the total resistance as the Re(Z)-intercept.

Table S5.6. VT-EIS data for the $Dy_{0.08}Er_{0.04}Bi_{0.88}O_{1.5}$ composition during both heating and cooling cycles.

Temperature /°C	300	350	400	450	500
Heating					
R1 /Ω	124719	21511	4216	1109	469.9
C1 /F.s$^{(a1-1)}$	12.59 x 10^{-12}	14.27 x 10^{-12}	23.13 x 10^{-12}	27 x 10^{-12}	12.12 x 10^{-12}
R2 /Ω	402560	22328	4237	1260	434.8
Q2 /F.s$^{(a2-1)}$	0.2437 x 10^{-6}	0.732 x 10^{-6}	10.28 x 10^{-6}	38.29 x 10^{-6}	73.01 x 10^{-6}
a2	0.4228	0.397	0.221	0.191	0.141
s2 /Ω.s$^{-0.5}$	4.757 x 10^{5}	1.876 x 10^{5}	8.647 x 10^{5}	4.323 x 10^{4}	2.923 x 10^{4}
Temperature /°C	500	450	400	350	300
Cooling					
R1 /Ω	77.1	287.5	759.2	3478	17859
C1 /F.s$^{(a1-1)}$	-	37.59 x 10^{-12}	70.88 x 10^{-12}	40.62 x 10^{-12}	49.73 x 10^{-12}

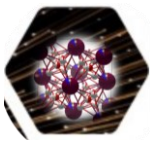

R2 /Ω	-	136.3	1024	4004	56441
Q2 /F.s$^{(a2-1)}$	-	18.1 3x 10^{-5}	49.97 x 10^{-6}	2.165 x 10^{-6}	4.005 x 10^{-9}
a2	-	0.255	0.193	0.370	0.243
s2 /Ω.s$^{-0.5}$	-	1.311 x 10^{4}	2.171 x 10^{4}	3.502 x 10^{4}	9.222 x 10^{4}

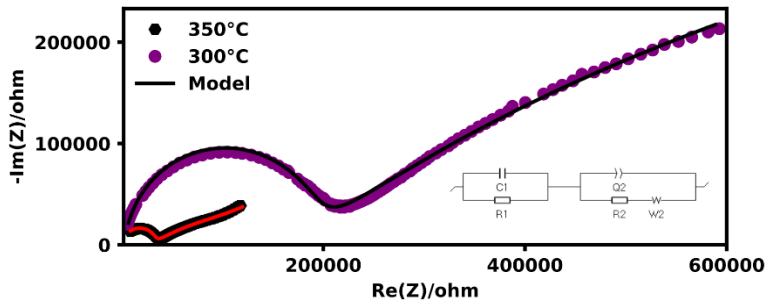

Figure S5.11. EIS data of the $Er_{0.2}Bi_{0.8}O_{1.5}$ (20ESB) composition during a heating cycle from 300-350 °C. Solid and dotted lines represent the fit from the given model in the equivalent circuit.

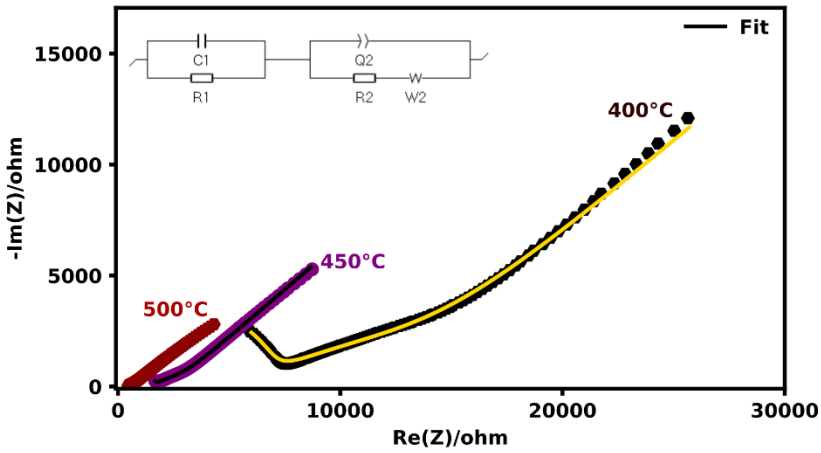

Figure S5.12. EIS data for $Er_{0.2}Bi_{0.8}O_{1.5}$ (20ESB) composition during a heating cycle from 400-500 °C. Solid and dotted lines represent the fit from the given model in the equivalent circuit.

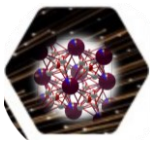

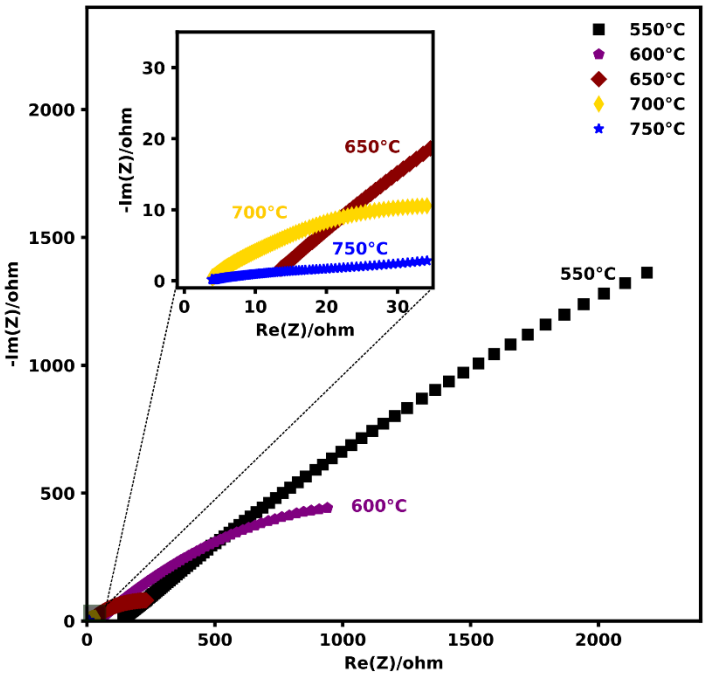

Figure S5.13. EIS data for $Er_{0.2}Bi_{0.8}O_{1.5}$ (20ESB) composition during a heating cycle from 750-500 °C. No fitting was done in this temperature range. Total conductivities were estimated by taking the total resistance as the Re(Z)-intercept.

Table S5.7. VT-EIS data for the $Er_{0.2}Bi_{0.8}O_{1.5}$ (20ESB) composition during a heating cycle.

Temperature /°C Heating	300	350	400	450
R1 /Ω	173372	29713	5909	1499
C1 /F.s$^{(a1-1)}$	9.81 x 10^{-12}	10.78 x 10^{-12}	11.29 x 10^{-12}	10.61 x 10^{-12}
R2 /Ω	1625000	158972	14386	2660
Q2 /F.s$^{(a2-1)}$	0.303 x 10^{-6}	1.11 x 10^{-6}	4.12 x 10^{-6}	10.33 x 10^{-6}
a2	0.405	0.382	0.352	0.387
s2 /Ω.s$^{-0.5}$	6.009 x 10^{5}	2.724 x 10^{5}	1.522 x 10^{5}	8.180 x 10^{4}

5.5.3 Calibration and SMA + Parametric Rietveld Refinement

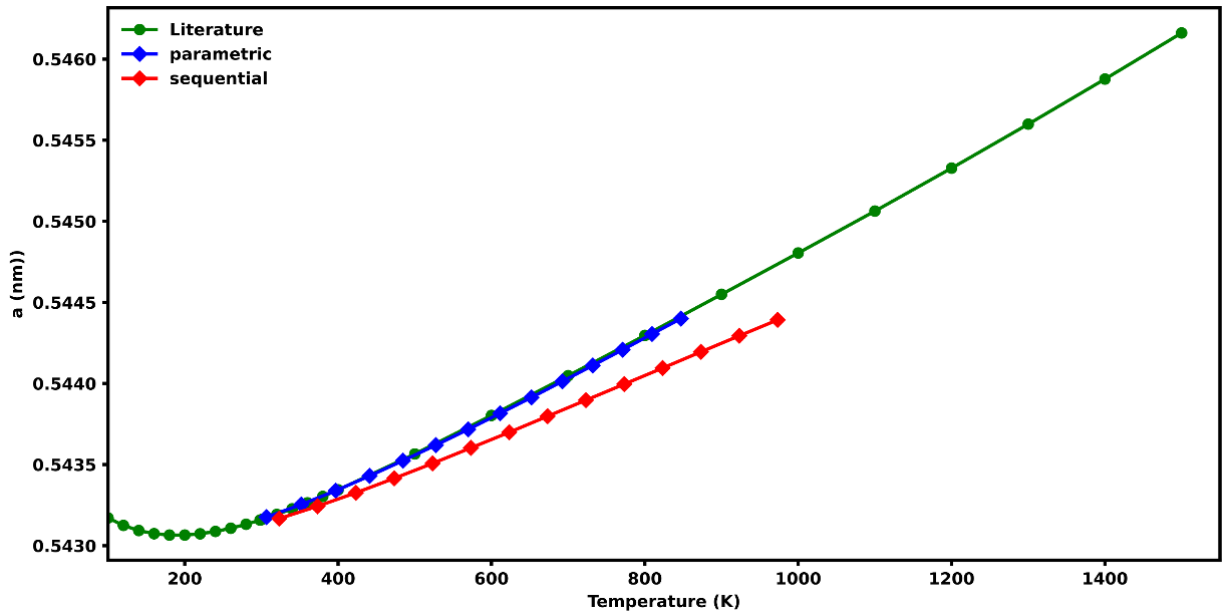

Figure S5.14. Lattice parameter of Si standard reference material as a function of temperature obtained using parametric and sequential Rietveld refinements of SXRD data. Normalized data from literature were taken from Ref. [3].

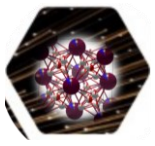

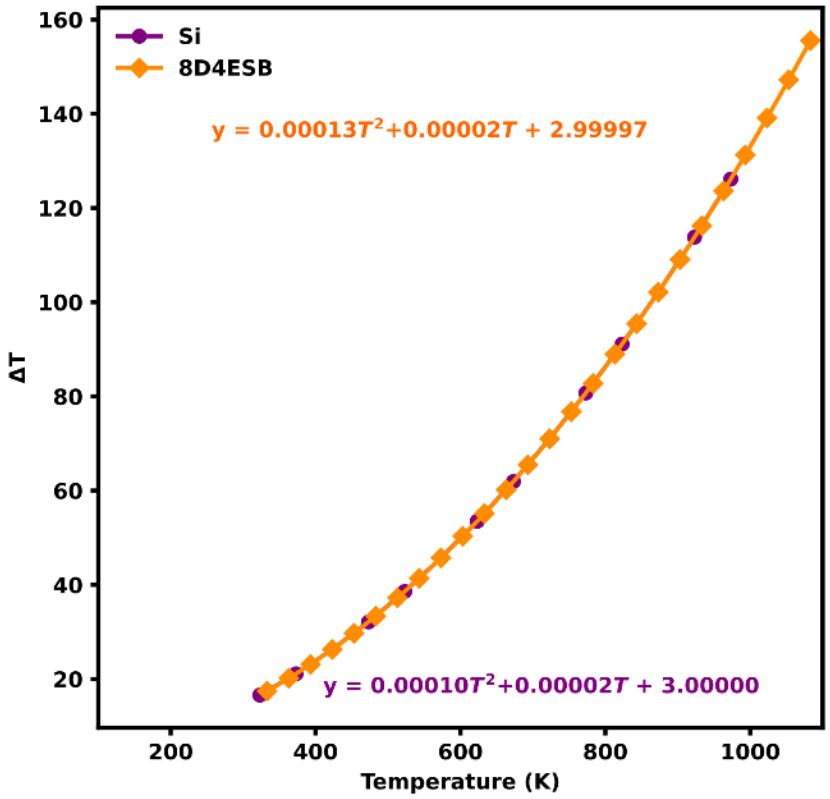

Figure S5.15. Difference between set temperature point of the hot air blower and sample temperature as a function of the set temperature point of the hot air blower for Si standard and 8D4ESB composition obtained from parametric Rietveld refinement of SXRD data. The fitted model was obtained from Ref. [4].

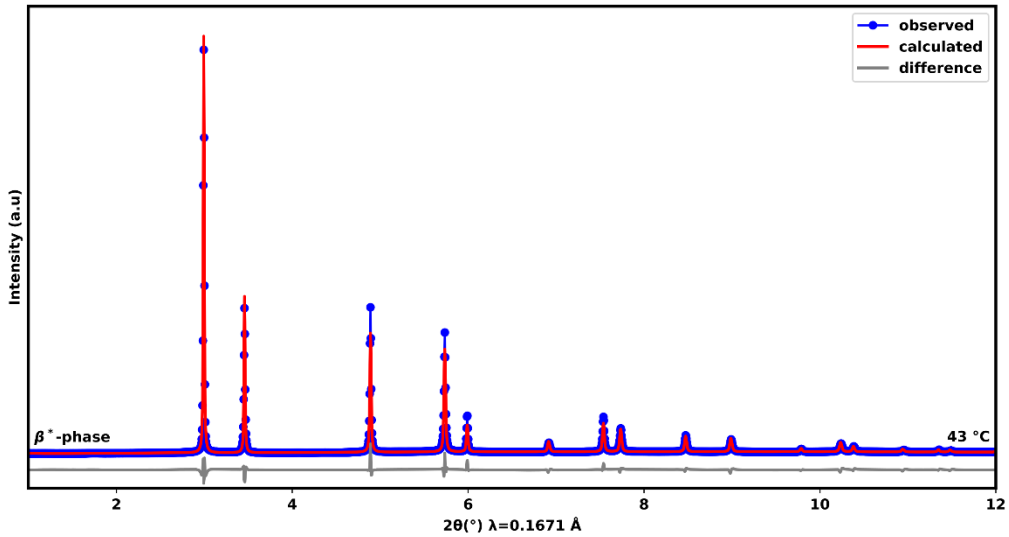

Figure S5.16. Bragg data and Rietveld refinement of the $Dy_{0.08}Er_{0.04}Bi_{0.88}O_{1.5}$ (8D4ESB) composition at 43 °C during a heating cycle. The fit was done using the β*- phase obtained from the ISODISTORT server [5,6].

Table S5.8. Crystallographic data of $Dy_{0.08}Er_{0.04}Bi_{0.88}O_{1.5}$ (8D4ESB) composition at 43 °C.

Phases	β*-phase
R_{wp} (%)	9.97
Weight %	100
Space group	*P*-42$_1$*c*
a /Å	3.8691
c /Å	5.4612
Cell volume /Å^3	81.767

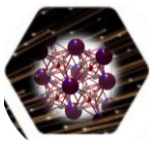

Table S5.9. Refined structural parameters for the $Dy_{0.08}Er_{0.04}Bi_{0.88}O_{1.5}$ (8D4ESB, β*-phase) composition at 43 °C.

Atom	Site	x	y	z	Occ	B_{iso} (Å²)
Bi	$2a$	0	0	0	0.88	2.62
Dy	$2a$	0	0	0	0.08	2.62
Er	$2a$	0	0	0	0.04	2.62
O(1)	$4\,d$	0	0.50	0.31(5)	0.243	2.62
O(2)	$8e$	-0.127(4)	0.497(9)	0.180(6)	0.127	2.62
O(3)	$8e$	0.512(4)	0.917(9)	0.796(6)	0.127	2.62

Table S5.10. Crystallographic data of β-Bi_2O_3 as reported by Blower and Greaves [7].

Phases	β-phase
Space group	$P\text{-}42_1c$
a /Å	7.741(3)
c /Å	5.634(2)
Cell volume /Å^3	337.61

Table S5.11. Structural parameters for β-Bi_2O_3 as reported by Blower and Greaves [7]

Atom	Site	x	y	z	Occ	B_{iso} (Å²)
Bi	$8e$	0.0178(8)	0.2539(7)	0.2532(10)	1.0	1.18(11)
O(1)	$8\,e$	0.295(1)	0.3074(7)	0.027(2)	1.0	1.7(2)
O(2)	$4d$	0	0.5	0.101(2)	1.0	2.62(4)

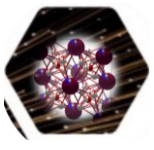

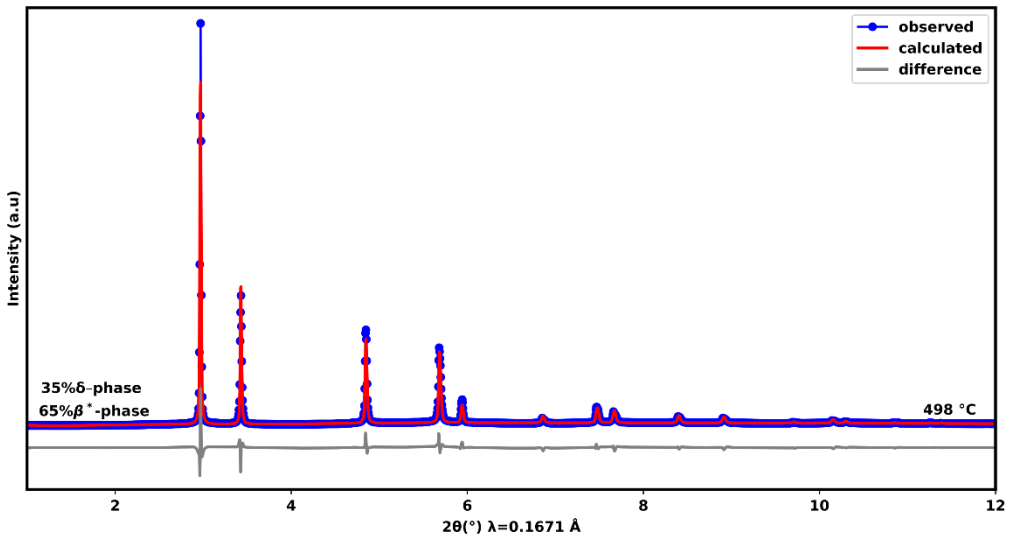

Figure S5.17. Bragg data and Rietveld refinement of the $Dy_{0.08}Er_{0.04}Bi_{0.88}O_{1.5}$ (8D4ESB) composition at 498 °C during a heating cycle and across a phase transition. The fit was done using the β*- and δ-phases obtained from the ISODISTORT server [5,6] and the structural model modified from that of Webster *et al.* [1], respectively.

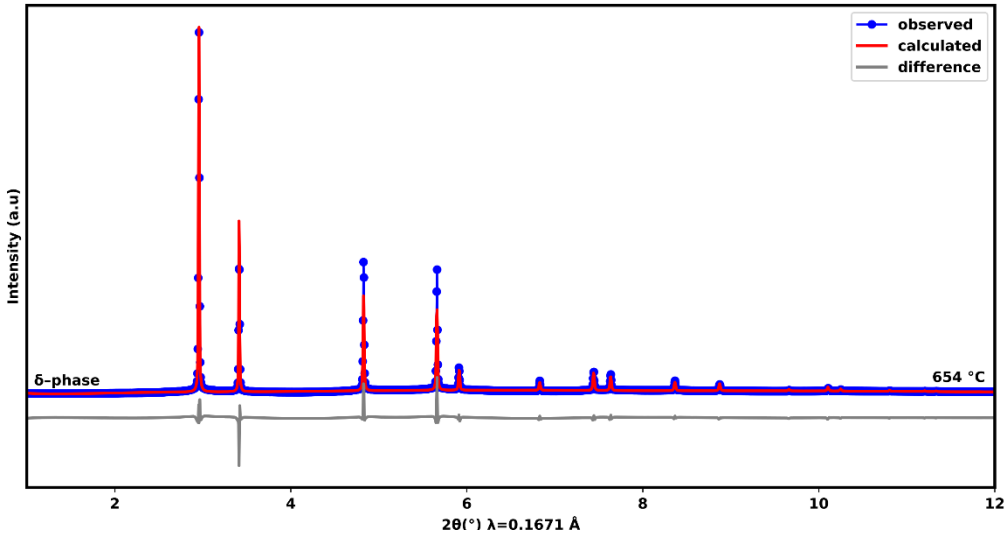

Figure S5.18. Bragg data and Rietveld refinement of the $Dy_{0.08}Er_{0.04}Bi_{0.88}O_{1.5}$ (8D4ESB) composition at 654°C during a heating cycle. The fit was done using the β*- and δ-phases obtained from the ISODISTORT server [5,6] and the structural model modified from that of Webster *et al.* [1], respectively.

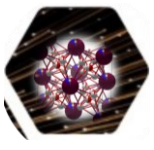

Table S5.12. Crystallographic data of $Dy_{0.08}Er_{0.04}Bi_{0.88}O_{1.5}$ (8D4ESB, *Fm*-3*m*) composition at 654°C.

Phases	δ-phase
R_{wp} (%)	16.8
Weight %	100
Space group	*Fm*-3*m*
a /Å	5.5396
Cell volume /Å^3	169.991

Table S5.13. Structural parameters for $Dy_{0.08}Er_{0.04}Bi_{0.88}O_{1.5}$ (8D4ESB, *Fm*-3*m*) composition at 654°C

Atom	Site	x	y	z	*Occ*	B_{iso} (Å^2)
Bi	4a	0	0	0	0.88	3.57
Dy	4a	0	0	0	0.08	3.57
Er	4a	0	0	0	0.04	3.57
O(1)	8 c	0.25	0.25	0.25	0.5	3.57
O(2)	32f	0.274	0.274	0.274	0.0625	3.57

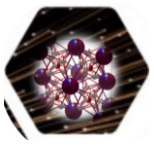

1. References

[1] Webster, N.A., Ling, C.D., Raston, C.L. and Lincoln, F.J., 2007. The structure and conductivity of new fluorite-type Bi_2O_3–Er_2O_3–PbO materials. *Solid State Ionics*, *178*(25-26), pp.1451-1457.

[2] Hull, S., Norberg, S.T., Tucker, M.G., Eriksson, S.G., Mohn, C.E. and Stølen, S., 2009. Neutron total scattering study of the δ and β phases of Bi_2O_3. *Dalton transactions*, (40), pp.8737-8745.

[3] Okada, Y. and Tokumaru, Y., 1984. Precise determination of lattice constant and thermal expansion coefficient of silicon between 300 and 1500 K. *Journal of applied physics*, *56*(2), pp.314-320.

[4] Stinton, G.W. and Evans, J.S., 2007. Parametric Rietveld refinement. *Journal of Applied Crystallography*, *40*(1), pp.87-95.

[5] Stokes, H.T., Orden, S.V. and Campbell, B.J., 2016. ISOSUBGROUP: an internet tool for generating isotropy subgroups of crystallographic space groups. *Journal of Applied Crystallography*, *49*(5), pp.1849-1853.

[6] Stokes, H.T., Hatch, D.M., Campbell, B.J. and Tanner, D.E., 2006. ISODISPLACE: a web-based tool for exploring structural distortions. *Journal of Applied Crystallography*, *39*(4), pp.607-614.

[7] Blower, S.K. and Greaves, C., 1988. The structure of β-Bi_2O_3 from powder neutron diffraction data. *Acta Crystallographica Section C: Crystal Structure Communications*, *44*(4), pp.587-589.

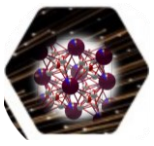

Chapter 6: Probing the Local Structure of Bi_2O_3 Chemical Derivatives: The Neglected Cation Sublattice

Sikhumbuzo M. Masina[1*], Gugulethu C. Nkala[1,2], Kevin H. Stone[3], Daniel Olds[4], Caren Billing[1], David G. Billing[1,2]

[1]Molecular Science Institute, School of Chemistry, University of the Witwatersrand, Private Bag X3, Johannesburg, 2050, South Africa

[2]DSI-NRF Centre of Excellence in Strong Materials, University of the Witwatersrand, Private Bag X3, Johannesburg, 2050, South Africa

[3]Stanford Synchrotron Radiation Lightsource, SLAC National Accelerator Laboratory, 2575 Sand Hill Road, Menlo Park, CA, 94025, USA

[4]National Synchrotron Light Source II, Brookhaven National Laboratory, Upton 11973, New York, United States

Abstract:

This work highlights the importance of the cation sublattice in influencing both the average and local structures of δ–Bi_2O_3-like phases (δ–phases). High resolution synchrotron Bragg data confirmed the stabilization of the average structure as the defect fluorite structure at ambient temperatures in ternary and quaternary oxides of Bi_2O_3 where some Bi cations were replaced with Dy^{3+} and/or Er^{3+}, Nb^{5+} and W^{6+}. Rietveld refinement of the Bragg data indicated that when the bigger cation Er^{3+}, is replaced with smaller cations W^{6+} and/or Nb^{5+}, the lattice parameter a counterintuitively increases. Total scattering data showed that the identity of the cation substituent is important in determining the positions of some Bi cations in the defect fluorite structure. Er^{3+} and Dy^{3+} cations induce monoclinic-like distortions that extends only locally in the Bi^{3+} sublattice. X-ray absorption spectroscopy provided evidence that some Dy cations, in the δ–phases, prefer to keep a similar local environment to that in the parent Dy_2O_3. W cations were found to be predominantly tetrahedrally coordinated in the δ–phases explored in this work.

Keywords: Local structure; Total scattering data; X-ray absorption spectroscopy; δ–phase; Cation sublattice

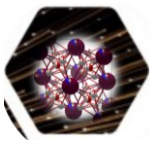

6.1 Introduction

In-depth knowledge of both the average and local structural details of functional materials is a prerequisite to establishing reliable correlations with physical properties and paves the way to designing advanced materials with enhanced properties. One of the functional materials that has found extensive use in the fabrication of devices of technological importance is Bi_2O_3 [1-4]. Bi_2O_3 exists in many different polymorphs. One of the four main polymorphs is the monoclinic α–Bi_2O_3 phase with space group type (S.G.) $P2_1/c$ which is the thermodynamically stable polymorph from ambient temperature to 729 °C [5]. Beyond this temperature, the α–Bi_2O_3 phase transitions into the cubic defect fluorite δ–Bi_2O_3 phase (S.G. $Fm\text{-}3m$), and Bi_2O_3 melts at 825 °C [5]. Depending on the cooling conditions, the δ–Bi_2O_3 phase can either transition into the tetragonal β–Bi_2O_3 phase (S.G. $P\text{-}42_1c$) at ~650 °C or into the body centred cubic γ–Bi_2O_3 phase (S.G. $I23$) at ~640 °C before reverting to the α–Bi_2O_3 phase [6, 7]. The β–Bi_2O_3 has been reported to have essentially the same cation sublattice as the δ–Bi_2O_3 phase with the oxygen vacancies being ordered along the equivalent of the <100> direction in the fluorite phase [8, 9].

In its δ–Bi_2O_3 phase, Bi_2O_3 has the highest ionic conductivity (≥ 1 S cm^{-1}) ever reported for an oxide ion conductor in its narrow stable temperature range (730 – 824 °C) [5]. To stabilise δ–Bi_2O_3-like phases at ambient temperature, hence forth referred to as stabilised δ–phases, isovalent and aliovalent cations have been used extensively to substitute the Bi^{3+} cations albeit with a moderate decrease in ionic conductivity [10-15]. The extent to which the conductivity is decreased depends on the identity of the cation and the total substituent concentration. Factors such as decrease in both polarizability and ionic radius of the substituent, trapping of vacancies and vacancy-substituent clustering have been reported to contribute to the decrease in conductivity observed in the solid solutions [16-19]. The average structures of the stabilised δ–phases are also described by the $Fm\text{-}3m$ space group type where the metal cations share the $4a$ site (0 0 0), while the oxygen ions are distributed among three different crystallographic sites, viz, the $8c$ site (0.25 0.25 0.25), the $32f$ site (x x x) where x ~0.3 and the $48i$ site (0.5 y y) where y ~0.2 [20]. The $48i$ site is an interstitial site and there is no evidence of its occupation in the parent δ–Bi_2O_3 phase [21-23], its occupation is attributed to the substituents.

The stabilised δ–phases obtained by substituting Bi^{3+} with lanthanides such as Dy^{3+} and Er^{3+} have been shown to be highly conductive but metastable and exhibit phase separation upon prolonged

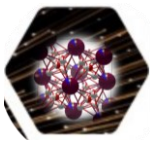

annealing at temperatures ≤600 °C [24-26]. The oxide ions and oxygen vacancies order in these systems and ionic conductivity decreases significantly as a result. These problems are normally circumvented by adding low concentrations of supervalent cations such as W^{6+}, Nb^{5+} and Hf^{4+} [14, 27], a strategy adopted in this work. Systems fabricated in this way exhibit both high conductivity and stability relative to the singly substituted systems. In this work, the systems $(Bi_2O_3)_{1-x-y}(Dy_2O_3)_x(Er_2O_3)_y$, $(Bi_2O_3)_{1-x-y-z}(Dy_2O_3)_x(Er_2O_3)_y(WO_3)_z$, $(Bi_2O_3)_{1-x-y-z}(Dy_2O_3)_x(Er_2O_3)_y(Nb_2O_5)_z$, and $(Bi_2O_3)_{1-x-y-2z}(Dy_2O_3)_x(Nb_2O_5)_y(WO_3)_{2z}$ were fabricated to stabilise the δ–phase and study the effects of the substituents in the cation sublattice which have been neglected in the literature [14, 24-27].

The local structure of the stabilised δ–phases is a subject of intense research, with the focus on the distribution of the oxide ions around the metal cations, i.e., the metal-oxygen (M–O) correlations [20, 21, 28-30]. Very few studies have been done on the metal-metal (M–M) correlations [31, 32]. Therefore, this work seeks to bridge this gap and provide a complementary picture of the local structure of the stabilised δ–phases. To this end, total scattering data, the X-ray pair distribution function (XPDF) technique and X-ray absorption spectroscopy have been used to probe the metal-metal correlations and the local environment around a specific substituent to gain insight into the local structure of the material around the metal cations.

6.2 Experimental Methods

6.2.1 Synthetic methods

Samples of $(Dy_2O_3)_x(Er_2O_3)_y(Bi_2O_3)_{1-x-y}$ (called 100xD100yESB), $(Dy_2O_3)_x(Er_2O_3)_y(WO_3)_z(Bi_2O_3)_{1-x-y-z}$ (called 100xD100yE100zWSB), $(Dy_2O_3)_x(Er_2O_3)_y(Nb_2O_5)_z(Bi_2O_3)_{1-x-y-z}$ (called 100xD100yE100zNSB), and $(Dy_2O_3)_x(Nb_2O_5)_y(WO_3)_{2z}(Bi_2O_3)_{1-x-y-2z}$ (called 100xD100yN 200zWSB) where $0.08 \leq x \leq 0.16$, $0.04 \leq y \leq 0.08$ and $0 \leq z \leq 0.02$ were prepared via the solid state reaction method. Bi_2O_3 (Sigma-Aldrich, nano, 99.999% pure), Er_2O_3 (Sigma-Aldrich, 99.999% pure), and WO_3 (Acros Organics, 99+% pure) were pre-fired at 700 ºC to remove any possible bismutite ($Bi_2O_3 \cdot CO_2$) and moisture. These have been shown to alter the phase evolution in the formation of Bi_2O_3 solid solutions [7]. Dy_2O_3 and Nb_2O_5 were obtained by thermal decomposition of $Dy(NO_3)_3 \cdot 6H_2O$ (Sigma-Aldrich, 99.99% pure) and ammonium niobate(V) oxalate hydrate (Sigma-Aldrich, 99.99% pure) using the method employed by Melnikov *et al.* [33].

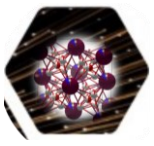

Stoichiometric amounts of Bi_2O_3, Dy_2O_3, Er_2O_3, Nb_2O_5, and WO_3, were mixed in an agate mortar and manually ground for an hour in acetone (99.56% pure, KEM*i*CAL) to create the desired systems. The ground powders were dried in an oven at 80 ºC for 12 hrs before being fired in a furnace from ambient temperature to 800 ºC at a heating rate of ~6 ºC/min. The powders were then soaked at 800 ºC in air for 24 hrs before being left in the furnace to cool to ambient temperature (over a period of ~12 hrs). An intermediate grinding step was performed before the powders were pressed into pellets using a uniaxial cold press at a constant pressure of 75 MPa and a 13 mm die. The pellets were then sintered at 850 ºC for a further 24 hours before being quenched in air to ambient temperatures.

6.2.2 Bragg data

Beamline 2-1 at the Stanford Synchrotron Radiation Light Source (SSRL) was used to collect the Bragg data. The source is a 1.3 T bending magnet, and the diffractometer is equipped with a Huber 2-circle goniometer. The radiation was monochromatized by using a Si (111) crystal in standard configuration. The wavelength was 0.72929 Å and the measurements were performed in transmission mode using a Kapton capillary. The wavelength used was chosen so that all the absorption edges of the elements (Bi, Dy, Er, Nb and W) in the samples were avoided to increase data quality. The diffractometer employs a Pilatus 100K small area detector that was mounted at an ~700 mm distance downfield of the sample. A diamond powder was mixed with the sample to act as an internal standard to account for sample displacement. 2-D images were calibrated and integrated into a typical powder diffraction pattern.

6.2.3 Total scattering and the PDF technique

Data for total scattering was collected at the beamline 28-ID-1 at NSLS II at Brookhaven National Laboratory. The X-ray source is a damping wiggler, and the beam is focused horizontally and vertically by a side bounce monochromator (SBM) and a vertically focusing mirror (VFM) respectively. A monochromatic wavelength of 0.1671 Å in Debye-Scherrer geometry was used. The diffractometer employs a PerkinElmer area detector (200 × 200 μm pixel size) which was mounted at a direct distance of ~241 mm for measuring total scattering data. Kapton capillaries with an outside diameter of 0.9 mm were used to hold the sample. LaB_6 (NIST SRM 660c) and Si (NIST SRM 640d) were used as external calibrants for the measurements. Total scattering data

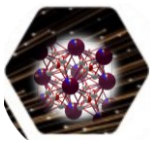

were reduced using xPDFsuite [34]. The reduced PDFs were obtained by the sine Fourier transform of the Q weighted and reduced total scattering structure function S(Q), i.e.,

$$G(r) = \left(2/\pi\right) \int_{Q_{min}}^{Q_{max}} Q[S(Q) - 1]\, sin(Qr)\, dQ$$

where $G(r)$ is the reduced PDF, $Q = 4\pi \sin\theta / \lambda$ is the magnitude of the scattering vector and r is the radial distance. Q_{min} and Q_{max} values were 0.1 and 25.1 Å^{-1} respectively. The reduced PDFs were analysed using small box modelling as implemented in TOPAS Academic [35, 36].

6.2.4 X-ray Absorption Spectroscopy

BL2-2 at the SSRL was used to perform the X-ray absorption spectroscopy (XAS) measurements. The source is a bending magnet and can perform measurements in the energy range of 4.5-37 keV. The energy of the unfocused radiation was tuned by using a double crystal Si (220) monochromator to scan across the L_3-edges of Dy, Er, and W. The measurements were done in fluorescence mode and the samples were pelletized. Spectra were processed by using the Demeter package [37] to obtain the first and second derivative spectra. Only the X-ray absorption near edge structure (XANES) part of the spectra were considered in this work.

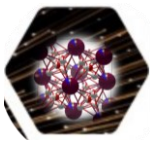

6.3 Results and Discussion

6.3.1 Average Structure Analysis

In all four of the synthesised systems, the δ–phase was stabilised to ambient temperature (Fig. 6.1). No extra peaks were observed, suggesting that the materials consisted of a single crystalline phase.

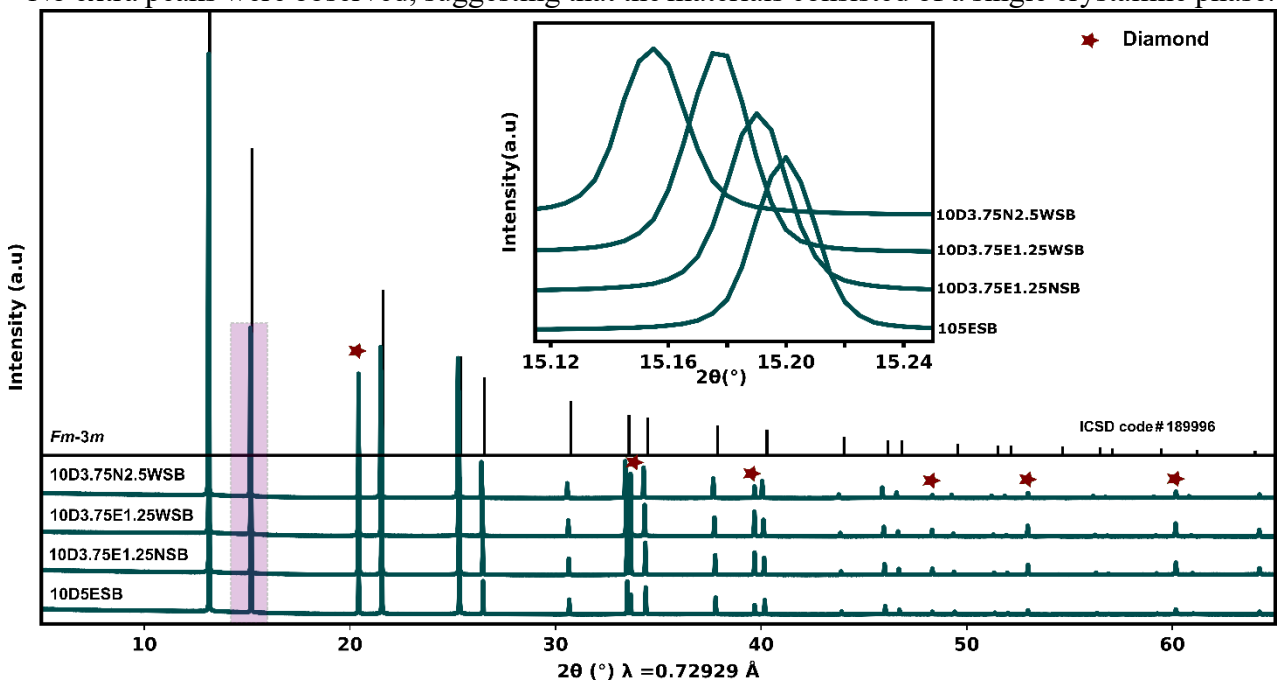

Figure 6.1. Bragg data showing that the average structure of the solid solutions belong to the same space group type (*Fm*-3*m*) as that of δ–Bi_2O_3. The inset highlights significant variations in the peak positions of the second peak, but all the peaks were shifted. Diamond powder was used as an internal standard.

Interestingly, a peak shift to lower 2θ for all the systems where Er^{3+} was substituted partially or totally with W^{6+} and/or Nb^{5+} (Fig. 6.1 inset) was noted. This implied an expansion in the unit cell occurred which is counterintuitive because the larger Er^{3+} (0.89 Å) cations were being replaced by smaller cations, W^{6+} (0.60 Å) and Nb^{5+} (0.64 Å), so a reduction in the unit cell would be expected. The ionic radii given in brackets are for the octahedrally coordinated metal ions to oxygen [38], as would be expected in the cubic δ–phase.

The use of the diamond internal standard allowed the direct inference from the Bragg data of the change in the unit cell with changing identity of the substituent cation by revealing the effects of capillary displacement and beam optics on the peak positions.

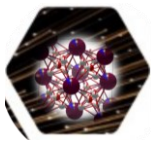

Rietveld refinement results (Fig. 6.2(a), Table S6.1-S6.8 and Fig. S6.1-S6.3) confirmed the average structure to be that of the δ–phase and an increase in lattice cell parameter, *a,* as the concentration of Er^{3+} was being reduced (Fig. 6.2(b)). As noted by Borowska-Centkowska *et al.* [28] and Leszczynska *et al.* [39], since W^{6+} and Nb^{5+} are smaller than Er^{3+}, they favour a tetrahedral geometry in the structure (even when tetrahedrally coordinated W^{6+} (0.42 Å) and Nb^{5+} (0.48 Å)

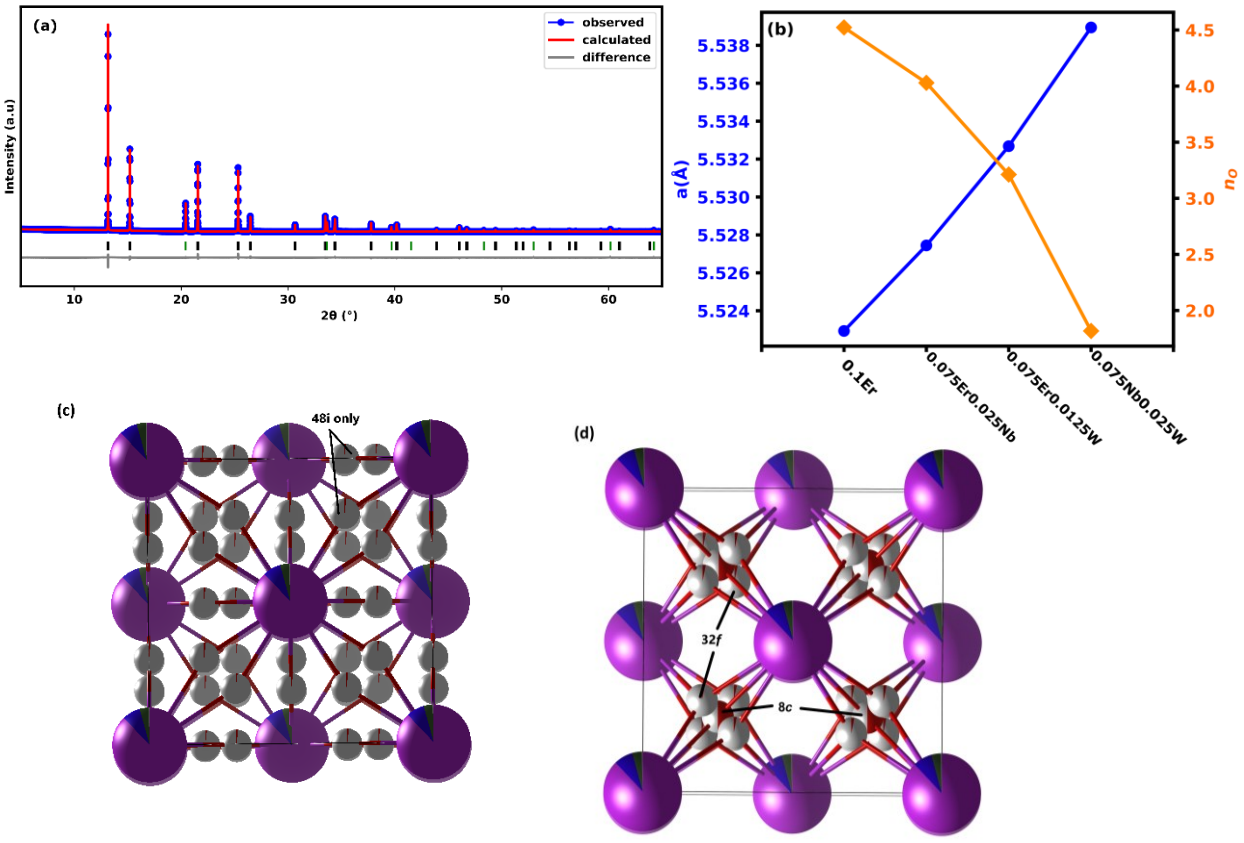

Figure 6.2. **(a)** Rietveld refinement fit of the 10D5ESB composition (R_{wp} =1.62). Green hkl's are for the diamond internal standard. **(b)** The correlation between the unit cell parameter *a* and the number of oxygens (n_O) in the 8*c* site per unit cell as the concentration of Er is reduced. **(c)** and **(d)** show the position of the O ions in the 48*i* and the 32*f* and 8*c* sites, respectively, relative to the cations. Purple spheres represent cations, red fractions represent oxide ions and white fractions represent oxide ion vacancies.

are smaller than Er^{3+} [38]). This results in oxygens occupying more 32*f* and/or 48*i* sites rather than the 8*c* sites around these metal ions as compared to that for Er^{3+}. This leads to an expansion in the unit cell due to the position of the 48*i* and 32*f* sites relative to the cations (Fig. 6.2(c) & 6.2(d)), counteracting possible contraction due to the reduced average radius of the W^{6+} and Nb^{5+} cations. The decrease in the occupancy of the 8*c* sites as Er^{3+} is replaced by W^{6+} and/or Nb^{5+} was observed despite the reduced sensitivity of X-rays to oxide ions in the midst of heavy metals like

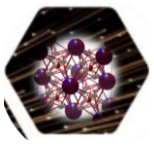

Bi (see Fig. 6.2(b)). A similar trend in the occupancy of the 8*c* sites was also observed from neutron diffraction data in a similar system [39].

6.3.2 Total scattering and the PDF Technique

Information such as average bond lengths obtained from peak positions and disorder inferred from peak broadness can be extracted in a model-independent way (i.e., without a structural model) from a PDF because of its definition as the measure of the probability of finding an atom at a distance *r* from a reference atom [40]. Qualitative analysis of the reduced PDFs of all the systems explored in this work showed that the observed PDFs are similar to the simulated reduced PDF of 25ESB which has been reported to have the δ–phase with space group type *Fm*-3*m* (Fig. 6.3) [41]. This confirmed the results obtained from the Rietveld refinement. The modal M–O bond length obtained from fitting the first peak using xPDFsuite (shown by a black arrow in Fig. 6.3) varied between 2.15 – 2.16 Å for the systems synthesised (Table 6.1). These are in the same range as the modal bond lengths reported by Hull *et al.* [21] and Norberg *et al.* [42] for the pure α–, β– and δ–Bi_2O_3 polymorphs. The M–O peak is also highly asymmetric for the synthesised samples, reflecting a non-Gaussian distribution of M–O bond lengths in the structure. Comparison of these bond distances with those obtained from Rietveld refinement of Bragg data (Table 6.1) of the synthesised samples when the oxygens are predominantly placed in the 8*c* site (which should give

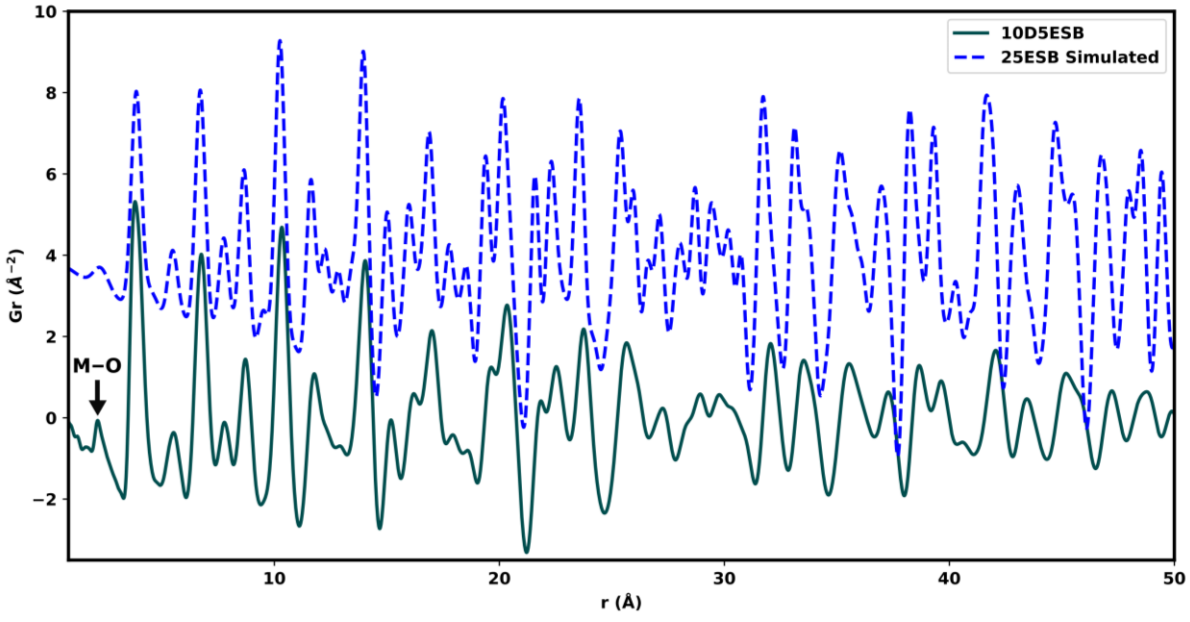

Figure 6.3. Simulated and experimental reduced total PDFs of 25ESB and 10D5ESB, respectively.

modal M–O distances) shows some discrepancy and this indicates a difference between the average and local structures as explained in greater detail by Norberg *et al.* [42].

Table 6.1. Modal bond lengths obtained from both PDF peak fitting and Rietveld refinement of Bragg data for a given composition.

System	Modal M–O bond length (Å) from PDF	Modal M–O bond length (Å) from Rietveld
10D5ESB	2.15	2.39
10D3.75E1.25WSB	2.15	2.40
10D3.75E1.25NSB	2.16	2.39
10D3.75N2.5WSB	2.16	2.40

Small box modelling of the PDF data of 10D5ESB using the *Fm*-3*m* model produced a very good fit in the *r*-range 5-50 Å (Fig. 6.4). This means that the model describes the average structure of the system very well and agrees with the Rietveld refinements results discussed earlier. However, a closer look at the first M–M peak at around 3.9 Å, reveals a poor fit (Fig. 6.4 inset) which is due to the presence of a pronounced shoulder and indicates that there really are at least two distinct M–M distances. Furthermore, the shoulder occurs at higher *r* than the main peak, which cannot be explained by a shorter weighted average M–M distance expected from the shorter radii of the substituents. The shorter weighted average M–M distance due to the substituents should cause an asymmetry to appear at lower *r* than the main peak if the substituents were occupying the 4*a* site in *Fm*-3*m* as observed by Gateshki *et al.* [43]. There was also no observed evidence of phase separation in the high-resolution synchrotron Bragg data (see Fig. 6.1). This suggested a shift in

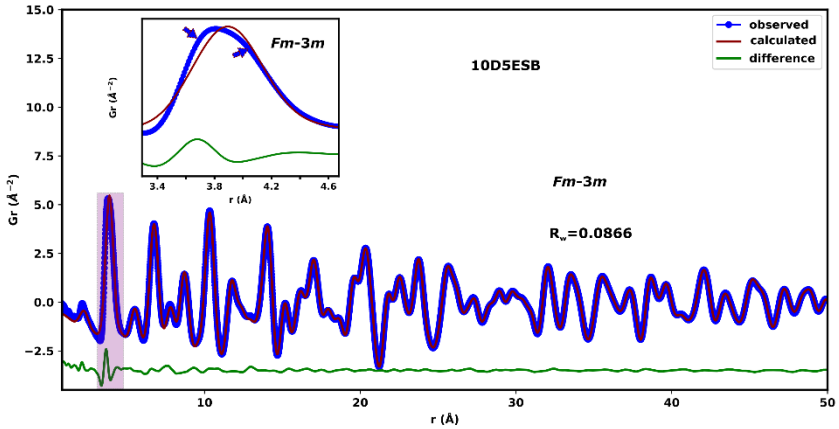

Figure 6.4. Small-box modelling of the reduced total PDF data of 10D5ESB. The inset and arrows highlight the misfit and asymmetry on the second peak dominated by the shortest M–M distances.

the metal cations to different positions in the local structure – an observation that cannot be easily captured by a Rietveld refinement.

The peak asymmetry and shoulder were amplified with the increase in total substituent concentration (TSC), suggesting that the peak asymmetry was induced by the substituents **(**Fig. 6.5). All the PDF were produced by using the same parameters (such as Q_{min} and Q_{max}). Interestingly, in the system without the cation Er^{3+} i.e., DNWSB, the peak asymmetry is very subtle, but the peak is still broad and is just flatter at the top (Fig. 6.5). This suggested that the Er^{3+}

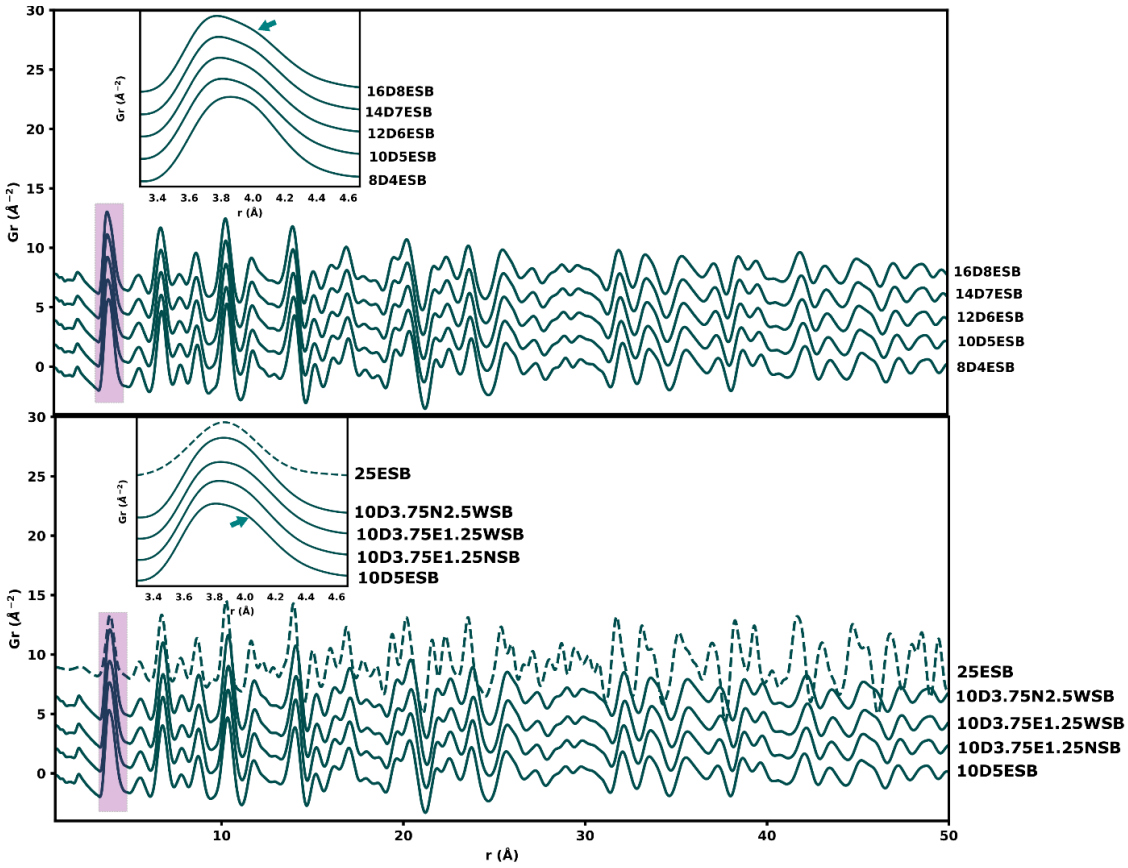

Figure 6.5. Reduced experimental total PDFs of the four specified systems as well as that simulated for 25ESB are shown. Evolution of the PDFs as a function of TSC is also shown. The insets and arrows highlight the shoulders on the second peak dominated by the shortest M–M distances.

cations contribute more to the asymmetry. In the simulated data for 25ESB, there is no peak asymmetry because both the Bi and Er cations were distributed in one site (4*a*) in this structure.

It has been reported that the cations can be displaced along the <100>, <110> and <111> directions which correspond to the displacement of cations from 4*a* to the 24*e*, 48*h* and 32*f* sites, respectively [21, 41, 44]. In this work, when some of the Bi^{3+} (50% maximum) and the substituent cations (50%

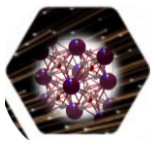

maximum) were placed on these sites while the rest remained at the 4*a* sites in the structure and the models were refined against the data of the 10D5ESB composition, there were no improvements in the fits (Fig. S6.4-S6.6). This was observed in all the substituted systems explored. The positions of the main peak (at ~3.81 Å) in the first M-M peak (see Fig. 6.5 inset) and that of the shoulder (at~4.10 Å) are not at the position (~3.91 Å) you would expect for the cell size obtained from Rietveld refinement of the 10D5ESB composition, hence the mismatch in the fit (see Fig. 6.4 inset). The intensity of the shoulder is also more than halfway above that of the main peak (Fig. 6.5 insets, green arrows). The total substituents concentration and the X-ray atomic form factors are less than those of Bi for all the substituents, therefore a displacement of substituents alone away from 4*a* site is not enough to cause the shoulder. The Bi^{3+} cations should be involved in forming the shoulder and/or asymmetry.

The model for the β–Bi_2O_3 phase (*P*-42$_1$*c*) was also tested at the local length scale ($r \leq 4.5$ Å, Fig. 6.6) in 10D5ESB since the cation sublattice of this phase is essentially similar to that of the δ–Bi_2O_3 phase. The *P*-42$_1$*c* model fitted the data better than the *Fm*-3*m* model (see Fig. 6.4 and compare with Fig. 6.6) in the range $r \leq 4.5$ Å but does not give a shoulder. Therefore, both these models are not satisfactory in describing the overall local structure of the metal sublattice and the first M–O peak on their own for all the substituted systems explored.

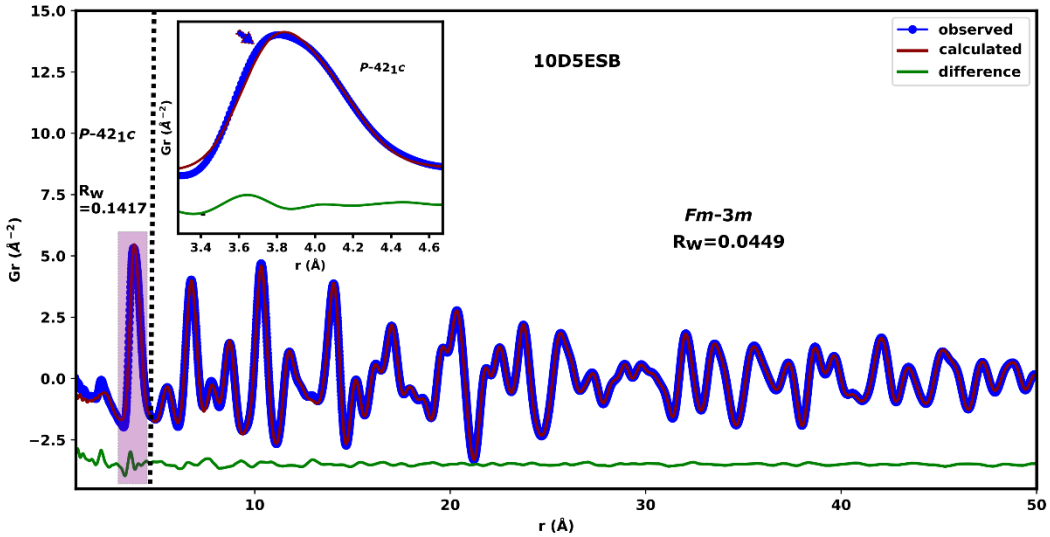

Figure 6.6. Small-box modelling of the reduced total PDF data of 10D5ESB illustrating how the *P*-42$_1$*c* model reproduces the asymmetry on the first M–M peak.

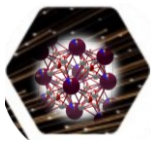

A plot of the simulated PDFs of the four main unsubstituted polymorphs of Bi_2O_3 revealed that the model structures with space group types *Fm*-3*m* and *P*-42$_1$*c* do not exhibit any shouldering in the second peaks (Fig. 6.7 inset), and that second peaks are at a slightly higher *r* position than that obtained from the observed data of the substituted systems. The model of the γ–Bi_2O_3 phase (*I*23) has its first M–M peak at a similar position to that of the first M–M peak in the observed data of 10D5ESB but does not display any asymmetry or a shoulder. The *P*2$_1$/*c* model of the monoclinic α–Bi_2O_3 phase show some similarity to the observed data of 10D5ESB (Fig. 6.8 inset). The

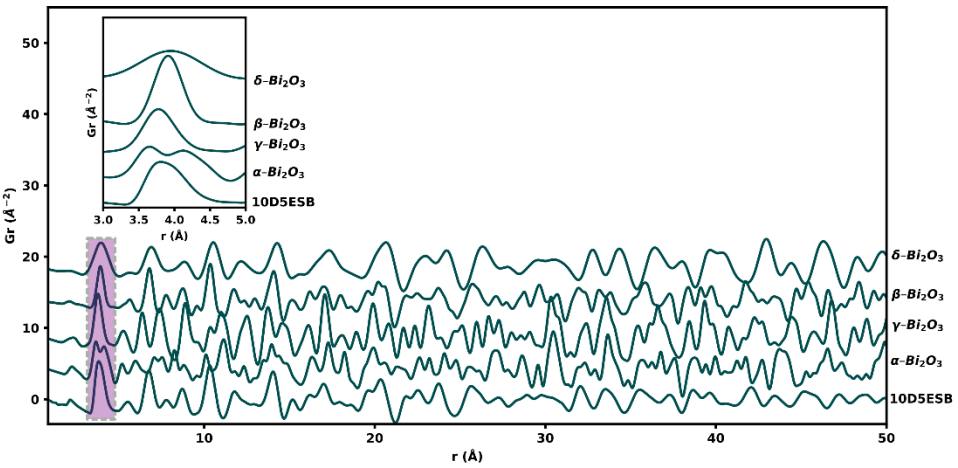

Figure 6.7. Simulated reduced total PDFs of the different polymorphs of Bi_2O_3.

shoulder and asymmetry of the first M–M peak and the direction of tailing are similar. However, the peak positions are not closely matched to that for the substituted sample. The highly asymmetric first peak at ~2.15 Å (predominantly from the M–O correlations) for the α–Bi_2O_3 polymorph also reflects that seen for the substituted systems. A similar situation was reported by Gateshki *et al.* [45] for zirconium oxide involving the monoclinic (*P*2$_1$/*c*) and cubic (*Fm*-3*m*) phase.

Small-box modelling using *P*2$_1$/*c* at the local level (up to 4.5 Å) produced a very good fit (Fig. 6.8 inset). This is a very short range and thus the parameters are highly correlated, but this does suggest that the substituents induced some local level monoclinic-like distortions to stabilize the δ–Bi_2O_3-like phase to ambient temperature; a phenomenon common in materials with the fluorite structure [43, 46]. This is also a common strategy for fitting and showing local level distortions in PDF [43, 47-49]. It should be noted that the average structure of the α–Bi_2O_3 phase is different from both the observed data of the substituted systems and the δ–Bi_2O_3 phase (see Fig. 6.7 beyond 4.5 Å). These results demonstrate the inadequacy of traditional crystallographic methods in fully

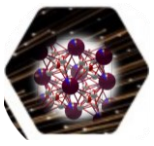

describing the structure of some functional materials and reinforce the idea of using both the local and average structure to describe the structure of such materials more comprehensively.

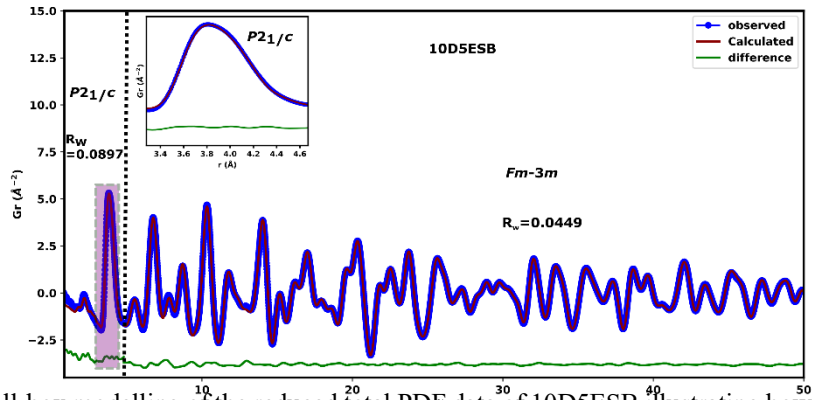

Figure 6.8. Small-box modelling of the reduced total PDF data of 10D5ESB illustrating how the $P2_1/c$ model fits the data at low r.

6.3.3 The L_3-edge XANES analyses of Dy, Er and W dopants

Total atomic X-ray PDF can have some limitations as a local structure probe. Peaks from different atomic pairs with comparable interatomic distances can overlap and make it hard to obtain an accurate picture of the local environment around a particular type of atom. This limitation is amplified when the weighted X-ray atomic form factors of the atomic pairs with overlapping peaks are comparable (e.g. Dy–O and Er–O). When lighter atoms are in the midst of heavier ones, the signals from the heavier atoms dominate and sensitivity of the technique to the lighter atoms is significantly reduced as is the case of O in the presence of Bi, Dy and W in this work. To probe the local environment of a particular substituent, an element-specific technique such as XAS can provide insights into the electronic structure, oxidation state and geometry of the site occupied by a specific absorber. In this work, XANES data of Dy, Er, and W were used to provide some insights into the geometry of the sites occupied by the substituent in the materials.

The normalized spectra of the Dy L_3-edge XANES in all four systems and the pure Dy_2O_3 oxide are shown in Fig. 6.9. The white line (intense peak) feature in the Dy L_3-edge XANES spectra (as well as the Er L_3-edge XANES spectrum in Fig. S6.7(a)) is attributed predominantly to the promotion of an electron from $2p_{3/2}$ to $5d$ orbitals and all the spectra showed similar characteristics. The Dy_2O_3 powder was included as a reference to probe the oxidation state of Dy in the bismuth oxide solid solutions. The peak at approximately 7810 eV indicated with an arrow in Fig. 6.9 is characteristic of Dy_2O_3 and is associated with a well-ordered average structure [50]. It was

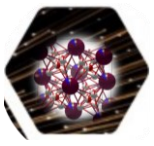

virtually absent in the spectra of the δ–phases, suggesting that the Dy cations were successfully incorporated into the disordered Bi_2O_3 average structure.

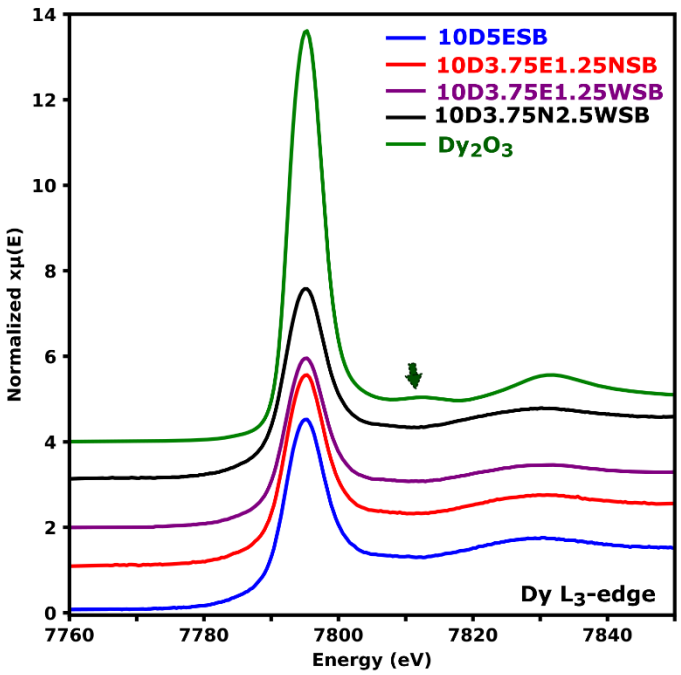

Figure 6.9. Normalized spectra of the Dy L_3-edge. The arrow indicates the peak characteristic of the *C-type* (*Ia*-3) structure of Dy_2O_3.

The first derivative normalized spectra showed virtually the same edge position – taken as the position of the highest point in the plot (Fig. 6.10(a), dashed line). The edge position is heavily dependent on the oxidation state of the absorber and the local environment around it. This unsurprisingly suggests that the Dy has a similar oxidation state across all compositions including in Dy_2O_3 [51]. To better understand the electronic structure of Dy, the second derivative of the white lines of the substituted systems were considered as it is commonly done for most rare earth elements [52, 53] and were compared with those of the parent oxide (Dy_2O_3). Dy_2O_3 showed two distinct minima in the second derivative spectrum (Fig. 6.10(b)) indicating that there are at least two different electronic transitions giving rise to the observed white line. With Dy_2O_3 having the space group type *Ia*-3 (Fig. S6.8), the Dy cations occupy two sites; *viz*: the 8*b* site which has C_{3i} site symmetry and the 24*d* site with a site symmetry of C_2 (Fig. S6.8 inset). The 5*d* states will be split differently in these sites. Therefore, the overall XAS spectrum of Dy_2O_3 should at least reflect the weighted average from the two sites occupied by the cations. From the crystallographic information file for Dy_2O_3 (ICSD# 66736), each site has a full occupancy of one, therefore, at most, the ratio of the contribution to the spectra of the 8*b* and 24*d* sites is expected to be 1:3.

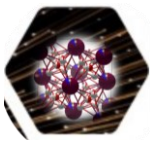

It has been reported that for the Dy and Er cations in a pure O_h environment, essentially, a single minimum is obtained from the second derivative of the spectra [52]. This would be expected from the spectra of Dy^{3+} and Er^{3+} at the 4*a* sites in the average structure of δ–Bi_2O_3 which has O_h site symmetry. However, the overall shape of the second derivatives of the spectra obtained from the compositions with Dy^{3+} (Fig. 6.10(b)) and Er^{3+} (Fig. S6.7(b)) resembles that of Dy^{3+} in Dy_2O_3. This is an indication that at least some of the Dy^{3+} and Er^{3+} cations are not occupying the 4*a* sites in the *Fm*-3*m*. This is more pronounced for the Nb containing compositions. The smaller peak minima on the left side of the second derivatives were not prominent in the substituted bismuth oxide compositions compared to the parent oxide (Dy_2O_3), probably due to a lower ligand field splitting energy of the 5*d* orbitals in the structure and the slight changes in the site symmetries of Dy^{3+} and Er^{3+} in the substituted compositions compared to the environments of Dy^{3+} and Er^{3+} in the pure oxides (Fig. 6.10(b) and Fig. S6.7(b)).

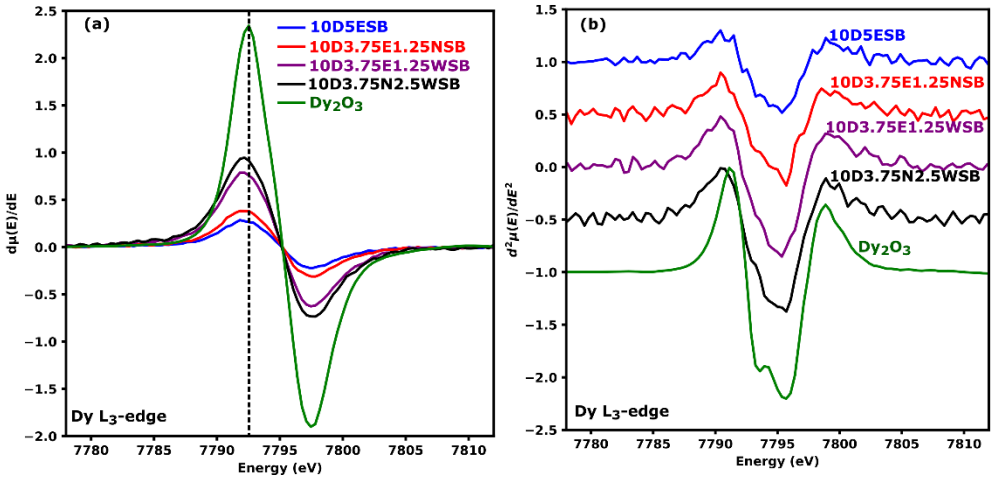

Figure 6.10. Normalized first **(a)** and second **(b)** derivative Dy L_3-edge XANES spectra of the Dy containing compositions.

The study of the W L_3-edge XANES was conducted to gain insight into the coordination environment and oxidation state in W-doped bismuth oxide solid solutions. These spectra correspond to the electronic transition from the $2p_{3/2}$ to the empty 5*d* orbitals of W. The normalized XANES spectra are provided in Fig. 6.11.

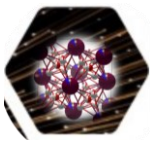

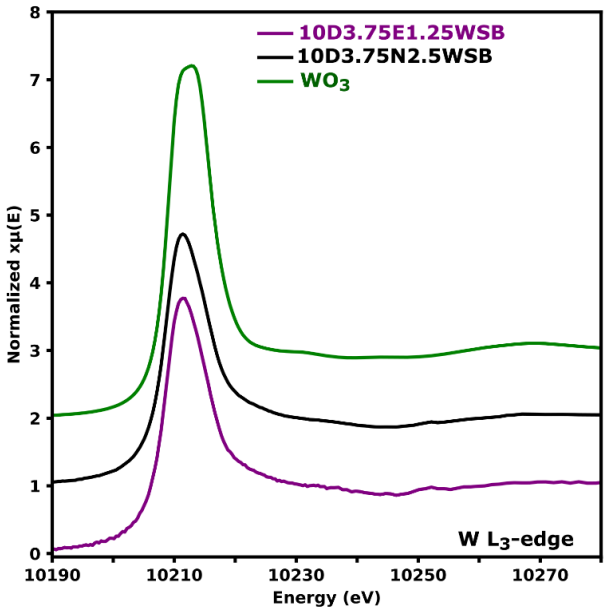

Figure 6.11. The Normalized W L_3-edge XANES spectra of WO_3, 10D3.75E1.25WSB and 10D3.75N2.5WSB.

The WO_3 spectrum is consistent with that from literature [54]; the broad feature in the white line of octahedrally coordinated W is attributed to the relatively large crystal field splitting of the d-orbitals and is large enough to produce two distinct peaks, each corresponding to the t_2 and e set of orbitals, respectively. However, in the 10D3.75E1.25WSB and 10D3.75N2.5WSB compositions, the white line peaks were more asymmetric and narrower, showing no clear distinction of the 5*d* orbitals splitting. These results suggest that in these formulations W might be tetrahedrally coordinated, since the crystal field splitting between the e and t_2 sets of orbitals in tetrahedrally coordinated W is relatively smaller which would lead to narrower white lines for these compositions. From the normalized first derivative spectra (Fig. 6.12(a)) it was seen that

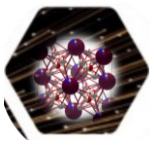

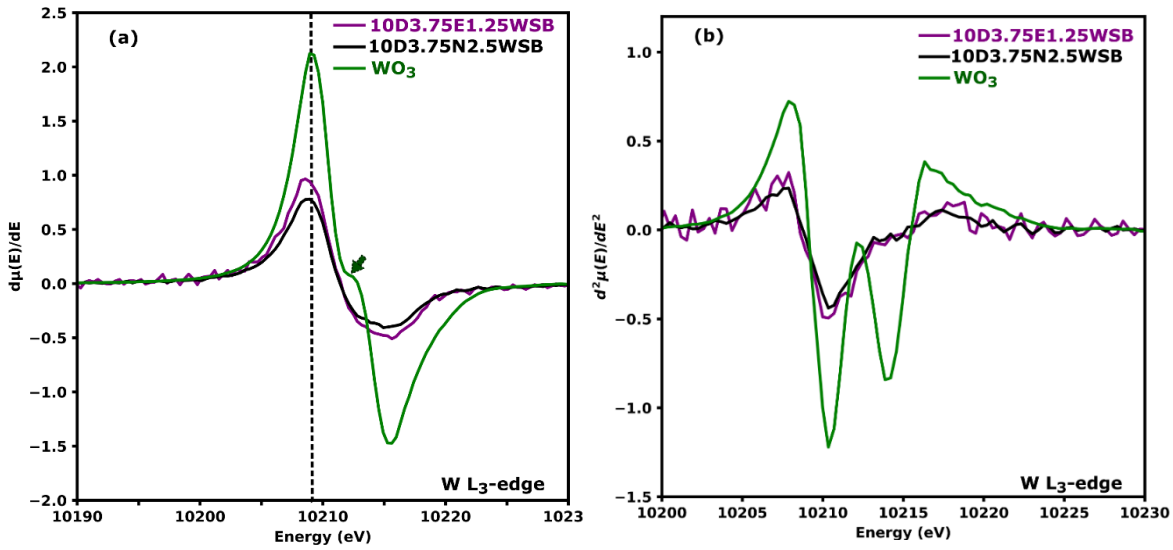

Figure 6.12. Normalized first **(a)** and second **(b)** derivative W L_3-edge XANES spectra of 10D3.75E1.25WSB, 10D3.75N2.5WSB and WO_3. The arrow indicates an inflection point characteristic of 6-coordinated W^{6+} species.

the relatively smaller ligand field splitting in tetrahedrally coordinated W results in derivate spectra that have peaks from transitions to e and t_2 that cannot be deconvoluted hence the absence of a pronounced inflection point and a sharper white line. The small inflection at approximately 10211 eV shown by the green arrow in Fig. 6.12 (a) is an indicator of octahedral coordination around W for the WO_3 powder (Fig. 6.12(a)) as measured in this work and is also reported by Wind *et al.* [55]. For the 10D3.75E1.25WSB and 10D3.75N2.5WSB compositions, the small inflection is undiscernible at 10212 eV. This further suggests that these compositions might contain predominantly tetrahedral W environments as observed by Wind *et al.* [55] and also alluded to by the expansion of the unit cell in the Bragg data without a change in average structure.

The second derivative of the XANES spectrum of WO_3 shows well resolved minima (Fig. 6.12(b)) and WO_3 has distorted octahedra units as shown in the inset of Fig. S6.9. However, for the 10D3.75E1.25WSB and 10D3.75N2.5WSB formulations, the second minimum at higher energy are far less pronounced, with only significant asymmetry discernible. This has been attributed to the presence of the mixture of octahedral coordination and a predominantly tetrahedral coordination environment in W containing materials [54]. To the authors knowledge, this is the first spectroscopic evidence showing that W in some δ–phases occupy predominantly tetrahedrally coordinated environments. This is further evidence that the average structure is not a comprehensive description of the structure of these materials.

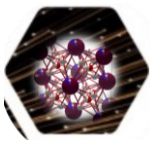

6.4 Conclusions

In this work high resolution synchrotron Bragg and PDF data were used to confirm the stabilization of δ–phases to ambient temperature using a minimum total substituent concentration in the range 15-16.25 mol% in ternary and quaternary oxides of Bi_2O_3. It was observed that when Er^{3+} substituent cations were replaced with W^{6+} and/or Nb^{5+}, the lattice parameter a counterintuitively expanded and this was correlated to a decrease in the occupancy of the oxide ions in the 8c sites. It was also observed from total scattering and XAS data that the substituent cations are not all replacing Bi at the 4a site in the stabilised δ–phases, but instead they seem to induce local monoclinic-like distortions in the metal sublattice. This effect was more pronounced in the system with Er and Dy cations only and seemed to increase with increase in Er concentration. X-ray absorption spectroscopy showed that the local structure around the Dy^{3+} cations in the substituted systems was similar to that of Dy^{3+} in Dy_2O_3 which is different from the site geometry of metal cations in the average structure of δ–Bi_2O_3. X-ray absorption spectroscopy also indicated that the W cations are predominantly tetrahedrally coordinated in the stabilised δ–phases (therefore predominantly not in the 4a site), which is likely a contributing factor to the lattice expansion of compositions where W cations were replacing Er and pushing more oxide ions into interstitial (48i) or interstitial-like (32f) sites. This highlights the role of the substituents cations in influencing the local structure of the metal sublattice of the host and warrants further investigation using advanced methods such as Big-box modelling.

6.5 Acknowledgements

The authors acknowledge financial support for their research from the National Research Foundation (NRF, South Africa) and Department of Science and Innovation (DSI, South Africa), as well as the University of the Witwatersrand. S.M. Masina also acknowledges the ICDD for a Ludo Frevel scholarship. This research used beamline 28-ID-1 of the National Synchrotron Light Source II, a U.S. Department of Energy (DOE) Office of Science User Facility operated for the DOE Office of Science by Brookhaven National Laboratory under Contract No. DE-SC0012704. Use of the Stanford Synchrotron Radiation Light Source, SLAC National Accelerator Laboratory, is supported by the U.S. Department of Energy, Office of Science, Office of Basic Energy Sciences under Contract No. DE-AC02-76SF00515.

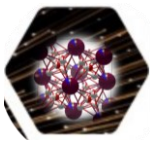

6.6 References

[1] Cabot, A., Marsal, A., Arbiol, J. and Morante, J.R., 2004. Bi_2O_3 as a selective sensing material for NO detection. *Sensors and Actuators B: Chemical*, *99*(1), pp.74-89.

[2] Bhande, S.S., Mane, R.S., Ghule, A.V. and Han, S.H., 2011. A bismuth oxide nanoplate-based carbon dioxide gas sensor. *Scripta Materialia, 65*(12), pp.1081-1084.

[3] Li, R., Wang, D., Ge, L., He, S., Chen, H. and Guo, L., 2014. Effect of Bi_2O_3 on the electrochemical performance of $LaBaCo_2O_{5+\delta}$ cathode for intermediate-temperature solid oxide fuel cells. *Ceramics International, 40*(2), pp.2599-2603.

[4] Won-In, K., Pongkrapan, S. and Dararutana, P., 2011. Eco-glass based on Thailand quartz sands and bismuth oxide. *In Materials Science Forum* (Vol. 695, pp. 223-226). Trans Tech Publications Ltd.

[5] Harwig, H.A. and Gerards, A.G., 1978. Electrical properties of the α, β, γ, and δ phases of bismuth sesquioxide. *Journal of Solid State Chemistry, 26*(3), pp.265-274.

[6] Sammes, N.M., Tompsett, G.A., Näfe, H. and Aldinger, F., 1999. Bismuth based oxide electrolytes–structure and ionic conductivity. *Journal of the European Ceramic Society, 19*(10), pp.1801-1826.

[7] Levin, E.M. and Roth, R.S., 1964. Polymorphism of bismuth sesquioxide. I. Pure Bi_2O_3. *Journal of Research of the National Bureau of Standards. Section A, Physics and Chemistry, 68*(2), p.189.

[8] Blower, S.K. and Greaves, C., 1988. The structure of β-Bi_2O_3 from powder neutron diffraction data. *Acta Crystallogr., Sect. C: Cryst. Struct. Commun, 44*(4).

[9] Aurivillius, B. and Malmros, G., 1972. Crystal Structure of β-Bi_2O_3. *Trans. R. Inst. Technol., Stockholm*, *291*, pp.545-562.

[10] Jiang, N., Wachsman, E.D. and Jung, S.H., 2002. A higher conductivity Bi_2O_3-based electrolyte. *Solid State Ionics*, *150*(3-4), pp.347-353.

[11] Watanabe, A. and Sekita, M., 2005. Stabilized δ-Bi_2O_3 phase in the system Bi_2O_3–Er_2O_3–WO_3 and its oxide-ion conduction. *Solid State Ionics*, *176*(31-34), pp.2429-2433.

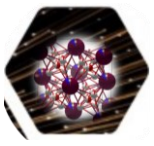

[12] Mercurio, D., El Farissi, M., Frit, B., Reau, J.M. and Senegas, J., 1990. Fast ionic conduction in new oxide materials of the Bi_2O_3–Ln_2O_3–TeO_2 systems (Ln= La, Sm, Gd, Er). *Solid State Ionics*, *39*(3-4), pp.297-304.

[13] Portefaix, N., Conflant, P., Boivin, J.C., Wignacourt, J.P. and Drache, M., 1997. New Bi–Ln–V–O Anionic Conductors with δ-Bi_2O_3 Fluorite-Type Structure (Ln= Y, Sm, Eu, Gd, Tb, Dy, Er, Yb). *Journal of Solid State Chemistry*, *134*(2), pp.219-226.

[14] Shitara, K., Moriasa, T., Sumitani, A., Seko, A., Hayashi, H., Koyama, Y., Huang, R., Han, D., Moriwake, H. and Tanaka, I., 2017. First-principles selection of solute elements for Er-stabilized Bi_2O_3 oxide-ion conductor with improved long-term stability at moderate temperatures. *Chemistry of Materials*, *29*(8), pp.3763-3768.

[15] Bandyopadhyay, S. and Dutta, A., 2018. A structural insight into the electrical properties of Dy-Ho co-doped phase stabilized bismuth oxide based electrolytes. *Journal of Electroanalytical Chemistry*, *817*, pp.55-64.

[16] Kharton, V.V., Marques, F.M.B. and Atkinson, A., 2004. Transport properties of solid oxide electrolyte ceramics: a brief review. *Solid State Ionics*, *174*(1-4), pp.135-149.

[17] Borowska-Centkowska, A., Leszczynska, M., Krok, F., Malys, M., Wrobel, W., Hull, S. and Abrahams, I., 2018. Local structure and conductivity behaviour in $Bi_7WO_{13.5}$. *Journal of Materials Chemistry A*, *6*(13), pp.5407-5418.

[18] Laarif, A. and Theobald, F., 1986. The lone pair concept and the conductivity of bismuth oxides Bi_2O_3. *Solid State Ionics*, *21*(3), pp.183-193.

[19] Boyapati, S., Wachsman, E.D. and Jiang, N., 2001. Effect of oxygen sublattice ordering on interstitial transport mechanism and conductivity activation energies in phase-stabilized cubic bismuth oxides. *Solid State Ionics*, *140*(1-2), pp.149-160.

[20] Abrahams, I., Liu, X., Hull, S., Norberg, S.T., Krok, F., Kozanecka-Szmigiel, A., Islam, M.S. and Stokes, S.J., 2010. A combined total scattering and simulation approach to analyzing defect structure in Bi_3YO_6. *Chemistry of Materials*, *22*(15), pp.4435-4445.

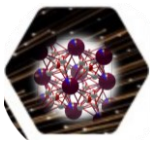

[21] Hull, S., Norberg, S.T., Tucker, M.G., Eriksson, S.G., Mohn, C.E. and Stølen, S., 2009. Neutron total scattering study of the δ and β phases of Bi_2O_3. *Dalton Transactions*, (40), pp.8737-8745.

[22] Battle, P.D., Catlow, C.R.A., Drennan, J. and Murray, A.D., 1983. The structural properties of the oxygen conducting δ phase of Bi_2O_3. *Journal of Physics C: Solid State Physics*, *16*(17), p.L561.

[23] Yashima, M. and Ishimura, D., 2003. Crystal structure and disorder of the fast oxide-ion conductor cubic Bi_2O_3. *Chemical Physics Letters*, *378*(3-4), pp.395-399.

[24] Verkerk, M.J., Keizer, K. and Burggraaf, A.J., 1980. High oxygen ion conduction in sintered oxides of the Bi_2O_3-Er_2O_3 system. *Journal of Applied Electrochemistry*, *10*(1), pp.81-90.

[25] Verkerk, M.J. and Burggraaf, A.J., 1981. High Oxygen Ion Conduction in Sintered Oxides of the Bi_2O_3-Dy_2O_3 System. *Journal of the Electrochemical Society*, *128*(1), p.75.

[26] Jung, D.W., Nino, J.C., Duncan, K.L., Bishop, S.R. and Wachsman, E.D., 2010. Enhanced long-term stability of bismuth oxide-based electrolytes for operation at 500° C. *Ionics*, *16*(2), pp.97-103.

[27] Yun, B.H., Lee, C.W., Jeong, I. and Lee, K.T., 2017. Dramatic Enhancement of Long-Term Stability of Erbia-Stabilized Bismuth Oxides via Quadrivalent Hf Doping. *Chemistry of Materials*, *29*(24), pp.10289-10293.

[28] Borowska-Centkowska, A., Leszczynska, M., Wrobel, W., Malys, M., Hull, S., Krok, F. and Abrahams, I., 2020. Stability of tungsten-doped δ-Bi_3YO_6. *Solid State Ionics*, *345*, p.115173.

[29] Abrahams, I., Liu, X., Hull, S., Norberg, S.T., Krok, F., Kozanecka-Szmigiel, A., Islam, M.S. and Stokes, S.J., 2010. A combined total scattering and simulation approach to analyzing defect structure in Bi_3YO_6. *Chemistry of Materials*, *22*(15), pp.4435-4445.

[30] Liu, X., Abrahams, I., Hull, S., Norberg, S.T., Holdynski, M. and Krok, F., 2011. A neutron total scattering study of defect structure in $Bi_3Nb_{0.5}Y_{0.5}O_{6.5}$. *Solid State Ionics*, *192*(1), pp.176-180.

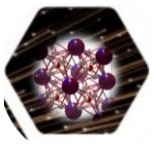

[31] Leszczynska, M., Liu, X., Wrobel, W., Malys, M., Krynski, M., Norberg, S.T., Hull, S., Krok, F. and Abrahams, I., 2013. Thermal variation of structure and electrical conductivity in $Bi_4YbO_{7.5}$. *Chemistry of Materials*, *25*(3), pp.326-336.

[32] Borowska-Centkowska, A., Liu, X., Krynski, M., Leszczynska, M., Wrobel, W., Malys, M., Hull, S., Norberg, S.T., Krok, F. and Abrahams, I., 2019. Defect structure in δ-$Bi_5PbY_2O_{11.5}$. *RSC Advances*, *9*(17), pp.9640-9653.

[33] Melnikov, P., Arkhangelsky, I.V., Nascimento, V.A., Silva, A.F., de Oliveira, L.C.S., Consolo, L.Z. and Herrero, A.S., 2015. Thermolysis mechanism of dysprosium hexahydrate nitrate $Dy(NO_3)_3 \cdot 6H_2O$ and modeling of intermediate decomposition products. *Journal of Thermal Analysis and Calorimetry*, *122*(2), pp.571-578.

[34] Yang, X., Juhas, P., Farrow, C.L. and Billinge, S.J., 2014. xPDFsuite: an end-to-end software solution for high throughput pair distribution function transformation, visualization and analysis. *arXiv preprint arXiv:1402.3163*.

[35] Coelho, A.A., Chater, P.A. and Kern, A., 2015. Fast synthesis and refinement of the atomic pair distribution function. *Journal of Applied Crystallography*, *48*(3), pp.869-875.

[36] Coelho, A.A., 2018. TOPAS and TOPAS-Academic: an optimization program integrating computer algebra and crystallographic objects written in C++. *Journal of Applied Crystallography*, *51*(1), pp.210-218.

[37] Ravel, B. and Newville, M., 2005. ATHENA, ARTEMIS, HEPHAESTUS: data analysis for X-ray absorption spectroscopy using IFEFFIT. *Journal of Synchrotron Radiation*, *12*(4), pp.537-541.

[38] Shannon, R.D., 1976. Revised effective ionic radii and systematic studies of interatomic distances in halides and chalcogenides. *Acta Crystallographica Section A: Crystal physics*, *32*(5), pp.751-767.

[39] Leszczynska, M., Liu, X., Wrobel, W., Malys, M., Dygas, J.R., Norberg, S.T., Hull, S., Krok, F. and Abrahams, I., 2014. Oxide ion distribution, vacancy ordering and electrical behaviour in the Bi_3NbO_7–Bi_3YbO_6 pseudo-binary system. *Journal of Materials Chemistry A*, *2*(43), pp.18624-18634.

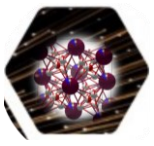

[40] Egami, T. and Billinge, S.J., 2003. *Underneath the Bragg peaks: structural analysis of complex materials*. Elsevier.

[41] Battle, P.D., Catlow, C.R.A. and Moroney, L.M., 1987. Structural and dynamical studies of δ-Bi_2O_3 oxide-ion conductors: II. A structural comparison of $(Bi_2O_3)_{1-x}(M_2O_3)_x$ for M= Y, Er, and Yb. *Journal of Solid State Chemistry*, *67*(1), pp.42-50.

[42] Norberg, S.T., Eriksson, S.G. and Hull, S., 2011. Comparison of short-range ion–ion correlations in the α, β and δ phases of Bi_2O_3. *Solid State Ionics*, *192*(1), pp.409-412.

[43] Gateshki, M., Niederberger, M., Deshpande, A.S., Ren, Y. and Petkov, V., 2007. Atomic-scale structure of nanocrystalline CeO_2–ZrO_2 oxides by total x-ray diffraction and pair distribution function analysis. *Journal of Physics: Condensed Matter*, *19*(15), p.156205.

[44] Battle, P.D., Catlow, C.R.A., Heap, J.W. and Moroney, L.M., 1986. Structural and dynamical studies of δ-Bi_2O_3 oxide ion conductors: I. The structure of $(Bi_2O_3)_{1-x}$ $(Y_2O_3)_x$ as a function of x and temperature. *Journal of Solid State Chemistry*, *63*(1), pp.8-15.

[45] Gateshki, M., Petkov, V., Hyeon, T., Joo, J., Niederberger, M. and Ren, Y., 2006. Interplay between the local structural disorder and the length of structural coherence in stabilizing the cubic phase in nanocrystalline ZrO_2. *Solid State Communications*, *138*(6), pp.279-284.

[46] Ishizawa, N., Matsushima, Y., Hayashi, M. and Ueki, M., 1999. Synchrotron radiation study of yttria-stabilized zirconia, $ZrO_{0.758}Y_{0.242}O_{1.879}$. *Acta Crystallographica Section B: Structural Science*, *55*(5), pp.726-735.

[47] Sardar, K., Playford, H.Y., Darton, R.J., Barney, E.R., Hannon, A.C., Tompsett, D., Fisher, J., Kashtiban, R.J., Sloan, J., Ramos, S. and Cibin, G., 2010. Nanocrystalline cerium− bismuth oxides: synthesis, structural characterization, and redox properties. *Chemistry of Materials*, *22*(22), pp.6191-6201.

[48] Scavini, M., Coduri, M., Allieta, M., Brunelli, M. and Ferrero, C., 2012. Probing Complex Disorder in $Ce_{1-x}Gd_xO_{2-x/2}$ Using the Pair Distribution Function Analysis. *Chemistry of Materials*, *24*(7), pp.1338-1345.

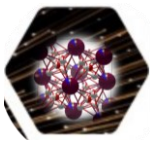

[49] Mamontov, E., Brezny, R., Koranne, M. and Egami, T., 2003. Nanoscale heterogeneities and oxygen storage capacity of Ce0. 5Zr0. 5O2. *The Journal of Physical Chemistry B*, *107*(47), pp.13007-13014.

[50] Tiwari, N., Kumar, S., Ghosh, A.K., Chatterjee, S., Jha, S.N. and Bhattacharyya, D., 2017. Structural investigations of (Mn, Dy) co-doped ZnO nanocrystals using X-ray absorption studies. *RSC advances*, *7*(89), pp.56662-56675.

[51] Das, C., Upadhyay, A., Ansari, K.U., Ogiwara, N., Kitao, T., Horike, S. and Shanmugam, M., 2018. Lanthanide-based porous coordination polymers: syntheses, slow relaxation of magnetization, and magnetocaloric effect. *Inorganic Chemistry*, *57*(11), pp.6584-6598.

[52] Ishii, M., Komuro, S., Morikawa, T., Aoyagi, Y., Ishikawa, T. and Ueki, T., 1999. XANES Analysis of Optical Activation Process of Er in Si: Er_2O_3 Thin Film: Electronic and Structural Modifications around Er. *Japanese Journal of Applied Physics*, *38*(S1), p.191.

[53] Anjana, R., Jayaraj, M.K., Yadav, A.K., Jha, S.N. and Bhattacharyya, D., 2018. Investigating the evolution of local structure around Er and Yb in ZnO: Er and ZnO: Er, Yb on annealing using X-ray absorption spectroscopy. *Journal of Applied Physics*, *123*(15), p.153102.

[54] Yamazoe, S., Hitomi, Y., Shishido, T. and Tanaka, T., 2008. XAFS study of tungsten L1- and L3-edges: structural analysis of WO_3 species loaded on TiO_2 as a catalyst for photo-oxidation of NH_3. *The Journal of Physical Chemistry C*, *112*(17), pp.6869-6879.

[55] Wind, J., Kayser, P., Zhang, Z., Evans, I.R. and Ling, C.D., 2017. Stability and range of the type II $Bi_{1-x}W_xO_{1.5+1.5x}$ solid solution. *Solid State Ionics*, *308*, pp.173-180.

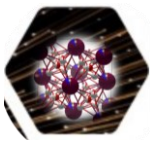

6.7 Supporting Information

Probing the Local Structure of Bi_2O_3 Chemical Derivatives: the Neglected Cation Sublattice

Sikhumbuzo M. Masina[1*], Gugulethu C. Nkala[1,2], Kevin H. Stone[3], Daniel Olds[4], Caren Billing[1], David G. Billing[1,2]

[1]Molecular Science Institute, School of Chemistry, University of the Witwatersrand, Private Bag X3, Johannesburg, 2050, South Africa

[2]DSI-NRF Centre of Excellence in Strong Materials, University of the Witwatersrand, Private Bag X3, Johannesburg, 2050, South Africa

[3]Stanford Synchrotron Radiation Lightsource, SLAC National Accelerator Laboratory, 2575 Sand Hill Road, Menlo Park, CA, 94025, USA

[4]National Synchrotron Light Source II, Brookhaven National Laboratory, Upton 11973, New York, United States

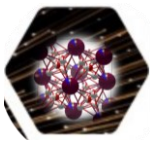

Table S6.1. Crystallographic data and refinement parameters for the $Bi_{1.7}Dy_{0.2}Er_{0.1}O_3$ composition at ambient temperatures.

Composition	$Bi_{1.7}Dy_{0.2}Er_{0.1}O_3$
R_{wp} (%)	1.61
Formular weight	906.210
Space group	*Fm*-3*m*
a /Å	5.522934(3)
Cell volume /Å^3	169.358
Z	2
Crystal density /g.cm^{-3}	8.92030

Table S6.2. Refined structural parameters for the $Bi_{1.7}Dy_{0.2}Er_{0.1}O_3$ composition at ambient temperatures.

Atom	Site	x	y	z	Occ	B_{iso} (Å^2)
Bi	4a	0	0	0	0.85	2.660(7)
Dy	4a	0	0	0	0.10	2.660(7)
Er	4a	0	0	0	0.05	2.660(7)
O(1)	8c	0.25	0.25	0.25	0.56(3)	6.48(17)
O(2)	32f	0.350(7)	0.350(7)	0.350(7)	0.046(7)	6.48(17)

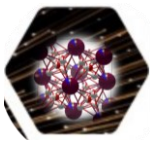

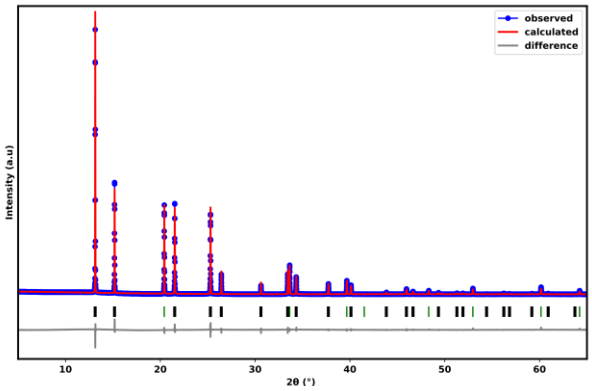

Figure S6.1. Rietveld refinement for the $Bi_{1.7}Dy_{0.2}Er_{0.075}W_{0.0125}O_3$ composition at ambient temperatures. Green and black hkls are for the diamond internal standard and δ-phase, respectively, with the model modified from Hull *et al.* [1] and Leszczynska *et al.* [2].

Table S6.3. Crystallographic data and refinement parameters for the $Bi_{1.7}Dy_{0.2}Er_{0.075}W_{0.0125}O_3$ composition at ambient temperatures.

Composition	$Bi_{1.7}Dy_{0.2}Er_{0.075}W_{0.0125}O_3$
R_{wp} (%)	2.74
Formular weight	906.210
Space group	*Fm*-3*m*
a /Å	5.532680(5)
Cell volume /Å^3	169.359(4)
Z	2
Crystal density /g.cm^{-3}	8.88529(3)

Table S6.4. Refined structural parameters for the $Bi_{1.7}Dy_{0.2}Er_{0.075}W_{0.0125}O_3$ composition at ambient temperatures.

Atom	Site	x	y	z	Occ	B_{iso} (Å^2)
Bi	4a	0	0	0	0.8556	2.63(1)
Dy	4a	0	0	0	0.1007	2.63(1)
Er	4a	0	0	0	0.0378	2.63(1)
W	4a	0	0	0	0.0062	2.63(1)
O(1)	8c	0.25	0.25	0.25	0.40(3)	4.27(77)
O(2)	32f	0.350(4)	0.350(4)	0.350(4)	0.087(6)	4.27(77)

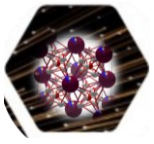

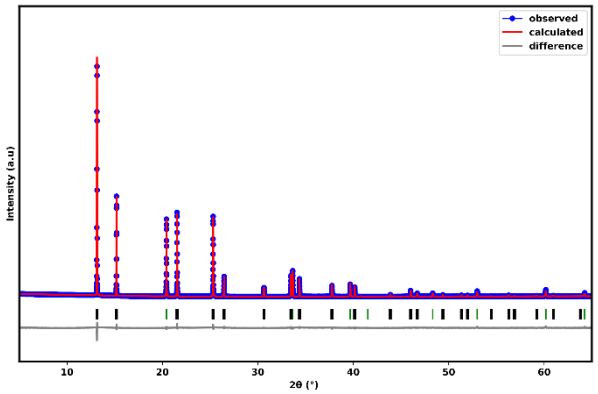

Figure S6.2. Rietveld refinement for the $Bi_{1.7}Dy_{0.2}Er_{0.075}Nb_{0.025}O_{3.025}$ composition at ambient temperatures. Green and black hkls are for the diamond internal standard and δ-phase, respectively, with the model modified from Hull *et al.* [1] and Leszczynska *et al.* [2].

Table S6.5. Crystallographic data and refinement parameters for the $Bi_{1.7}Dy_{0.2}Er_{0.075}Nb_{0.025}O_{3.025}$ composition at ambient temperatures.

Composition	$Bi_{1.7}Dy_{0.2}Er_{0.075}Nb_{0.025}O_{3.025}$
R_{wp} (%)	1.70
Formular weight	902.064
Space group	*Fm*-3*m*
a /Å	5.527446(3)
Cell volume /Å^3	168.878
Z	2
Crystal density /g.cm^{-3}	8.86979

Table S6.6. Refined structural parameters for the $Bi_{1.7}Dy_{0.2}Er_{0.075}Nb_{0.025}O_{3.025}$ composition at ambient temperatures.

Atom	Site	x	y	z	Occ	B_{iso} (Å^2)
Bi	4a	0	0	0	0.85	2.47(1)
Dy	4a	0	0	0	0.10	2.47(1)
Er	4a	0	0	0	0.0375	2.47(1)
Nb	4a	0	0	0	0.0125	2.47(1)
O(1)	8c	0.25	0.25	0.25	0.50(3)	5.75(64)
O(2)	32f	0.35(1)	0.35(1)	0.35(1)	0.034(8)	5.75(64)
O(3)	48i	0.5	0.195(20)	0.195(20)	0.019(6)	5.75(64)

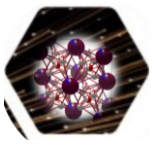

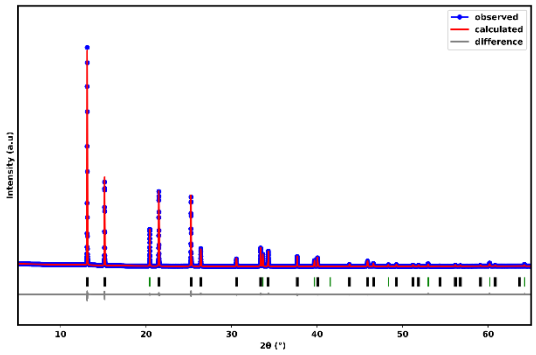

Figure S6.3. Rietveld refinement for the $Bi_{1.7}Dy_{0.2}Nb_{0.075}W_{0.025}O_{3.075}$ composition at ambient temperatures. Green and black hkls are for the diamond internal standard and δ-phase, respectively, with the δ-phase model modified from Hull *et al.* [1] and Leszczynska *et al.* [2].

Table S6.7. Crystallographic data and refinement parameters for the $Bi_{1.7}Dy_{0.2}Nb_{0.075}W_{0.025}O_{3.075}$ composition at ambient temperatures.

Composition	$Bi_{1.7}Dy_{0.2}Nb_{0.075}W_{0.025}O_{3.075}$
R_{wp} (%)	1.55
Formular weight	898.258
Space group	*Fm*-3*m*
a /Å	5.538943(3)
Cell volume /Å^3	169.934
Z	2
Crystal density /g.cm^{-3}	8.77747

Table S6.8. Refined structural parameters for the $Bi_{1.7}Dy_{0.2}Nb_{0.075}W_{0.025}O_{3.075}$ composition at ambient temperatures.

Atom	Site	x	y	z	Occ	B_{iso} (Å^2)
Bi	4a	0	0	0	0.85	2.430(7)
Dy	4a	0	0	0	0.10	2.430(7)
Nb	4a	0	0	0	0.0375	2.430(7)
W	4a	0	0	0	0.0125	2.430(7)
O(1)	8c	0.25	0.25	0.25	0.23(4)	4.91(26)
O(2)	32f	0.318(3)	0.318(3)	0.318(3)	0.137(8)	4.91(26)

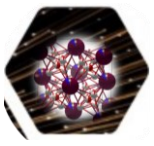

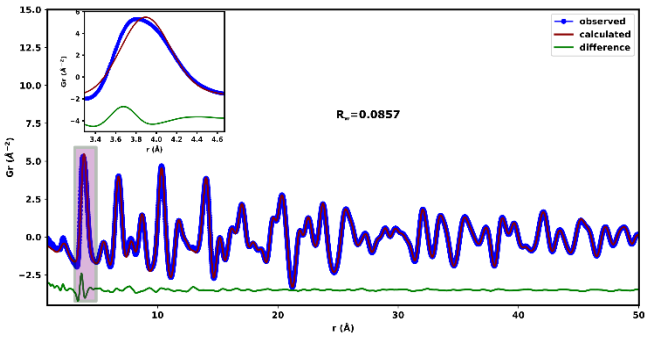

Figure S6.4. Small-box modelling of the PDF data collected for the $Bi_{1.7}Dy_{0.2}Er_{0.1}O_3$ composition at ambient temperature. This shows how moving half of each type of the metal cations to 24*e* does not improve the fit on the first M-M peak.

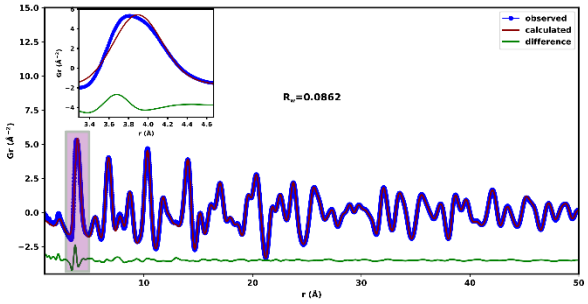

Figure S6.5. Small-box modelling of the PDF data collected for the $Bi_{1.7}Dy_{0.2}Er_{0.1}O_3$ composition at ambient temperature. This shows how moving half of each type of the metal cations to 48*h* does not improve the fit on the first M-M peak.

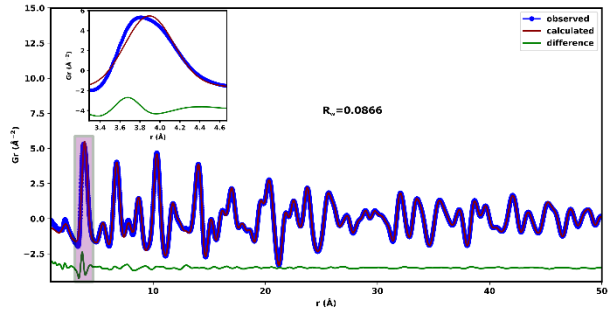

Figure S6.6. Small-box modelling of the PDF data collected for the $Bi_{1.7}Dy_{0.2}Er_{0.1}O_3$ composition at ambient temperature. This shows how moving half of each type of the metal cations to 32*f* does not improve the fit on the first M-M peak.

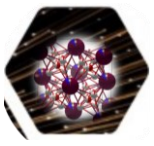

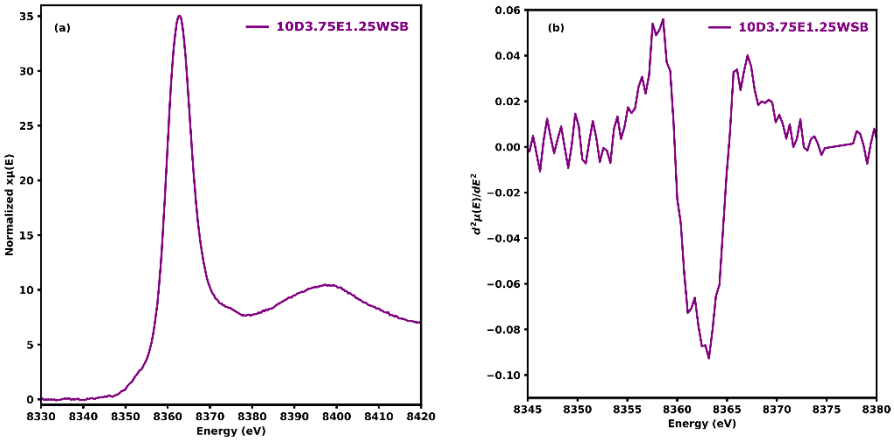

Figure S6.7. (a) Normalized Er L_3-edge XANES and **(b)** second derivative of the normalized XANES spectrum of Er^{3+} in the $Bi_{1.7}Dy_{0.2}Er_{0.075}W_{0.0125}O_3$ composition at ambient temperature.

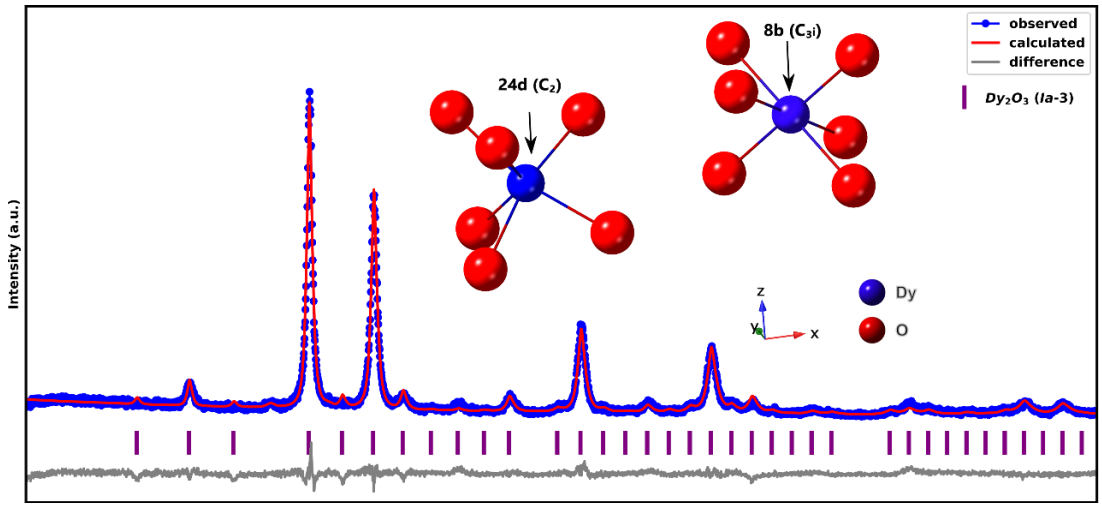

Figure S6.8. Rietveld refinement of the Dy_2O_3 sample at ambient temperatures. Purple hkl ticks are for the Dy_2O_3 phase (I*a*-3) obtained from the Antic *et al.* model [3]. The inset show the two different sites of the Dy^{3+} cations found in the I*a*-3 model.

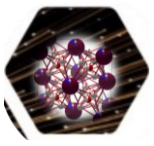

Table S6.9. Crystallographic data of Dy_2O_3 at ambient temperature. R_{wp} = 9.29% and goodness of fit (GOF) =1.44.

Phases	Bixbyite (I*a*-3)
Weight %	100
Space group	*Ia*-3
a /Å	10.6743(3)
Cell volume /$Å^3$	31216.2(1)
Crystal density /$g.cm^{-3}$	8.1481(7)

Table S6.10. Refined structural parameters for the Dy_2O_3 at ambient temperatures.

Atom	Site	x	y	z	Occ	B_{iso} ($Å^2$)
Dy(1)	8b	0.25	0.25	0.25	1.00	1.6 (2)
Dy(2)	24d	-0.0264(2)	0	0.25	1.00	1.6 (2)
O(1)	48e	0.484(2)	0.181(1)	0.254(1)	1.00	5.0(7)

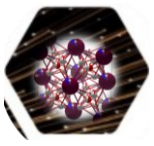

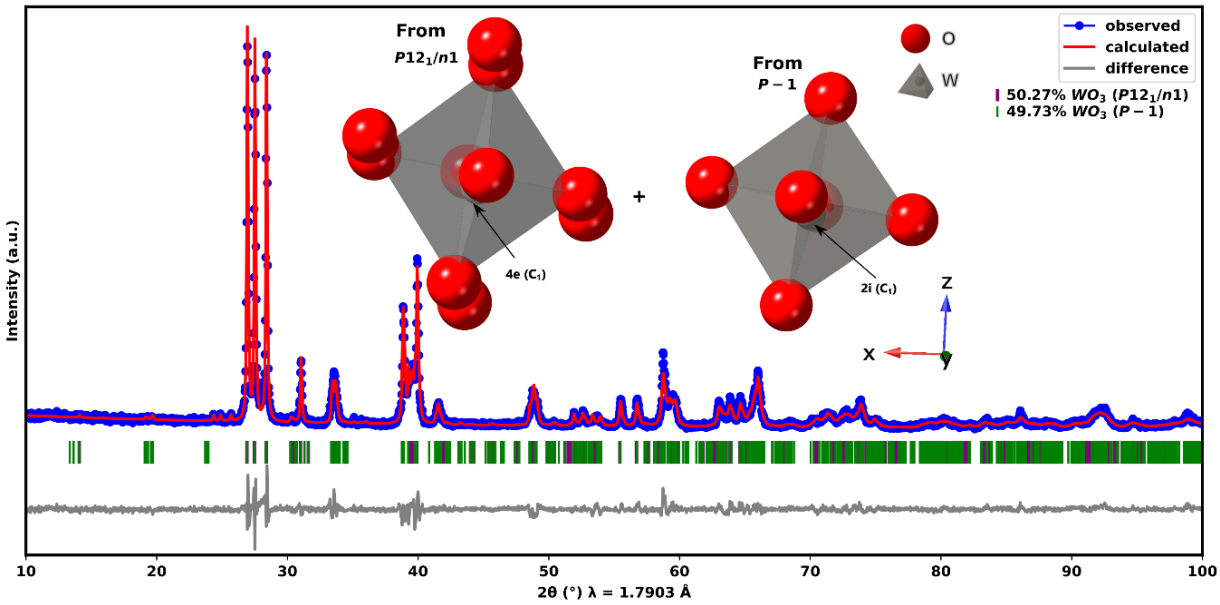

Figure S6.9. Rietveld refinement of the WO_3 sample at ambient temperatures. Purple and green hkl ticks are for the WO_3 ($P12_1/n1$) and WO_3 phases (P-1) obtained from the Vogt *et al.* and Diehl *et al.* models respectively [4,5]. The inset shows the distorted octahedra of WO_3 found in some of the sites in these models.

Table S6.11. Crystallographic data of WO_3 composition at ambient temperature. R_{wp} =10.46% and GOF = 1.54.

Phases	Monoclinic ($P12_1/n1$)	Triclinic(P-1)
Weight %	50(4)	50(4)
Space group	$P12_1/n1$	P-1
a /Å	7.301(1)	7.305(1)
b /Å	7.5347(9)	7.5317(8)
c /Å	7.692(1)	7.692(1)
α	90	89.770(8)
β	90.13(1)	90.677(6)
γ	90	89.98(1)
Cell volume /Å^3	423.1(1)	423.15(9)
Crystal density /g.cm^{-3}	7.278(1)	7.278(1)

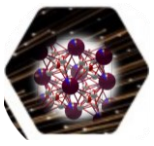

Table S6.12. Refined structural parameters for the WO_3 ($P12_1/n1$) at ambient temperatures.

Atom	Site	x	y	z	Occ	B_{iso} (Å^2)
W(1)	4e	0.255(5)	0.009(4)	0.267(2)	1.00	4.9(3)
W(2)	4e	0.259(5)	0.010(5)	0.749(3)	1.00	4.9(3)
O(1)	4e	-0.05(2)	0.07(2)	0.25(7)	1.00	0.003
O(2)	4e	0.01(4)	0.51(3)	0.25 (7)	1.00	0.003
O(3)	4e	0.50(3)	-0.01(3)	0.25(4)	1.00	0.003
O(4)	4e	0.25(5)	0.26(4)	0.75(3)	1.00	0.003
O(5)	4e	0.25(4)	-0.04(4)	0.05(1)	1.00	0.003
O(6)	4e	0.26(3)	0.54(4)	-0.03(1)	1.00	0.003

Table S6.13. Refined structural parameters for the WO_3 (P-1) at ambient temperatures.

Atom	Site	x	y	z	Occ	B_{iso} (Å^2)
W(1)	2i	0.253(6)	0.038(5)	0.293(6)	1.00	0.001
W(2)	2i	0.255(6)	0.538(5)	0.212(6)	1.00	0.001
W(3)	2i	0.254(6)	0.039(5)	0.795(7)	1.00	0.001
W(4)	2i	0.253 (6)	0.535(5)	0.710(6)	1.00	0.001
O(1)	2i	0.23(4)	0.01(5)	-0.01(5)	1.00	0.001
O(2)	2i	0.58(2)	0.40(2)	0.20(2)	1.00	0.001
O(3)	2i	-0.15(2)	0.35(2)	0.42(2)	1.00	0.001
O(4)	2i	0.54(2)	0.94(3)	0.25(2)	1.00	0.001
O(5)	2i	0.24(4)	0.25(2)	0.31(3)	1.00	0.001
O(6)	2i	0.20(4)	0.75(3)	0.22(3)	1.00	0.001
O(7)	2i	0.16(3)	0.31(3)	0.74(3)	1.00	0.001
O(8)	2i	0.27(4)	0.74(3)	0.76(4)	1.00	0.001
O(9)	2i	0.23(4)	0.23(3)	1.18(3)	1.00	0.001
O(10)	2i	0.56(2)	0.55(2)	0.34(2)	1.00	0.001
O(11)	2i	0.24(3)	0.51(3)	1.00(3)	1.00	0.001
O(12)	2i	0.23 (4)	1.02(5)	0.51(5)	1.00	0.001

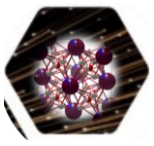

References

[1] Hull, S., Norberg, S.T., Tucker, M.G., Eriksson, S.G., Mohn, C.E. and Stølen, S., 2009. Neutron total scattering study of the δ and β phases of Bi_2O_3. *Dalton transactions*, (40), pp.8737-8745.

[2] Leszczynska, M., Liu, X., Wrobel, W., Malys, M., Krynski, M., Norberg, S.T., Hull, S., Krok, F. and Abrahams, I., 2013. Thermal variation of structure and electrical conductivity in $Bi_4YbO_{7.5}$. *Chemistry of Materials*, *25*(3), pp.326-336.

[3] Antic, B., Oennerud, P., Rodic, D. and Tellgren, R., 1993. The structure characteristics of the diluted magnetic semiconductor $Y_{2-x}Dy_xO_3$. *Powder Diffraction*, *8*(4), pp.216-220.

[4] Vogt, T., Woodward, P.M. and Hunter, B.A., 1999. The high-temperature phases of WO_3. *Journal of Solid State Chemistry*, *144*(1), pp.209-215.

[5] Diehl, R., Brandt, G. and Salje, E., 1978. The crystal structure of triclinic WO_3. *Acta Crystallographica Section B: Structural Crystallography and Crystal Chemistry*, *34*(4), pp.1105-1.

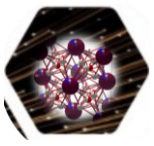

Chapter 7: Application of "Pseudo-Complex" Structural Analysis Methods to Unravel the Complexities of the Ageing Process in Bi_2O_3 "Solid Solutions"

Sikhumbuzo M. Masina[a], Gugulethu C. Nkala[a,b], Caren Billing[a], Yuanpeng Zhang[c], Daniel Olds[d], Rudolph M. Erasmus[b,e], David G. Billing[a,b]

[a]Molecular Science Institute, School of Chemistry, University of the Witwatersrand, Private Bag X3, Johannesburg, 2050, South Africa

[b]DSI-NRF Centre of Excellence in Strong Materials, University of the Witwatersrand, Private Bag X3, Johannesburg, 2050, South Africa.

[c]Neutron Scattering Division, Oak Ridge National Laboratory, Oak Ridge, Tennessee 37831, United States

[d]National Synchrotron Light Source II, Brookhaven National Laboratory, Upton 11973, New York, United States

[e]Material Physics Research Institute, School of Physics, University of the Witwatersrand, Private Bag X3, Johannesburg, 2050, South Africa.

Abstract:

The contribution to phase and local structural stability by Dy, Er, W and Nb substituents in stabilized Bi_2O_3 have been systematically investigated. The combination of Er and W has been confirmed to improve phase stability in the $(Dy_2O_3)_x(Er_2O_3)_y(WO_3)_z(Bi_2O_3)_{1-x-y-z}$ (DEWSB) and $(Er_2O_3)_x(Nb_2O_3)_y(WO_3)_{2z}(Bi_2O_3)_{1-x-y-2z}$ (ENWSB) systems. Dy has been found to be detrimental to the phase stability upon annealing at ~500 °C for over 300 h in the DEWSB system. Nb was found to promote the disorder-order of the local structure in $(Dy_2O_3)_x(Er_2O_3)_y(Nb_2O_5)_z(Bi_2O_3)_{1-x-y-z}$ (DENSB) but mildly suppresses the transformation of the δ-phase to the rhombohedral phase upon annealing at ~500 °C for ~100 h. Photoluminescence spectroscopy, extended X-ray absorption fine structure and total scattering data revealed that some of the Er cations are not replacing Bi^{3+} cations at the 4a sites as expected for an ideally stabilized δ-phase with the defect fluorite average structure.

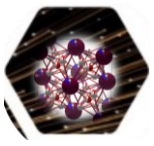

Keywords: EXAFS; Photoluminescence spectroscopy; Total scattering; Ageing phenomenon; Local structure

7.1 Introduction

Fast solid oxide ion conductors as functional materials have played a big role in the advancement of technology in the last 50 years. They are instrumental in the function of many devices of technological importance such as oxygen sensors, memristors, catalytic converters and solid oxide fuel cells (SOFCs) [1-4]. SOFCs have shown incredible fuel flexibility and reduced greenhouse gas emissions [5]. From their use of H_2 gas, fossil fuels and NH_3 gas as fuel to their reported efficiencies of over 80% when operated in combined heat and power mode, SOFCs have garnered considerable research interest in the last half-century [6-10].

The major challenge facing SOFCs is the high operation temperatures (800 – 1000 °C) which is determined primarily by the solid oxide electrolyte used. The state-of-the-art solid oxide electrolyte used is yttria-stabilized zirconia $(ZrO_2)_{1-x}(Y_2O_3)_x$ (YSZ) [11]. YSZ has appreciable conductivity (0.01 – 0.1 S cm^{-1}) only at high temperatures (800 – 1000 °C) [11]. These high temperatures lead to reduced cell life due to cell component degradation, use of expensive materials with high melting points as interconnects and high capital costs [12]. These prevent large scale commercialization of SOFCs. Fast solid oxide ion conductors that show chemical stability at intermediate temperatures (500-800 °C) are imperative for pushing SOFCs towards large scale commercialization.

Ceria and Bi_2O_3 based solid solutions have appreciable conductivities at intermediate temperatures (IT). However, ceria based solid solutions show appreciable electronic conductivity when exposed to low p_{O_2} pressures which leads to low open-circuit voltages [13]. Bi_2O_3 in its pure δ-Bi_2O_3 phase has ionic conductivities of about 1 S cm^{-1} at 730 °C [14]. However, upon cooling to temperatures below 730 °C, Bi_2O_3 can transform into three different major polymorphs, (the monoclinic α-, tetragonal β-, and cubic γ-polymorph) that have oxide conductivities orders of magnitude lower than the δ-Bi_2O_3 phase [14, 15]. δ-Bi_2O_3 like phases can be stabilized to ambient temperatures−albeit with slightly reduced conductivity−by substituting the Bi^{3+} cation with some isovalent and aliovalent cations [16-18]. The major problems with solid solutions of Bi_2O_3 are their structural degradation after prolonged annealing at temperatures ≤ 600 °C and their low chemical stability

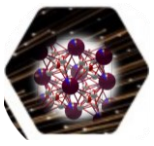

under reducing environments [19]. These are the target temperatures at which SOFCs need to operate to achieve widespread commercialization.

Bi^{3+} in solid solutions of Bi_2O_3 is reduced to metallic Bi under reducing conditions which prevents direct use of Bi_2O_3 in SOFCs [19, 20]. Forming a bilayer of Bi_2O_3 and ceria based solid solutions has been shown to produce electrolytes that prevent the reduction of Bi^{3+} to metallic Bi and the short circuiting exhibited by ceria due to electronic conduction as discussed in Ref. [13]. However, the structural and phase degradations exhibited by solid solutions of Bi_2O_3 after prolonged annealing at ≤ 600 °C for over 100 h are still a major concern. Various solid solutions of Bi_2O_3 show phase degradation from the δ-phase to a rhombohedral phase after prolonged annealing at ≤ 600 °C [21, 22]. At this temperature range, the O^{2-} sublattice in the stabilized δ-phase is also reported to undergo a disorder–order transition without a change in the average structure measured by powder X-ray diffraction (PXRD) [23-26]. These structural changes reduce the conductivity by more than an order of magnitude [24]. Evidence of the ordering phenomenon is provided by an endothermic displacement at ∼600 °C in differential thermal analysis thermograms for a PXRD pure δ-phase sample [24].

Various studies have been done to eliminate both the phase degradation and ordering of the O^{2-} sublattice in the δ-phase after prolonged annealing [27-29]. Watanabe and Sekita [29] showed that the composition $(Er_2O_3)_{0.245}(WO_3)_{0.05}(Bi_2O_3)_{0.705}$ (24.5E5WSB) is both phase stable and resistant to the O^{2-} sublattice ordering. Jung *et al*. [30] fabricated the $(DyO_{1.5})_{0.08}(WO_3)_{0.04}(BiO_{1.5})_{0.88}$ composition which had the highest conductivity for any substituted Bi_2O_3 system but exhibited significant phase degradation upon prolonged annealing. Inspired by these developments, in our earlier work, $(Dy_2O_3)_{0.08}$ $(Er_2O_3)_{0.03}(WO_3)_{0.01}(Bi_2O_3)_{0.88}$ (8D3E1WSB) was designed and it showed significant improvement in phase stability after prolonged annealing [31]. In our earlier work [31], it was shown that the addition of Er and reduction of the concentration of W is important for the phase stability of the DEWSB system compared to DWSB. However, the ordering of the O^{2-} sublattice and the role of each impurity cation to the phase stability was not investigated in that work. This work seeks to address these gaps. The $(Dy_2O_3)_x(Er_2O_3)_y(WO_3)_z(Bi_2O_3)_{1-x-y-z}$ (100xD100yE100zWSB), $(Er_2O_3)_y(Nb_2O_3)_z(Bi_2O_3)_{1-x-y-z}$ (100xD100yE100zNSB), $(Er_2O_3)_x(Nb_2O_3)_y(WO_3)_{2z}(Bi_2O_3)_{1-x-y-2z}$ (100xE100yN200zWSB), $(Dy_2O_3)_x(Nb_2O_3)_y(WO_3)_{2z}(Bi_2O_3)_{1-x-y-2z}$ (100xD100yN200zWSB), $(Dy_2O_3)_x(Er_2O_3)_y(Bi_2O_3)_{1-x-y}$

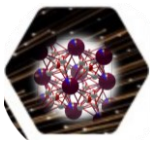

(100xD100yESB) and $(Dy_2O_3)_x(WO_3)_y(Bi_2O_3)_{1-x-y}$ (100xD100yWSB) systems were fabricated and characterised. The average and local structures were probed using complementary techniques such as total scattering and X-ray absorption spectroscopy. A correlation between the local structure and the ageing phenomenon was established.

Experimental Methods

7.1.1 Synthetic method

The citrate gel synthetic method used in this work was the same as the one used in our earlier work [31]. The $C_4H_4NNbO_9 \cdot H_2O$ (99.99% pure, Aldrich) was dissolved in the same way as $(NH_4)_6H_2W_{12}O_{40} \cdot H_2O$ (Sigma-Aldrich) [31]. The prepared powders were pressed into pellets using a uniaxial cold press at a constant pressure of 400 MPa and an 8 mm die. The green bodies were put in an alumina boat and were sintered in air using a tube furnace at 850 °C for 24 h. The sintered pellets were quenched in air from 850 °C to ambient temperature by quickly removing them from the furnace. PXRD measurements were taken before the quenched pellets were annealed again at 500 °C for 50 and 100 h. The pellets were quenched again from 500 °C to ambient temperature before further characterization. In this work, the total substituent concentration (TSC) is with respect to the oxides for the DWSB, DEWSB, DESB and DENSB to be consistent with those from Ref. [31]. The TSC was with respect to the cations for ENWSB and DNWSB so that they can be similar to those that were synthesised by Ref. [28].

7.1.2 Powder X-ray diffraction

7.1.2.1 In-house powder X-ray diffraction

Ambient temperature scans were taken using a Bruker D2 Phaser in Bragg-Brentano geometry. The radiation source was a sealed Co tube with Fe K_β secondary beam filter. Primary and secondary Soller slits were used to reduce axial divergence. This system was equipped with a Lynxeye position sensitive detector. Phase identification was done using DIFFRAC.SUITE EVA linked to the crystallography open database (COD) [32] and Rietveld refinements were done using TOPAS *Academic* (v.6) [33].

7.1.2.2 Total Scattering

The PDF beamline 28-ID-1 at NSLS II at Brookhaven National Laboratory (BNL) was used to collect the total scattering data. The X-ray source is a damping wiggler and the beam is focused horizontally and vertically by a side bounce monochromator (SBM) and a vertically focusing

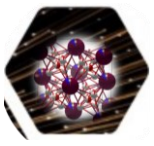

mirror (VFM), respectively. A monochromatic wavelength of 0.1665 Å in Debye-Scherrer geometry was used. The diffractometer employs a PerkinElmer area detector (200 × 200 μm pixel size) which was positioned at 222 and 1236 mm direct distance to collect data suitable for total scattering analysis and Bragg data, respectively. Kapton capillaries with an outside diameter (OD) of 0.9 mm were used for ambient temperature data collection. Si, LaB_6 and CeO_2 were used as external calibrants for the ambient temperature measurements.

Total scattering data were reduced by using PDFgetX2 [34]. The total scattering structure function S(Q) obtained was first rebinned (dQ = 0.02, Q_{min} = 0.2, Q_{max} = 21-24) to a uniform Q binning. Q is the magnitude of the scattering vector ($Q = 4\pi \sin\theta / \lambda$) where λ is the wavelength of the radiation used and θ is the scattering angle. S(Q) was then transformed into F(Q) as defined by Keen [35, 36]. Reverse Monte Carlo methods as implemented in the RMCProfile package v 6.7.9.2 [37, 38] was used to analyse the total scattering data. The Bragg data, reciprocal space data (F(Q)) and real space data (D(r)) were fitted simultaneously. An automatic weight optimization algorithm was used for data and constraints weighting [38]. A $10 \times 10 \times 10$ supercell was constructed by using the lattice parameters from Rietveld refinement results and the initial atomic positions were obtained from the Gattow and Schröder model of δ-Bi_2O_3 [39]. A series of constraints were implemented to provide some physical guidance for the RMC modelling. This included the distance window constraint which provided control over the minimum and maximum distances between different atomic pairs and the bond valence sum to guarantee reasonable chemical bonding environments. Atom swapping was allowed between different types of atoms occupying the same crystallographic site and contributed 10% of the total moves generated for the given site. A maximum move distance of 0.05 Å was allowed for a given atom type in each random move. Ten different configurations were used for each composition to improve statistics on the extracted parameters.

7.1.3 Differential thermal analysis

Differential thermal analysis (DTA) was conducted using a Perkin Elmer STA 6000 with alumina crucibles. Temperature calibration was performed by melting an indium standard in an alumina crucible. The instrument was operated in the simultaneous thermogravimetric analysis (TGA)-DTA mode. The measurements were done between 30 and 800°C for both heating and cooling

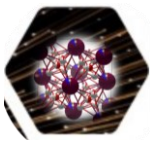

cycles at a heating/cooling rate of 10°C min^{-1}. Nitrogen was used as the purging gas at a flow rate of 20 ml min^{-1}.

7.1.4 Electrochemical Impedance Spectroscopy (EIS)

The powders were pressed into pellets using a uniaxial cold press at a constant pressure of 500 MPa and a 13 mm die. The pellets were sintered in air at 850 °C and quenched to ambient temperature by quickly removing them from the furnace. The pellets had a thickness of about 1 mm after sintering. Variable temperature (VT)-EIS was done using an MTZ-35 frequency response analyser from BioLogic, the same instrument as in Ref. [31]. The measurements were done in air, using a heating/cooling rate of 10 °C min^{-1}. Initial measurements were done at 700 °C to establish intimacy between the electrodes and electrolyte, and then the pellet was cooled down to 500 °C to start the ageing process. The system was allowed to soak for about 90 minutes at 500 °C before each measurement during the whole experiment. The whole measurement process took about 100 h at 500 °C. The frequency range was from 10 Hz to 30 MHz with an A.C. amplitude of 10 mV.

7.1.5 Photoluminescence Spectroscopy (PL)

Photoluminescence emission spectra were obtained using a Horiba QM8000 spectrofluorometer equipped with double excitation and emission monochromators with 1200 lines/mm gratings and a Xe lamp source. The detector was a Horiba PPD-850. The emission spectra intensities were corrected for the throughput of the emission monochromator and the detector efficiency. For the Er containing samples, an excitation line (λ_{exc}) of 520 nm was used. Powdered samples were prepared by grinding the sintered pellets (as described in section 7.2.1). The powders were loaded into a cuvette and PL measured in air and at ambient temperature.

7.1.6 X-ray Absorption Fine Structure (XAFS)

The 6-BM beamline at the NSLS II was used to perform the XAFS measurements. A Si (111) double-crystal monochromator was used to tune the energy of the incident radiation to the energy required to scan across the threshold energy of the absorber. Calibration was done prior to performing the measurements by determining the angular position of the monochromator for K- and L_3-edges of ten transition metals (Fe, Co, Ni, Cu, Zn, Pt, Au, Pb, Nb, Mo). The Bragg equation was then used to determine the offsets by using standardized values [40]. For the Bi L_3-edge, the data were collected in transmission mode using an unfocused beam with a slit size of 1 mm × 5 mm. For the Er L_3-edge, the data were collected in fluorescence mode with the detector positioned

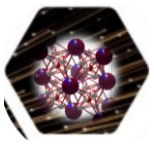

at 90° to the incident beam. The samples were pelletized powders, diluted with cellulose (Avicel® PH-101, Sigma-Aldrich). The pellets were sandwiched between two Kapton tape strips which were mounted over 3 mm × 14 mm rectangular holes on a rotating polycarbonate plastic wheel.

XAFS spectra were prepared for analysis by averaging 3-5 individual spectra for a given edge and composition in Demeter suite of software packages v0.9.26 [41]. Larch v0.9.55 [42] was used to perform data reduction. A straight-line function was used to fit the pre-edge region and a spline function was used to fit the post edge region to reduce the data. A parameter (R_{bkg}) for adjusting the spline function to accommodate the slowly varying features in the post edge region was used and it ranged between 1.1 and 1.3. The edge position was chosen to correspond to the maximum of the first derivative of the spectra. The EXAFS spectra ($\chi(k)$) were normalized by using the edge-jump, and Fourie transformed to real space using k^2-weighted data. The EXAFS equation:

$$\chi(k) = \sum_j \frac{S_0^2 N_j f_j(k) e^{-2R_j/\lambda(k)} e^{-2k^2\sigma_j^2}}{kR_j^2} \sin\left[2kR_j + \delta_j(k)\right]$$

was used to model the data. S_0^2 represents intrinsic losses and was obtained from fitting standards (α-Bi_2O_3 and Er_2O_3). $f_j(k)$, $\lambda(k)$, and $\delta_j(k)$ represent the scattering amplitude function, mean free path, and phase shifts in j^{th} shell, respectively, and were calculated by the FEFF 8.0 code as implemented in Larch v0.9.55 for each crystalline model used. N_j, σ_j^2, and R_j are the number of atoms in the jth shell, the mean-square displacement in the bond distance and the bond distance, respectively, and they are fitted parameters.

7.2 Results and Discussion

7.2.1 Phase Stability and Ageing in the DEWSB System

In the DEWSB system, the 8D3E1WSB composition explored in our earlier work exhibited no discernible new phases in the ambient temperature diffraction patterns after annealing at 500 °C in air for 100 h [31]. The annealing process (isothermal annealing at 500 °C for 100h) was repeated in this work and the results were reproduced (Fig. 7.1(a)). However, DTA results of the annealed sample show an endothermic displacement with an onset at ~606.6 °C during the heating cycle for the 12 mol% TSC composition (Fig. 7.1(b)). This endothermic peak is ascribed to an order-disorder transition of the O-sublattice exhibited by numerous solid solutions of Bi_2O_3 after prolonged annealing at temperatures ≤ 600 °C [24]. It was impossible to do a second cycle for the

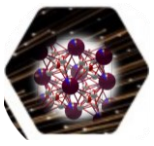

8D3E1WSB composition because the δ-phase could only be stabilized through prolonged annealing and then quenching for this composition [31]. An increase in TSC within the solubility range for the impurity cations used, has been reported to stabilize the disordered state of the O-sublattice in selected systems [21]. The TSC was therefore increased from 12 mol% to18 and 24 mol% keeping the ratio (8:3:1) between substituents constant. These compositions were still within the solubility range as no new phases were observed by PXRD even after 100 h of annealing at 500 °C (Fig. 7.1(a)**)**. DTA of the 18 mol% composition exhibited a small endotherm with an onset at ~584.1 °C characteristic of the order-disorder transition and this was virtually undiscernible in the 24 mol% (Fig. 7.1(b)). This reinforces the idea that an increase in TSC reduces the extent of the order-disorder transition of the O-sublattice.

No significant changes in the broadness of the peaks in the PDF of the aged compared to the as-sintered material were observed in the 8D3E1WSB composition (Fig. 7.1(c)). This suggested that the metal sublattice remained virtually unperturbed despite the large endothermic displacement

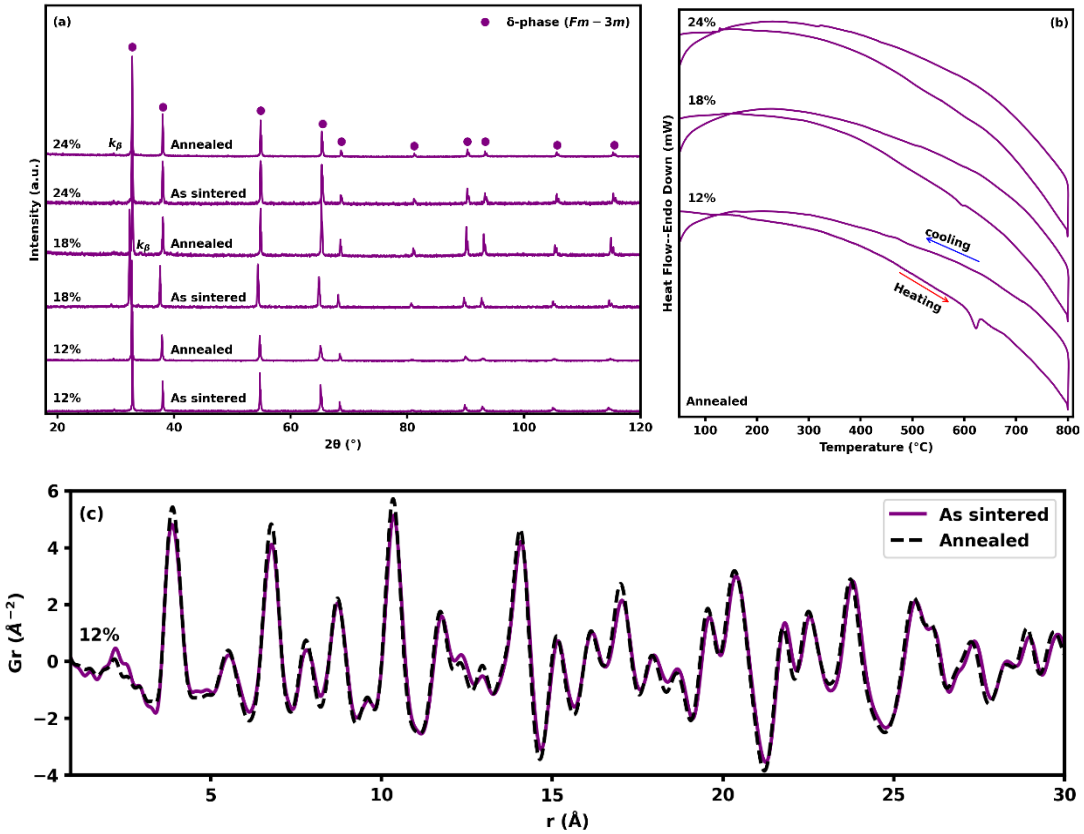

Figure 7.1. (a) PXRD data of the pellets of the DEWSB system before and after annealing at 500 °C for 100 h showing phase stability. Plots are stacked for clarity. **(b)** DTA curves showing how an increase in substituent concentration reduces the endothermic displacement characteristic of the order-disorder transition. Plots are stacked for clarity. **(c)** The reduced total PDFs from powders of from ground pellets showing how the 8D3E1WSB composition exhibited very little change on the metal sublattice upon annealing.

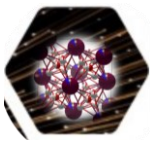

observed in the DTA data. The DEWSB system was designed to improve the phase stability of the DWSB system (based on result by Jung *et al.* [30]) by adding the Er^{3+} cation while keeping the TSC low. This was inspired by the stability of the EWSB system reported by Watanabe and Sekita [29]. The role of the various cation components in the performance of the DEWSB system was not extensively investigated in our earlier work [31] - this is attempted here by studying the range of systems with different cation substituents.

7.2.2 Phase Stability in the DWSB System–A Comparison with the DEWSB System

To illustrate the effects of Er^{3+} on phase stability, Er^{3+} was completely removed from the DEWSB system to form the DWSB while keeping the TSC constant [31]. However, only the 8D4WSB composition was used to illustrate how the addition of Er^{3+} improve phase stability in our earlier work [31]. In this work the TSC was increased from 12 mol% to 18 and 24 mol% for the DWSB system as it was done for DEWSB. In contrast to DEWSB, the DWSB system exhibited phase degradation throughout the 12-24 mol% range as illustrated by Fig. 7.2. The 12 mol% composition upon annealing in air for 100 h at 500 °C and quenched showed phase degradation from the δ-phase to a mixture of 36% δ-phase, 49% $7Bi_2O_3{\cdot}2WO_3$ phase ($I4_1$) and 15% $7Bi_2O_3{\cdot}WO_3$ phase ($I4/m$) as obtained through Rietveld refinements of synchrotron X-ray diffraction data (Fig. S7.1 and Table S7.1). Jung *et al.* [30] made similar observations in their DWSB system for all the compositions explored. The 18 mol% composition exhibited subtle anisotropic peak broadening and the 24 mol% composition showed significant peak splitting upon annealing in the same annealing conditions. There seems to be no correlation on the extent of phase degradation and the TSC in this system, also similar to the results obtained by Jung *et al.* [30].

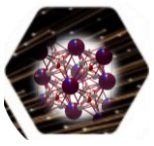

These results suggested that the presence of Er^{3+} and a corresponding reduction in the concentration of W^{6+} is important in stabilizing the δ-phase in the DEWSB system even at higher TSC. It can be argued that the reduced number of impurity cations in the DWSB system also played a role by reducing the stabilizing effect of configurational entropy, but Watanabe and Sekita [29] achieved the stable system EWSB with the same number of impurity elements and comparable TSC. The EWSB system was investigated at 600 °C, a temperature where DWSB was again reported to exhibit phase degradation [29, 30]. The contrast in phase stability between the DWSB and EWSB systems could suggest that Dy^{3+} might be playing a role in the poor phase stability exhibited by DWSB which is ameliorated by the combination of Er^{3+} and W^{6+} in DEWSB. Increasing the Er^{3+} content while decreasing the Dy^{3+} concentration and keeping the TSC constant in the DEWSB system produced an even more phase stable composition after annealing for over 300 h (illustrated in Fig. S7.2 by comparing 16D6E2WSB and 16E6D2WSB). The 16D6E2WSB

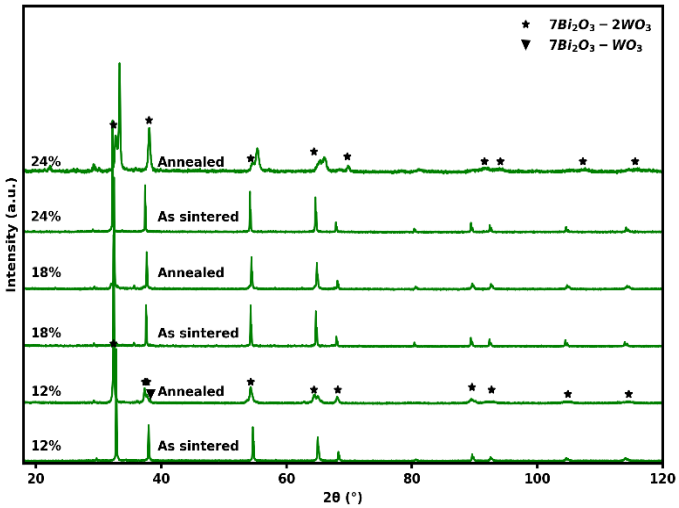

Figure 7.2. PXRD data of the pellets of the DWSB system before and after annealing at 500 °C for 100 h of the pellets showing phase separation across the composition range from 12-24 mol% TSC. Plots are stacked for clarity.

composition decomposed into a mixture of the δ- and rhombohedral phases while the 16E6D2WSB composition did not. This further reinforced the idea that Dy^{3+} is detrimental in the stability of the δ-phase compared to Er^{3+}.

7.2.3 Phase stability of the ENWSB and DNWSB Systems

From the previous section, the question then is why add Dy at all. To further understand the effects of the Dy^{3+} cation on the performance of the materials and the significance of the configurational entropy on phase stability in triple doped systems, a new DNWSB system was fabricated. This is

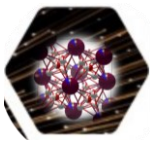

analogous to the $Er_{0.15}Nb_{0.025}W_{0.025}Bi_{0.80}O_{1.525}$ (15E2.5N2.5WSB) system reported by Shitara *et al.* [28] that did not exhibit any phase degradation nor order-disorder transition after annealing at 500 °C for 100 h. In this work, the ENWSB system (cation ratio Er:Nb:W = 8:3:1) was also fabricated—albeit with a different ratio for the cations to those of Shitara *et al.* [28] (cation ratio Er:Nb:W = 6:1:1) to match the oxide ratio used in this work for the triply substituted systems. Therefore, the TSC for these systems (ENWSB and DNWSB) is with respect to the cations. The objective was to verify the reported resistance to both phase degradation and ordering of the O^{2-} sublattice in the ENWSB system and demonstrate the effect of the Dy^{3+} cations.

The 12 mol% TSC of ENWSB showed minor phase separation which was observed through anisotropic peak broadening (Fig. 7.3(a)). However, the 18 and 24 mol% compositions exhibited the resistance to phase separation expected from the ENWSB system after prolonged annealing. The DTA curve of the 18 mol% ENWSB system exhibited an endothermic peak, characteristic of the order-disorder transition (Fig. 7.3(b)). At 24 mol% the endothermic peak in the DTA curve was not observed as expected for compositions with more than 20 mol% TSC in the ENWSB system as reported by Ref. [28].

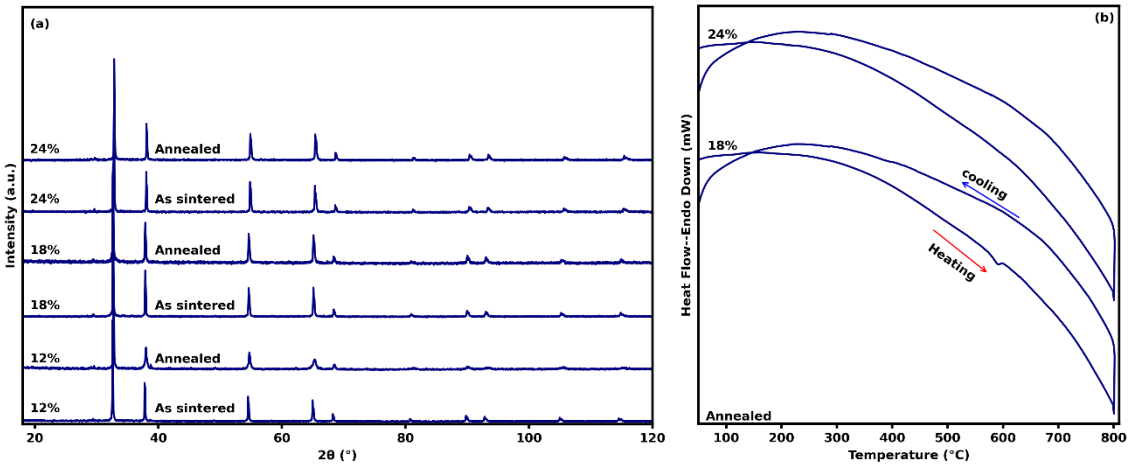

Figure 7.3. **(a)** PXRD data of the pellets of the ENWSB system before and after annealing at 500 °C for 100 h showing phase stability across the composition range explored. **(b)** DTA curves showing how the 12E4.75N2.25WSB exhibit an endothermic displacement characteristic of the order-disorder transition yet the 16E6N4WSB does not. Plots are stacked for clarity.

In contrast, DNWSB showed significant anisotropic peak broadening and peak splitting indicative of phase separation after annealing in conditions virtually identical to those of ENWSB throughout the 12-24 mol% range of TSC (Fig. 7.4(a)). The 12 mol% composition decomposed into a mixture of the δ-phase (*Fm*-3*m*) and γ-phase (*I*23) and cation-ordered C-type like phase ($I2_13$) while the

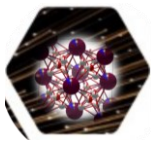

18 mol% composition decomposed into a mixture of δ-phase and the cation-ordered C-type like phase. These results further highlight the influence of the identity of the substituent on phase stability compared to the number of substituents used, emphasising that it is not only the number of constituents that are important, but their identities too. As observed in the DWSB [30] and EWSB [28] systems, the bigger Dy^{3+} (0.912 Å) cation seems to offer less resistance to phase separation than the smaller Er^{3+} (0.89 Å) cation after prolonged annealing. Jiang and Wachsman [43] made similar observations when they compared the phase stabilities of different solid solutions of Bi_2O_3 made from rare earths.

Interestingly, the DTA curve of 24 mol% DNWSB did not exhibit any endothermic peaks, nor the endothermic peaks ascribed to the order-disorder transition despite evidence of anisotropic peak broadening characteristic of a mixture of phases [31]. This means that either the DTA was not sensitive enough to subtle changes and/or this composition does not exhibit any DTA detectable phase changes in the temperature range probed and the δ-phase showed no observable ordering of the local structure.

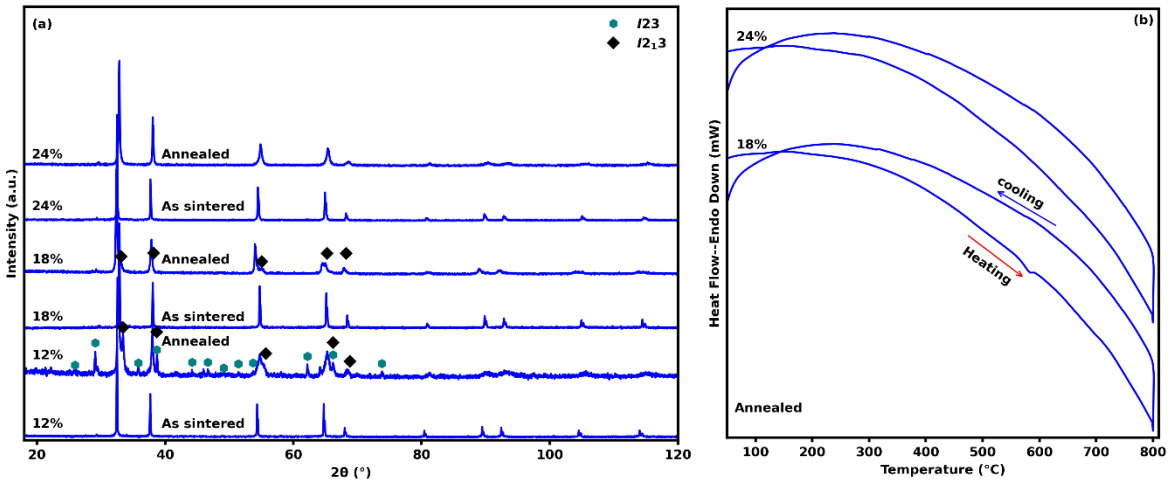

Figure 7.4. **(a)** PXRD data of the pellets of the DNWSB system before and after annealing at 500 °C for 100 h showing phase separation across the composition range explored. Plots are stacked for clarity. **(b)** DTA curves showing how the 12D4.75N2.25WSB exhibit an endothermic displacement characteristic of the order-disorder transition yet the 16D6N4WSB does not. No extra displacements were observed despite a mixture of phases forming upon annealing. Plots are stacked for clarity.

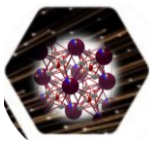

7.2.4 Phase stability in the DESB System−A Comparison with the DEWSB System

To investigate the influence of W^{6+} in the phase stability exhibited by DEWSB, the DESB system was fabricated without any W^{6+}. The DESB system (ratio of Dy_2O_3: Er_2O_3 = 8:4) was also annealed in air at 500 °C for 100 h. It exhibited phase degradation from the δ-phase to a mixture of

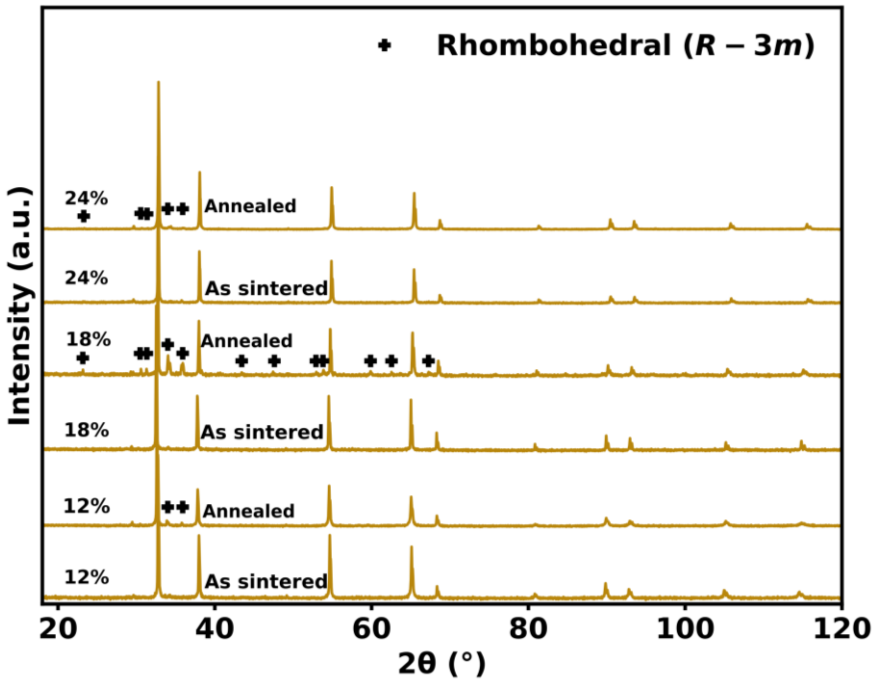

Figure 7.5. PXRD data of the pellets of the DESB system before and after annealing at 500 °C for 100 h showing phase separation from the δ-phase to a rhombohedral phase across the composition range from 12-24 mol% TSC. Plots are stacked for clarity.

rhombohedral (*R*-3*m*) and δ-phases throughout the explored range of 12-24 mol% (Fig. 7.5). These results highlighted the importance of the W^{6+} impurity cation in stabilizing the δ-phase in the DEWSB system.

7.2.5 The DENSB System−the Role of Nb^{5+} in the Order–Disorder Transition

Yun *et al.* [27] reported that the addition of some transition metal cations into Bi_2O_3 solid solutions substituted with some rare earths prevents the ordering of the O^{2-} sublattice. Shitara *et al.* [28] explored the ENWSB system to illustrate how the transition metal cations W^{6+} and Nb^{5+} substituted into ESB eliminates the ordering phenomenon. However, using two transition metals simultaneously made it difficult to explore the influence of each impurity cation. In this work, DEWSB and DENSB systems were used to investigate the influence of Nb^{5+} compared to W^{6+} on the ordering of the local structure when substituted separately into different but analogous systems.

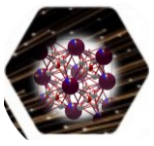

The DENSB system (ratio of substituents is 8:3:1 with respect to oxides) was subjected to virtually identical annealing conditions to those of DEWSB (ratio of substituents is 8:3:1 with respect to oxides). For the 12 mol% TSC composition in DENSB, an unknown impurity phase was observed after quenching the sample in air from 850 °C which remained even after annealing at 500 °C for 100 h. For the 18 and 24 mol% compositions, there was no observable phase degradation of the δ-phase (Fig. 7.6(a)). However, DTA curves from both the 18 and 24 mol% TSC compositions in the DENSB system exhibited endothermic peaks characteristic of the order-disorder transition– albeit very subtle for the 24 mol% TSC composition (Fig. 7.6(b)). A second cycle of heating and cooling (cycle II) exhibited no endothermic peak on the DTA signal of the 24 mol% TSC composition (Fig. 7.6 (b)). This means that the disordered state was recovered after heating beyond 600 °C and the kinetics of ordering are slow on cooling. This behaviour is common among aged solid solutions of Bi_2O_3 [27].

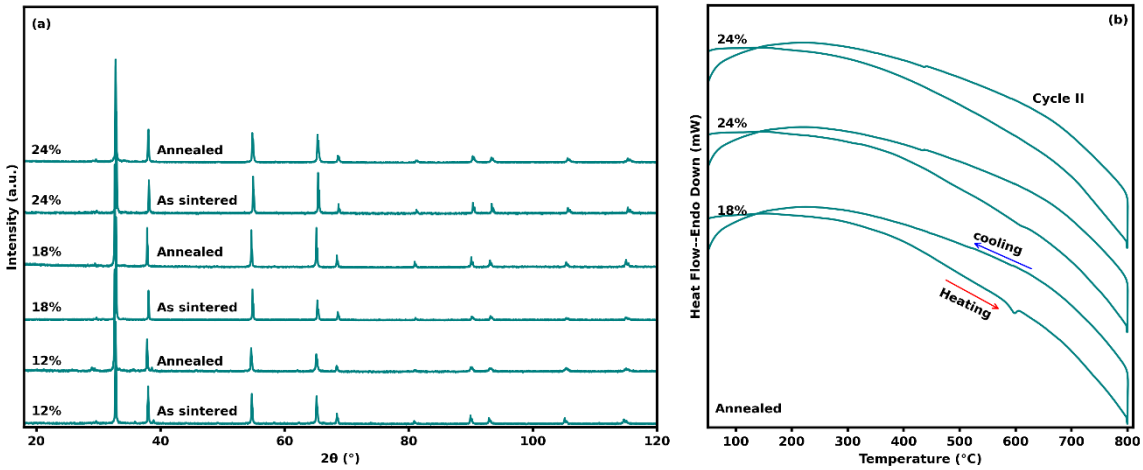

Figure 7.6. **(a)** PXRD data of the pellets of the DENSB system after annealing at 500 °C for 100 h showing phase stability across the composition range explored. Plots are stacked for clarity. **(b)** shows DTA curves of 18 and 24 mol% TSC compositions exhibiting the endothermic displacement characteristic of the order-disorder transition. This was absent after cycle II in the 24 mol% TSC composition indicating that the process is reversible. Plots are stacked for clarity.

These results mean that the addition of the Nb^{5+} cation was, to a certain extent, able to suppress the phase degradation observed in the DESB system. These results agree with those from Joshi *et al.* [44] and Tung *et al.* [45]. However, Nb^{5+} without W^{6+} present could not prevent the ordering of the local structure during annealing for the DENSB system, even at 24 mol% TSC. The DTA results of 24 mol% TSC of the DESB system did not exhibit the characteristic endothermic peak for the order-disorder transition (Fig. S7.3). This suggests that without W^{6+}, the Nb^{5+} cation might actually be promoting the ordering of the local structure to a small extent.

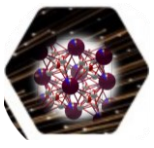

7.2.6 Electrochemical Impedance Spectroscopy

To check ageing on the systems for compositions that did not exhibit any phase degradation after 300 h of annealing (see section 7.2.2 and Fig. S7.2), VT-EIS was conducted as described in section 7.2.4. The compositions 16E6D2WSB and 16E6N4WSB were probed since they were the most stable after 300 h of annealing. The sample with composition 12E4.5N3WSB was used as a reference of a composition that exhibited only local structure ordering and no phase transitions.

The 16E6N4WSB composition did not exhibit any observable ageing in the EIS results (Fig. 7.7).

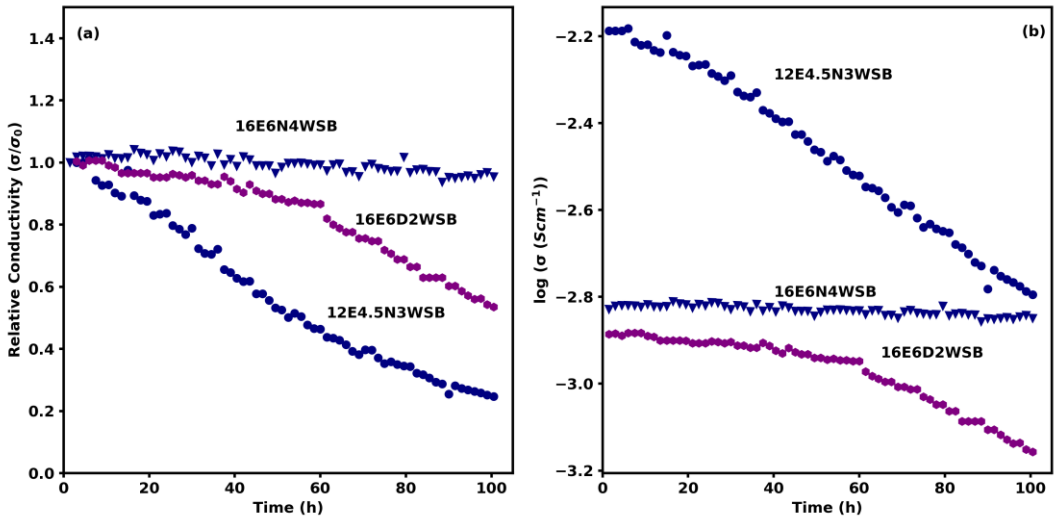

Figure 7.7. **(a)** Relative conductivity and **(b)** log of the conductivity at 500 °C showing ageing for the 12E4.75N2.5WSB, and 16E6DWSB compositions and resistance to ageing for 16E6N4WSB composition for up to 100 h.

The 16E6D2WSB and 12E4.5N3WSB showed ~50 and 80% decrease in relative conductivity after 100 h of isothermal annealing at 500 °C, respectively (Fig. 7.7(a)). No changes in the PXRD patterns were detected after the EIS data were collected. No discolouration of the electrolyte-electrode interface was observed to suggest reaction between electrodes and electrolyte. No additional semi-circle was detected in the EIS results (Fig. S7.4) to suggest changes at the grain boundary resistance. This suggests that the ageing could be primarily and predominantly as a result of changes in the local structure of these compositions as widely reported [23-26]. Interestingly, after 100 h of isothermal annealing, the conductivity of 12E4.5N3WSB was similar to that of 16E6N4WSB (Fig. 7.7 (b)).

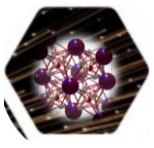

7.2.7 Photoluminescence Spectroscopy

Photoluminescence (PL) of the lanthanides has been used extensively to probe the local environment around these elements in crystalline materials and glasses [46-50]. It has been reported that PL from the lanthanides is predominantly as a result of the Laporte forbidden intra $4f^N$-$4f^N$ dipole transitions [51, 52]. The selection rules for the intra $4f^N$-$4f^N$ dipole transitions are described by the Judd-Ofelt theorem [53, 54]. When the lanthanide ion is in a strictly centrosymmetric environment, the intra $4f^N$-$4f^N$ electric dipole transitions are parity forbidden unless the centrosymmetry is broken by vibrations. In this case, broad PL peaks of low intensity are barely observed if at all. For an ideal crystalline material of δ-phase (space group *Fm*-3*m*) Bi_2O_3, Bi^{3+} occupies the 4*a* site which has octahedral (O_h) site symmetry, i.e., it is a centrosymmetric site. When Er is substituted in this Bi_2O_3 system, it is expected to replace Bi^{3+} in the 4*a* site. Therefore, PL signals for the Er^{3+} cations should, at most, be weak and broad. However, as evident in Fig. 7.8, the Er^{3+} cations exhibit a very strong, sharp PL signal in the compositions probed.

This suggests that not all the Er^{3+} cations are substituting for the Bi^{3+} cations at exactly the 4*a* site. This supports the total scattering measurements reported previously [55]. It can be observed that after quenching the material from 850 °C, the PL signal is more intense compared to that of the same material which was subsequently annealed isothermally at a lower temperature (500 °C) and then also quenched. This suggests that quenching from the higher temperature leaves more Er^{3+} cations in a non-centrosymmetric environment compared to those in the same sample, but isothermally annealed at 500 °C for 50 hrs and also quenched. Upon further isothermal annealing,

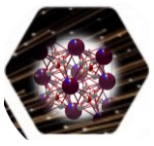

even for a material that exhibited ageing beyond the 50-hour mark in EIS (Fig. 7.7), the PL signal does not change significantly (Fig. 7.8).

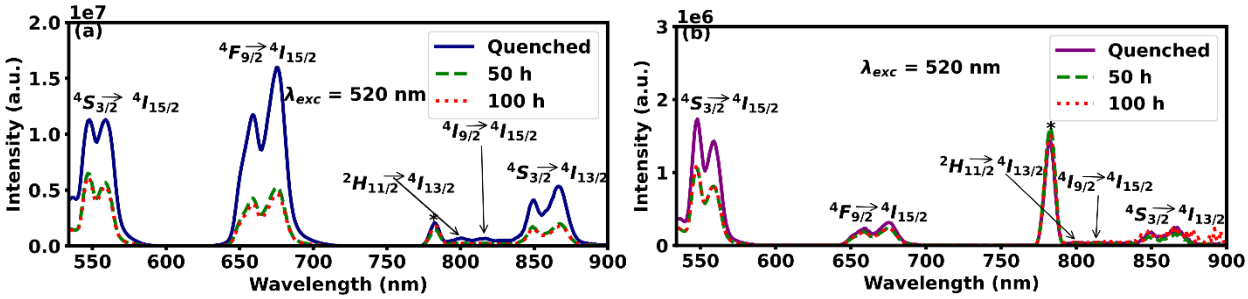

Figure 7.8. PL spectra of **(a)** 12E4.5N3WSB, and **(b)** 16E6D2WSB measured at ambient temperature after quenching from 850 °C, and after annealing at 500 °C for 50 and 100 h. The peak with an asterisk (*) at ~ 782 nm represents an instrument contribution.

Most importantly, isothermal annealing at 500 °C and ageing do not seem to move the Er^{3+} cations to centrosymmetric environments. The consequence of this observation is that it brings into question the validity of the model that suggests that upon ageing, in a simple cubic system formed by the oxide ions and vacancies around the metal cations, the vacancies order along the <111> direction in the stabilized δ-phases [23]. This is the first evidence from PL to suggest that, at least around some of the Er dopants, the environment remains non-centrosymmetric after isothermal annealing at 500 °C in the range 50-100 h for both an aged sample and a sample that did not exhibit ageing (Fig. S7.5).

7.2.8 X-ray Absorption Fine Structure

To further study the effects of ageing on the local structure of the materials that exhibited ageing, XAFS was used to probe the local environment around some of the metal cations in samples where PL and VT-EIS were done. This technique shows incredible element specificity and can be very sensitive to the local structural changes around a specific cation. In this study, XAFS measurements were conducted around the Bi and Er L_3-edges as described in section 7.2.6 and provide local structural insights into the ageing process. The k^2-weighted EXAFS spectra and the magnitude of their Fourier transforms for both Bi- and Er-L_3 edges show no major differences between samples annealed for 100 h at 500 °C (henceforth, referred to as annealed) and those quenched from 850 °C, henceforth, referred to as sintered (Fig. 7.9 and Fig. S7.6). This was observed across all the compositions that were tested for ageing using EIS and PL.

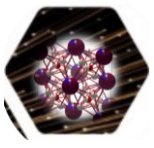

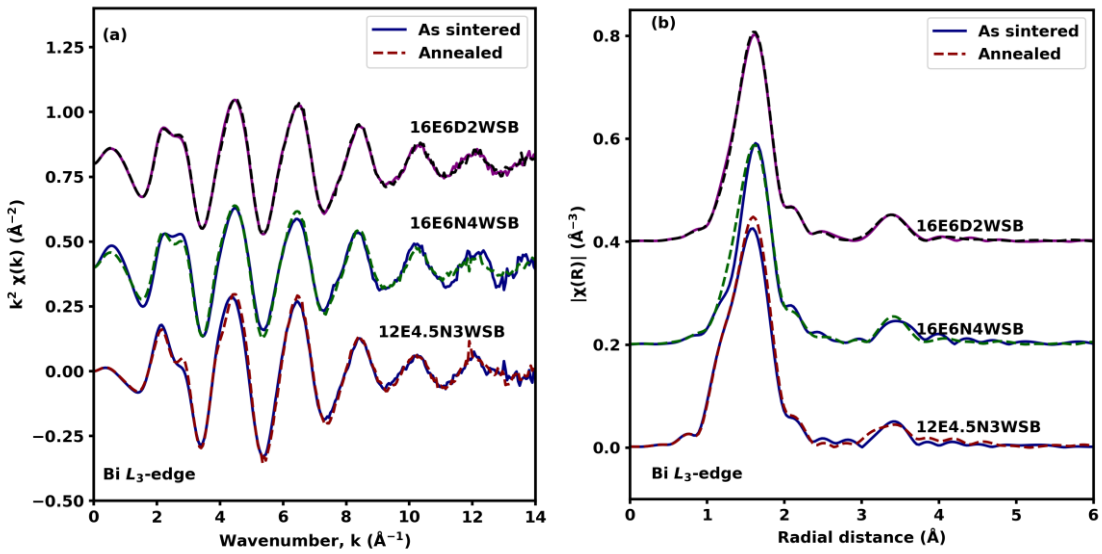

Figure 7.9. **(a)** k^2-weighted Bi L_3-edge EXAFS spectra and **(b)** the magnitude of their Fourier transforms without phase correction before and after annealing at 500 °C for 100 h for the 12E4.5N3WSB, 16E6N4WSB and 16E6D2WSB compositions. Plots are stacked for clarity.

The first peaks at around 1.61 and 1.86 Å in the magnitude of the Fourier transforms of the k^2-weighted EXAFS spectra without phase corrections for the Bi (Fig. 7.9 (b)) and Er L_3-edges (Fig. S7.6), respectively, are mainly attributed to the backscattering from the nearest neighbours of the absorber (i.e., oxide ions). Changes in the coordination number and/or order of the oxygen sublattice around the absorber is normally reflected by an increase or decrease in the amplitude of this peak [56, 57]. Changes in bond length are normally reflected by a shift in peak position for a given sample [56]. However, no significant peak shifts or changes in the amplitude of the first peaks in the Fourier transforms of the k^2-weighted EXAFS spectra were observed in all the annealed samples compared to the as sintered samples for a given edge and composition (Fig. 7.9 and Fig. S7.6).

A combination of different models were used to fit the first peaks in the EXAFS data for both the Bi and Er L_3-edges in all the compositions to ascertain the extent of ordering in the local structure. For the Bi L_3-edge, the model where all 6 oxygens around the Bi^{3+} cation (δ-polymorph, *Fm*-3*m*) have the same bond length did not fit the data well (Fig. S7.7). However, the model adapted from both the $P2_1/c$ (monoclinic α-polymorph) and *Fm*-3*m* models where an average of ~3.12 oxygens with average bond length of ~2.09 Å and 2 oxygens with average bond length of ~2.58 Å, respectively, fitted the data well across all compositions as shown in Fig. 7.10 and Fig. S7.8. This

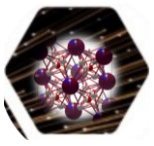

agrees with the observation made by Battle *et al.* [58] that the Bi cations have an asymmetric bonding environment and upon doping the Bi cations can be displaced away from the 4*a* site.

For the Er L_3-edge the model (path from 8b site of *Ia*-3) where all oxygens around the Er^{3+} cation have the same bond length fitted the first peak well (Fig. S7.9 and S7.10), giving an average Er–O bond length of ~ 2.31 Å and coordination number ranging between 5.24 and 5.92 for all samples fitted (Table S7.4). These values agree well with those obtained by Mignotte [59] where Er rich domains suspected to be those of Er_2O_3 were reported. No significant changes in the bond lengths or coordination numbers were observed between as sintered and aged samples. This intimated that the ageing process does not involve a significant change in the average bond length or coordination number around the probed absorbers for these sample compositions. These observations do not explain the significant decrease in conductivity and the observed endothermic peak in DTA characteristic of the order-disorder transition in aged samples.

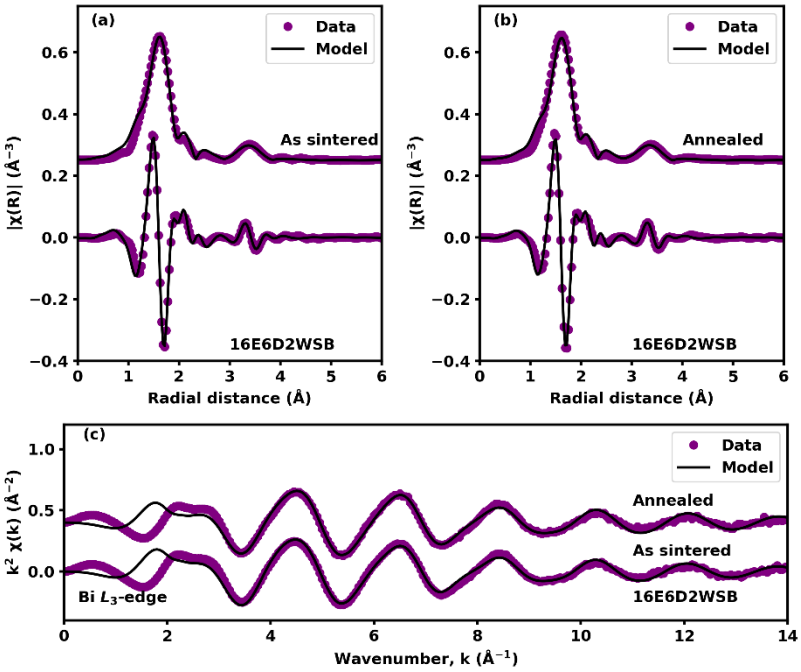

Figure 7.10. A fit to the magnitude of the Fourier transform and its real component of Bi L_3-edge k^2-weighted EXAFS spectra: **(a)** before and **(b)** after annealing at 500 °C for 100 h of the 16E6D2WSB composition. **(c)** A fit to the k^2-weighted Bi L_3-edge EXAFS spectrum (fitting range was from 3.000 to ~12.500 $Å^{-1}$). Backscattering paths from both *Fm*-3*m and P2₁/c* models were used for the fitting. Plots are stacked for clarity.

Fitting the peaks that are predominantly emanating from the backscattering from the next nearest neighbours (NNNs) is always a challenge in EXAFS. This is because in addition to the high correlation between parameters and contributions from multiple scattering, thermal displacement

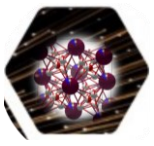

and static disorder effects are dominant in this region. As a result, the data is reduced to the noise level. Therefore, the accuracy of the results in this region is low. Nevertheless, different models were used to fit the data to obtain obvious trends in the cation sublattice of Bi and Er absorbers.

In the *Fm*-3*m* space group type, the metals in the 4*a* (0 0 0) site should be surrounded by 12 NNNs with a degeneracy of 12. However, in the Bi L_3-edge, this model failed to produce a reasonable fit in any of the modelled compositions. This was also observed by Battle *et al.* [58] and Gambino *et al.* [60] from EXAFS data of stabilized δ-phases. When a combination of the *Fm*-3*m* and $P2_1/c$ models was used [55, 61], the fit improved significantly (Fig. 7.10). In all explored systems and for the Bi L_3-edge, there were three different types of Bi–NNN(M) distances (where M = metal). In the 16E6D2WSB composition for instance, the first NNN distance was for Bi–Er observed at ~3.61 Å with a degeneracy of about 2. The second and third Bi–Bi distances were found at ~3.78 and ~3.91 Å with degeneracies of 6 and 4, respectively. This trend was observed in all explored systems and the results are summarized in Table 7.1.

Table 7.1. Summary of the fitted parameters from EXAFS for the 12E4.5N3WSB, 16E6N4WSB and 16E6D2WSB compositions at the Bi L_3-edge. N is coordination number, R is bond length, σ^2 is mean-square displacement of R. Backscattering paths from both *Fm*-3*m and* $P2_1/c$ models were used for the fitting.

Sample		12E4.5N3WSB As sintered	12E4.5N3WSB Annealed	16E6N4WSB As sintered	16E6N4WSB Annealed	16E6D2WSB As sintered	16E6D2WSB Annealed
Bi—O	N	1.56 ± 0.04	1.64 ± 0.07	1.52 ± 0.1	1.63 ± 0.03	1.56 ± 0.04	1.59 ± 0.04
	R(Å)	2.08 ± 0.01	2.08 ± 0.009	2.08 ± 0.006	2.08 ± 0.005	2.08± 0.007	2.08 ± 0.006
	σ^2(Å^2)	0.0034 ± 0.0006	0.0034 ± 0.0006	0.0025 ± 0.0003	0.0031 ± 0.0003	0.0026 ± 0.0003	0.0022 ± 0.0003
Bi—O	N	1.56 ± 0.04	1.64 ± 0.07	1.52 ± 0.1	1.63 ± 0.03	1.56 ± 0.04	1.59 ± 0.04
	R(Å)	2.12 ± 0.1	2.12 ± 0.1	2.09 ± 0.1	2.09 ± 0.1	2.09 ± 0.1	2.09 ± 0.1
	σ^2(Å^2)	0.019 ± 0.006	0.0192 ± 0.006	0.0830 ± 0.04	0.0828 ± 0.04	0.0600 ± 0.02	0.0828 ± 0.04
Bi—O	N	2.00	2.00	2.00	2.00	2.00	2.00
	R(Å)	2.55± 0.02	2.55 ± 0.02	2.59 ± 0.02	2.59 ± 0.01	2.60 ± 0.02	2.59 ± 0.02
	σ^2(Å^2)	0.013 ±0.004	0.013 ± 0.003	0.011 ± 0.002	0.012 ± 0.002	0.012 ± 0.002	0.011 ± 0.002
Bi—Bi	N	6.00	6.00	6.00	6.00	6.00	6.00
	R(Å)	3.68 ± 0.05	3.70 ± 0.08	3.73 ± 0.04	3.71 ± 0.02	3.78 ± 0.2	3.78 ± 0.2
	σ^2(Å^2)	0.021 ± 0.005	0.020 ± 0.01	0.015 ± 0.005	0.017 ± 0.004	0.029 ± 0.02	0.029 ± 0.03
Bi—Bi	N	4.00	4.00	4.00	4.00	4.00	4.00
	R(Å)	3.87 ± 0.04	3.88 ± 0.09	3.91 ± 0.03	3.89 ± 0.02	3.91	3.91 ± 0.1
	σ^2(Å^2)	0.018 ± 0.004	0.017 ± 0.008	0.013 ± 0.003	0.015 ±0.004	0.021 ± 0.01	0.022 ± 0.01
Bi—Er	N	2.00	2.00	2.00	2.00	2.00	2.00
	R(Å)	3.56 ± 0.03	3.56 ± 0.08	3.58 ± 0.04	3.58 ± 0.04	3.61 ± 0.09	3.61 ± 0.05
	σ^2(Å^2)	0.015 ± 0.004	0.0178 ± 0.01	0.0125 ± 0.005	0.0119 ± 0.003	0.0164 ± 0.007	0.0162 ± 0.007
Bi—O	N	24.00	24.00	24.00	24.00	24.00	24.00
	R(Å)	4.20 ± 0.03	4.24 ± 0.14	4.23 ± 0.04	4.23 ± 0.04	4.29 ± 0.08	4.29 ± 0.06
	σ^2(Å^2)	0.040 ± 0.007	0.045 ± 0.02	0.035 ± 0.007	0.015 ± 0.004	0.040 ± 0.01	0.040 ± 0.01

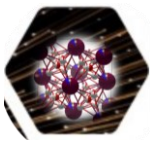

The 12 degenerate NNN distances from the *Fm*-3*m* model also failed to fit the magnitude of the Fourier transform data in the Er-L_3 edge in all systems. Battle *et al.* [61] had indicated that Er has a tendency to keep a similar environment in the substituted systems to that in the pure Er_2O_3 (space group *Ia*-3). Comparing the magnitude of the Fourier transform of the EXAFS data of Er_2O_3 to those from the substituted systems revealed some similarities between the Er_2O_3 and the substituted systems (Figs. 7.11 and S7.11). This suggested the possible aggregation of Er ions into Er_2O_3-like domains. The magnitude of the Fourier transforms of the EXAFS data from the substituted systems also show similar behaviour and features on the intensity of the NNN peaks to the data obtained from nanoparticles of Lu_2O_3 (space group *Ia*-3) when compared to the bulk as observed by Ref. [62]. Thus the decrease in the amplitudes of the peaks attributed predominantly to the backscattering from NNNs in the magnitude of the Fourier transform of the EXAFS data could be attributed to disorder in the metal sublattice due to doping and/or the formation of Er_2O_3-like nanodomains in the substituted systems rather than a complete phase separation. The formation of nanodomains is a common occurrence for rare earth (RE) cations in fluorite structures [63-65].

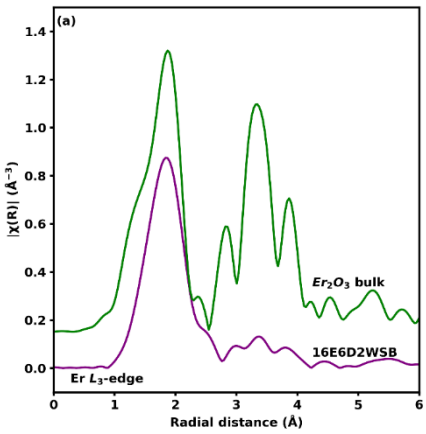

Figure 7.11. The magnitude of the Fourier transforms of the k^2-weighted Er L_3-edge EXAFS data for the Er_2O_3 and 16E6D2WSB compositions. The plots are stacked for clarity.

A model incorporating the Er in both *Ia*-3 and *Fm*-3*m* phases was used to fit the EXAFS data. The fits improved significantly across all systems (Fig. S7.9 and S7.10) and the data is summarized in Table S7.4. The results provide evidence of clustering of Er cations in all the explored systems. The M-M distances obtained are slightly different from those in the *Ia*-3 model but consistent with those reported by Refs. [64, 65] for similar systems where clustering was observed, hinting at some distortions caused by the presence of Bi cations and reorientation of oxide ion vacancies. Since there were no significant changes between the EXAFS of aged and as-sintered material, consistent

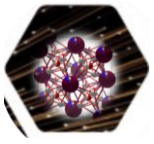

with the PL results, the nanodomains were not growing in size to form a separate phase with ageing. This is also consistent with the results from Bragg data since no discernible Er_2O_3 (*Ia*-3) phases were detected after ageing in the Bragg data.

The second derivative of XANES data of some lanthanides have been used to study the local geometry of the cations in substituted crystalline and amorphous systems [66-68]. The most intense peak (the white line) results predominantly from the dipole transition from the core $2p_{3/2}$ to the empty 5*d* states in the Er-L_3 edge. The degeneracy and density of the 5*d* states depends on the site symmetry of the Er cations in the host material. Therefore, the white line can be used to deduce the possible site symmetry of the cations. However, the white line needs high resolution to resolve contributions from non-degenerate compact electronic states, and the second derivative of the white line is normally preferred.

The EXAFS results indicated clustering and a tendency for some of the Er to maintain a similar environment to that found in Er_2O_3 in all the systems explored using XAFS in this work. In Fig. S7.12 there is a strong character of the Er_2O_3 in the XAFS spectra. The strong Er_2O_3 character is also evident on the second derivatives of the white lines of the substituted systems in both annealed and as sintered material (Fig. 7.12). There is a quasi-doublet in the second derivative data from the as sintered samples for the ENWSB system (Figs. 7.12(a) and 7.12 (b)) and a singlet in the second derivative data from the as sintered sample for the DEWSB system (Fig. 7.12 (c)) in addition to the doublet from the Er_2O_3 like character. This suggests that there are at least three different electronic transitions from the Er absorbers.

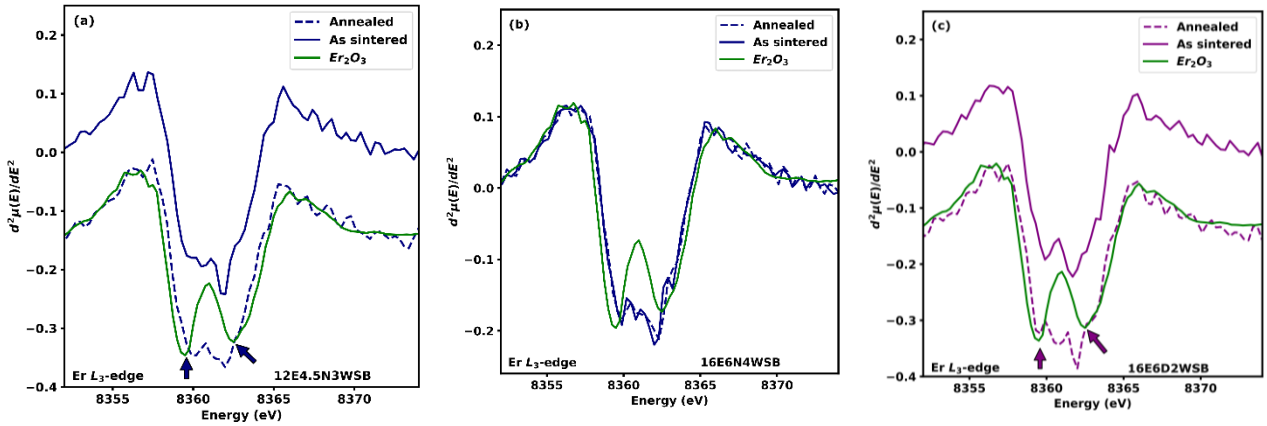

Figure 7.12. Second derivative spectra of commercial Er_2O_3, as sintered and annealed **(a)** 12E4.5N3WSB **(b)** 16E6N4WSB and **(c)** 16E6D2WSB. Some plots are stacked for clarity.

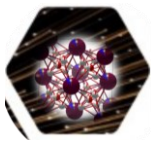

In Er_2O_3 (SG *Ia*-3), the Er occupies two crystallographically independent sites, viz: 8*b* (0.25, 0.25, 0.25) and 24*d* (*x*, 0, 0.25) in the ratio 1:3 which give an overall doublet in the second derivative data. In the substituted systems, there are distorted versions of these sites as evident from the Er–O bond lengths and M–M distances obtained from EXAFS (see Table S7.4). However, the complexity of the Bi rich domains makes it hard to ascertain the additional sites of the Er cation in this phase.

Comparison of the second derivatives of aged and as sintered material show that when a material has undergone ageing, the electronic structure of the Er changes, suggesting a change in the electric field around it due to a change in site geometry (see Figs. 7.12(a) and 7.12 (c)). This affects the splitting of the empty 5*d* orbitals. In the 12E4.5N3WSB composition, there is a narrowing of the gap between the quasi-doublet peaks, and a decrease in intensity of these minima after ageing (see Fig. 7.12(a)). The second derivative spectrum of the aged material exhibits an increased Er_2O_3-like character, suggesting that the domains are becoming more Er_2O_3-like. In the 16E6D2WSB composition, the singlet splits into a quasi-doublet upon ageing, showing a strong contribution from Er_2O_3-like nanodomains (Fig. 7.12 (b)).

The major changes in the second derivative are in the features that are attributed to the Er located in the Bi rich domains. This can be ascribed to the fact that in Er_2O_3, the vacancies are already ordered, so no major changes are expected during the ageing phenomenon, but Er cations from Bi rich domains are assuming the Er_2O_3-like environments upon ageing. The increase in Er_2O_3-like character around the Er in the aged material can be correlated with the decrease in conductivity observed in the 12E4.5N3WSB and 16E6D2WSB samples (see Fig. 7.7). In the 16E6N4WSB composition, no significant ageing was observed in the EIS, PL and DTA results and there were no changes observed in the second derivative of the white line and the EXAFS data (see Fig. 7.12(b)). This reinforces the idea that factors inducing the changes in the second derivatives of 12E4.5N3WSB and 16E6D2WSB are caused by the ageing phenomenon.

7.2.9 Total scattering Analysis

Total scattering data comprise Bragg and diffuse scattering components. The diffuse scattering data emanates from the short-range ion-ion correlations and appear as broad undulations in the reduced total scattering structure function F(Q). The Fourier transform of F(Q) can give the differential pair correlation function D(*r*). D(*r*) is a weighted sum of the individual ion-ion pair

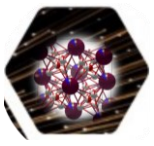

correlation functions $d_{ij}(r)$. These are related to $g_{ij}(r)$ as explained by Keen [35, 36] and the RMCProfile code calculates the individual $g_{ij}(r)$ functions which provide insights into the short-range order in the different sublattices. Only results from the annealed materials are considered here since there were no notable differences between the annealed and as-sintered material from the D(r) functions. Fitting of G(r) which is related to D(r) [35, 36] using small-box modelling revealed the inadequacy of the average structure in describing the local structure in these materials, as discussed at length by Ref. [55], therefore big-box modelling was used. The fitted F(Q), D(r) and some of the $g_{ij}(r)$ functions from the 16E6D2WSB system are plotted in Figs. 7.13 and 7.14. These results are complementary to the EXAFS results and only results from one composition will be shown. The $g_{ij}(r)$ functions for the ions with mol% ≥ 10 were plotted. The fit for the Bragg data is shown in Figure S7.13.

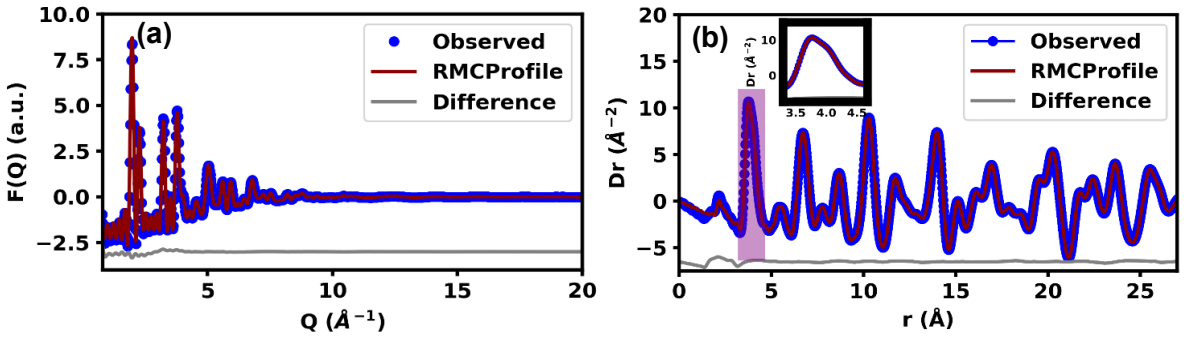

Figure 7.13. **(a)** Big-box fits of the reduced total scattering function and **(b)** the differential pair correlation function of the 16E6D2WSB composition.

The Bi–Bi modal distance was found at ~3.78 Å, with a shoulder appearing at ~4.09 Å and the Bi–Bi coordination number of ~10.22 was obtained by integrating $g_{BiBi}(r)$ up to the first minimum. A summary of the results is provided in Table S7.6 These values are comparable to those obtained from EXAFS in Table 7.1. The Bi-Bi distances and the shape of the first M–M peak as plotted for D(r) (Fig. 7.13 (b)) provide evidence that most of the Bi cations are displaced from the 4*a* site in the *Fm*-3*m* and are consistent with the distribution of the metal cations in a distorted $P2_1/c$ model of the pure α-Bi_2O_3 at local level.

The modal Bi–O distance is ~2.15 Å and the coordination number was ~4.86. These values are comparable to those obtained from neutron diffraction by Refs [72, 73]. The results also show that the $g_{BiO}(r)$ in this substituted system is similar to those of the ordered α-Bi_2O_3 (SG $P2_1/c$) and β-Bi_2O_3 (SG $P\text{-}42_1c$) polymorphs (Fig. S7.14). This was also observed by Mohn *et al*. [69], Norberg

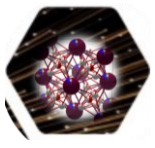

et al. [70] and Hull *et al*. [71] from both theoretical calculations and RMC modelling results. The average Bi–O distance obtained from the RMC modelling in this work was ~2.35 Å which is similar to the weighted average Bi–O distance of ~2.33 Å obtained from the Bragg data of

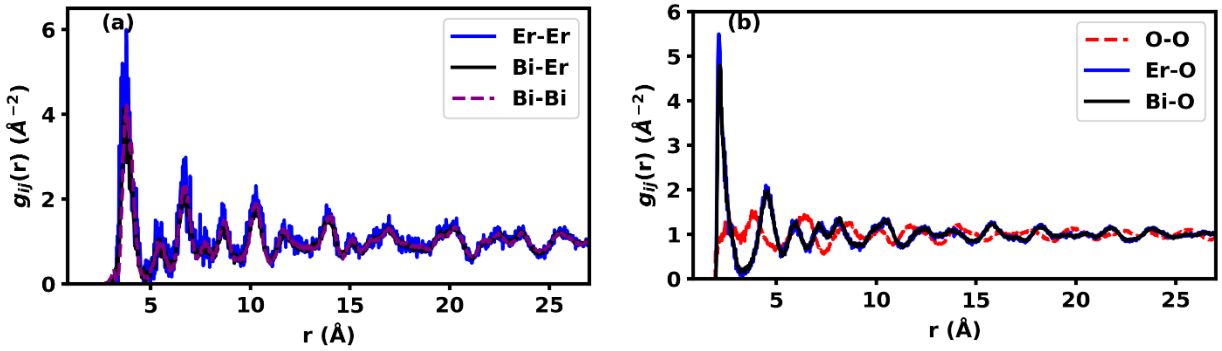

Figure 7.14. Ion-ion pair correlation functions for selected **(a)** M–M pairs and **(b)** M–O and O–O pairs of the annealed 16E6D2WSB composition.

16E6D2WSB. These results are comparable to those reported by Ref. [71] for pure δ-Bi_2O_3. The weighted average Bi–O distances significantly differ from the modal Bi–O distances as a consequence of the differences between local and average structure.

For the Er–Er pair, the M–M distances were observed at ~3.66 and ~4.00 Å **(**Fig. 7.15**)**. These Er–Er distances are comparable to those obtained by Refs. [64, 65, 74] and from EXAFS in this work (see Table S7.4). The coordination number was ~3.02 which is comparable to the ~3 observed from EXAFS (see Table S7.4). However, this coordination number is too high for a statistically distributed substituent with 16 mol% nominal Er concentration in a fluorite structure. This provides further evidence of clustering of the Er cations observed from the XAFS results.

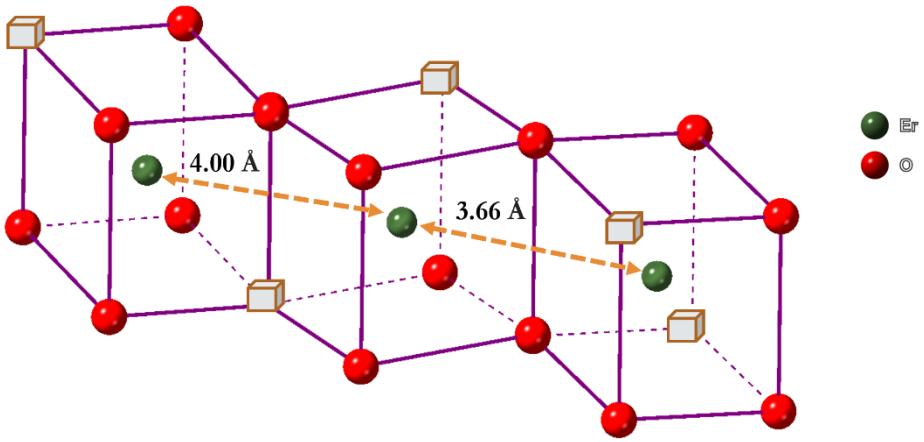

Figure 7.15. Representation of the distorted 8*b* and 24*d*-like environments around Er^{3+} cations in the 16E6D2WSB compositions obtained from both EXAFS and RMC modelling. The distances between the Er^{3+} cations were obtained from RMC and comparable to those obtained by Refs. [64, 65, 74]. The small solid cubes represent oxide ion vacancies.

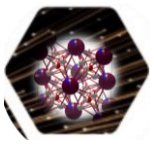

The modal Er–O distance was ~2.13 Å. This is shorter than the shortest Er–O distance in pure Er_2O_3 and points to distortions of the Er–O bonds in the substituted system. This has been observed for other rare earth (RE) and RE-like cations such as Yb^{3+} and Y^{3+} in Bi_2O_3 substituted systems from neutron diffraction data [72, 73]. The average Er–O distance and coordination number obtained from RMC modelling was ~2.31 Å and 6.25 respectively. These values are comparable to the average Er–O distance and coordination number of ~2.32 Å and 5.92 observed from EXAFS in this work.

7.3 Conclusions

In this work the contribution to phase and local structural stability by Dy, Er, W and Nb in stabilized Bi_2O_3 have been systematically investigated. It was found that the combination of Er and W in the DEWSB system improves phase stability, but that Dy is more detrimental to phase stability when annealing at 500 °C for over 300 h in this system. Nb was found to promote the disorder-order phenomenon in DENSB but suppresses the transformation of the δ-phase to rhombohedral phase upon annealing at ~500 °C for over 100 h. A 24 mol% TSC was found to stabilize the local structure and prevent the ageing phenomenon in the ENWSB system compared to 18 mol% TSC with respect to the cations TSC.

PL, EXAFS and total scattering data revealed that some of the Er cations are not replacing Bi^{3+} cations at the $4a$ sites as expected for an ideally stabilized δ-phase with the defect fluorite average structure. Both EXAFS and total scattering data revealed that most of the Bi^{3+} cations were displaced away from the ideal $4a$ sites and a clustering of Er cations were also observed in the ENWSB and DEWSB systems. These were all observed in the local structure, indicating that Er cations assumed a local environment similar to that in its parent oxide (Er_2O_3) within Bi_2O_3, more representative of nano-domains rather than complete phase separation. In the aged materials, the resemblance of the Er local structure to that of the parent oxide was more pronounced. This partly explain why the conductivity decreases with ageing since Er_2O_3 has an ordered oxygen sublattice and is a poor ionic conductor, so oxide ions will be partly blocked in the regions resembling Er_2O_3.

7.4 Acknowledgements

The authors acknowledge financial support for their research from the National Research Foundation (NRF, South Africa) and Department of Science and Innovation (DSI, South Africa), as well as the University of the Witwatersrand. S.M. Masina also acknowledges the ICDD for a

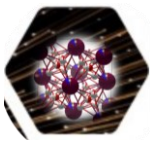

Ludo Frevel scholarship. This research used beamlines 28-ID-1 and 6-BM of the National Synchrotron Light Source II, a U.S. Department of Energy (DOE) Office of Science User Facility operated for the DOE Office of Science by Brookhaven National Laboratory under Contract No. DE-SC0012704.

7.5 References

[1] Jasinski, P., Suzuki, T. and Anderson, H.U., 2003. Nanocrystalline undoped ceria oxygen sensor. *Sensors and Actuators B: Chemical*, *95*(1-3), pp.73-77.

[2] Qu, B., Younis, A. and Chu, D., 2016. Recent progress in tungsten oxides based memristors and their neuromorphological applications. *Electronic Materials Letters*, *12*(6), pp.715-731.

[3] Balducci, G., Kašpar, J., Fornasiero, P., Graziani, M. and Islam, M.S., 1998. Surface and reduction energetics of the CeO_2− ZrO_2 catalysts. *The Journal of Physical Chemistry B*, *102*(3), pp.557-561.

[4] Shim, J.H., Chao, C.C., Huang, H. and Prinz, F.B., 2007. Atomic layer deposition of yttria-stabilized zirconia for solid oxide fuel cells. *Chemistry of materials*, *19*(15), pp.3850-3854.

[5] Adams, T.A., Nease, J., Tucker, D. and Barton, P.I., 2013. Energy conversion with solid oxide fuel cell systems: A review of concepts and outlooks for the short-and long-term. *Industrial and Engineering Chemistry Research*, *52*(9), pp.3089-3111.

[6] Park, S., Vohs, J.M. and Gorte, R.J., 2000. Direct oxidation of hydrocarbons in a solid-oxide fuel cell. *Nature*, *404*(6775), pp.265-267.

[7] Zhan, Z. and Barnett, S.A., 2005. An octane-fueled solid oxide fuel cell. *Science*, *308*(5723), pp.844-847.

[8] Kalinci, Y. and Dincer, I., 2018. Analysis and performance assessment of NH_3 and H_2 fed SOFC with proton-conducting electrolyte. *International Journal of Hydrogen Energy*, *43*(11), pp.5795-5807.

[9] Song, C., 2002. Fuel processing for low-temperature and high-temperature fuel cells: Challenges, and opportunities for sustainable development in the 21st century. *Catalysis today*, *77*(1-2), pp.17-49.

[10] Pomfret, M.B., Demircan, O., Sukeshini, A.M. and Walker, R.A., 2006. Fuel oxidation efficiencies and exhaust composition in solid oxide fuel cells. *Environmental Science and Technology*, *40*(17), pp.5574-5579.

[11] Wachsman, E.D. and Lee, K.T., 2011. Lowering the temperature of solid oxide fuel cells. *Science*, *334*(6058), pp.935-939.

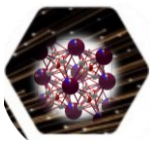

[12] Adams, T.A., Nease, J., Tucker, D. and Barton, P.I., 2013. Energy conversion with solid oxide fuel cell systems: A review of concepts and outlooks for the short-and long-term. *Industrial and Engineering Chemistry Research*, *52*(9), pp.3089-3111.

[13] Wachsman, E.D., Jayaweera, P., Jiang, N., Lowe, D.M. and Pound, B.G., 1997. Stable high conductivity ceria/bismuth oxide bilayered electrolytes. *Journal of the Electrochemical Society*, *144*(1), p.233.

[14] Harwig, H.A. and Gerards, A.G., 1978. Electrical properties of the α, β, γ, and δ phases of bismuth sesquioxide. *Journal of Solid State Chemistry*, *26*(3), pp.265-274.

[15] Levin, E.M. and Roth, R.S., 1964. Polymorphism of bismuth sesquioxide. I. Pure Bi_2O_3. *Journal of Research of the National Bureau of Standards. Section A, Physics and Chemistry*, *68*(2), p.189.

[16] Jiang, N., Wachsman, E.D. and Jung, S.H., 2002. A higher conductivity Bi_2O_3-based electrolyte. *Solid State Ionics*, *150*(3-4), pp.347-353.

[17] Watanabe, A. and Sekita, M., 2005. Stabilized δ-Bi_2O_3 phase in the system Bi_2O_3–Er_2O_3–WO_3 and its oxide-ion conduction. *Solid State Ionics*, *176*(31-34), pp.2429-2433.

[18] Mercurio, D., El Farissi, M., Frit, B., Reau, J.M. and Senegas, J., 1990. Fast ionic conduction in new oxide materials of the Bi_2O_3–Ln_2O_3–TeO_2 systems (Ln= La, Sm, Gd, Er). *Solid State Ionics*, *39*(3-4), pp.297-304.

[19] Wachsman, E.D., Ball, G.R., Jiang, N. and Stevenson, D.A., 1992. Structural and defect studies in solid oxide electrolytes. *Solid State Ionics*, *52*(1-3), pp.213-218.

[20] Takahashi, T., Esaka, T. and Iwahara, H., 1977. Conduction in Bi_2O_3-based oxide ion conductors under low oxygen pressure. I. Current blackening of the Bi_2O_3-Y_2O_3 electrolyte. *Journal of Applied Electrochemistry*, *7*(4), pp.299-302.

[21] Jung, D.W., Nino, J.C., Duncan, K.L., Bishop, S.R. and Wachsman, E.D., 2010. Enhanced long-term stability of bismuth oxide-based electrolytes for operation at 500° C. *Ionics*, *16*(2), pp.97-103.

[22] Fung, K.Z. and Virkar, A.V., 1991. Phase stability, phase transformation kinetics, and conductivity of Y_2O_3—Bi_2O_3 solid electrolytes containing aliovalent dopants. *Journal of the American Ceramic Society*, *74*(8), pp.1970-1980.

[23] Jiang, N., Buchanan, R.M., Stevenson, D.A., Nix, W.D., Li, J.Z. and Yang, J.L., 1995. Anion ordering in aged stabilized bismuth oxide. *Materials Letters*, *22*(5-6), pp.215-219.

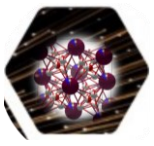

[24] Jiang, N., Buchanan, R.M., Henn, F.E.G., Marshall, A.F., Stevenson, D.A. and Wachsman, E.D., 1994. Aging phenomenon of stabilized bismuth oxides. *Materials Research Bulletin*, *29*(3), pp.247-254.

[25] Jung, D.W., Lee, K.T. and Wachsman, E.D., 2016. Dysprosium and gadolinium double doped bismuth oxide electrolytes for low temperature solid oxide fuel cells. *Journal of The Electrochemical Society*, *163*(5), p.F411.

[26] Fung, K.Z., Chen, J. and Virkar, A.V., 1993. Effect of aliovalent dopants on the kinetics of phase transformation and ordering in RE_2O_3-Bi_2O_3 (RE= Yb, Er, Y, or Dy) solid solutions. *Journal of the American Ceramic Society*, *76*(10), pp.2403-2418.

[27] Yun, B.H., Lee, C.W., Jeong, I.C. and Lee, K.T., 2017. Dramatic enhancement of long-term stability of erbia-stabilized bismuth oxides via quadrivalent Hf doping. *Chemistry of Materials*, *29* (24), pp.10289−10293.

[28] Shitara, K., Moriasa, T., Sumitani, A., Seko, A., Hayashi, H., Koyama, Y., Huang, R., Han, D., Moriwake, H. and Tanaka, I., 2017. First-principles selection of solute elements for Er-stabilized Bi_2O_3 oxide-ion conductor with improved long-term stability at moderate temperatures. *Chemistry of Materials*, *29*(8), pp.3763-3768.

[29] Watanabe, A. and Sekita, M., 2005. Stabilized δ-Bi_2O_3 phase in the system Bi_2O_3–Er_2O_3–WO_3 and its oxide-ion conduction. *Solid State Ionics*, *176*(31-34), pp.2429-2433.

[30] Jung, D.W., Duncan, K.L., Camaratta, M.A., Lee, K.T., Nino, J.C. and Wachsman, E.D., 2010. Effect of Annealing Temperature and Dopant Concentration on the Conductivity Behavior in $(DyO_{1.5})_x$–$(WO3)_y$–$(BiO_{1.5})_{1-x-y}$. *Journal of the American Ceramic Society*, *93*(5), pp.1384-1391.

[31] Masina, S.M., Billing, C., Erasmus, R.M. and Billing, D.G., 2021. A Temperature Dependent Phase Evolution Study of a Quaternary Bi_2O_3 Solid Electrolyte. [unpublished; submitted].

[32] Gražulis, S., Chateigner, D., Downs, R.T., Yokochi, A.F.T., Quirós, M., Lutterotti, L., Manakova, E., Butkus, J., Moeck, P. and Le Bail, A., 2009. Crystallography Open Database–an open-access collection of crystal structures. *Journal of Applied Crystallography*, 42(4), pp.726-729.

[33] Coelho, A.A., 2018. TOPAS and TOPAS-Academic: an optimization program integrating computer algebra and crystallographic objects written in C++. *Journal of Applied Crystallography*, *51*(1), pp.210-218.

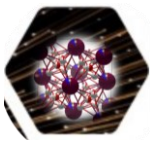

[34] Qiu, X., Thompson, J.W. and Billinge, S.J., 2004. PDFgetX2: a GUI-driven program to obtain the pair distribution function from X-ray powder diffraction data. *Journal of Applied Crystallography*, *37*(4), pp.678-678.

[35] Keen, D.A., 2020. Total scattering and the pair distribution function in crystallography. *Crystallography Reviews*, *26*(3), pp.143-201.

[36] Keen, D.A., 2001. A comparison of various commonly used correlation functions for describing total scattering. *Journal of Applied Crystallography*, *34*(2), pp.172-177.

[37] Tucker, M.G., Keen, D.A., Dove, M.T., Goodwin, A.L. and Hui, Q., 2007. RMCProfile: reverse Monte Carlo for polycrystalline materials. *Journal of Physics: Condensed Matter*, *19*(33), p.335218.

[38] Zhang, Y., Eremenko, M., Krayzman, V., Tucker, M.G. and Levin, I., 2020. New capabilities for enhancement of RMCProfile: instrumental profiles with arbitrary peak shapes for structural refinements using the reverse Monte Carlo method. *Journal of Applied Crystallography*, *53*(6), pp.1509-1518.

[39] Gattow, G. and Schröder, H., 1962. Über Wismutoxide. III. Die Kristallstruktur der Hochtemperaturmodifikation von Wismut (III)-oxid (δ-Bi2O3). *Zeitschrift für anorganische und allgemeine Chemie*, *318*(3-4), pp.176-189.

[40] Kraft, S., Stümpel, J., Becker, P. and Kuetgens, U., 1996. High resolution x-ray absorption spectroscopy with absolute energy calibration for the determination of absorption edge energies. *Review of scientific instruments*, *67*(3), pp.681-687.

[41] Ravel, B. and Newville, M., 2005. ATHENA, ARTEMIS, HEPHAESTUS: data analysis for X-ray absorption spectroscopy using IFEFFIT. *Journal of synchrotron radiation*, *12*(4), pp.537-541.

[42] Newville, M., 2013, April. Larch: an analysis package for XAFS and related spectroscopies. In *Journal of Physics: Conference Series* (Vol. 430, No. 1, p. 012007). IOP Publishing.

[43] Jiang, N. and Wachsman, E.D., 1999. Structural stability and conductivity of phase-stabilized cubic bismuth oxides. *Journal of the American Ceramic Society*, *82*(11), pp.3057-3064.

[44] Joshi, A.V., Kulkarni, S., Nachlas, J., Diamond, J., Weber, N. and Virkar, A.V., 1990. Phase stability and oxygen transport characteristics of yttria-and niobia-stabilized bismuth oxide. *Journal of Materials Science*, *25*(2), pp.1237-1245.

[45] Chou, T., Liu, L.D. and Wei, W.C.J., 2011. Phase stability and electric conductivity of Er_2O_3–Nb_2O_5 co-doped Bi_2O_3 electrolyte. *Journal of the European Ceramic Society*, *31*(16), pp.3087-3094.

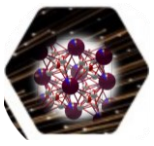

[46] Fornasiero, P., Speghini, A., Di Monte, R., Bettinelli, M., Kašpar, J., Bigotto, A., Sergo, V. and Graziani, M., 2004. Laser-excited luminescence of trivalent lanthanide impurities and local structure in CeO_2-ZrO_2 mixed oxides. *Chemistry of materials*, *16*(10), pp.1938-1944.

[47] Avram, D., Sanchez-Dominguez, M., Cojocaru, B., Florea, M., Parvulescu, V. and Tiseanu, C., 2015. Toward a unified description of luminescence–local structure correlation in Ln doped CeO_2 nanoparticles: roles of Ln ionic radius, Ln concentration, and oxygen vacancies. *The Journal of Physical Chemistry C*, *119*(28), pp.16303-16313.

[48] Sethi, A., Pandey, J., Uma, S. and Nagarajan, R., 2020. Luminescence properties of Eu^{3+}-and Tb^{3+}-doped δ-Bi_2O_3 stabilized by Th^{4+} substitution. *Journal of the American Ceramic Society*, *103*(2), pp.1027-1036.

[49] Krishnaiah, K.V. and Jayasankar, C.K., 2011, July. White light generation in Dy^{3+}-doped fluorosilicate glasses for W-LED applications. In *International Conference on Applications of Optics and Photonics* (Vol. 8001, pp. 708-713). SPIE.

[50] Zhang, F., Xiao, Z., Yan, L., Zhu, F. and Huang, A., 2010. Visible luminescence properties of Er^{3+}–Dy^{3+} codoped tellurite glasses. *Applied Physics A*, *101*(4), pp.777-780.

[51] de Bettencourt-Dias, A. ed., 2014. *Luminescence of Lanthanide Ions in Coordination Compounds and Nanomaterials*. John Wiley & Sons.

[52] Tanner, P.A., 2013. Some misconceptions concerning the electronic spectra of tri-positive europium and cerium. *Chemical Society Reviews*, *42*(12), pp.5090-5101.

[53] Judd, B.R., 1962. Optical absorption intensities of rare-earth ions. *Physical review*, *127*(3), p.750.

[54] Ofelt, G.S., 1962. Intensities of crystal spectra of rare-earth ions. *The Journal of Chemical Physics*, *37*(3), pp.511-520.

[55] Masina, S.M., Nkala, G.C., Stone, K.H., Olds, D., Billing, C., and Billing, D.G., 2021. Probing the Local Structure of Bi_2O_3 Chemical Derivatives: The Tale of the Neglected Cation Sublattice. [unpublished].

[56] Koettgen, J. and Martin, M., 2019. Coordination numbers in Sm-doped ceria using x-ray absorption spectroscopy. *The Journal of Physical Chemistry C*, *123*(11), pp.6333-6339.

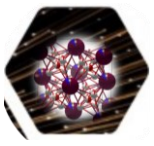

[57] Kondoh, J., Kikuchi, S., Tomii, Y. and Ito, Y., 1998. Effect of Aging on Yttria-Stabilized Zirconia: III. A Study of the Effect of Local Structures on Conductivity. *Journal of the Electrochemical Society*, *145*(5), p.1550.

[58] Battle, P.D., Catlow, C.R.A., Chadwick, A.V., Cox, P., Greaves, G.N. and Moroney, L.M., 1987. Structural and dynamical studies of δ-Bi_2O_3 oxide ion conductors: IV. An EXAFS investigation of $(Bi_2O_3)_{1-x}(M_2O_3)_x$ for M= Y, Er, and Yb. *Journal of Solid State Chemistry*, *69*(2), pp.230-239.

[59] Mignotte, C., 2001. EXAFS studies on erbium-doped TiO2 and ZrO2 sol–gel thin films. *Journal of Non-crystalline Solids*, *291*(1-2), pp.56-77.

[60] Gambino, M., Giannici, F., Longo, A., Di Tommaso, S., Labat, F. and Martorana, A., 2015. Dopant clusterization and oxygen coordination in Ta-doped bismuth oxide: A structural and computational insight into the mechanism of anion conduction. *The Journal of Physical Chemistry C*, *119*(47), pp.26367-26373.

[61] Gateshki, M., Petkov, V., Williams, G., Pradhan, S.K. and Ren, Y., 2005. Atomic-scale structure of nanocrystalline ZrO_2 prepared by high-energy ball milling. *Physical Review B*, *71*(22), p.224107.

[62] Qi, Z., Liu, M., Chen, Y., Zhang, G., Xu, M., Shi, C., Zhang, W., Yin, M. and Xie, Y., 2007. Local structure of nanocrystalline Lu_2O_3: Eu studied by X-ray absorption spectroscopy. *The Journal of Physical Chemistry C*, *111*(5), pp.1945-1950.

[63] Ohashi, T., Yamazaki, S., Tokunaga, T., Arita, Y., Matsui, T., Harami, T. and Kobayashi, K., 1998. EXAFS study of $Ce_{1-x}Gd_xO_{2-x/2}$. *Solid State Ionics*, *113*, pp.559-564.

[64] Checchia, S., Scavini, M., Allieta, M., Brunelli, M., Ferrero, C. and Coduri, M., 2015. Size and spatial correlation of defective domains in yttrium-doped CeO2. *Powder Diffraction*, *30*(S1), pp.S119-S126.

[65] Scavini, M., Coduri, M., Allieta, M., Masala, P., Cappelli, S., Oliva, C., Brunelli, M., Orsini, F. and Ferrero, C., 2015. Percolating hierarchical defect structures drive phase transformation in $Ce_{1-x}Gd_xO_{2-x/2}$: a total scattering study. *IUCrJ*, *2*(5), pp.511-522.

[66] Ishii, M., Komuro, S., Morikawa, T., Aoyagi, Y., Ishikawa, T. and Ueki, T., 1999. XANES Analysis of Optical Activation Process of Er in Si: Er_2O_3 Thin Film: Electronic and Structural Modifications around Er. *Japanese Journal of Applied Physics*, *38*(S1), p.191.

[67] Anjana, R., Jayaraj, M.K., Yadav, A.K., Jha, S.N. and Bhattacharyya, D., 2018. Investigating the evolution of local structure around Er and Yb in ZnO: Er and ZnO: Er, Yb on annealing using X-ray absorption spectroscopy. *Journal of Applied Physics*, *123*(15), p.153102.

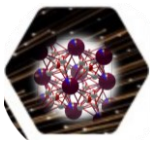

[68] Yamamoto, T., Tanaka, T., Matsuyama, T., Funabiki, T. and Yoshida, S., 1999. XAFS study of the structure of the silica-supported ytterbium oxide catalyst. *Solid State Communications*, *111*(3), pp.137-142.

[69] Mohn, C.E., Stølen, S., Norberg, S.T. and Hull, S., 2009. Ab initio molecular dynamics simulations of oxide-ion disorder in the δ-Bi_2O_3. *Physical Review B*, *80*(2), p.024205.

[70] Norberg ST, Eriksson SG, Hull S. Comparison of short-range ion–ion correlations in the α, β and δ phases of Bi_2O_3. Solid State Ionics. 2011 Jun 16;192(1):409-12.

[71] Hull, S., Norberg, S.T., Tucker, M.G., Eriksson, S.G., Mohn, C.E. and Stølen, S., 2009. Neutron total scattering study of the δ and β phases of Bi_2O_3. *Dalton Transactions*, (40), pp.8737-8745.

[72] Leszczynska, M., Liu, X., Wrobel, W., Malys, M., Krynski, M., Norberg, S.T., Hull, S., Krok, F. and Abrahams, I., 2013. Thermal variation of structure and electrical conductivity in Bi4YbO7. 5. *Chemistry of Materials*, *25*(3), pp.326-336.

[73] Borowska-Centkowska, A., Leszczynska, M., Wrobel, W., Malys, M., Hull, S., Krok, F. and Abrahams, I., 2020. Stability of tungsten-doped δ-Bi3YO6. *Solid State Ionics*, *345*, p.115173.

[74] Coduri, M., Scavini, M., Allieta, M., Brunelli, M. and Ferrero, C., 2013. Defect structure of Y-doped ceria on different length scales. *Chemistry of Materials*, *25*(21), pp.4278-4289.

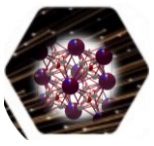

7.1 Supporting Information

Application of "Pseudo-Complex" Structural Analysis Methods to Unravel the complexities of the Ageing Process in Bi_2O_3 "solid solutions"

Sikhumbuzo M. Masina[a], Gugulethu C. Nkala[a,b], Caren Billing[a], Yuanpeng Zhang[c], Daniel Olds[d], Rudolph M. Erasmus[b,e], David G. Billing[a,b]

[a]Molecular Science Institute, School of Chemistry, University of the Witwatersrand, Private Bag X3, Johannesburg, 2050, South Africa

[b]DSI-NRF Centre of Excellence in Strong Materials, University of the Witwatersrand, Private Bag X3, Johannesburg, 2050, South Africa.

[c]Neutron Scattering Division, Oak Ridge National Laboratory, Oak Ridge, Tennessee 37831, United States

[d]National Synchrotron Light Source II, Brookhaven National Laboratory, Upton 11973, New York, United States

[e]Material Physics Research Institute, School of Physics, University of the Witwatersrand, Private Bag X3, Johannesburg, 2050, South Africa.

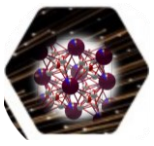

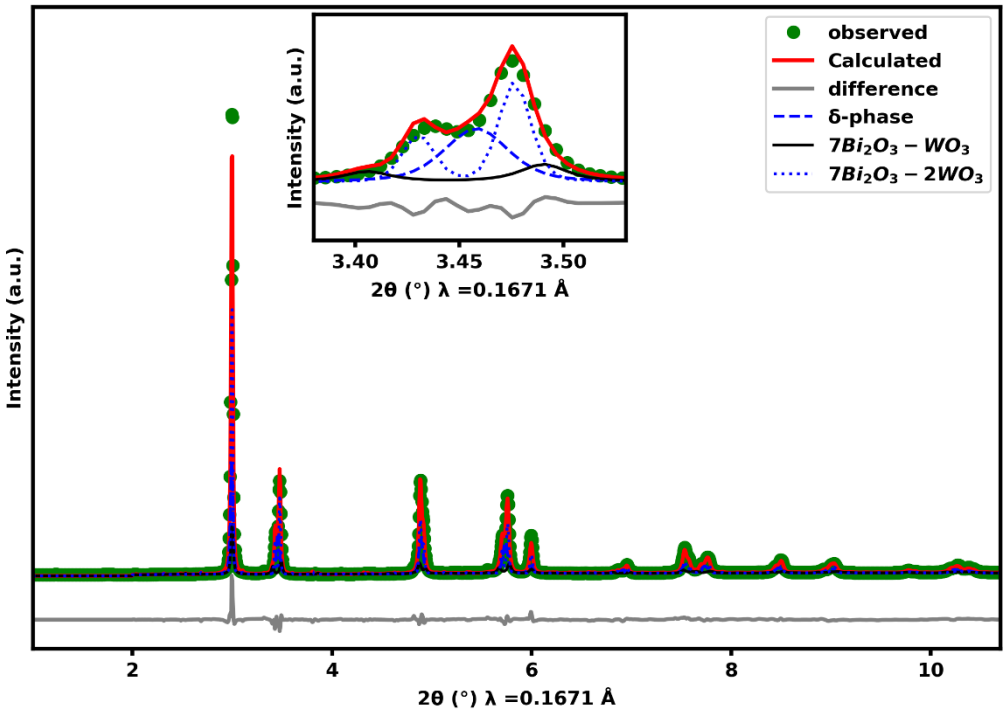

Figure S7.1. Rietveld refinement of the 8D4WSB composition at ambient temperature after annealing for 100 hours at 500 °C.

Table S7.1. Crystallographic data and Rietveld refinement parameters for the 8D4WSB composition at ambient temperatures after annealing for 100 hours at 500 °C. R_{wp} (%) = 10.07

Phases	δ-phase	$7Bi_2O_3$-$2WO_3$	$7Bi_2O_3$-WO_3
Weight %	36(1)	49(1)	15(1)
Space group	*Fm*-3*m*	$I4_1$	*I*4/*m*
a /Å	5.5379(3)	12.3169(5)	8.675(1)
c /Å	-	11.1654(7)	16.870(4)
Cell volume /Å^3	169.84(3)	1693.9(1)	1269.6(6)
Crystal density /g.cm^{-3}	8.839(1)	9.1306(9)	9.139(4)

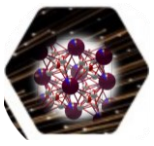

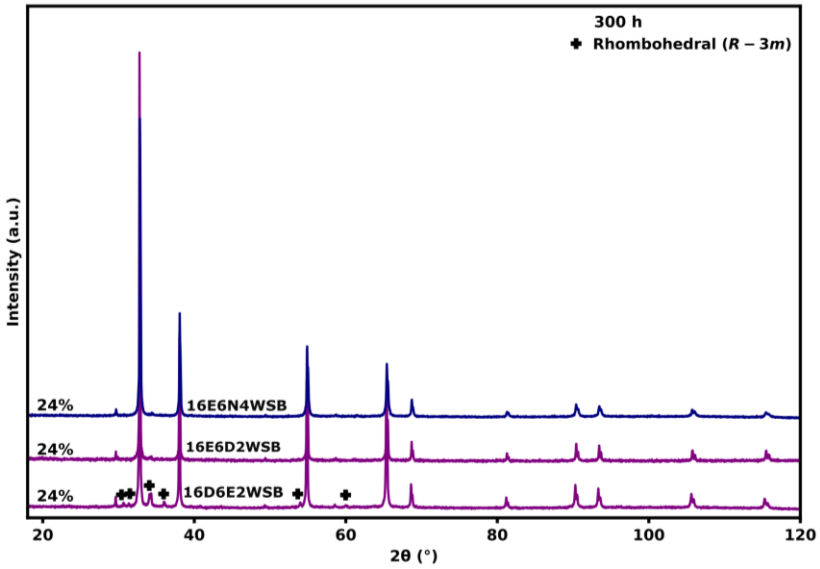

Figure S7.2. PXRD data of the DEWSB and ENWSB systems after annealing at 500 °C for 300 hours showing phase separation in 16D6E2WSB (mixture of the δ- and rhombohedral phases) but none in 16E6D2WSB and 16E6N4WSB. Plots are stacked for clarity.

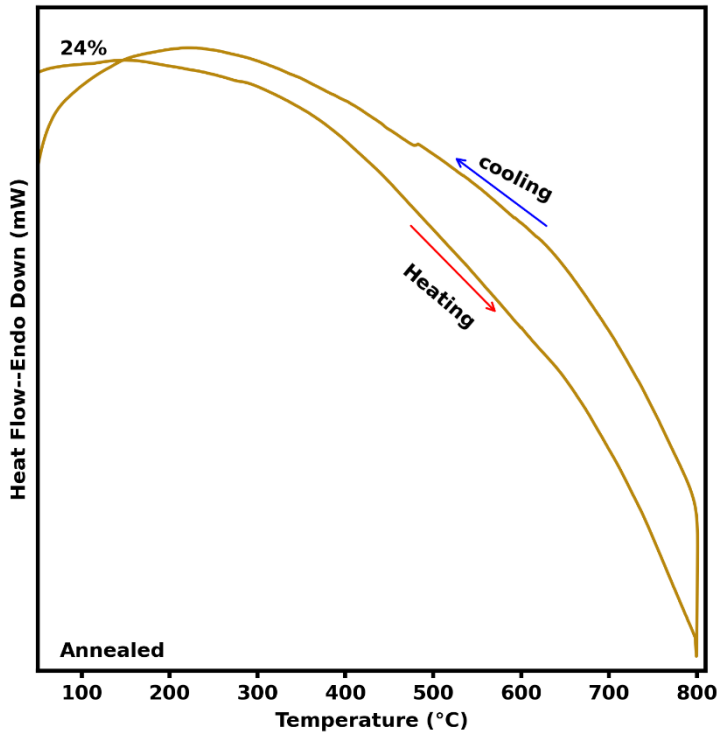

Figure S7.3. DTA curves showing how the 16D8ESB system exhibits no observable endothermic displacement characteristic of the order-disorder transition.

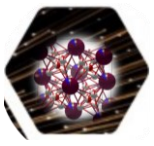

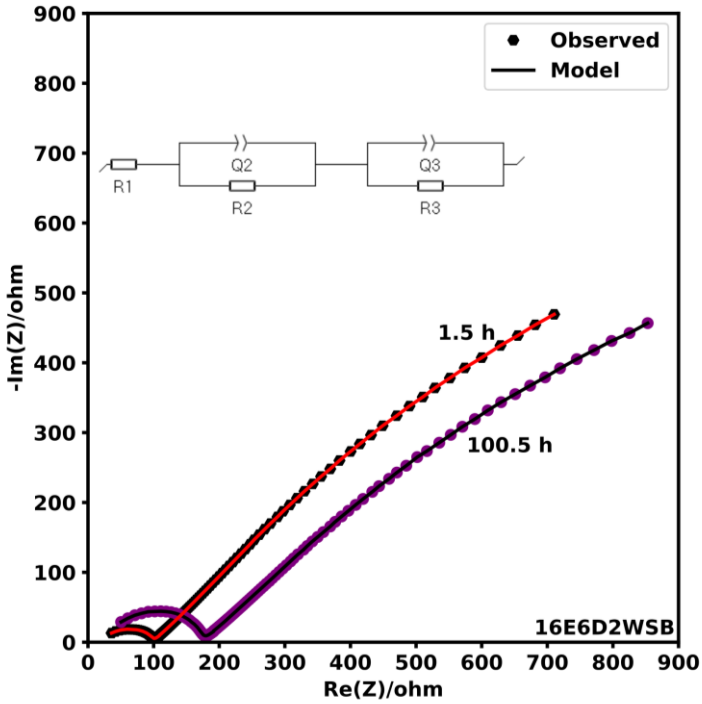

Figure S7.4. Complex impedance plots for data measured in situ at 500 °C for the 16E6D2WSB composition after ~1.5 and 100.5 hours of annealing. Solid lines represent the fit from the given equivalent circuit model.

Table S7.2. EIS data for the 16E6D2WSB composition from ~1.5-100.5 hours obtained after modelling the data using an equivalent circuit. The meaning of the parameters used were described in Refs. [1, 2]. R2 represent the bulk resistance and was used to calculate the conductivities.

Time (h)	R1(Ω)	Q2(F.s $^{(a-1)}$)	a_2	R2(Ω)	Q3(F.s $^{(a-1)}$)	a_3	R3(Ω)
1.5	17.7	80.48 x 10^{-9}	0.575	84.63	125 x 10^{-6}	0.524	3507
3	17.7	70 x 10^{-8}	0.540	84.36	143 x 10^{-6}	0.503	4737
4.5	17.7	70 x 10^{-8}	0.550	85.41	143 x 10^{-6}	0.503	4737
6	17.7	40 x 10^{-8}	0.550	84.12	143 x 10^{-6}	0.501	4629
7.5	17.7	40 x 10^{-8}	0.550	84.12	143 x 10^{-6}	0.501	4629
9	17.7	40 x 10^{-8}	0.550	84.12	143 x 10^{-6}	0.501	4629
10.5	17.7	40 x 10^{-8}	0.550	85.42	141 x 10^{-6}	0.502	4417
12	17.7	95 x 10^{-8}	0.550	85.95	141 x 10^{-6}	0.502	4377
13.5	17.7	40 x 10^{-8}	0.550	87.6	141 x 10^{-6}	0.501	4381
15	17.7	40 x 10^{-8}	0.550	87.6	141 x 10^{-6}	0.501	4381
16.5	17.7	40 x 10^{-8}	0.550	87.6	141 x 10^{-6}	0.501	4381

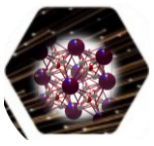

18	17.7	40×10^{-8}	0.550	87.6	141×10^{-6}	0.501	4381
19.5	17.7	40×10^{-8}	0.550	87.62	139×10^{-6}	0.503	4182
21	17.7	40×10^{-8}	0.550	88.84	141×10^{-6}	0.499	4449
22.5	17.7	40×10^{-8}	0.550	88.84	141×10^{-6}	0.499	4449
24	17.7	40×10^{-8}	0.550	88.84	141×10^{-6}	0.499	4449
25.5	17.7	40×10^{-8}	0.550	87.89	141×10^{-6}	0.500	4132
27	17.7	40×10^{-8}	0.550	88.21	140×10^{-6}	0.501	4010
28.5	17.7	40×10^{-8}	0.550	88.82	142×10^{-6}	0.498	4199
30	17.7	40×10^{-8}	0.550	88.23	141×10^{-6}	0.500	3991
31.5	17.7	40×10^{-8}	0.550	89.88	140×10^{-6}	0.499	4083
33	17.7	40×10^{-8}	0.550	89.88	140×10^{-6}	0.499	4083
34.5	17.7	40×10^{-8}	0.550	90.99	139×10^{-6}	0.500	3996
36	17.7	40×10^{-8}	0.550	90.99	139×10^{-6}	0.500	3996
37.5	17.7	40×10^{-8}	0.550	88.68	141×10^{-6}	0.499	3887
39	17.7	40×10^{-8}	0.550	90.02	141×10^{-6}	0.499	3915
40.5	17.7	40×10^{-8}	0.550	92.46	141×10^{-6}	0.497	4037
42	17.7	40×10^{-8}	0.550	93.7	140×10^{-6}	0.498	3982
43.5	17.7	40×10^{-8}	0.550	91.1	141×10^{-6}	0.498	3873
45	17.7	40×10^{-8}	0.550	93.13	141×10^{-6}	0.497	3921
46.5	17.7	40×10^{-8}	0.550	94.13	140×10^{-6}	0.498	3853
48	17.7	40×10^{-8}	0.550	94.13	140×10^{-6}	0.498	3853
49.5	17.7	40×10^{-8}	0.550	95.97	141×10^{-6}	0.497	3833
51	17.7	40×10^{-8}	0.550	95.97	141×10^{-6}	0.497	3833
52.5	17.7	40×10^{-8}	0.550	96.96	141×10^{-6}	0.496	3819
54	17.7	40×10^{-8}	0.550	96.44	140×10^{-6}	0.497	3660
55.5	17.7	30×10^{-8}	0.57	97.17	140×10^{-6}	0.496	3675
57	17.7	30×10^{-8}	0.57	97.17	140×10^{-6}	0.496	3675
58.5	17.7	30×10^{-8}	0.57	97.67	140×10^{-6}	0.497	3605
60	17.7	30×10^{-8}	0.57	97.67	140×10^{-6}	0.497	3605
61.5	17.7	30×10^{-8}	0.57	103.3	140×10^{-6}	0.496	3643
63	17.7	30×10^{-8}	0.57	105.8	141×10^{-6}	0.494	3763
64.5	17.7	30×10^{-8}	0.57	107.3	139×10^{-6}	0.495	3652
66	17.7	30×10^{-8}	0.57	109	140×10^{-6}	0.494	3693
67.5	17.7	30×10^{-8}	0.57	109	140×10^{-6}	0.494	3693
69	17.7	30×10^{-8}	0.57	112	140×10^{-6}	0.493	3673

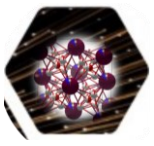

70.5	17.7	30 x 10^{-8}	0.57	112	140 x 10^{-6}	0.493	3673
72	17.7	30 x 10^{-8}	0.57	113.3	141 x 10^{-6}	0.492	3600
73.5	17.7	30 x 10^{-8}	0.57	113.3	141 x 10^{-6}	0.492	3600
75	17.7	30 x 10^{-8}	0.57	117.9	139 x 10^{-6}	0.492	3528
76.5	17.7	30 x 10^{-8}	0.57	119.7	139 x 10^{-6}	0.492	3540
78	17.7	30 x 10^{-8}	0.57	123	139 x 10^{-6}	0.490	3598
79.5	17.7	30 x 10^{-8}	0.57	123	139 x 10^{-6}	0.490	3598
81	17.7	30 x 10^{-8}	0.57	124.7	142 x 10^{-6}	0.487	3639
82.5	17.7	30 x 10^{-8}	0.57	127.7	139 x 10^{-6}	0.489	3595
84	17.7	30 x 10^{-8}	0.57	134.4	138 x 10^{-6}	0.487	3699
85.5	17.7	30 x 10^{-8}	0.57	134.4	138 x 10^{-6}	0.487	3699
87	17.7	30 x 10^{-8}	0.57	134.4	138 x 10^{-6}	0.487	3699
88.5	17.7	30 x 10^{-8}	0.57	134.4	138 x 10^{-6}	0.487	3699
90	17.7	30 x 10^{-8}	0.57	140.4	138 x 10^{-6}	0.486	3577
91.5	17.7	30 x 10^{-8}	0.57	140.4	138 x 10^{-6}	0.486	3577
93	17.7	30 x 10^{-8}	0.57	144.3	138 x 10^{-6}	0.485	3543
94.5	17.7	30 x 10^{-8}	0.600	148.1	138 x 10^{-6}	0.484	3595
96	17.7	30 x 10^{-8}	0.600	151.2	137 x 10^{-6}	0.484	3542
97.5	17.7	30 x 10^{-8}	0.600	150.6	139 x 10^{-6}	0.482	3546
99	17.7	30 x 10^{-8}	0.600	155.9	138 x 10^{-6}	0.481	3643
100.5	17.7	30 x 10^{-8}	0.600	158.1	138 x 10^{-6}	0.481	3647

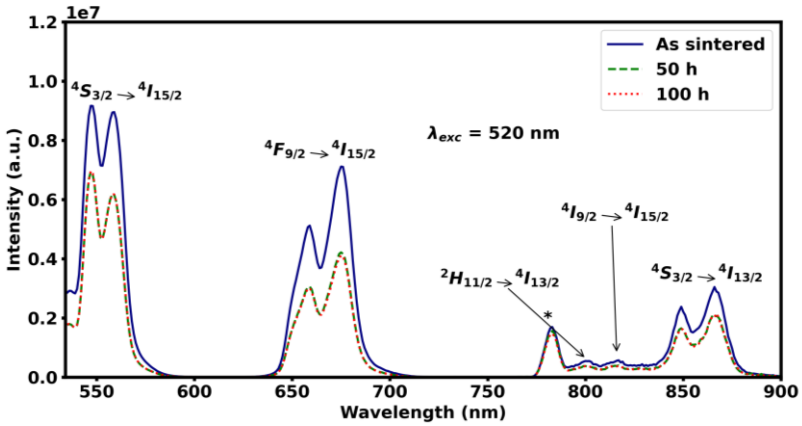

Figure S7.5. PL spectra of 16E6N4WSB measured at ambient temperature after quenching from 850 °C, annealing at 500 °C for 50 and 100 hours. The peak with an asterisk (*) at ~ 782 nm represent an instrument contribution.

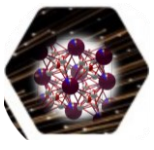

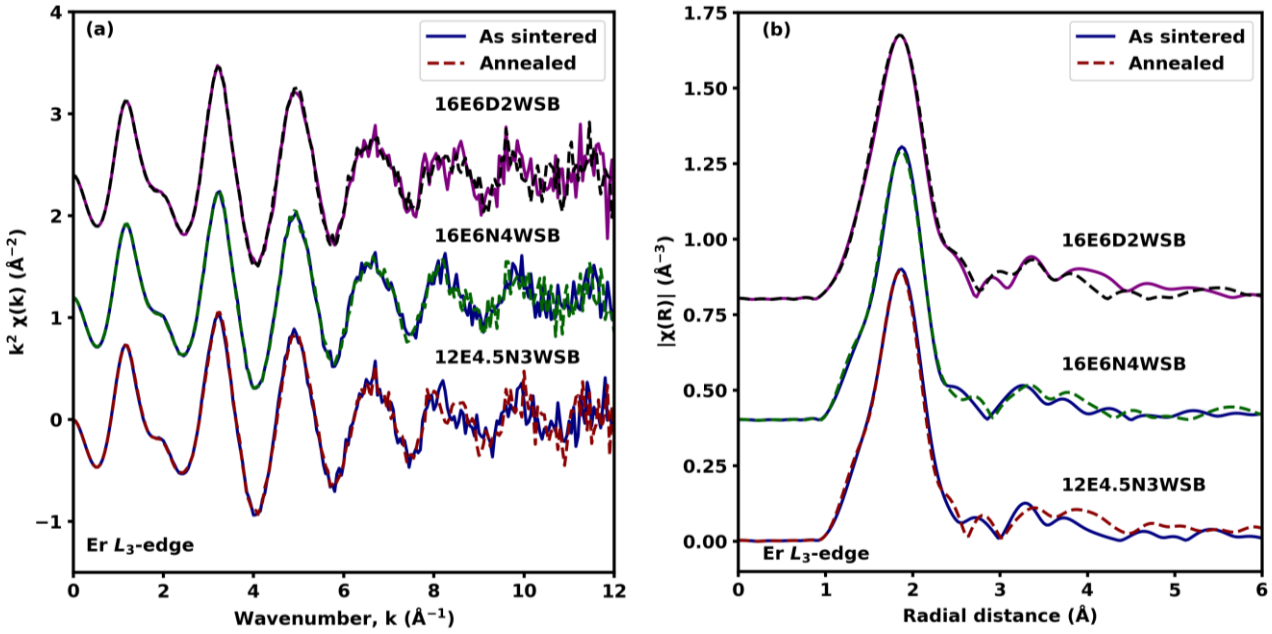

Figure S7.6. **(a)** k^2-weighted Er L_3-edge EXAFS spectra and **(b)** the magnitude of their Fourier transforms before and after annealing at 500 °C for 100 hours for the 12E4.75N2.5WSB, 16E6N4WSB and 16E6D2WSB compositions. Plots are stacked for clarity.

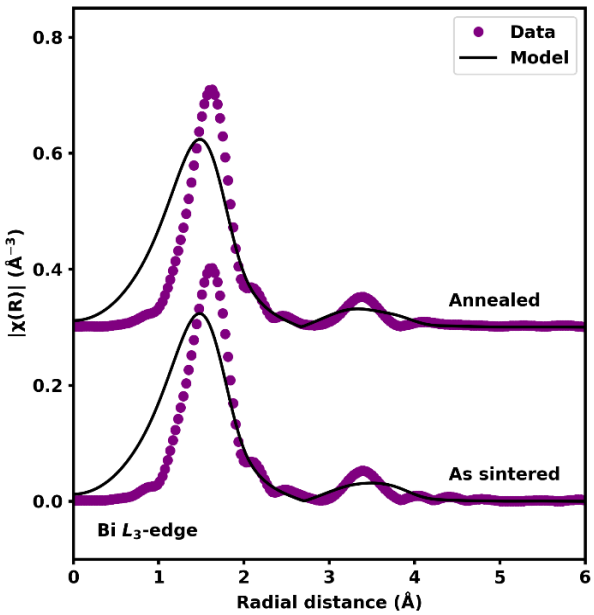

Figure S7.7. Magnitude of the Fourier transformed EXAFS data on the Bi L_3-edge of as sintered and annealed material for the 16E6D2WSB composition. The *Fm*-3*m* model gives a poor fit on both the Bi–O and Bi–Bi peaks. The fitting range in R-space was from 1.200 to ~6.000 Å. Plots are stacked for clarity.

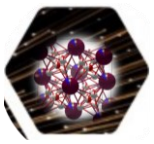

The Bi–O bond length was found to be 2.10±0.04 Å with a coordination number of 6 and the Bi–Bi distance was found to be 4.0±0.1 Å with a degeneracy of 12 when using only the *Fm*-3*m* model. The fits were poor (k-factor =0.35) and these values have no physical meaning.

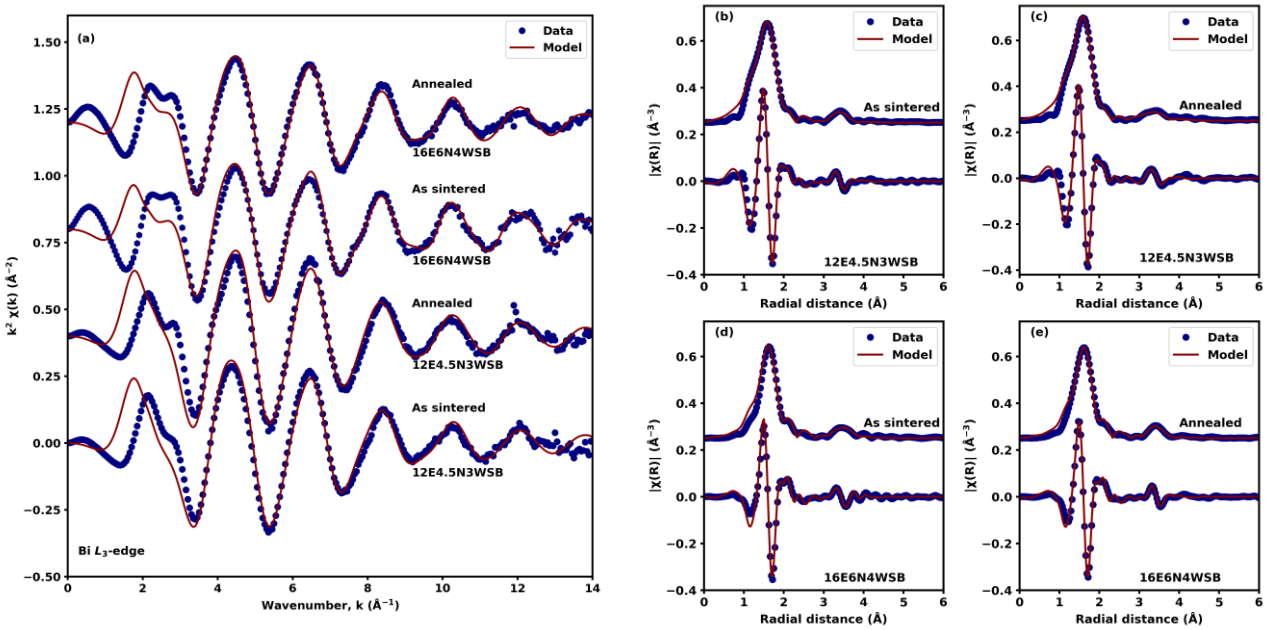

Figure S7.8. (a) k^2-weighted EXAFS data at the Bi L_3-edge for the 16E6N4WSB and 12E4.5N3WSB compositions (fitting range was from 3.000 to ~12.500 Å^{-1}). Magnitude of the Fourier transformed EXAFS data and real component on the Bi L_3-edge of: **(b)** as sintered and **(c)** annealed material for the 12E4.5N3WSB composition. Magnitude of the Fourier transformed EXAFS data and real component on the Bi L_3-edge of: **(d)** as sintered and **(e)** annealed materials for the 16E6N4WSB composition. The fitting range in R-space was from 1.200 to ~6.000 Å. The *Fm*-3*m and* $P2_1/c$ models were used for fitting the data. Plots are stacked for clarity.

Table S7.3. A summary of some parameters used for the EXAFS fitting for the 12E4.5N3WSB, 16E6N4WSB and 16E6D2WSB compositions at the Bi L_3-edge. S_0^2 is the amplitude reduction factor obtained from fitting Bi_2O_3 and fixed. N_{idp} is the number of independent points, P is the number of variables fitted, ΔE_0 is the difference between threshold energy from theory and experiment, Δk is the fitting range in k-space, ΔR is the fitting range in real space and the r-factor measures the closeness of the model to the experimental data.

Parameter	12E4.5N3WSB As sintered	12E4.5N3WSB Annealed	16E6N4WSB As sintered	16E6N4WSB Annealed	16E6D2WSB As sintered	16E6D2WSB Annealed
S_0^2	0.799	0.799	0.799	0.799	0.799	0.799
k-weight	2	2	2	2	2	2
N_{idp}	29	29	29	31	31	29
P	16	16	16	16	16	16
ΔE_0(eV)	-8± 6	-8 ± 6	-9.1± 0.3	-8.8 ± 0.2	-7 ± 2	-7.9 ± 0.2
Δk(Å^{-1})	3.000-12.370	3.000-12.370	3.000-12.450	3.000-12.878	3.000-12.878	3.000-12.675
ΔR(Å)	1.200-6.000	1.200-6.000	1.300-6.000	1.200-6.000	1.200-6.000	1.200-6.000
r-factor	0.019	0.028	0.019	0.015	0.013	0.014

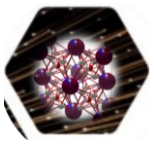

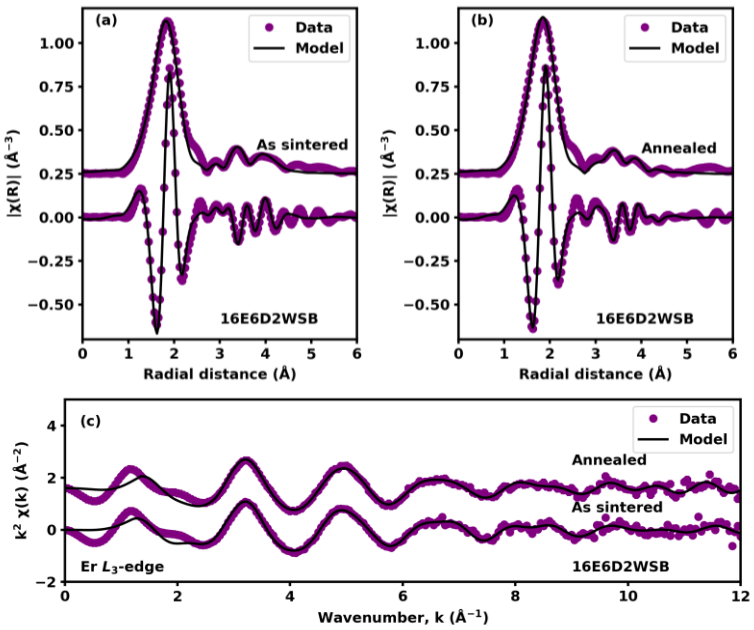

Figure S7.9. A fit to the magnitude of the Fourier transform and its real component of Er L_3-edge EXAFS spectra: **(a)** before and **(b)** after annealing at 500 °C for 100 hours of the 16E6D2WSB composition. The fitting range in R-space was from 1.300 to ~6.000 Å. **(c)** A fit to the k^2-weighted Er L_3-edge EXAFS spectrum (fitting range was from 2.500 to ~10.000 $Å^{-1}$). The *Fm*-3*m and Ia*-3 models were used for fitting the data. Plots are stacked for clarity.

Table S7.4. Summary of the fitted parameters from EXAFS for the 12E4.5N3WSB, 16E6N4WSB and 16E6D2WSB compositions at the Er L_3-edge. Backscattering paths from both *Fm*-3*m and Ia*-3 models were used for fitting.

Sample		12E4.5N3WSB As sintered	12E4.5N3WSB Annealed	16E6N4WSB As sintered	16E6N4WSB Annealed	16E6D2WSB As sintered	16E6D2WSB Annealed
Er—O	N	5.84 ± 0.36	5.73 ± 0.46	5.24 ± 0.38	5.51 ± 0.31	5.53 ± 0.16	5.92 ± 0.62
	R(Å)	2.313 ± 0.005	2.306 ± 0.006	2.319 ± 0.006	2.315 ± 0.004	2.314 ± 0.009	2.315 ± 0.009
	σ^2(Å^2)	0.0083 ± 0.0009	0.008 ± 0.001	0.007 ± 0.001	0.0078 ± 0.0008	0.009 ± 0.001	0.009 ± 0.001
Er—Bi	N	9.00	9.00	9.00	9.00	9.00	9.00
	R(Å)	3.73 ± 0.03	3.79 ± 0.06	3.78 ± 0.06	3.78 ± 0.07	3.81 ± 0.04	3.93 ± 0.07
	σ^2(Å^2)	0.023 ± 0.005	0.026 ± 0.001	0.04 ± 0.01	0.03 ± 0.01	0.0184 ± 0.005	0.03 ± 0.01
Er—Er	N	2.00	2.00	2.00	2.00	2.00	2.00
	R(Å)	3.66 ± 0.02	3.73 ± 0.03	3.67 ± 0.01	3.70 ± 0.02	3.68 ± 0.02	3.73 ± 0.02
	σ^2(Å^2)	0.006 ± 0.002	0.008 ± 0.002	0.006 ± 0.002	0.007 ± 0.002	0.00166 ± 0.003	0.004 ± 0.002
Er—Er	N	1.00	1.00	1.00	1.00	1.00	1.00
	R(Å)	3.86 ± 0.07	4.12 ± 0.04	3.83 ± 0.04	3.86 ± 0.4	3.83 ± 0.03	3.96 ± 0.1
	σ^2(Å^2)	0.01 ± 0.01	0.006 ± 0.005	0.008 ± 0.006	0.03 ± 0.08	0.003	0.01 ± 0.01

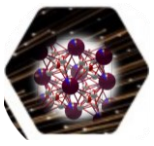

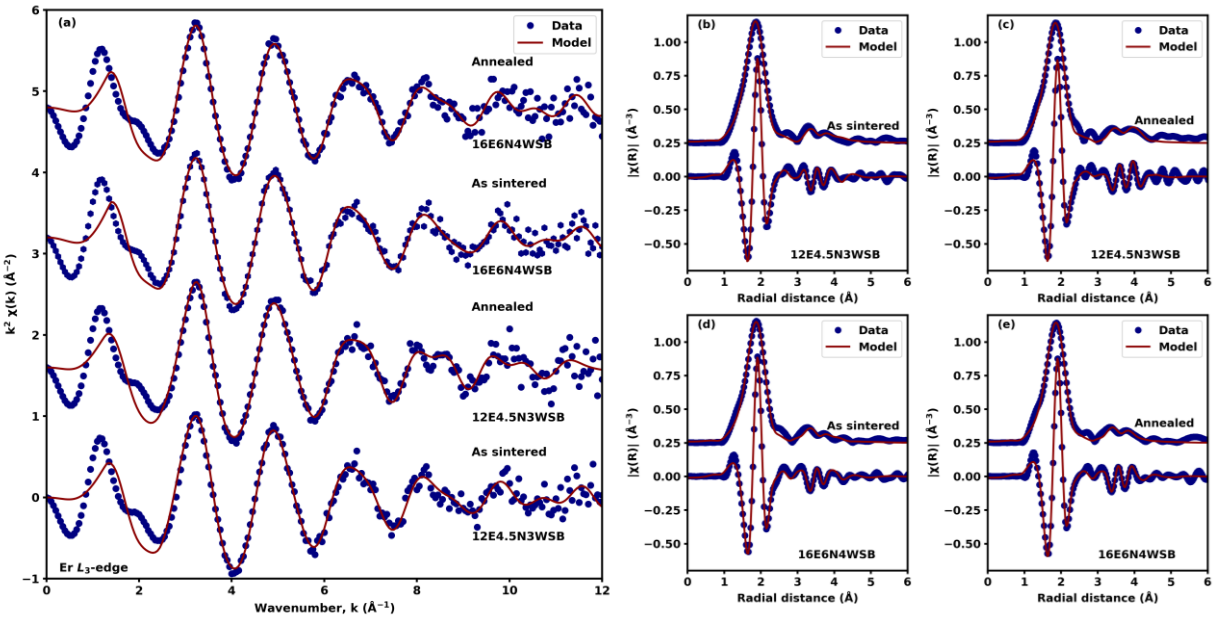

Figure S7.10. **(a)** Fitted k^2-weighted EXAFS data at the Er L_3-edge for the 16E6N4WSB and 12E4.5N3WSB compositions (fitting range was from 2.500 to ~10.000 Å^{-1}). Fitted magnitude of the Fourier transformed EXAFS data and its real component at the Er L_3-edge of: **(b)** as sintered and **(c)** annealed material for the 12E4.5N3WSB composition. Fitted magnitude of the Fourier transformed EXAFS data and its real component at the Er L_3-edge of: **(d)** as sintered and **(e)** annealed materials for the 16E6N4WSB composition. The fitting range in R-space was from 1.300 to ~6.000 Å. Plots are stacked for clarity.

Table S7.5. A summary of some parameters used for the EXAFS fitting for the 12E4.5N3WSB, 16E6N4WSB and 16E6D2WSB compositions at the Er L_3-edge. S_0^2 is the amplitude reduction factor obtained from fitting Er_2O_3 and fixed. N_{idp} is the number of independent points, P is the number of variables fitted, ΔE_0 is difference between threshold energy from theory and experiment, Δk is the fitting range in k-space, ΔR is the fitting range in real space and the r-factor measures the closeness of the model to the experimental data.

Parameter	12E4.5N3WSB As sintered	12E4.5N3WSB Annealed	16E6N4WSB As sintered	16E6N4WSB Annealed	16E6D2WSB As sintered	16E6D2WSB Annealed
S_0^2	1.00 ± 0.07	1.00±0.07	1.00±0.07	1.00±0.07	1.00±0.07	1.00±0.07
k-weight	2	2	2	2	2	2
N_{idp}	27	27	27	27	27	27
P	12	12	12	12	12	12
ΔE_0(eV)	6.4 ± 0.5	6.2 ± 0.7	7.4± 0.2	7.0 ± 0.4	7.1 ± 0.8	7.0 ± 0.2
Δk(Å^{-1})	2.500-11.220	2.500-11.220	2.500-11.220	2.500-11.200	2.500-10.191	2.500-10.191
ΔR(Å)	1.240-6.000	1.240-6.000	1.270-6.000	1.270-6.000	1.300-6.000	1.300-6.000
r-factor	0.012	0.020	0.009	0.010	0.019	0.014

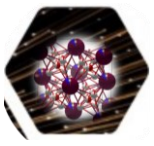

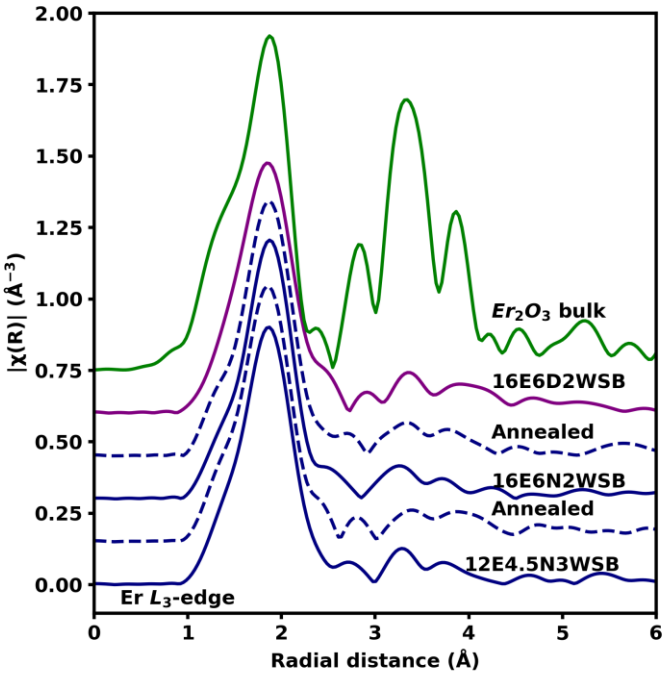

Figure S7.11. The magnitude of the Fourier transforms of the k^2-weighted Er L_3-edge EXAFS data for the Er_2O_3, EDWSB and ENWSB systems. Plots are stacked for clarity.

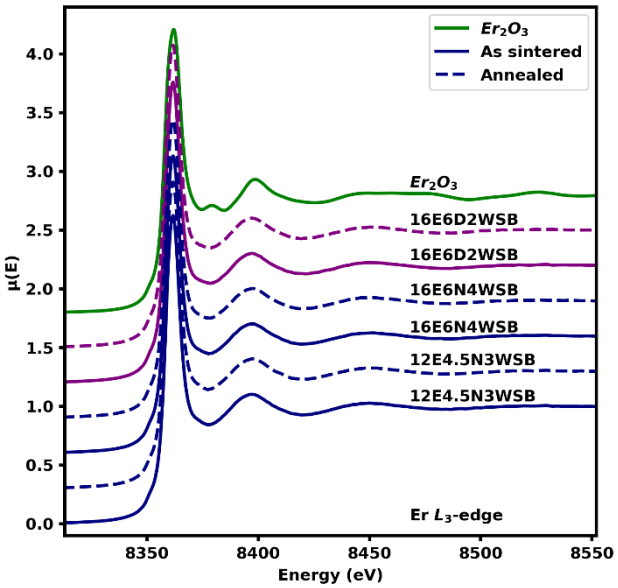

Figure S7.12. XAFS spectra at the Er L_3-edge of commercial Er_2O_3, EDWSB and ENWSB systems. Plots are stacked for clarity.

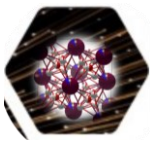

Table S7.6. Summary of the fitted parameters for the 16E6D2WSB composition obtained from RMC modelling as implemented in the RMCProfile code [3, 4]. Mode distance value was taken from the highest point of the first peak of the partial PDFs($g_{ij}(r)$) after fitting gaussians. The mean distance is a weighted mean calculated by using the centroids and area of the different gaussians used for integrating the first peak.

Distance type	Length (Å)	N	Distance type	Length (Å)	N
Bi–Bi mode	3.78	-	Bi–O mode	2.15 ± 0.01	-
Bi–Bi mean	3.94 ± 0.01	10.22 ± 0.17	Bi–O mean	2.35 ± 0.003	4.86 ± 0.19
Bi–Er mode	3.72	-	Er–O mode	2.13 ± 0.009	-
Bi–Er mean	3.89 ± 0.01	2.30 ± 0.04	Er–O mean	2.31 ± 0.007	6.24 ± 0.12
Er–Er mode	3.66± 0.02	-	-	-	-
Er–Er mean	3.83 ± 0.01	3.02 ± 0.24	-	-	-

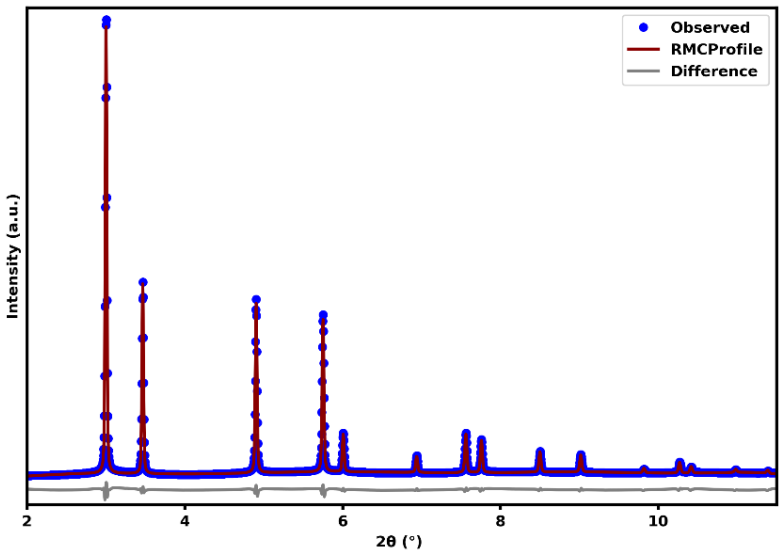

Figure S7.13. Bragg data of the 16E6D2WSB system after annealing at 500 °C for 100 hours fitted using RMC modelling as implemented in the RMCProfile code [3, 4].

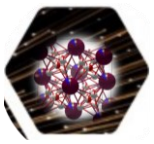

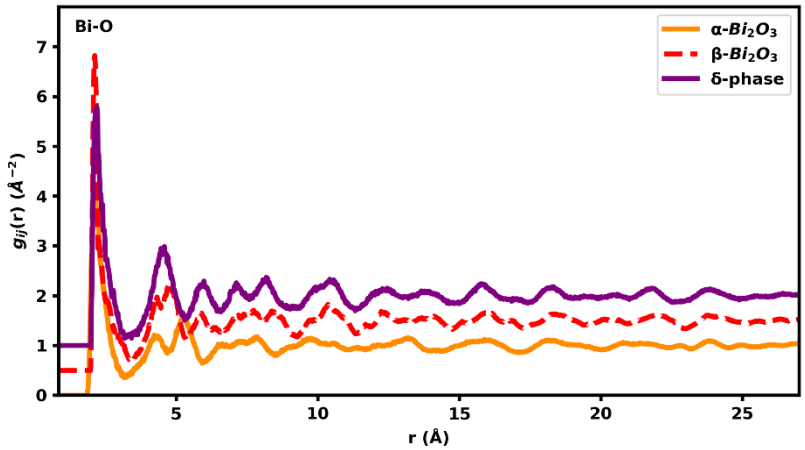

Figure S7.14. Ion-ion pair correlation functions of Bi–O pairs for the α-Bi_2O_3, β-Bi_2O_3 and stabilized δ-phases obtained from Big-box modelling as implemented in the RMCProfile code [3, 4]. These pair correlation functions show how the Bi–O environment is similar for the three phases at less than 4 Å but differ at long r-range. Plots are stacked for clarity.

References

[1] Masina, S.M., Billing, C., Erasmus, R.M. and Billing, D.G., 2021. Insights on the phase transitions, stability and conductivity in the Bi_2O_3-WO_3 system. *Journal of Electroceramics*, *46*(2), pp.47-56.

[2] Barsoukov, E. and Macdonald, J.R., 2005. *Impedance Spectroscopy Theory, Experiment, and. Applications, 2nd ed. (Hoboken, NJ: John Wiley &Sons, Inc., 2005)*.

[3] Tucker, M.G., Keen, D.A., Dove, M.T., Goodwin, A.L. and Hui, Q., 2007. RMCProfile: reverse Monte Carlo for polycrystalline materials. *Journal of Physics: Condensed Matter*, *19*(33), p.335218.

[4] Zhang, Y., Eremenko, M., Krayzman, V., Tucker, M.G. and Levin, I., 2020. New capabilities for enhancement of RMCProfile: instrumental profiles with arbitrary peak shapes for structural refinements using the reverse Monte Carlo method. *Journal of Applied Crystallography*, *53*(6), pp.1509-1518.

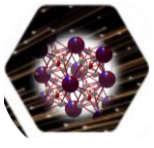

Chapter 8: General Conclusions and Recommendations

A range of different substituted bismuth oxide systems were fabricated and characterised using different but complementary techniques. These techniques included in-house powder X-ray diffraction, synchrotron powder X-ray diffraction, the pair distribution function, Raman spectroscopy, X-ray absorption spectroscopy, photoluminescence, differential thermal analysis and electrochemical impedance spectroscopy. The structures of the systems were probed at different length scales (long and short range) and changes in structure were correlated with the physical property, namely, conductivity. The trends across the various systems and the structure-property correlations established in this work have been summarized here. This work has also raised some questions that can be probed in further studies.

8.1 The effects of W, Dy and/or Er on phase stability

This work confirmed the observations made by Nespolo *et al.* [1] and Watanabe and Ono [2] that W on its own in the Bi_2O_3-WO_3 system did not stabilize the δ-phase. It was found in this work that, a mixture of two tetragonal phases ($7Bi_2O_3{\cdot}2WO_3$ and $7Bi_2O_3{\cdot}WO_3$) are the true equilibrium phases for the Bi_2O_3-WO_3 system in the composition range 22-27 mol% of WO_3. The $7Bi_2O_3{\cdot}2WO_3$ composition has a structure related to that of the δ-phase as discussed in Chapter 1 and was reported to have high conductivity [3]. Therefore, it is easy to erroneously determine its structure to be that of the δ-phase, especially when using in-house x-ray diffraction methods where the superlattice reflections are not clearly visible. It was also observed in this work that the phase fractions of the $7Bi_2O_3{\cdot}2WO_3$ and $7Bi_2O_3{\cdot}WO_3$ phases depends on both annealing temperature and content of WO_3. High annealing temperature (≥ 650 °C) and high WO_3 content favours the highly conductive $7Bi_2O_3{\cdot}2WO_3$ phase. The conductivity of the mixture of the two phases in the composition with 22 mol% WO_3 was found to be higher than that of YSZ but slightly lower than the phase that was reported by Takahashi and Iwahara to be the pure δ-phase [4].

Addition of Dy_2O_3 on the Bi_2O_3-WO_3 system led to the Bi_2O_3-Dy_2O_3-WO_3 system, hence forth referred to as DWSB (Dy, and W stabilised bismuth oxide). Stabilization of the δ-phase was achieved when the Dy_2O_3 and WO_3 contents were in the 2:1 ratio. The minimum total substituent concentration (TSC) with respect to the oxides needed to stabilise the δ-phase was found to be 15 mol% when the material was annealed for about 70 hours and slow cooled to ambient temperatures.

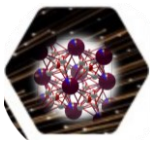

However, when the material annealed for 70 hours was pelletized and annealed for 24 more hours, the δ-phase was stabilised at 12 mol% in this system. This was significant because WO_3 on its own did not stabilise the δ-phase in the Bi_2O_3-WO_3 system and 28.5 mol% of Dy_2O_3 was needed to stabilise the δ-phase in the Bi_2O_3-Dy_2O_3 system as discussed in Chapter 1. Codoping was confirmed to help stabilise the δ-phase at reduced total substituent concentrations compared to the singly substituted systems. However, isothermal annealing at ~500 °C for 100 hrs resulted in phase degradation for all compositions explored in the DWSB system as reported in Chapters 4 and 7. The inability of WO_3 to stabilise the δ-phase on its own and the phase degradation exhibited by the DWSB system had been observed before [1, 2, 5]. This was repeated in this work to verify the findings and use this as a basis for finding materials which exhibit the high conductivities shown by the DWSB systems while maintaining phase stability even after isothermal annealing at ~500 °C for a prolonged period.

Er when combined with W was found by Watanabe and Sekita [6] to create a system Bi_2O_3-Er_2O_3-WO_3 (EWSB) that was resistant to the phase degradation exhibited by DWSB after isothermal annealing for a prolonged period and was resistant to the ageing phenomenon. This led to the design of the novel quaternary oxide Bi_2O_3-Dy_2O_3-Er_2O_3-WO_3 (DEWSB) explored in this work and found to possess both the high conductivity shown by DWSB and improved stability exhibited by EWSB. The newly designed system did not show the phase degradation experienced by DWSB after isothermal annealing at virtually identical conditions as those used in DWSB and maintained the high conductivity exhibited by DWSB at ~700 °C. This means that the addition of Er into the DWSB system did introduce the stability observed in EWSB and had very little impact on the conductivity as well.

The addition of Er into DWSB also had an impact on the phase evolution observed during heating in DEWSB where the total substituent concentration was 12 mol% (8D3E1WSB). When slow cooled, the 8D3E1WSB composition was found to have a mixture of the β-Bi_2O_3 like tetragonal (β-) and δ-phases at ambient temperature which transformed to the pure δ-phase at high temperature. This is in contrast to the 8D4WSB composition which was found to have a mixture of δ-, $7Bi_2O_3{\cdot}2WO_3$ and $7Bi_2O_3{\cdot}WO_3$ phases at ambient temperatures and transformed to the δ-phase at high temperature. This highlighted the impact of adding Er and reducing the WO_3 content not only on phase stability, but also on the pathway taken to obtain the δ-phase. It should be noted

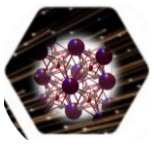

that the presence of $7Bi_2O_3 \cdot 2WO_3$ and β-phase, since they have a structure similar to that of the δ-phase, it was difficult to discern them at ambient temperature. It only took the use of VT-PXRD and Raman spectroscopy to detect and identify them (see discussion in Chapter 4). This highlighted the need to use complementary techniques to probe the structure of the material to confirm the actual phases present.

8.2 The Bi_2O_3-Dy_2O_3-Er_2O_3 (DESB) system compared to DWSB and DEWSB

When comparing the two general systems, DWSB and DEWSB, the role of W in stabilising the δ-phase during the isothermal annealing at ~500 °C for 100 hrs was not apparent, but it was clear that the addition of Er to DWSB helped improve the stability. To investigate the effects of W on the stability observed in the DEWSB system upon prolonged isothermal annealing, the DESB system was created, where W was removed completely and replaced with Er while keeping the TSC constant. The prolonged isothermal annealing was done under virtually identical conditions to those used in the DWSB and DEWSB systems. It was observed that the DESB system suffered from phase degradation (where the pure δ-phase transformed to a mixture of the δ- and rhombohedral phases). This highlighted the importance of WO_3 in stabilising the δ-phase in the DEWSB system when combined with Er. It can be argued that the number of impurity cations, via the configurational entropy stabilization, plays a role in stabilising the δ-phase in DEWSB than the role played by Er and W, but EWSB was also shown to be resistant to phase degradation at similar TSC and has the same number of impurity cations as DWSB and DESB [6].

Interestingly, the 8D4ESB composition also showed an apparent pure δ-phase at ambient temperature when slow-cooled (as was also done for the 8D4WSB and 8D3E1WSB compositions). It was only after using VT-SXRD, VT-PDF, VT-EIS and the advanced symmetry mode-based Rietveld refinement analysis technique that the phase present at ambient temperature was found not to be the pure δ-phase, but a distorted version of this phase with tetragonal symmetry (see discussion in Chapter 5). This again, highlighted the need to use advanced analysis techniques to unravel the complexities inherent in analysing structural details in phases with close symmetry relationships.

It is also noteworthy that the initial phase/s present at ambient temperature in 8D4ESB is slightly different to those present in 8D3E1WSB, but significantly different than those in 8D4WSB. Consequently, the phase evolution as a function of temperature in 8D4ESB is also slightly different

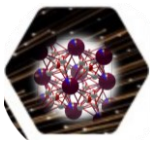

to that in 8D3E1WSB and significantly different to that in 8D4WSB (see Chapters 4 and 5). However, the final product at high temperature in all three compositions is the pure δ-phase and consequently, the conductivities of these three compositions follow the same behaviour as the phase evolution, i.e., different at low temperatures but very similar at high temperatures (see Chapters 4 and 5). This highlights the correlation between conductivity and the structure of a material, which is linked to the identity of the elements present and their concentration.

8.3 The Effects of the Dy and Nb Cations on Phase Stability and the Ageing Phenomenon

The composition 15Er2.5Nb2.5WSB in the ENWSB system (ratio Er:Nb:W is 6:1:1) was shown to resist phase separation and the ageing phenomenon by Shitara *et al*. [7]. In this work, a similar system was created with a ratio of Er:Nb:W of 8:3:1 and the 16E6N2WSB (where the ratio is with respect to cations) composition was shown to resist both phase separation and the ageing phenomenon during isothermal annealing at ~500 °C for 100 hours.

An analogous, novel system DNWSB was also fabricated to observe the effects of Dy on phase stability and/or its effect on the ageing phenomenon. The diffraction pattern of 16D6N2WSB after isothermal annealing at ~500 °C for 100 hours showed anisotropic peak broadening, evidence of phase degradation (see Chapter 7). This indicated that the Dy cations, when mixed with Nb and W in the given ratio and total substituent concentration do not prevent the phase degradation as much as Er does. This was further confirmed when the compositions 16D6E2WSB and 6D16E2WSB (here the ratio is with respect to the metal oxides in both compositions) were isothermally annealed at ~500 °C for 300 hours and compared. The 16D6E2WSB composition, with higher Dy content, finally exhibited phase separation into a mixture of a rhombohedral phase and the δ-phase while the 6D16E2WSB composition, with lower Dy content, maintained the pure δ-phase under virtually identical conditions. The reduced phase stability upon introducing more Dy compared to Er is not fully understood. Whether it is purely the differences in ionic radii or the effects of the different number of 4f electrons between Dy and Er that causes the difference in phase stability is not fully understood and was not explored in this work. This question falls under the realm of electronic structure calculations such as density functional theory and *ab initio* molecular dynamics and needs to be probed further.

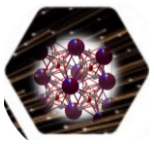

The role of the Nb cation on both phase stability and the ageing phenomenon was not explored in Ref. [7]. In this work, a novel system DENSB was fabricated to investigate this. It was found that the introduction of Nb improved the phase stability on the DESB system, i.e., DENSB showed no observable phase degradation while DESB, as discussed earlier and in Chapter 7, exhibited phase separation after annealing for 100 hours at 500 °C. However, the 16D6E2NSB composition, after annealing for 100 hours at 500 °C, exhibited an endothermic displacement characteristic of the ordering of the local structure in the DTA curve. This meant that at the given concentration, Nb was able to prevent the phase separation, but could not prevent the ordering of the local structure in this composition.

8.4 The Effects of the Substituents on the Metal Sublattice in the δ-phase

Most studies assume that the substituent cations in the stabilised pure δ-phases are distributed randomly in the 4*a* site in the defect fluorite structure and they focus more on the oxygen sublattice since it is the mobile ion [8-10]. However, some studies have suggested that Er and Yb do exhibit some ordering phenomenon at the local level, and sometimes are displaced away from the 4*a* site [11, 12]. Some authors have warned about treating the metal sublattice as a rigid framework through which the oxide ions diffuse [11] and have shown that the cations (including the host) can be displaced away from the 4*a* sites and that the cation sublattice is also dynamic. In this work, X-ray PDF, XAS and PL were used as local probes to study the metal sublattice and the oxide ion distribution around the host cation and some of the substituents.

The X-ray PDF revealed (for the first time in Bi_2O_3 solid solutions) that in the DESB, DEWSB and DENSB systems (Chapter 6), the Bi cations are displaced slightly from the 4*a* site and resemble the local arrangements of Bi cations in the α-Bi_2O_3 phase. Both the X-ray PDF and EXAFS indicated that the distribution of the oxygens around the Bi cations is similar to that found in α-Bi_2O_3 and β-Bi_2O_3 as reported by Hull *et al.* [13] and Norberg *et al.* [14] (see Chapters 6 and 7). The average structure of these materials is still the defect fluorite structure. It was also shown through big-box modelling of total scattering data, EXAFS and XANES analysis that some of the Er and Dy cations and the oxide ions around them assume a similar but distorted arrangement as in their parent oxides (space group *Ia*-3). It is as though the Er and Dy cations cluster in very small droplet-like domains that extend over only about 4 – 5 Å. This means that the vacancies at the local level are slightly ordered and could be one of the reasons why upon substituting with Er

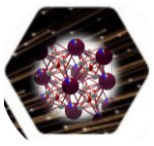

and/or Dy the material experience a decrease in conductivity compared to the pure δ-Bi_2O_3 phase at high temperatures. This needs to be probed further by using ab initio molecular dynamics and theoretical XANES.

After the ageing phenomenon, XANES indicated that some of the environments around the Er cations resembled more those found in its pure oxide. This means that the intrinsic oxygen vacancies order along the <110> and <111> directions (see Chapter 7). So if domains resembling more the arrangement of oxygens and vacancies in Er_2O_3 exist within the δ-phases, the oxide ions moving through the material might be partly blocked in these regions and conductivity would decrease significantly as observed in rare earth doped ceria [15]. It was also shown through photoluminescence that indeed some of the Er cations in the substituted materials are not occupying centrosymmetric sites. This was also the case for material which exhibited ageing. This suggested that as the material ages, the Er cations maintain a non-centrosymmetric environment. This contradicts the models used to describe ageing in solid solutions of bismuth oxide where the vacancies are said to only order along the <111> direction where the oxygens and vacancies form a simple cubic system arrangement around the cations. More work still needs to be done to understand the ageing phenomenon. Neutron total scattering data of aged and as sintered materials needs to be collected and analysed using big-box modelling that also incorporates X-ray total scattering and EXAFS data simultaneously. High resolution transmission electron microscopy would also help in revealing any extra superlattice reflections during the ordering of the local structure should the ordering lead to superstructure formation.

XANES analysis of the oxygen arrangement around the W was also found not to strictly form an octahedral coordination, it had a mixture of both octahedral and tetrahedral coordination. This means that some of the W cations will not occupy the 4*a* site (strictly O_h), and as a consequence of this, occupancy of interstitial sites such as 48*i* and interstitial-like sites such as 32*f* was found to increase with increase in W concentration. If the W is replacing a bigger cation that favours the occupation of the regular 8*c* site for its bonded oxygens, it results in unit cell expansion. This was noted by Refs. [9, 16] and is observed here using XANES for the first time, to the author's knowledge, and explains the unit cell expansion observed from Rietveld analysis in systems where Er was replaced by either W and/or Nb (see Chapter 6).

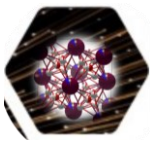

In this work, it was shown that each element has an effect on phase stability on the substituted systems of bismuth oxide. Changes in both the average and local structure were shown to impact the conductivity of the material and confirm a correlation between the structure and the physical property of conductivity. This work has demonstrated the possibility of using rational design to fabricate novel materials with improved stability which has the potential for use in SOFCs. The systematic study of the contribution of each substituent to phase stability demonstrated the need to carefully study the effects of the components that make up the material. This study also demonstrated that the average structure on its own is not enough to describe the true structure of the material, but the local structure is also a vital component of the puzzle and the two are not always the same. Most importantly, complementary techniques are vital in trying to solve a complex problem such as designing complex functional materials with the desired physical properties.

8.5 References

[1] Nespolo, M., Watanabe, A. and Suetsugu, Y., 2002. Re-Investigation of the Structure of $7Bi_2O_3 \cdot 2WO_3$ by Single-Crystal X-ray Diffraction. *Crystal Research and Technology: Journal of Experimental and Industrial Crystallography*, *37*(4), pp.414-422.

[2] Watanabe, A. and Ono, A., 2004. Thermostable region of an oxide ion conductor, $Bi_7WO_{13.5}$ (= $7Bi_2O_3 \cdot 2WO_3$), and the solid solubility extension. *Solid State Ionics*, *174*(1-4), pp.15-18.

[3] Borowska-Centkowska, A., Leszczynska, M., Krok, F., Malys, M., Wrobel, W., Hull, S. and Abrahams, I., 2018. Local structure and conductivity behaviour in $Bi_7WO_{13.5}$. *Journal of Materials Chemistry A*, *6*(13), pp.5407-5418.

[4] Takahashi, T. and Iwahara, H., 1973. High oxide ion conduction in sintered oxides of the system Bi_2O_3-WO_3. *Journal of Applied Electrochemistry*, *3*(1), pp.65-72.

[5] Jung, D.W., Duncan, K.L., Camaratta, M.A., Lee, K.T., Nino, J.C. and Wachsman, E.D., 2010. Effect of Annealing Temperature and Dopant Concentration on the Conductivity Behavior in $(DyO_{1.5})_x$–$(WO_3)_y$–$(BiO_{1.5})_{1-x-y}$. *Journal of the American Ceramic Society*, *93*(5), pp.1384-1391.

[6] Watanabe, A. and Sekita, M., 2005. Stabilized δ-Bi_2O_3 phase in the system Bi_2O_3–Er_2O_3–WO_3 and its oxide-ion conduction. *Solid State Ionics*, *176*(31-34), pp.2429-2433.

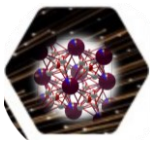

[7] Shitara, K., Moriasa, T., Sumitani, A., Seko, A., Hayashi, H., Koyama, Y., Huang, R., Han, D., Moriwake, H. and Tanaka, I., 2017. First-principles selection of solute elements for Er-stabilized Bi_2O_3 oxide-ion conductor with improved long-term stability at moderate temperatures. *Chemistry of Materials*, *29*(8), pp.3763-3768.

[8] Krynski, M., Wrobel, W., Dygas, J.R., Wrobel, J., Malys, M., Śpiewak, P., Kurzydlowski, K.J., Krok, F. and Abrahams, I., 2013. Ab-initio molecular dynamics simulation of δ-Bi_3YO_6. *Solid State Ionics*, *245*, pp.43-48.

[9] Borowska-Centkowska, A., Leszczynska, M., Wrobel, W., Malys, M., Hull, S., Krok, F. and Abrahams, I., 2020. Stability of tungsten-doped δ-Bi_3YO_6. *Solid State Ionics*, *345*, p.115173.

[10] Leszczynska, M., Liu, X., Wrobel, W., Malys, M., Norberg, S.T., Hull, S., Krok, F. and Abrahams, I., 2013. Total scattering analysis of cation coordination and vacancy pair distribution in Yb substituted δ-Bi_2O_3. *Journal of Physics: Condensed Matter*, *25*(45), p.454207.

[11] Battle, P.D., Catlow, C.R.A. and Moroney, L.M., 1987. Structural and dynamical studies of δ-Bi_2O_3 oxide-ion conductors: II. A structural comparison of $(Bi_2O_3)_{1-x}(M_2O_3)_x$ for M= Y, Er, and Yb. *Journal of Solid State Chemistry*, *67*(1), pp.42-50.

[12] Battle, P.D., Catlow, C.R.A., Chadwick, A.V., Cox, P., Greaves, G.N. and Moroney, L.M., 1987. Structural and dynamical studies of δ-Bi_2O_3 oxide ion conductors: IV. An EXAFS investigation of $(Bi_2O_3)_{1-x}(M_2O_3)_x$ for M= Y, Er, and Yb. *Journal of Solid State Chemistry*, *69*(2), pp.230-239.

[13] Hull, S., Norberg, S.T., Tucker, M.G., Eriksson, S.G., Mohn, C.E. and Stølen, S., 2009. Neutron total scattering study of the δ and β phases of Bi_2O_3. *Dalton transactions*, (40), pp.8737-8745.

[14] Norberg, S.T., Eriksson, S.G. and Hull, S., 2011. Comparison of short-range ion–ion correlations in the α, β and δ phases of Bi_2O_3. *Solid State Ionics*, *192*(1), pp.409-412.

[15] Ou, D.R., Mori, T., Ye, F., Kobayashi, T., Zou, J., Auchterlonie, G. and Drennan, J., 2006. Oxygen vacancy ordering in heavily rare-earth-doped ceria. *Applied Physics Letters*, *89*(17), p.171911.

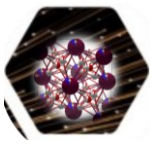

[16] Leszczynska, M., Liu, X., Wrobel, W., Malys, M., Dygas, J.R., Norberg, S.T., Hull, S., Krok, F. and Abrahams, I., 2014. Oxide ion distribution, vacancy ordering and electrical behaviour in the Bi_3NbO_7–Bi_3YbO_6 pseudo-binary system. *Journal of Materials Chemistry A*, *2*(43), pp.18624-18634.

